Characterization and modeling of the dichroic mirror of the Euclid space telescope

Maël Baron

Université Claude Bernard Lyon 1

THESE de DOCTORAT DE L'UNIVERSITE CLAUDE BERNARD LYON 1

Ecole Doctorale 52
Physique et Astrophysique

Discipline : « Physique des matériaux pour l'optique»

Soutenue publiquement le 3 mai 2024, par :

Maël Baron

Characterization and modeling of the dichroic mirror of the *EUCLID* space telescope

---

Devant le jury composé de :

MCCRACKEN Henry Joy,	Astronome, IAP Paris	Rapporteur
ZERRAD Myriam	Chargée de recherche-HDR, CNRS Marseille	Rapportrice
CUCCHETTI Edoardo,	Ingénieur de recherche, CNES Toulouse	Examinateur
FRUGIER Pierre-Antoine	Ingénieur de recherche, CEA Saclay	Examinateur
LANGLOIS Maud,	Directrice de recherche-HDR, CNRS Lyon	Examinatrice
PERRIES Stéphane	Professeur de l'université Lyon-1	Examinateur
EALET Anne,	Directrice de recherche-HDR, CNRS Lyon	Directrice de thèse
SASSOLAS Benoît,	Ingénieur de recherche, CNRS Lyon	Co-encadrant de thèse
GASPAR VENANCIO Luis Miguel,	Ingénieur, ESA-ESTEC Noordwijk	Invité

Remerciements

Lors de mes années de thèse, j'ai souvent envisagé la rédaction des remerciements comme étant le point final du doctorat, et je voyais cela comme un objectif ultime désespérément lointain. Et pourtant, nous y sommes. Je suis fier d'être arrivé jusqu'au bout. Comme toutes les thèses, celle-ci s'est avérée éprouvante, stressante vers la fin – d'autant plus que mes encadrants commençaient à se rendre compte que je travaillais bien plus efficacement sous la pression – mais ce long chemin restera malgré tout gravé positivement dans ma mémoire. J'ai appris énormément de choses passionnantes, grâce à bon nombre de personnes qui m'ont fait passer du stade de malheureux petit étudiant à celui de malheureux petit docteur.

(Excellente introduction qui débouche sur une parfaite transition. Voici donc lesdits remerciements.)

En premier lieu, je voudrais remercier **Benoît**, mon coencadrant. Tu as été présent et à l'écoute au quotidien pendant toute ma thèse. Tu as su me donner les bons conseils avec bienveillance pour me guider dans ce long travail, et c'est grâce à toi que j'ai pu réussir cette thèse. J'ai ressenti ton altruisme aussi bien pendant les périodes les plus compliquées de ces dernières années que pour des instants aussi insignifiants de la vie de tous les jours, par exemple lorsque tu me prêtais ton abominable parapluie en me voyant sortir dehors sous la pluie.

Merci à **Anne** également. Malgré votre emploi du temps de ministre vous avez su prendre le temps de m'aider pour terminer ce travail. Je vous félicite pour l'énergie que vous avez dépensée pour m'expliquer la cosmologie et la PSF (en vain, j'en ai peur). En relisant aujourd'hui – non sans effort – mes premières versions de mon manuscrit en 2021, je m'aperçois à quel point votre aide m'a été utile, malgré votre aversion envers mon humour que vous partagez avec Benoît. Mais, je dois bien reconnaître à contrecœur que mes vannes sur les éléphants d'Asie auraient été un pur désastre si laissées dans mon manuscrit.

Un grand merci aux **membres du jury** pour avoir accepté votre rôle, considéré et évalué positivement mon travail. (Du moins, je l'espère. Compte tenu du fait que je rédige ces lignes une semaine avant la soutenance, c'est d'une certaine manière un pari que je fais ici). Je remercie donc M. Edoardo Cucchetti (CNES), M. Pierre-Antoine Frugier (CEA), Mme Maud Langlois (CRAL), M. Stéphane Perriès (IP2I), M. Luis Miguel Gaspar Venancio (ESA) d'avoir fait partie de mon jury en tant qu'examinateurs et invités, ainsi que M. Henry Joy McCracken et Mme Myriam Zerrad pour votre rôle en tant que rapporteurs. Merci également au CNRS et au CNES pour le financement de ma thèse, et qui ont rendu ce travail possible.

Ensuite, je tiens à remercier toute **l'équipe du LMA** – déjà, pour m'avoir supporté pendant presque 4 ans – mais aussi pour votre soutien, vos encouragements, votre bonne humeur, et l'aide que vous m'avez apportés pendant toute la durée de ma thèse. J'espère pouvoir continuer à travailler avec des collègues tels que vous pendant le reste de ma carrière.

Je dois également beaucoup à **l'équipe de travail** « Dichroïque Euclid » : Pierre-Antoine, Luis, Rémy, et tous les autres. J'ai appris énormément de choses grâce à vous, et vous m'avez fait confiance pendant 3 ans. J'espère que cela a été autant un plaisir pour vous que pour moi que nous ayons travaillé ensemble. J'ai également une pensée pour les personnes de la collaboration Euclid et de l'IP2I avec qui j'ai pu échanger tout au long de ces 4 dernières années.

Enfin, je tiens à remercier tout particulièrement la **machine à café** du LMA. Litres après litres, tu as su me fournir l'énergie nécessaire pour survivre à la phase finale de la thèse. Même si je dois bien avouer que je préférais la machine précédente, je n'oublierai jamais la chaleur réconfortante de tes cafés au goût si singulier.

(Après la partie « objets », passons maintenant à la partie « proches ».)

Merci à **ma famille – et belle-famille** –, pour leur présence pendant ma thèse mais aussi pendant ma soutenance. J'ai été extrêmement fier de vous présenter mon travail. Vous n'avez probablement pas compris un traitre mot de ce que je vous ai raconté pendant 50 minutes mais vous avez tout de même pris la peine de venir à Lyon m'écouter, et c'est un effort de votre part que je trouve admirable. Je remercie bien entendu mes proches qui n'ont pas pu être présents (j'aurais fait pareil à votre place) mais qui m'ont soutenu.

De même, merci à **mes amis** pour leur soutien et, pour la plupart, d'être venus également m'écouter. Exilé à Lyon loin de vous, votre présence m'a fait chaud au cœur ! J'ajoute une dédicace spéciale à mes amis également en fin de préparation de thèse (vous vous reconnaîtrez). Nos échanges m'ont été très bénéfiques.

Et enfin, un merci spécial pour **Jeanne** ! Merci d'avoir été là pendant les phases les plus stressantes de ce travail. Merci pour ta pseudo-patience de m'écouter soir après soir te parler de sujets très – trop – techniques. Je comprends bien que mes récits de 40 minutes sur la façon dont j'ai dû ajuster les miroirs du banc de sorte à obtenir des résultats utilisables avec mes modèles ne soit pas des plus intéressants. D'ailleurs je suis sûr que tu as baillé en lisant ça. Mais malgré ça, tu es restée mon support émotionnel (et inversement). Merci pour tout !

Résumé - Français

Le miroir dichroïque du télescope spatial *Euclid* est un composant optique muni d'un revêtement multicouche servant à réfléchir la lumière visible vers l'instrument VIS et à transmettre la lumière infrarouge vers l'instrument NISP. Les multiples couches de l'empilement ont des épaisseurs optimisées de sorte à obtenir la réponse optique adaptée. Cependant, il a été découvert que les infimes variations d'uniformité d'épaisseur des couches conduisent à une erreur de front d'onde (WFE) qui varie avec la longueur d'onde, contrairement au cas classique d'un miroir métallique classique. Cette WFE complexe rend très chromatique la fonction d'étalement du point (PSF) du télescope, qui est l'un des paramètres critiques pour la mission *Euclid* et qui doit être par conséquent parfaitement caractérisée.

Le premier objectif de cette thèse est donc de mesurer la WFE du miroir dichroïque d'*Euclid* en fonction de la longueur d'onde au moyen d'un banc métrologique dédié. Ce banc inédit financé par l'ESA et développé par Imagine Optic, doit atteindre une précision inégalée sur la mesure de WFE tout en permettant de multiples configurations d'illumination (longueur d'onde, angle d'incidence …). La mise en route ainsi que l'optimisation du banc ont été l'une des premières étapes principales avant de pouvoir mesurer le miroir dichroïque dans diverses configurations.

L'autre objectif de cette thèse est de modéliser précisément le miroir dichroïque et toutes ses couches pour mieux appréhender la WFE induite. Pour cela, nous avons développé plusieurs méthodes basées sur la physique des couches minces et qui permettent de remonter à la source de la WFE : les non-uniformités d'épaisseur des couches, qui ne peuvent pas être mesurées directement. Les modèles de l'empilement dichroïque ainsi obtenu seront une donnée utile et nécessaire pour caractériser la PSF globale du télescope *Euclid*.

Mots-clés : Euclid, Métrologie optique, Empilements de couches minces, Front d'onde, PSF, WFE, Modélisation optique.

Abstract – English

The *Euclid* dichroic mirror is an optical component coated with a multilayer stack designed to reflect the visible light towards the VIS instrument and transmit the near-infrared light towards the NISP instrument. The different layers have thicknesses optimized to achieve the required optical response. However, it has been highlighted that the small thickness non-uniformities in the layers lead to a "WaveFront Error" (WFE) that depends on the wavelength, unlike the case of a classic metal mirror. This complex WFE makes the telescope's "Point-Spread Function" (PSF) highly chromatic, which is one the key parameter for the *Euclid* mission and needs to be accurately characterized.

One of the goals of this thesis is therefore to measure the WFE of *Euclid* dichroic mirror using a dedicated metrological bench. This brand-new bench funded by ESA and developed by Imagine Optic, shall achieve unrivalled accuracy in WFE measurement, according to multiple illumination configurations (wavelength, angle of incidence …). In addition to WFE measurements, we also worked on the commissioning, testing, and validation of the bench, to optimize its performance and the quality of the measurements. The commissioning of the bench was an important requisite during this work before to be able to measure the dichroic mirror under various conditions.

The other objective of this thesis is to model the dichroic mirror's layers, in order to gain a better understanding of the induced WFE. To this end, we have developed several methods based on thin-film physics that enable us to trace the source of the WFE back to the non-uniformities in the layer thickness, which cannot be measured directly. Subsequently, dichroic stacking models will be very useful for characterizing the whole PSF of the *Euclid* telescope.

Keywords: Euclid, Optical Metrology, Thin-films coatings, Wavefront, PSF, WFE, optical modeling.

Introduction

The *Euclid* space telescope was launched on July 1, 2023 by SpaceX to the Lagrange point L2. Its scientific objectives are the study of Dark Matter and Dark Energy, two of the great enigmas of modern cosmology. To this end, *Euclid* is equipped with two instruments, “VIS” and “NISP”. VIS is a very high-definition imaging camera made of 36 CDD sensors, enabling the precise measurement of galaxy shapes. NISP is an infrared spectrophotometer for measuring galaxy distances. The information obtained by these two instruments enables the application of two cosmological probes: Weak Lensing and Galaxy-Clustering, essential for characterizing Dark Energy and Dark Matter. To enable the two instruments to be used simultaneously in the same field of view, a “dichroic” mirror has been placed in the telescope. The latter reflects the visible light towards VIS, and is transparent to infrared light (towards NISP).

The VIS instrument is designed to study the shape of galaxies, which makes it extremely sensitive to the full optical answer of the instrument described by its Point-Spread Function (PSF). The PSF characterizes the quality of the images and its knowledge is then mandatory. An extensive PSF calibration program has been set up within the *Euclid* project, to measure and model the PSF as a function of wavelength, position in the field, time and other physical parameters. This work involves characterizing all the contributors including the dichroic mirror that induces chromaticity on the PSF.

The dichroic mirror consists of a set of 182 Nb_2O_5 and SiO_2 thin layers deposited on a silica substrate. Depending on the thickness of the layers, the refractive indices of the materials, and the wavelength, the optical response can be shaped thanks to interference effects. The thickness of the layers has therefore been optimized to define a dichroic filter with a reflection band in the 510 to 950 nm wavelength range.

It has been highlighted that the tiny thickness non-uniformities of the coating layers lead to a wavefront error (WFE) in reflection, which is highly complex: in the case of a metal mirror, the WFE is constant and easily characterized, but in the case of the dichroic mirror, comprising dielectric films, the WFE varies chromatically. This chromaticity is due to the variations of the reflected phase function of the mirror. This WFE then contributes to the telescope’s PSF.

The aim of this thesis is therefore to characterize the wavefront in reflection of the dichroic mirror of Euclid. As the flight model of the dichroic is already integrated, this work will be done on a “spare” model considered as a “twin” of the actual optic installed in the telescope.

To do the characterization, we will use a highly unique and innovative metrological bench: OBSERVE, designed by the French company Imagine Optic and funded by ESA. This bench will enable us to measure (among other properties) the WFE of the dichroic mirror over the entire visible band, with an extreme precision, and in various optical configurations (incidence, polarization). This bench has been installed at LMA in clean room conditions to be operated in very stable and controlled environment. The thesis will describe the work done to install then operate and understand the bench. The commissioning, the validation and the first campaign of measurements are presented.

We present then models to understand the physic of the dichroic based on the understanding of the physic of the thin-film layer coating. We described two numerical approaches that have been developed to model the mirror’s coating layers, in order to predict the WFE under any illumination condition. The resulting model of the mirror will be adjusted with the WFE measurements obtained with the OBSERVE bench. First results on the WFE measured with OBSERVE will be presented both to describe the dichroic properties and to validate the dichroic numerical model. A first estimation of errors and biases induced by the bench are also presented.

Outline of the Thesis

- **Chapter 1** introduces the scientific context and the cosmological questions to be answered by the *Euclid* mission. This chapter presents also the *Euclid* cosmological probes, survey, telescope, and its instruments VIS and NISP.

- **Chapter 2** presents the concept of the Point-Spread Function (PSF) and how it is related to the Weak-Lensing cosmological probe used by *Euclid* VIS instrument. The PSF characterization needs are explained, and we establish the link between PSF and wave front error (WFE).

- **Chapter 3** introduces the dichroic mirror of Euclid. Its optical requirements and its function in the telescope as a thin film coating are presented. The last part of the chapter is devoted to the chromatic contribution of the dichroic mirror to Euclid PSF.

- **Chapter 4** is devoted to the metrology bench "OBSERVE" conceived by Imagine Optic. The requirements of the bench, its functioning principle, a detailed description and its operating mode are presented.

- **Chapter 5** presents the OBSERVE bench commissioning and validation at LMA.

- **Chapter 6** presents two numerical methods based on thin-films physics which must allow the construction of a numerical model of the *Euclid* dichroic spare mirror, adjusted from WFE data.

- **Chapter 7** contains the description of first data WFE measured with the OBSERVE bench and first results on the dichroic properties. The Dichroic coating models results will be adjusted from this data and an estimation of the current precision of the bench and data will be presented.

Table of contents

Part A Context of the thesis

Part B Euclid dichroic mirror characterization

Part A

Context of the thesis

Chapter 1

Euclid mission

Cosmology is the science devoted to the study of the Universe as a whole. This includes its geometry, its composition, and its evolution. Mankind has devoted itself to this question since antiquity, imagining various cosmogonies, often placing himself at the center of the Universe. The 20th century has been rich in discoveries questioning our understanding of this Universe, making it immensely larger, more complex, and more dynamic than what was thought at the time. In 1929, for example, the observations made by E. Hubble [1] showed that the Universe is far from being unchanging and limited to our Galaxy, being in expansion for billions of years, starting from an instant zero that modern cosmology still struggles to describe.

The *Euclid* mission has been developed to answer several major cosmological questions of our time, related to the nature of the content of the Universe, as well as to its dynamics. In this chapter the current cosmological model will be described, as well as its inherent physical quantities and the observations which allowed its validation. We will then evoke the great open questions that are the nature of Dark Energy and Dark Matter, and then present the *Euclid* mission, dedicated to their study. After a reminder of the mission objectives, we will introduce the cosmological probes of *Euclid* which are observations with measurable signatures, allowing the quantification of the cosmological parameters describing the Universe dynamics. Finally, we will present the space mission and the expected scientific performances.

1. MODERN COSMOLOGY

In this section, we will go over the basics of modern cosmology and discuss the measurements that led to the development of the current cosmological model. We will also review the cosmological parameters used to describe it and outline some key unresolved questions, explaining why addressing them is crucial for the future understanding of our Universe.

1.1. The modern cosmology basis

The theory of General Relativity, proposed by A. Einstein in 1915, is today the framework used to describe the Universe as a whole. This theory is based on a conception of space and time as a single field, the space-time, whose deformations are interpreted by the so-called Gravitational Force. Einstein formalized this space-time dynamic as a function of the Universe content (galaxies, stars...) by his famous "field equation" [2]:

$$R_{\mu\nu} - g_{\mu\nu}\left(\frac{R}{2} - \Lambda\right) = \frac{8\pi G}{c^4} T_{\mu\nu} \quad (1)$$

The entire left part of Eq. 1 describes the geometry of the Universe. The term $R_{\mu\nu}$ is the Ricci tensor and R its doubly contracted form. Also appears the metric $g_{\mu\nu}$, and the cosmological constant Λ. The right part of the field equation describes the Universe energy content, where $T_{\mu\nu}$ is the energy-impulse tensor, G the Gravitational Constant, equal to à $6.67 * 10^{-11}\ m^3.kg^{-1}.s^{-2}$, and finally c the speed of light in vacuum, equal to 299 792 458 $m.s^{-1}$. Although the field equation allows describing precisely the dynamics of space-time, it is extremely complex. To solve such an equation, physicists need to make simplifications and assumptions, especially the metric $g_{\mu\nu}$ that defines the geometry of the Universe.

The Friedmann [3]-Lemaître [4]-Robertson [5]-Walker [6] (FLRW) metric, resulting from the work of scientists of the same name between 1922 and 1937, makes it possible to greatly simplify Einstein's field equation and to solve it as follows:

$$\frac{\dot{a}^2}{a^2} + \frac{k}{a^2} = \frac{8\pi G\rho}{3} + \frac{\Lambda}{3} \quad (2)$$

The term a in the Friedmann-Lemaître Equation (Eq. 2), which is time-dependent, corresponds to the Universe's scale factor, in other words its "size" relatively to its current size. Its time derivative is noted as $\dot{a}$. We also note the energy density ρ, and finally k the curvature of the Universe. If $k = 0$ then the Universe geometry is plane, closed if $k > 0$, and open if $k < 0$. The Universe is considered here as being a homogeneous and isotropic medium, as far as we consider it at very large scale. Finally, the Universe is assumed to be a thermodynamically closed system, without any external energy exchange, although the cosmological constant Λ can be interpreted as input energy.

Two important quantities are then defined. First, the expansion rate $H = \dot{a}/a$, which translates the expansion speed of the Universe, which evolves with time. Nowadays H corresponds to the Hubble constant $H_0 = 72 \pm 8\ km\ s^{-1}Mpc^{-1}$ [7]. The second quantity is the critical density of the Universe $\rho_c = 3H^2/8\pi G$, obtained from Eq. 2 for $k, \Lambda = 0$.

From ρ_c, the four types of reduced densities Ω_i are deduced, as simply the ratio of the density of each energy type and the critical density:

Name	$\Omega_m = \Omega_b + \Omega_c$	Ω_r	Ω_k	Ω_Λ
Energy type	Matter (total)	Radiation	Curvature	Λ Constant
Expression	$8\pi G\rho_m/3H^2$	$8\pi G\rho_r/3H^2$	$-k/H^2a^2$	$\Lambda/3H^2$

Table 1: Name, type, and expression of the main reduced energy parameters Ω_i [8]

The total matter density Ω_m is itself subdivided into two contributions: baryonic (ordinary) matter Ω_b and Dark Matter Ω_c. In this chapter, the term "matter" includes both baryonic matter and Dark Matter, except where the nature of this latter is specified. Assessing the value of these densities over time is crucial to understanding the mechanics of the Universe, including its evolution: collapse, accelerated expansion, slowed expansion... There are therefore a variety of models of the Universe with each one having a different value of these parameters at each epoch.

To go further, the parameters are estimated by measurements and cosmological observations more and more precise. The set of these observations led to the Cosmological Model, commonly called ΛCDM which will be described in the following part.

1.2. The Dark Matter

In 1933, the work of F. Zwicky [9] on the estimation of the mass of galaxy clusters revealed a "missing mass". This work was corroborated by observations of galaxy rotation velocities by V. Rubin [10] in 1970, which seem to show that galaxies are in fact much more massive than what theoretical deductions from their luminosity alone [11] seem to show. That suggests that there would thus exist a distribution of exotic matter in the galaxy, very massive but invisible. This observation marks the birth of the Dark Matter concept. Since then, the nature of Dark Matter has become one of the great enigmas of modern cosmology. The most popular model describing the Dark Matter is Cold Dark Matter model (CDM). Proposed by Peebles [12] in 1982, it includes non-relativistic matter which fills a geometrically flat Universe and whose dynamics depends mainly on the amount of matter it contains (Ω_m). The actual amount of Dark Matter Ω_c in the Universe impacts the value of Ω_m in the CDM model (sum of Ω_b and Ω_c). A direct way to detect it is to look at the gravitational effects it may have on baryonic matter.

1.3. An accelerating Universe

Universal Expansion and redshift of galaxies

The first evidence of the Expansion of the Universe was provided by the observations of E. Hubble [13] by the method known as Cepheid [14], showing that the galaxies have a separation speed almost proportional to their distance: about $22\ km\ s^{-1}$ for a galaxy located at one million light-years from the Earth. These velocities cannot be due only to the proper motions of the galaxies; they are caused by the Expansion of the Universe, which makes space stretch in a practically uniform way in all directions, thus moving away the galaxies from each other. These speeds of distance lead to a shift of their emission spectrum to higher wavelengths, called "redshift". This is quantified by the value z expressed in Eq. 3, corresponding to the shift between the emitted wavelengths λ_{em} and observed one λ_{obs}:

$$z = \frac{\lambda_{obs} - \lambda_{em}}{\lambda_{em}} \quad (3)$$

SN1A and Universe Expansion acceleration discovery

At the beginning of 21th century, measurements from Type Ia supernovae [15, 16] have seemed to indicate an acceleration in the expansion of the universe, suggesting the presence of a significant cosmological constant (Ω_Λ ~ 0.7). Type Ia supernovae are stellar explosions occurring in galaxies [17]. They are unique because their explosions always occur at the same luminosity. This allows determining their distance based on the peak luminosity they emit. By also measuring the "redshift" of the host galaxy, we can accurately characterize the expansion dynamics.

This observation challenged the Cold Dark Matter (CDM) model, which did not anticipate a dynamic component in universal expansion. The reason for this recent acceleration of the Expansion and the physical meaning is still poorly understood and confirmation was needed to better understand these results.

Complementary probes: CMB and BAO

Two additional cosmological measurements in the early 2000s indirectly confirmed the findings from Type Ia supernovae: the Cosmic Microwave Background (CMB) and the Baryonic Acoustic Oscillations (BAO).

The CMB is the first image of the Universe, only 380 000 years after the Big-Bang. The Universe, until then composed of a hot and opaque plasma, has relaxed and cooled enough to release photons, still trapped in the plasma. This is called photon-baryon decoupling. This very old black body radiation, of very long wavelength due to a redshift greater than 1000, and arriving to us in all directions of the sky, was measured for the first time by accident by Arno Penzias and Robert W. Wilson in 1964. Since then, several more accurate surveys have taken place, like WMAP [18] and Planck [19].

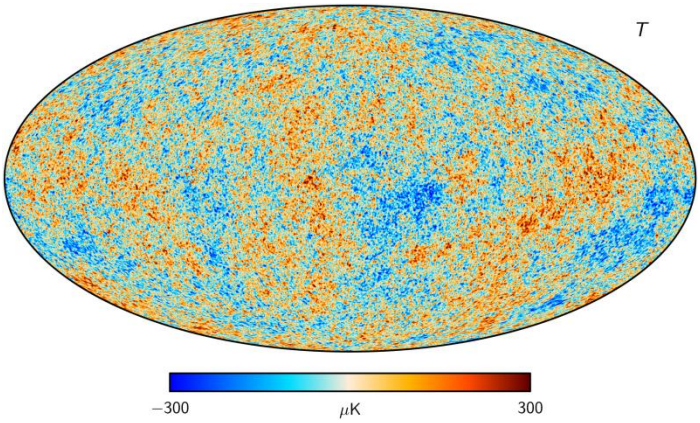

Figure 1: The Cosmic Microwave Background (CMB) obtained by the Planck survey in 2018, in Mollweide representation. [19]

The cosmological background is extremely homogeneous and isotropic and shows that the observable Universe is flat. It contains a primordial fluctuation whose measurement allows fixing the cosmological parameters and confirms a value of Ω_Λ around 0.7, allowing then the confirmation of the cosmological model ΛCDM.

It also contains small anisotropies of the order of 10^{-5} shown in Figure 1 as temperature gaps of a few mK, which are interpreted as gravitational wells. These were the starting point for the formation of the current large galactic structures by gravitational collapse of matter. The near-uniformity of the CMB agrees very well with the assumption of a flat, nearly homogeneous Universe in the CDM model, and the anisotropies are consistent with a value of Ω_m of the order of 0.3.

The BAO constitutes a complementary cosmological probe. Before the photon-baryon decoupling, the primordial plasma filling the Universe was made of baryons (protons, neutrons) constantly agitated by the effect of gravity and pressure forces opposed to each other. This resulted in oscillations of the density of this plasma, which remain visible in the baryonic matter, at the time of the decoupling of the baryons with the photons. These traces are called BAOs [20]. After the photon-baryon decoupling, the baryons were “frozen” in a specific distribution. The BAOs have left traces on this distribution, detectable at any time in the Universe.

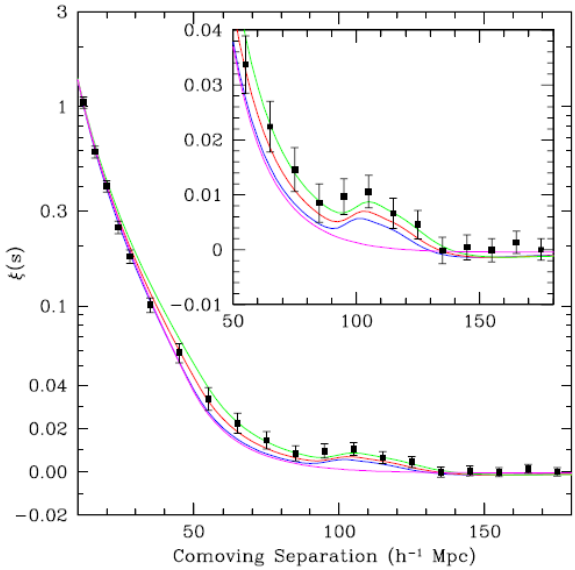

Figure 2: Correlation function ξ on the separation of galaxies in comoving distance, determined from SDSS data [21]. The BAO peak appears around $100\ h^{-1}\ Mpc$.

By looking at the correlation function of the distribution of galaxies in the sky for a given redshift interval (Figure 2), we can detect the BAO peak, corresponding to an over-representation of some distances between galaxies compared to a hypothetical random distribution. This BAO peak is a precious source of information on the evolution of the Universe Expansion, on the amount of matter and is a proof of the progressive structuration of galaxies and clusters from the baryonic matter it contains.

The ΛCDM concordance model

The SN1A, CMB, and BAO probes that we have briefly been described infer signatures of the dynamics of the Universe in radically different aspects and at different epochs, which ensure that they complement each other very well to know Ω_m and Ω_Λ accurately. In Figure 3 are presented the confidence contours on Ω_m and Ω_Λ at 99% (very dark), 95% (dark), and 90% (light) for the three probes. The CMB probe (orange) constrains the cosmological parameters in the case of a flat or nearly flat Universe, while the BAO probe constrains the value of Ω_m in a narrow corridor. The combination (intersection) of these confidence contours with that of the SNIA (blue) thus leads to a very fine estimate for Ω_m and Ω_Λ (Table 2). The combined results confirm well the accelerated Expansion of the Universe, measured by SNIA.

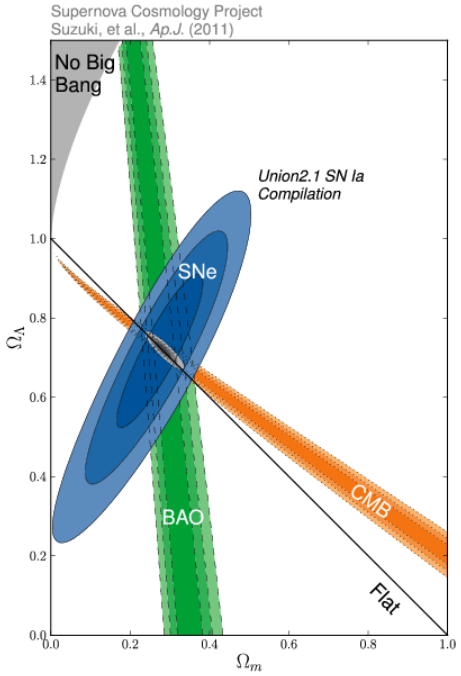

Figure 3: Confidence contours on cosmological parameters Ω_m and Ω_Λ by three probes: SN1A (blue), CMB (orange), and BAO (green) [22].

Parameter (ΛCDM)	Ω_m	Ω_Λ
Value	0.315	0.685
Accuracy	$\pm$0.03	$\pm$0.03

Table 2: Current values Ω_m and Ω_Λ parameters are listed within the ΛCDM model framework and their accuracy [23].

The derived concordance model ΛCDM, therefore includes a cosmological constant commonly denoted Λ, and is considered as the current standard model of cosmology. However, the nature of this acceleration quantified by Λ is still unknown. If described as an Energy, this non zero cosmological constant account for more than 70 % of the content of the Universe. It is then called "Dark Energy".

To make the difference between these two interpretations (constant or energy), one possibility is to look at the evolution in time of this component, and to measure it at several epochs in the Universe.

Dynamic Dark Energy

The problem of the acceleration of the Universe can indeed be approached by considering the Dark Energy as a dynamic field which immerses the whole Universe. We then consider a parametric equation of state [24] for the Dark Energy:

$$w(a) = p(a)/\rho(a)c^2 \quad (4)$$

Eq. 4 involves the pressure $p(a)$ and the Dark Energy density $\rho(a)c^2$, as a function of the Universe scale factor $a = 1/(1+z)$. We can then write $w(a)$ as a sum of a constant term w_0 and a dynamic term w_a:

$$w(a) = w_0 + w_a(1 - a) \quad (5)$$

A Dark Energy simply due to the cosmological constant Λ would result in a value of $w_0 = -1$ and $w_a = 0$ in Eq. 5. Any deviation from these values would be the sign of a dynamical field. It is thus crucial to constrain these two parameters precisely. The aim of this formalism is not to describe the Dark Energy physically, but to quantify its dynamics, independently of the considered model. In Table 3 appear the current estimates of w_0 and w_a, still too uncertain to draw conclusions on the dynamic characteristics of the Dark Energy, and thus justifying a mission like *Euclid*.

Modified Gravity Theories

Theories of modified gravity approach the question of the Universe's accelerated Expansion from a different angle. These models propose to consider it as a gravitation property applying at very large distances, which would imply to modify the current General Relativity theory. To discriminate these models, it is proposed to study the evolution of the growth rate of large structures over time, with for example the parameterization [25] written in the form:

$$f(z) = \Omega_m(z)^\gamma \quad (6)$$

In Eq. 6, $f(z)$ is the growth rate of the structures, depending on z and evolving from the initial CMB fluctuations, and γ a parameter whose value is to be determined. Conventional General Relativity implies that γ equals 0.55. Any deviation from this value inevitably leads to a deviation from Einstein's theory, and would therefore be in favor of a modified gravitation model. The current measurements of γ, whose accuracy is given in Table 3 is not precise enough to discriminate between the different models [26]. It has been established that a factor of 10 on the accuracy level for γ, w_0, w_a is necessary to allow discrimination between the different models.

Parameter	$\Delta\Omega_\Lambda$	$\Delta\gamma$	Δw_0	Δw_a
Accuracy	0.06	0.2	0.1	1.5

Table 3: Current values of the accuracy level of the Dark Energy cosmological parameters. [22, 25, 27]

The ΛCDM model is a solid basis for determining the dynamics and composition of the Universe, establishing a concordance between results from very different cosmological probes. The measured parameters densities show a universe filled with over 70% dark energy and approximately 30% dark matter. The precision on the other parameters does not currently allow for further interpretation of the nature of these components.

The *Euclid* mission has been designed to answer these questions, in particular by making measurements ten times more precise with controlled systematics.

2. THE *EUCLID* MISSION

The *Euclid* mission has been set up to give answers to the Dark Energy and Dark Matter enigmas, by reducing the current uncertainties on the cosmological parameters related to Dark Matter and Dark Energy. In this section, we will detail the different cosmological probes that have been chosen for the mission, as well as the link between these probes and the cosmological parameters previously defined.

2.1. The great cosmologic enigmas

To answer these questions, *Euclid* will have to determine if the Dark Energy is the consequence of a cosmological constant Λ or results from a complex dynamical field, parameterized by w_a, w_0. Also, the mission will be able to test Modified Gravitation models that propose to interpret this Dark Energy as an intrinsic property of Gravitation. Answering these questions implies an unprecedented level of precision for the parameters w_a, w_0, γ presented in parts 1.2 and 1.3.

The Euclid survey will be done via two primary cosmological probes. The first one, the weak gravitational shear or "Weak-Lensing", uses the observation of the deflection of light rays by Dark Matter. The second is the study of large structures, or "Galaxy-Clustering", which consists in the analysis of the distribution of baryonic matter in the Universe by looking at the distribution of galaxies during its different epochs. The combination of these two probes allows the accurate determination of the galaxies correlation function [28], leading to an accurate estimation of cosmological parameters.

2.2. Weak-Lensing cosmological probe

Gravitational lensing

The trajectory of light rays emitted by a distant object such as a galaxy can be deviated by the gravitational action of a massive body or a zone of density of matter in the foreground. This applies to both ordinary and Dark Matter. As a result, a galaxy may have an apparent observed shape different from its actual shape, and the difference depends on the matter encountered on its path by the light beam. This phenomenon is called gravitational lensing. Its most extreme manifestation, called "strong lensing", has been already reported by the Hubble Space Telescope (HST). For example, Figure 4 is a picture taken by HST of a distant galaxy (in blue) which appears extremely stretched due to the strong lensing caused by another very massive galaxy (in yellow at the center), located in the foreground.

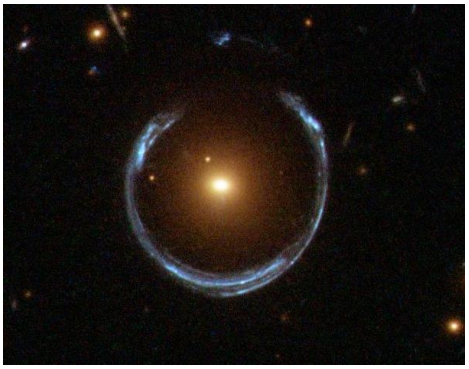

Figure 4: "Einstein's Ring" LRG 3-757 observed by Hubble Space Telescope [Image Credits: ESA/Hubble & NASA].

However, strong lensing like that shown in Figure 4 is very rare and localized. In the sky as a whole, the lensing is therefore generally very weak. Used statistically, it allows us in measuring the amount of Dark Matter, by comparing in a region of space the shape of apparent galaxies with the shapes that would theoretically be observed without Dark Matter in the foreground.

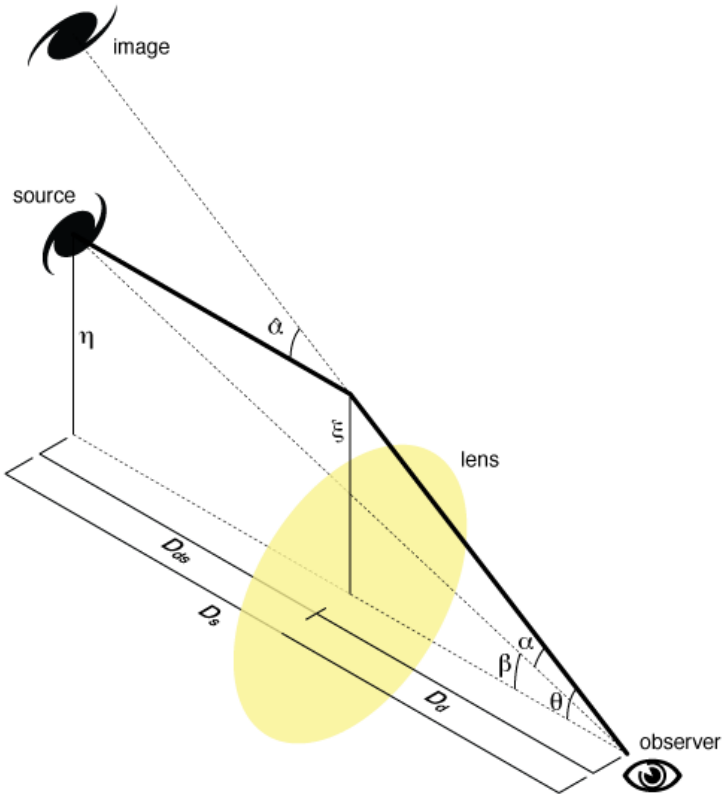

Figure 5: Illustration of Lensing. The mass of the lens (in yellow) deflects the light rays from the source from its true angular position β to an apparent position θ. Image credits: Michael Sachs.

The lensing illustrated in Figure 5, can be formalized [29] as a linear transformation from a Cartesian coordinate base "without lensing" (x_u, y_u) to a base "with lensing" (x_l, y_l) :

$$\begin{pmatrix} x_u \\ y_u \end{pmatrix} = \begin{pmatrix} 1-\gamma_1-\kappa & -\gamma_2 \\ -\gamma_2 & 1+\gamma_1-\kappa \end{pmatrix} \begin{pmatrix} x_l \\ y_l \end{pmatrix} \quad (7)$$

In the central matrix of Eq. 7 [29] we find the shear terms γ_1, $\gamma_2$which are visually interpreted as a stretching of the galaxy in either space direction. There is also a magnification term κ which causes the object to be seen larger because of the foreground mass.
The knowledge of γ_1, γ_2 and κ leads to the lensing potential ϕ [29], and then the geometry and the mass of the lens (the foreground source of this potential). The determination of γ_1, γ_2 and κ thus allows the characterization of the matter density area – and thus Dark Matter – at different locations in the sky. In the case of strong lensing, this calculation can be done by applying it to the mass of visible matter generating the lensing. However, when the actual galaxy shape is unknown, the calculation of γ_1, γ_2 and κ can only being done statistically by measuring the ellipticities of the background galaxies, which allows statistical estimation of their alignment. This is the principle of Weak-Lensing (WL) used in *Euclid*.

Correlation function on galaxies shape

At first sight, galaxies are not circular objects but more or less elliptical or spiral. Their intrinsic ellipticity is related to their shape and their orientation in space. The measurement of the ellipticity is thus a combination of the shear due to the lensing effect and the intrinsic ellipticity of the galaxies themselves. The intrinsic ellipticity is generally very large but since no orientation is favored, the random distribution of a large number of galaxies should result in a zero average intrinsic ellipticity over any population of galaxies. Any residual effect will then be considered as a lensing effect. Any Dark Matter in the foreground will create a gravitational lensing effect which will give a non-zero shear term locally in Eq. 7. This shear can be related to the Dark Matter distribution.

In practice, the detection of the gravitational lensing effect involves the calculation of several correlation functions. These functions measure the average product of two lensing observables $\gamma_1\gamma_2, \gamma_1\kappa$, and $\gamma_2\kappa$, for objects with the same angular separation in the sky. These three functions are used to trace back to the Dark Matter density correlation function, via a cosmological model, based on the power spectrum of the Dark Matter density. The power spectrum is defined as the Fourier Transform of the correlation function.

An example of measurements made with HST of measured power spectrum for two lines of sight (Figure 6, left), taken from the local lensing correlation function (Figure 6, center), allowing the link between the measurement and the density of Dark Matter (Figure 6, right).

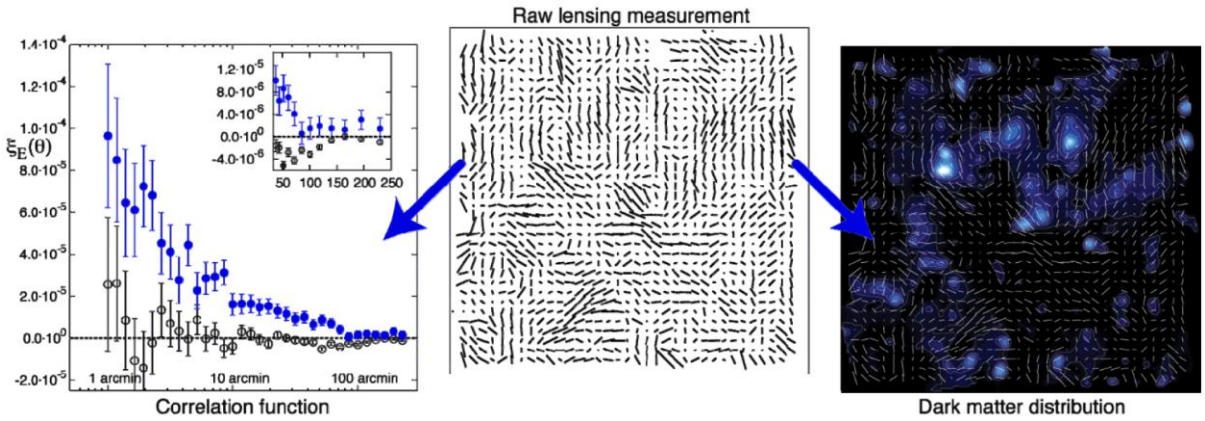

Figure 6: Detection of Dark Matter density zones by applying Weak-Lensing from HST data [28].

Requirements on Weak-Lensing for Euclid

The *Euclid* spacecraft will observe a very large number of galaxies at different distances, and over the largest possible area of the sky. The apparent shape of these galaxies will be determined, allowing the calculation of correlation functions specific to the WL. To best characterize Dark Matter, the most suitable redshift zone is $0.6 < z < 2.05$. This corresponds to epochs when the Universe is dominated by matter. The calculation accuracy of the correlation function depends on the number of galaxies, which should be maximized. It has been estimated that the density of objects must be at least 30 $gal/arcmin^2$, or more than 1.5 billion objects over an area of 15000 deg^2 (see 3.4) in this redshift area.

The accuracy of the shear calculation depends on the number of galaxies observed, but its accuracy depends on the experimental biases that can affect the measurement of the galaxy shape, which must be very precise. Among these biases, discussed in Chapter 2, is especially the diffraction, an intrinsic optical limit of any telescope, or pixelation by the detectors.

Measuring the shape of the galaxies alone is not enough; the distances between the lensing masses and the background sources are also required. These distances are often estimated with the help of the photometric redshift, which is sufficient in precision to make this measurement to within 5%. The photometric redshift is estimated by comparing the flux received in several photometric bands for each object. To cover the necessary redshift range ($0.6 < z < 2.05$), *Euclid* uses infrared "Y", "J", and "H" band measurements [30] taken in flight, and relies on complementary measurements in the visible domain made from the ground [28, 31]. The specifications of the WL by *Euclid* are given in Table 4.

Euclid Weak-Lensing requirements	Value
Density of objects	$30\ gal/arcmin^2$
Redshift coverage	$0.6 < z < 2.05$
Error on redshift	$\sigma_z < 0.05(1+z)$

Table 4: Weak Lensing probe requirements for Euclid [31]

2.3. Galaxy-Clustering cosmological probe

Galaxy Clustering (GC) is the other probe of *Euclid*. This probe allows the mapping in three dimensions of the large structures in space, by measuring the correlation function of the galaxy distribution. The correlation function leads to the power spectrum of the baryonic matter, sensitive in particular to the BAO measurement (see part 2.3). As for the WL probe, it is necessary to measure a large number of galaxies to reach the required statistical accuracy. The specification is a minimum galactic density of $1700\ gal/deg^2$ over a redshift range of $0.9 < z < 1.8$. This corresponds to about 50 million galaxies over $15000\ deg^2$.

For this probe, the accuracy on the position of each galaxy is primordial and much greater than for the WL, with an accuracy of 0.1%, requiring spectroscopic measurements. The measured galaxies being far away ($0.9 < z < 1.8$), the redshift is shifted in the infrared range. The estimation of the redshift is made from the detection of the $H\alpha$ emission line of the galactic spectrum, of initial wavelength $\lambda = 656.3\ nm$ with a sufficient signal-to-noise ratio (SNR) of 3.5σ minimum. The Table 5 summarizes the main specifications on galaxy clustering for *Euclid*.

Euclid Galaxy Clustering requirements	Value
Density of objects	$1700\ gal/deg^2$
Redshift coverage	$0.9 < z < 1.8$
Error on redshift	$\sigma_z < 0.001(1+z)$
Spectrum SNR	$SNR > 3.5\ \sigma$

Table 5: Galaxy Clustering probe requirements for Euclid [31]

2.4. Expected scientific performances for Euclid

With these two probes WL and GC (BAO), the *Euclid* mission will increase the level of accuracy on the parameters w_a, w_0 and γ. The gain brought by *Euclid* on the accuracy of these parameters will be greater than 10. In Table 6 are listed the values of these accuracies for different cases (current accuracies, *Euclid* alone, *Euclid* and Planck combined), then highlighting the scientific contribution of the *Euclid* mission.

Cosmological parameter	$\Delta\gamma$	Δw_0	Δw_a
Current	20%	10%	150%
Euclid	0.9%	1.3%	4.8%
Euclid + Planck	0.7%	0.7%	3.5%
Improvement factor	30	> 10	> 50

Table 6: Expected values of relative accuracy levels in γ, w_0, w_a before and after obtaining Euclid data [28].

To quantify *Euclid*'s performance, the Figure of Merit (FoM) [28] is often defined on the Dark Energy parameters with Eq. 8:

$$FoM = 1/(\Delta w_0 \Delta w_a) \tag{8}$$

The choices made on the *Euclid* WL and GC probes (Table 6), will allow a $FoM \geq 400$.

3. THE SPACE MISSION

The *Euclid* spacecraft was launched in July 2023 by a SpaceX's Falcon 9 launcher, and sent to the Earth-Sun Lagrange point L2, 1.5 million kilometers away from Earth. This is an M class mission within ESA's Cosmic Vision program. In this third and last part of this chapter, we will describe the space mission, the telescope, the instruments, and the observation strategy. *Euclid* allows observations in the visible and in the infrared range, giving access to redshifts inaccessible from the ground ($0.6 < z < 2$). Observations will be made on about two thirds of the sky during the 6-year mission, one of the largest surveys ever conducted.

The *Euclid* payload includes the telescope and two instruments: VIS (Visible Instrument) and NISP (Near Infrared SpectroPhotometer). VIS is in charge of galaxies imaging, leading to the analysis of their shape for the Weak-Lensing. NISP is the instrument dedicated to photometry (determination of the redshifts of galaxies used for the WL probe) and spectrometry (determination of the redshifts of galaxies used for the GC probe). The strategy is based on a simultaneous use of the two instruments on the same observed field, to reduce the experimental biases. With the help of a "dichroic" mirror, the luminous flux is thus split towards VIS and NISP.

3.1. Telescope and optical design

The choice of the *Euclid* telescope is the result of a compromise between the cost of the mission, which fixes a maximum diameter for the primary mirror and thus the collected flux, and the space mission itself whose estimated duration is 6 years. The experimental choices made must allow reaching absolute magnitudes higher than 24 for the WL and the GC on the $15000\ deg^2$ requested. The field of view chosen is 0.53 deg² and the survey will be conducted by "patches of sky" with exposure times of about 4*1000 s for each, thus respecting the 6 years of mission. The optical design is based on an aperture of 0.53 deg² and a primary mirror of 1.2 m in diameter, taking into account the compactness of the spacecraft, embedded in a rocket fairing.

The telescope is a "Korsch" type, whose optical scheme is presented in Figure 7. This design allows, among others, an image forming in a plane, plane on which the detectors will be placed. It is composed only of curved mirrors (M1, M2, and M3), to which are added 3 plane mirrors for the folding (FoM1, FoM2, and FoM3), as well as the flat dichroic mirror, which separates the flux. Very high constraints have been imposed on the different mirrors of the telescope in terms of positioning and polishing, ensuring an impulse response close to the diffraction limit in the visible range.

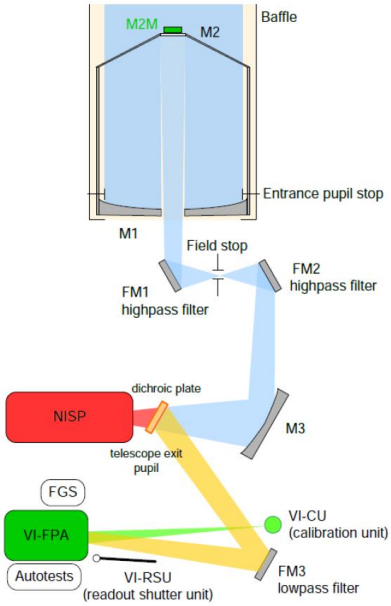

Figure 7: Optical schematic of the Euclid Payload Module (PLM) – Courtesy Airbus Defense and Space [32].

3.2. The dichroic mirror

The dichroic mirror splits the incident beam incoming from M3 mirror into an infrared part ($\lambda > 920\ nm$) and a visible part ($550 < \lambda < 920\ nm$). The infrared beam is transmitted towards the Near-Infrared SpectroPhotometer (NISP), which manages photometry and spectroscopy measurements, and the visible beam is reflected by the dichroic mirror towards the Visible Instrument (VIS), which is responsible for imaging galaxies. This dichroic mirror allows operating both instruments simultaneously. It is an essential element of the mission, also subject to strong constraints. Because of its different design from a common metallic mirror (see Chapter 3), it appeared that the latter requires a more thorough study to determine the complex optical aberrations that it is likely to generate in the visible range.

3.3. Instruments

Visible Instrument (VIS)

VIS is the instrument specified for imaging in the visible range related to the WL measurement. It is composed by a very high resolution CCD sensor array located at the image plane of the telescope. Figure 8 is a picture of VIS after its assembly. There are 6x6 CCDs sensors, each consisting of 4096x4096 pixels, allowing to obtain very resolved field images, about three times wider as the area covered by the full Moon in the Earth sky. The spectral coverage of the CCDs consists of the visible bands R, I, Z ($0.55 < \lambda(\mu m) < 0.92$) which allow collecting enough flux emitted by objects of magnitude 24.5 undergoing redshifts specified in Table 4.

Figure 8: VIS instrument after its integration at CEA-IRFU [Image Credits: CEA]

The expected performance of VIS is listed in Table 7. Its 600 million pixels on a 29x29 cm² area allow a resolution of 0.1 arcsec per pixel. Such a resolution minimizes the pixelation effect which adds an experimental bias on the shape of the observed objects. The CCD array, located at the focal plane at an operating temperature of 150K, is connected to the readout electronics (6 bars located at the back, visible in Figure 8). VIS also includes a calibration module, not visible here, providing a perfectly uniform beam on the image plane. Finally, a shutter located upstream of the optical path cuts the light beam very quickly at the end of each few hundred seconds exposure.

VIS instrument	
Field of view	$0.700 \times 0.778\ deg^2$
Detectors	36 CCD, 4096x4096 pixels
Pixel resolution	$0.1\ arcsec/pix$
Imagery bands	$R, I, Z:\ 0.55 < \lambda(\mu m) < 0.92$

Table 7: Euclid VIS instrumental requirements [31]

Near-Infrared SpectroPhotometer (NISP) instrument

NISP is a dual instrument: photometer and spectrometer at the same time. Its role is to provide photometric and spectroscopic redshift measurements in the infrared range for WL and GC. Its optical design, shown in Figure 9, is more complex than for VIS as it includes two 5-slot moving filter wheels, as well as a set of corrective lenses that adapt the beam shape towards the H2GR detectors (NIR light).

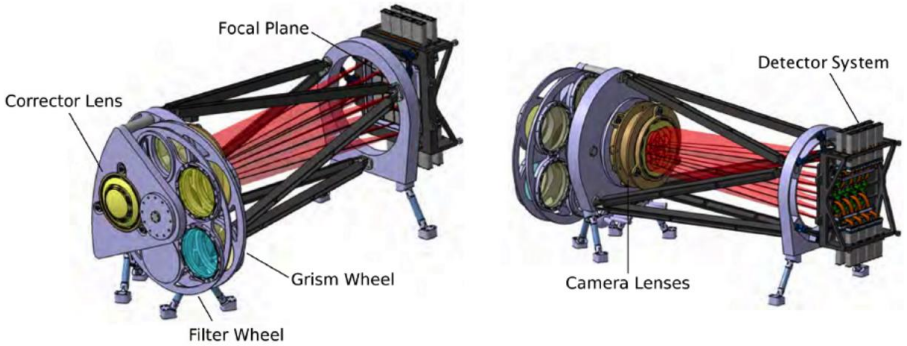

Figure 9: CAD view of Euclid NISP instrument [30].

The choice of photometric and spectrometric bands matches the need to measure the redshift for WL and GC respectively. The first filter wheel contains the infrared filters in Y, J, and H bands for photometric measurements ($0.92 < \lambda(\mu m) < 2$), one "open" location, and a fifth one that is closed. The second wheel, used for spectroscopy, contains 4 "GRISMS" which are slitless dispersers for galaxy spectra acquisition: the spectroscopic band is thus covered by three "red" GRISMS covering

$1.25 < \lambda(\mu m) < 1.85$ and one "blue" GRISM ($0.92 < \lambda(\mu m) < 1.25$). The red GRISMS are all rotated by 90 deg angle to each other. Indeed, a spectroscopic image is made of a set of spectral lines starting from each observed light source. These lines can thus be superimposed. By repeating the measurement with a different line orientation, the superposition differs, and it is possible to identify the spectra of each light source individually. The "Blue" GRISM is used for calibration and for observation of specific objects in deep fields (see 3.4). The specification on the spectra dispersion by the GRISMS in the image plane is $\lambda/\delta\lambda \geq 400$, guaranteeing the $H\alpha$ line to be identified with an SNR as presented in Table 5, as well as a line detection limit of $2 * 10^{-16} erg.s^{-1}.cm^{-2}$.

The focal plane is composed of 16 H2RG detectors of 2048x2048 pixels covering the NIR with a spatial resolution of 0.3 arcsec/pix. The NISP specifications are listed in Table 8.

NISP instrument		
Acquisition mode	Spectroscopy	Photometry
Band coverage	$1.25 < \lambda(\mu m) < 1.85$	Y: $0.92 < \lambda(\mu m) < 1.15$ J: $1.15 < \lambda(\mu m) < 1.32$ H: $1.32 < \lambda(\mu m) < 2.00$
Dispersion	$\lambda/\delta\lambda \geq 450$	/
Detection limit	$2 * 10^{-16}\ erg\ s^{-1}\ cm^{-2}$	/
Pixel resolution	$0.3\ arcsec/pix$	
Field of view	$0.763 \times 0.723\ deg^2$	
Detectors	16 H2RG, 2048x2048 pixels	

Table 8: Euclid NISP instrumental requirements [31]

3.4. Observation strategy

Euclid Wide Survey

The observational strategy must allow the necessary sky coverage for the statistical demands of the two probes WL and GC ($15\,000\ deg^2$ at minimum) in an estimated mission time of 6 years. The strategy is strongly constrained by the simultaneous operation of the two instruments VIS and NISP. It is indeed necessary to divide the observations into fixed exposure times which will be identical for both instruments. The exposure time is fixed by NISP, with the necessary time in spectrometry to have a minimal SNR on the spectra, which imposes the same rate for VIS. Indeed, the two instruments operate together.

To have a very accurate measurement, it is necessary that each exposure is not polluted by galactic dust, or by stars that are in the field. Therefore, the strategy requires to regularly exposing the sky in continuous zones, excluding as much as possible the areas containing a certain level of zodiacal radiation, gas or stars.

A compromise was thus made between the exposure time and the excluded areas of the sky, with a total field of $15\,000\ deg^2$ to cover. This compromise also takes into account the spacecraft capacities in terms of fuel, the total mission time, or the Sun position during the operations. The telescope will thus observe about two thirds of the sky. The excluded areas correspond mainly to the ecliptic (solar system plane), as well as the Milky Way plane. Indeed, the ecliptic is polluted by zodiacal light [33] infrared and the galactic plane is obstructed by the Milky Way itself, containing too many stars, gas and dust. Figure 10 shows the wide observation area of *Euclid*, each color corresponding to a year of observation.

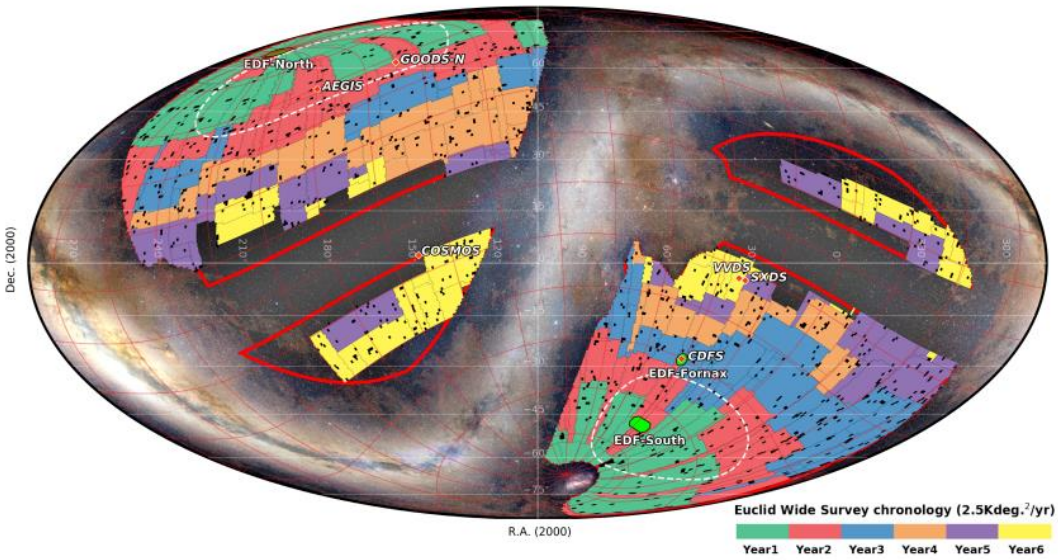

Figure 10: Map of the Euclid Large Survey, year by year, in Mollweide representation [31].

The telescope will make exposures of over an hour on an aperture of 0.53 deg². The total sequence is presented in Figure 11. The sequence is subdivided into 4 identical exposures taken with a slight offset (dithers), for pixel defects correction. During each cycle, the spacecraft performs simultaneously visible measurements (imaging) with the VIS instrument, and infrared measurements (spectroscopy) with the NISP instrument, then performs photometric measurements in the 3 bands Y, J, H successively, still with NISP. The optimization of this measurement sequence on 0.53 deg² allows reaching the good magnitudes on the whole wide field during the limited mission duration.

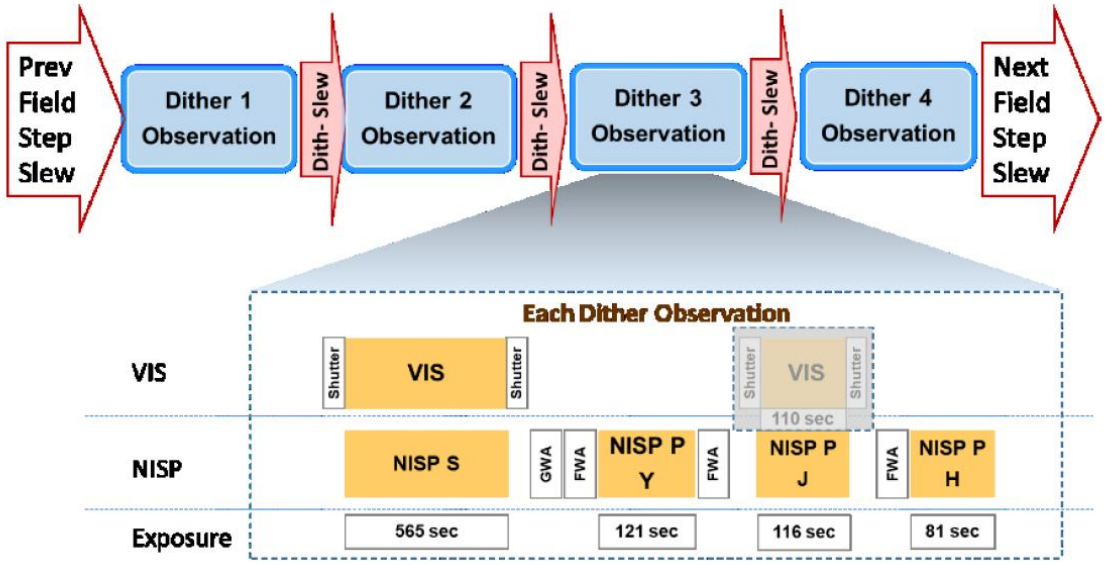

Figure 11: Euclid observation sequence in 4 identical cycles. NISP S corresponds to Spectroscopy; NISP P corresponds to photometry [34].

Euclid Deep Survey

In addition to the wide field, a deep field has been defined for the *Euclid* mission. This field, split in two parts close to the north ecliptic pole (NEP) and south (SEP), will be the subject of numerous revisits during the 6 years mission. These revisits have a double interest: firstly, to ensure the calibration of the telescope and its detectors over time. Secondly, to calibrate the purity of the spectroscopic sample used in GC, by observing a given field at much higher magnitudes than the wide field, with the same observational strategy in order to deduce the completeness and purity of the measurements. Finally it allows seeing much more distant objects (up to 26 in magnitude, or more) which are used by the so-called "legacy" science.

Survey	Wide Survey	Deep Survey
Covered area	$15000\ deg^2$	$40\ deg^2$
Magnitude	$M = 24\ AB$	$M = 26\ AB$

Table 9: Covered areas and magnitudes to reach for both Euclid surveys. [31]

4. CONCLUSION

The *Euclid* spacecraft has been sized and specified to meet the scientific challenges of cosmology. It will increase by a factor of at least 10 the accuracy of the essential cosmological parameters of Dark Matter and Dark Energy. The spacecraft has been specifically designed to operate in space for extragalactic surveys for 6 years on $15\,000\ deg^2$ of the sky, and to meet very stringent imaging, photometric, and spectroscopic constraints. The dichroic mirror, which allows the simultaneous operation of the two on-board instruments, is distinguished from the other mirrors of the telescope by its function of "beamsplitter", which makes it extremely critical. In the following chapter, we will discuss the PSF constraints related to VIS and Weak-Lensing, leading to a need for characterization of the dichroic mirror, and more particularly the unusual chromaticity of its optical properties.

5. REFERENCES

1 Hubble, E. P. (1926). Extragalactic nebulae. ApJ, 64 :321–369
2 Einstein, A. (1915). Die Feldgleichungen der Gravitation. Sitzungsberichte der Königlich Preußischen Akademie der Wissenschaften (Berlin), Seite 844-847
3 Friedmann, A. (1922). Über die Krümmung des Raumes. Zeitschrift fur Physik, 10 :377–386
4 Lemaître, G. (1933). L'Univers en expansion. Annales de la Société Scientifique de Bruxelles, 53.
5 Robertson, H. P. (1936). Kinematics and World-Structure III. ApJ, 83:257.
6 Walker, A. G. (1937). On Milne's Theory of World-Structure. Proceedings of the London Mathematical Society, s2-42(1):90–127.
7 Freedman, W. L. et al. (2001). Final Results from the Hubble Space Telescope Key Project to Measure the Hubble Constant. The Astrophysical Journal, 553(1) :47
8 M. Briday. Étude de l'impact de l'environnement galactique sur la standardisation des Supernovae de Type Ia. Cosmologie et astrophysique extra-galactique [astro-ph.CO]. Université de Lyon, 2021. Français. NNT: 2021LYSE1198. tel-03621515f
9 Zwicky, F. (1933). Die Rotverschiebung von extragalaktischen Nebeln. Helvetica Physica Acta, 6:110–127
10 Rubin, V. C. and Ford, Jr., W. K. (1970). Rotation of the Andromeda Nebula from a Spectroscopic Survey of Emission Regions. ApJ, 159:379.
11 S. M. Faber and J. S. Gallagher. "Masses and Mass-To-Light Ratios of Galaxies". Annual Review of Astronomy and Astrophysics 17.1 (1979), pp. 135–187
12 P. Peebles, "The mean mass density of the Universe." Nature 321, 27–32 (1986). https://doi.org/10.1038/321027a0
13 Hubble, E. P., "A Relation between Distance and Radial Velocity among Extra-Galactic Nebulae", Proc. Natl. Acad. Sci. USA, 15, 168 :173 (1929)
14 A. Gallenne. Les céphéides à haute résolution angulaire : enveloppe circumstellaire et pulsation. Astrophysique galactique [astro-ph.GA]. Université Pierre et Marie Curie - Paris VI, 2010.Français. tel-00641871
15 Perlmutter, S. et al, T. S. C. (1999). Measurements of Ω and Λ from 42 High-Redshift Supernovae. The Astrophysical Journal, 517(2):565.
16 A. G. Riess et al (1998), Observational Evidence from Supernovae for an Accelerating Universe and a Cosmological Constant, AJ 116 1009
17 P. Brown, P. Roming, P. Milne et al, (2010). "The Absolute Magnitudes of Type Ia Supernovae in the Ultraviolet". The Astrophysical Journal. 721. 1608. 10.1088/0004-637X/721/2/1608.
18 C. L. Bennett et al. Nine-year Wilkinson Microwave Anisotropy Probe (WMAP) Observations: Final maps and Results (2013) ApJS 208 20.
19 Planck Collaboration I, Planck 2018 results. I. "Overview, and the cosmological legacy of Planck". 2020, A&A, 641, A1, arXiv:1807.06205
20 N. Gillet. « Formation de galaxies pendant et après la réionisation ». Astrophysique [astro-ph]. Université de Strasbourg, 2016. Français. ⟨NNT: 2016STRAE019⟩. ⟨tel-01466746⟩
21 D. Eisenstein, I. Zehavi D. Hogg et al. (2005). Detection of the Baryon Acoustic Peak in the Large-Scale Correlation Function of SDSS Luminous Red Galaxies. The Astrophysical Journal. 633. 10.1086/466512.
22 N. Suzuki et al, (2011). The Hubble Space Telescope Cluster Supernova Survey: V. Improving the Dark Energy Constraints Above z>1 and Building an Early-Type-Hosted Supernova Sample. The Astrophysical Journal. 746. 10.1088/0004-637X/746/1/85.
23 M. Betoule, R. Kessler, J. Guy, J. Mosher, D. Hardin, et al. "Improved cosmological constraints from a joint analysis of the SDSS-II and SNLS supernova samples. Astronomy and Astrophysics" - A&A, 2014, 568, pp.A22
24 Chevallier, M. and Polarski, D. (2001) Accelerating Universes with Scaling Dark Matter. International Journal of Modern Physics, D10, 213.

25 D. Rapetti, S. W. Allen, A. Mantz, H. Ebeling. (2010). "The Observed Growth of Massive Galaxy Clusters III: Testing General Relativity on Cosmological Scales". Mon. Not. Roy. Astron. Soc., 406:1796–1804
26 Binétruy (2013). Dark energy and fundamental physics. The Astronomy and Astrophysics Review, 21(1):1–56.
27 E. Komatsu, K. M. Smith, J. Dunkley et al. (2011). Seven-year Wilkinson Microwave Anisotropy Probe (WMAP) Observations: Cosmological Interpretation. ApJS, 192:18.
28 R. Laureijs et al. (2011) "*Euclid* Definition Study Report" (*Euclid* Red book) ESA/SRE(2011)12
29 M. Kilbinger, Cosmology with cosmic shear observations: a review. Rep. Prog. Phys. 78 (2015) 086901, https://doi.org/10.48550/arXiv.1411.0115
30 *Euclid* Collaboration (2022) *Euclid* preparation. XVIII. The NISP photometric system, A&A 662, A92 (2022), https://doi.org/10.48550/arXiv.2203.01650
31 *Euclid* Collaboration (2022) *Euclid* preparation. I. The *Euclid* Wide Survey, A&A 662, A112 (2022), https://doi.org/10.1051/0004-6361/202141938
32 G.D. Racca, R. Laureijs, L. Stagnaro, J-C. Salvignol et al. "The *Euclid* mission design", Proceedings of the SPIE, vol. 9904, 07/2016, p. 1-23 (DOI 10.1117/12.2230762
33 V. Marchiori. In-flight photometry extraction of PLATO targets: optimal apertures for detecting extra-solar planets. Astrophysics [astro-ph]. Université Paris sciences et lettres; Universidade de São Paulo (Brésil), 2019. English. ⟨NNT: 2019PSLEO014⟩. ⟨tel-02891034v2⟩
34 J. Salvador Llorente et al, *Euclid* AOCS - Highest pointing stability for Dark Universe Investigation, 8th European Conference For Aeronautics And Space Sciences (EUCASS), (2019), DOI: 10.13009/EUCASS2019-902

Chapter 2

VIS instrument sensibility to Point-Spread Function

In the previous chapter, we presented the Weak lensing principle and the specifications for its measurement with the VIS instrument. We show that the measurement depends primarily on the shape of the galaxies, which can be biased by experimental measurements, especially due to the shape of the optical response of the instrument namely the PSF, coming from first order from the telescope itself.

In this chapter, we will look in detail to the PSF, examining its definition, the stringent requirements it must meet within the *Euclid* framework, and the diverse factors influencing its shape. Among these factors, we will particularly focus on the telescope itself and on the dichroic mirror, as ones of its most critical components.

1. PSF REQUIREMENTS FOR VIS AND WEAK-LENSING

To estimate the experimental bias arising from the PSF on the shape of galaxies observed by VIS, thus affecting the WL probe, we will first relate this bias to the WL measurement parameters introduced in Chapter 1. Secondly, we will specify the tolerances required on its shape and on these variations.

1.1. Systematic and multiplicative biases induced on shear

The measurement of gravitational shear γ, introduced in Chapter 1 - part 2.2, corresponds visually to induced ellipticity on galaxies. It is affected by PSF, which adds ellipticity to all observed objects. In practice, this result in a systematic bias σ_{sys} and a multiplicative bias m induced on the two-point lensing correlation function C_{ij} [28, 29], leading to an estimator $\widehat{C_{ij}}$:

$$\widehat{C_{ij}} = (1+m)^2 C_{ij} + \sigma_{sys}^2 \tag{9}$$

Simulations have been carried out [35] to estimate the maximum value of m and σ_{sys}^2 to achieve the expected scientific performance on the dynamical dark energy parameters w_a and w_0. The limits are listed in Table 10.

Bias induced on gravitational lensing	Upper limit that maintains $\Delta w_a, \Delta w_0 \leq 10\%$
m	$2 * 10^{-4}$
σ_{sys}^2	10^{-7}

Table 10: Maximum limits on multiplicative and systematic shear bias. [36]

1.2. PSF parameters

The PSF, as a function in two spatial dimensions, can be characterized by a set of parameters that capture key aspects of its shape and characteristics. Some parameters are generally used as the radius or the full-width at half-maximum (FWHM) of the PSF along its major and minor axes, the ellipticity which is the degree of elongation or compression of the PSF along its major and minor axes, the shape of the intensity distribution across the PSF, which can be described using Gaussian, Moffat, or other radial profiles. Additional parameters, such as skewness which are higher orders, can be used to capture more detailed information about the PSF's shape.
These PSF parameters must be constrained to establish tolerance levels within the *Euclid* framework. To establish these constraints, we will use the ellipticity parameters e_1, e_2 and the radius R.
PSF parameters are calculated [37] from the PSF moments:

- The zero order moment $E(\lambda)$ is simply the energy of the PSF signal, integrated over the entire image plane.
- The two first order moments correspond to the barycenters of the PSF in X and Y directions:

$$\hat{X}(\lambda) = \frac{1}{E}\iint [X\ PSF(X,Y)]dXdY\ ;\ \hat{Y}(\lambda) = \frac{1}{E}\iint [Y\ PSF(X,Y)]dXdY$$

- The moments of order 2 are the quadrupoles $Q_{ij}(\lambda)$:

$$Q_{ij}(\lambda) = \frac{1}{E}\iint [(i-\hat{\imath})\ (j-\hat{\jmath})\ PSF(X,Y,\lambda)]dXdY$$

With here $i = X, Y$ and $j = X, Y$.
These momentums are used to obtain the mean radius R and the ellipticities e_1, e_2 in each direction.

$$R^2 = Q_{XX} + Q_{YY}$$

$$e_1 = \frac{Q_{XX} - Q_{YY}}{R^2};\ e_2 = \frac{2Q_{XY}}{R^2}$$

$$e = \sqrt{e_1^2 + e_2^2}$$

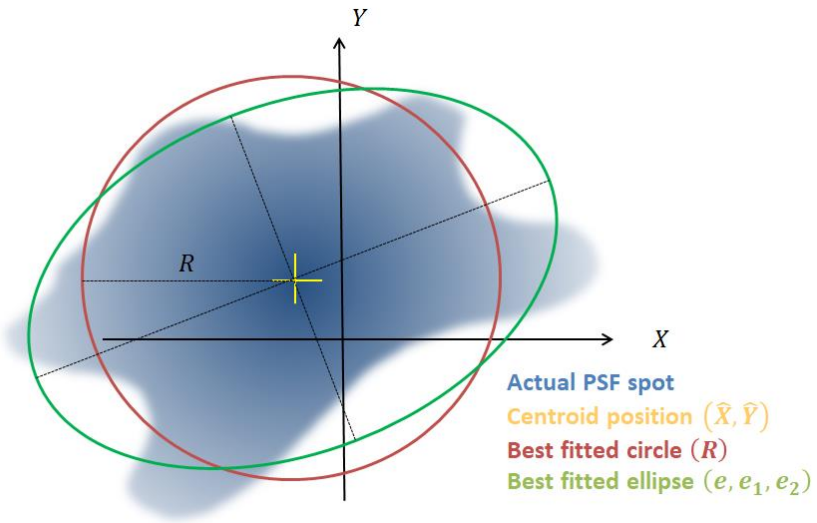

Figure 12: Illustration of PSF morphological parameters.

Figure 12 shows the radius and ellipticity parameters of the PSF. The radius R is that of the best equivalent circle, and e, between 0 and 1, is the ellipticity of the best equivalent ellipse. The quantity e can be declined into two contributions e_1, e_2, to take account of the orientation of the ellipse (see Figure 13). Note that R and e are wavelength-dependent quantities. Their chromatic variations will therefore also be investigated.

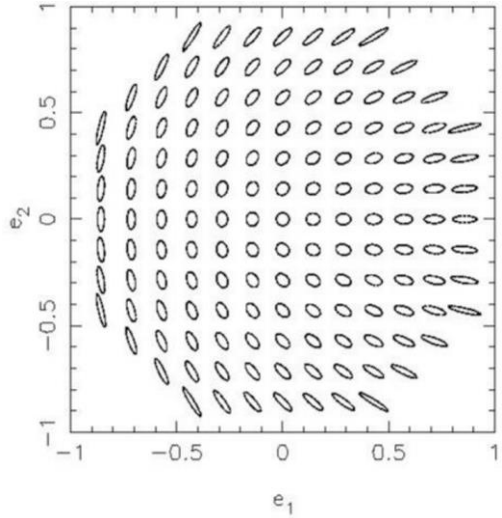

Figure 13: Illustration of ellipticity parameters e_1, e_2 [38].

1.3. Tolerance on PSF parameters from shear bias limit

We can relate the parameters of the PSF ellipticity "e_{PSF}" and its size expressed with R_{PSF}, to the biases σ_{sys}^2 and m (relation established by Paulin-Henriksson et al. [37]) with:

$$\sigma_{sys}^2 = \left(\frac{1}{P^{\gamma}}\right)^2 \left\langle \left(\frac{R_{PSF}^2}{R_{gal}^2}\right)^2 \right\rangle \left\{ \left[\frac{\sigma(R_{PSF}^2)}{R_{PSF}^2} + c\right]^2 |e_{PSF}|^2 + 2\sigma^2(e_{PSF}) \right\} \quad (10)$$

$$m = \frac{1}{P^{sh}} \left(\mu + \frac{\sigma(R_{PSF}^2)}{R_{PSF}^2}\right) \left\langle \frac{R_{PSF}^2}{R_{gal}^2} \right\rangle \quad (11)$$

With, in Eq. 10, 11,

$$P^{\gamma} \approx 2, P^{sh} \approx 1.84\,, c \approx 10^{-3}, \mu \approx 2 * 10^{-3}$$

The term R_{gal}^2, equal to 0.2 arcsec FWHM, corresponds to the standard radius of a galaxy (approximately a Gaussian profile) as seen by *Euclid*. The other terms in these equations are the absolute values of the PSF parameters: e_{PSF}, R_{PSF}^2 and their variations (standard deviations): $\sigma(e_{PSF})$ and $\sigma(R_{PSF}^2)$. The variations correspond to the gap between knowledge and reality, and therefore to the accuracy of *Euclid*'s PSF model.
Simulations were carried out to estimate the limit value of these parameters and their variations within the tolerance on σ_{sys}^2 and m. The results of these simulations are presented in Table 11:

Name	Expression	Tolerance
Absolute PSF ellipticity	e_{PSF}	≤ 0.15
PSF ellipticity variation	$\sigma^2(e_{PSF})$	$\leq 2 * 10^{-4}$
PSF size	R_{PSF}^2/R_{gal}^2	≤ 4
PSF size variation	$\sigma^2(R_{PSF}^2)/R_{PSF}^2$	$\leq 10^{-3}$

Table 11: Main constraints on PSF parameters associated with bias induced on gravitational shear [28].

The four tolerances above remain valid for all VIS wavelengths of interest, i.e. the band from 500 to 950 nm. *Euclid*'s PSF must therefore be characterized to assess the specifications given in Table 11, taking into account any chromatic effects that may arise.

2. POINT SPREAD FUNCTION AND WAVE FRONT ERROR

In this section, we will go back to the theoretical definition of the PSF, as specific to any optical system. The PSF of an optical system is a mathematical description of the intensity distribution of a point source as it appears on the image plane. It characterizes how the system spreads the light from a point source, providing insights into the spatial resolution and optical quality of the imaging system.

The corresponding image of a point like source thus appears as a blurred spot, more or less spread out and irregular. The shape of this spot depends on the actual geometry of optical elements such as mirrors, which may exhibit aberrations. In the case of *Euclid*, light arriving at the VIS focal plane passes through the telescope and the dichroic. The optical system therefore contains the telescope's mirror chain (7 mirrors) and the dichroic mirror. On this part, we will focus on the optical PSF only appearing on the image plane of the optical system, i.e. without taking into account any subsequent pixelation effects as those that can be related to the CCD detectors effects.

2.1. Diffractive PSF

Diffraction is affecting directly the shape of the PSF and refers to the bending or spreading of light beams as they pass through apertures. Even without aberrations, a PSF exists in a system of limited size as for *Euclid*, due to the telescope aperture. The diffractive PSF is equivalent, to within a proportional factor, to the square of the Fourier transform of the optical system's aperture function [38]:

$$PSF_{diff}(f_X, f_Y, \lambda) \propto |\mathcal{FT}[Aper(x,y)]|^2 \tag{12}$$

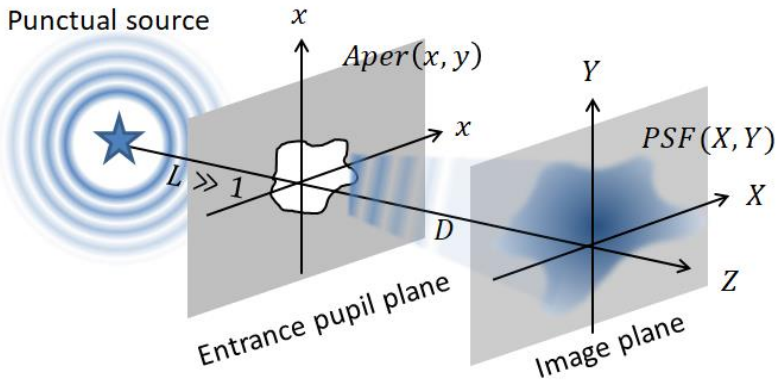

Figure 14: Illustration of a PSF created by an optical aperture $Aper(x,y)$.

In Eq. 12, the $Aper(x,y)$ function is the aperture of a telescope. The coordinates f_X, f_Y correspond to the image coordinates X, Y in the frequency domain. Figure 14 illustrates the PSF spot from an infinitely distant point source generating a spherical light wave, arriving flat at the $Aper(x,y)$ aperture, also known as the entrance pupil.
In the case of a circular-aperture telescope of diameter d and focal length f, the diffractive PSF corresponds to an Airy spot A [40] expressed here in polar coordinates:

$$A(x) \propto [J1(\pi x)/\pi x]^2 \tag{13}$$

In Eq. 13, $J1$ is the first-order Bessel function and x is equal to $dr/\lambda f$, r being the radial distance from the optical axis in the image focal plane. The radius r_{airy} of the central Airy spot is such that:

$$r_{airy} \approx 1.22\,\lambda f/d \tag{14}$$

The Airy spot, showed in Figure 15, is a central bright spot surrounded by concentric rings, and it represents the idealized diffraction pattern for a point source of light in an optical system. The radius of the central spot and rings are determined by the wavelength and the size of the circular aperture or optical system, which explains the rainbow aspect on Figure 15.

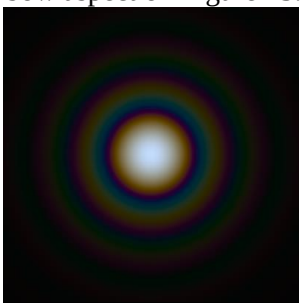

Figure 15: Airy spot [41]

Figure 16 (right) shows the *Euclid* aperture, which have a central obstruction (M2 mirror) and its support arms that mask part of the field. The resulting diffractive PSF thus presents a particular geometry as seen in Figure 17 showing a simulated *Euclid* PSF [43]. A hexagonal structure appears in the logarithmic representation.

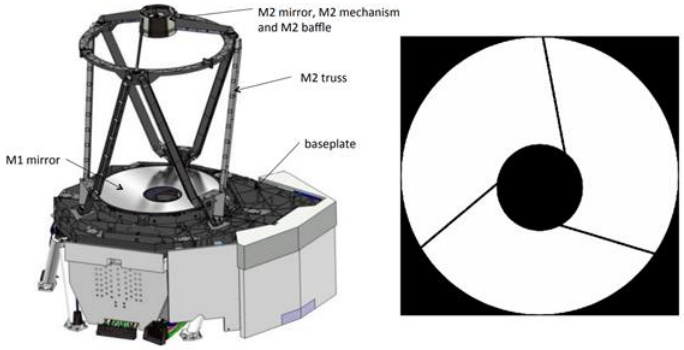

Figure 16: (Left) CAD view of Euclid's PLM showing mirrors M1, M2 and their supports [32]. (Right): Simulation of the Euclid telescope aperture [42].

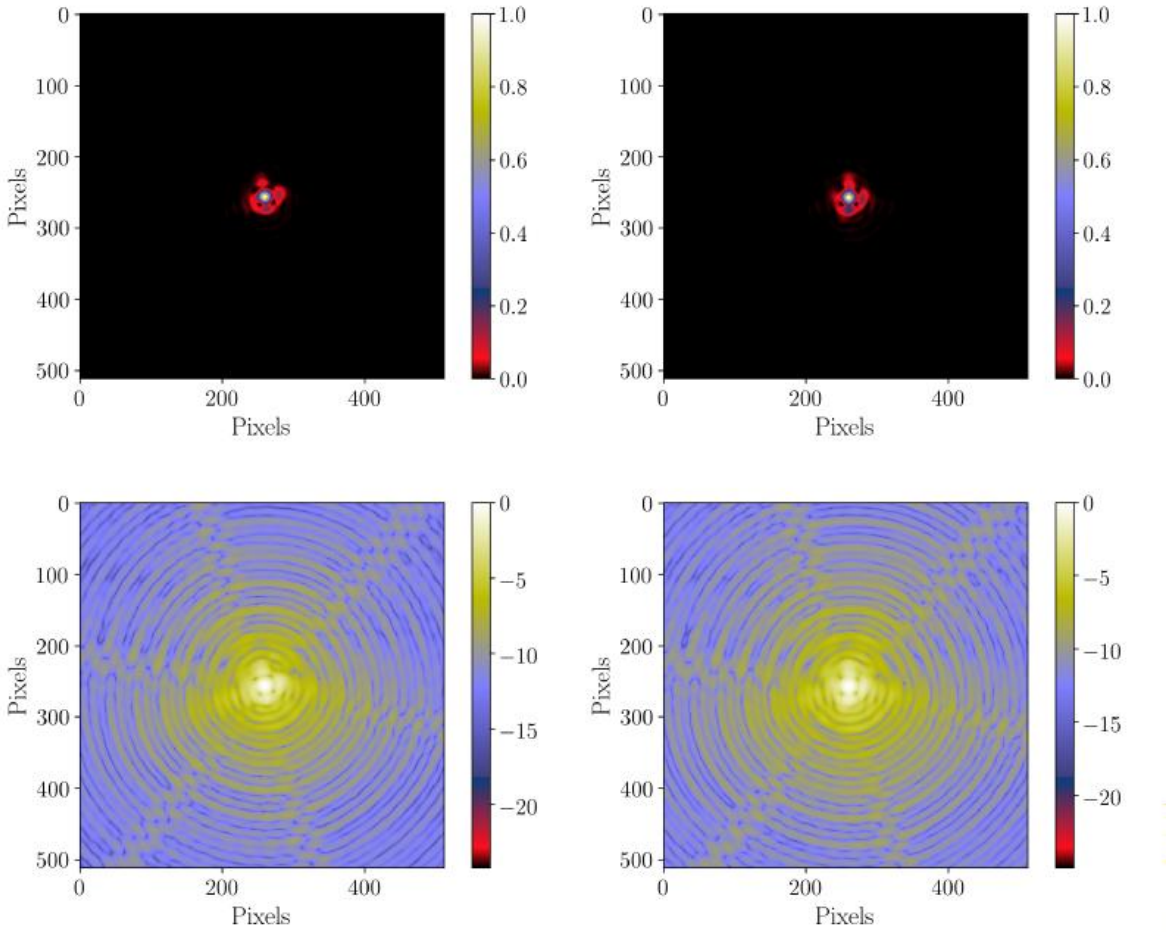

Figure 17: Visual examples of simulated Euclid PSF in the natural (top row) and logarithmic (bottom row) domains, at the original pixel sampling of the simulation (about 12 times finer than Euclid). Each stamp is approximately 4.25 arcsec across. [43]

2.2. PSF arising from aberrations

Optical aberrations are another effect which have a significant impact on the PSF. Aberrations are deviations from ideal optical behavior that can introduce distortions in the imaging process. These aberrations affect the shape and characteristics of the PSF in several ways, degrading the overall quality of the image and causing blurring, shape deformation, intensity variations, and a reduction in resolution. High-order aberrations, in particular, can contribute to a loss of spatial resolution. Mitigating or correcting aberrations is crucial to optimize the shape performance. When aberrations are present, they cause deviations from the ideal spherical wavefront. The wavefront in the context of optics is the spatial distribution of points that have the same optical phase. A perfectly spherical wavefront corresponds to an undistorted, ideal optical system. Figure 18 shows the WFE concept in a simplified case, inducing a PSF. To account for a non-zero wavefront error $\mathrm{WFE}(x_0, y_0, \lambda)$, an angular phase shift term must be added to the aperture function. Thus, taking Eq. 12 [44],

$$PSF(f_X, f_Y, \lambda) \propto \left| \mathcal{FT} \left[Aper(x,y) * e^{\frac{i2\pi}{\lambda} \mathrm{WFE}(x,y\lambda)} \right] \right|^2 \quad (15)$$

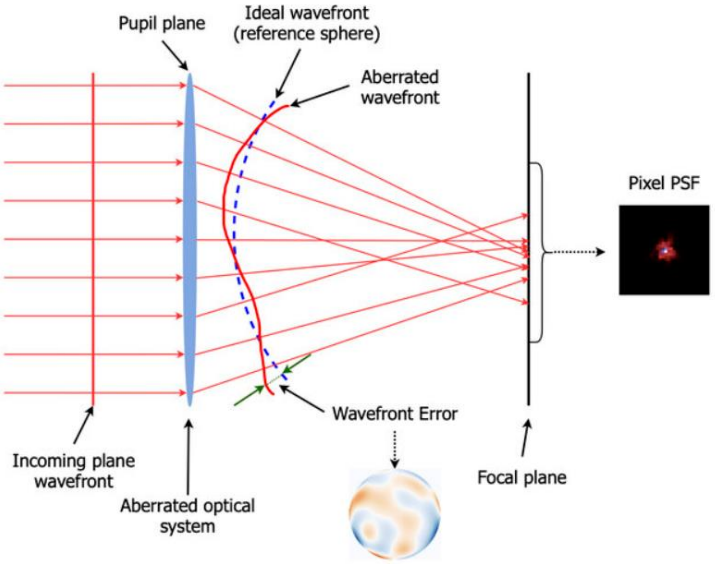

Figure 18: Illustration of the WFE in a one-dimensional projection of an ideal setting where the optical system is represented as a single lens [45]

Thin films, like coatings applied to mirrors, can introduce aberrations due to factors such as variations in refractive index across the film, thickness variations, and the presence of multiple layers. These aberrations can include spherical aberration, coma, and astigmatism and will produce degradations and then WFE which can be highly chromatic. A highly chromatic WFE undeniably leads to a highly chromatic PSF and should be corrected. The *Euclid* dichroic mirror presented in Chapter 3 is an example that produces such high chromatic effects because of the dielectric thin films coated onto the mirror.

2.3. PSF Convolution with source

Let us consider a polychromatic object, for example a galaxy, represented by the function $O(x_0, y_0, \lambda)$ giving the intensity of the light signal in the object plane coordinates x_0, y_0 at each wavelength λ. This object then appears on the image plane with coordinates X, Y, and its theoretically perfect image is $O(X, Y, \lambda)$... The PSF takes into account the inherent imperfections and limitations of an optical system such as diffraction, aberrations, and other optical distortions that affect the accuracy with which a point source is reproduced in the image.
Essentially, the PSF provides insights into the spatial resolution and quality of an optical system by showing how a point source is transformed in the final image. A well-defined and compact PSF indicates good imaging characteristics, while a broader or distorted PSF suggests potential issues affecting the system's performance. For each wavelength λ, the image $I(X, Y, \lambda)$ actually obtained by the optical system is then the convolution:

$$I(X,Y)_\lambda = O(X,Y)_\lambda \otimes PSF(X,Y)_\lambda \quad (16)$$

The image $I(X, Y, \lambda)$ is thus degraded in Eq. 16 by the PSF. When imaging extended objects like galaxies, this function will influence the observed shape and characteristics. The impact of the PSF on a galaxy's appearance is often manifested through the blurring or smearing of its features. Since a galaxy is not a point source but an extended structure with intricated details, the PSF acts as a convolution kernel, spreading the light from individual components across adjacent pixels. Figure 19 shows an example of this convolution [46], where the image is blurred by the PSF. This convolution

effect can lead to a reduction in spatial resolution and may cause difficulties in accurately determining the galaxy's intrinsic properties, such as its size, shape, and intensity distribution.

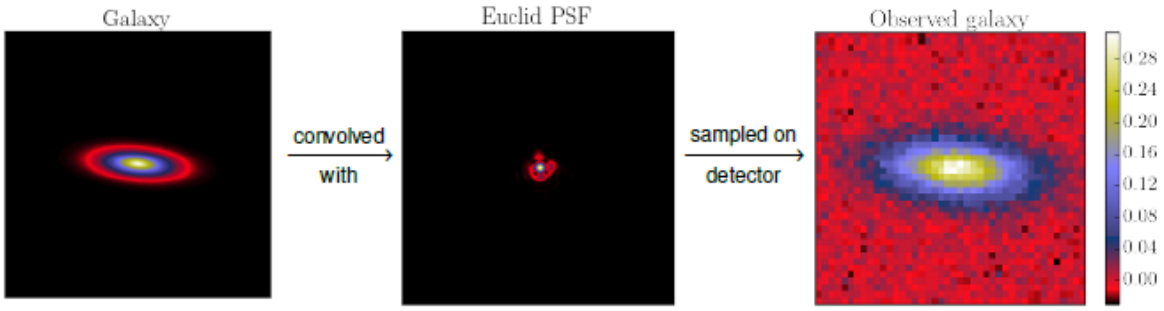

Figure 19: Illustration of the imaging process on a galaxy convolved by Euclid PSF (center), then sampled over a finite number of pixels (right). [46]

This means that the PSF introduces a convolutional distortion that needs to be considered when analyzing and interpreting observational data of galaxies. Understanding and deconvolving the PSF from the observed image is crucial to obtain a clearer representation of the true structure and characteristics of the galaxy being studied.

Finally, the PSF is a quantity that depends also on the field of view. Figure 20 illustrates this problem. Stars, supposedly point sources, show a different PSF depending on where in the field they are located. To be deconvoluted, the PSF must be identified at every field of view (and especially where the galaxies are located), which means that a certain number of stars must be used as landmarks to identify the PSF locally. This also means taking into account the overlap of PSFs when objects are close together in the field, the pixel sampling or the polychromatic emission spectrum of target stars, for which the (polychromatic) PSF depends,

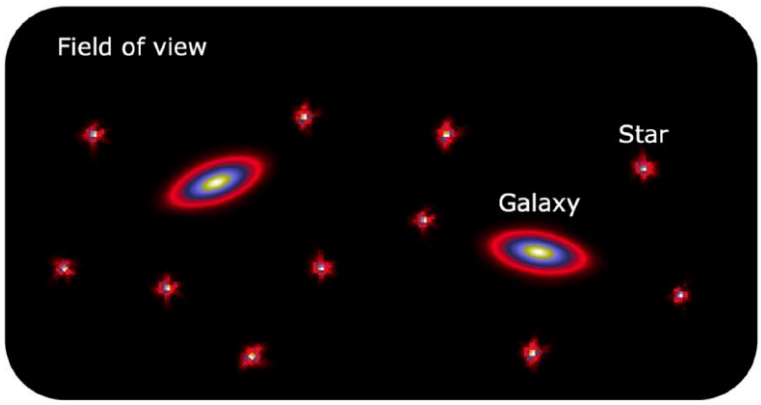

Figure 20: Illustration of a field of view showing the PSF modelling problem. Firstly, the PSF model should be estimated from the stars. The model should then be used to estimate the PSF at the target positions, e.g., galaxy positions. [47]

3. CONTRIBUTIVE ELEMENTS TO *EUCLID* PSF

In this part, we will examine different contributions to *Euclid*'s PSF and how they are handled. . The trade-off between all these contributions will be presented, with particular attention to the case of Euclid's dichroic mirror, which has a chromatic contribution.

3.1. Mirrors aberrations

In the PSF measurement process, the light passes through the telescope, comprising 3 spherical metal mirrors (M1, M2, M3), a plane metal mirror (FoM3), and 3 dielectric plane mirrors (FoM1, FoM2, and dichroic mirror) before arriving at the focal plane, made up 36 CCD detectors.

We have seen that the PSF include the diffraction effect due to the telescope aperture, and in addition surface aberrations from each mirror, resulting from errors in polishing [47], mechanical strain [48], or thin film coating. This is labelled as "Surface Figure Error" or $\mathrm{SFE}(x_i, y_i)$, a spatial function in the plane coordinates of each mirror x_i, y_i expressing the deviation between the mirror's actual surface and its theoretical surface. The mirror $\mathrm{SFE}(x_i, y_i)$ induces a slight phase shift between the reflected and incident wave. This results in a WaveFront Error $\mathrm{WFE}(x_i, y_i)$, namely in reflection, which corresponds to twice this $\mathrm{SFE}(x_i, y_i)$ in the case of a metal mirror. For a dielectric mirror, the $WFE(x_i, y_i)$ may be more complex to define. In all cases, $\mathrm{WFE}(x_i, y_i)$ modify $\mathrm{PSF}(X, Y, \lambda)$ with Eq. 15. Figure 21 illustrates the phenomenon, with a WFE that corresponds to twice the SFE of a mirror.

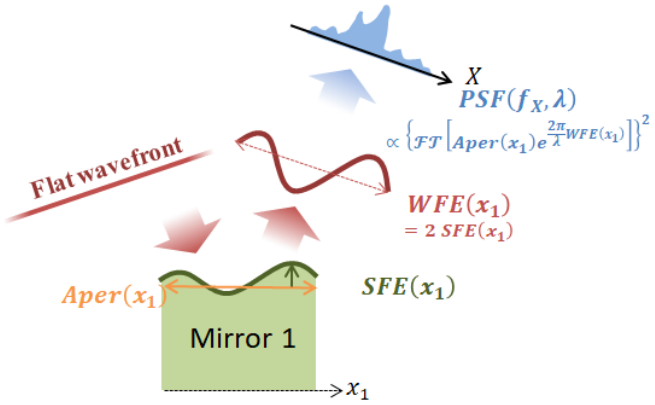

Figure 21: 1-dimensional example of a $PSF(f_X, \lambda)$ resulting from a reflection on a mirror with $SFE(x_1)$ and aperture $Aper(x_1)$. The induced WFE is twice this SFE..

Table 12 shows the maximum tolerances on the standard deviations of the $\mathrm{SFE}(x_i, y_i)$ of *Euclid*'s mirrors expressed in nm RMS, as well as vertical positioning errors, guaranteeing a PSF within the tolerances of Table 11.

Mirror	SFE (nm RMS)	Positioning (µm)
M1	≤ 15	± 20
M2	≤ 10	± 20
M3	≤ 15	± 30
FoM1	≤ 10	± 0.1
FoM2	≤ 10	± 60
FoM3	≤ 10	± 60
Dichroic mirror	≤ 10	± 60

Table 12: Surface error and vertical positioning tolerances for Euclid mirrors [49]

The order of magnitude of maximum surface errors is therefore around 10 nm RMS. It should be noted that the chromatism induced on the WFE by the coatings on FoM1, 2, and the dichroic mirror was not yet taken into account when these tolerances were initially established.

3.2. Dichroic mirror chromatic effects

As we have mentioned, without surface aberrations on the optics, and in the case of a circular aperture, the PSF would be an Airy spot whose central radius is proportional to λ. Aberrations produce a non-chromatic WFE(x, y) leading to a PSF(x, y, λ) undergoing a spatial variation depending only on λ. This remains true as far as the optical path to VIS has no refractive elements such as lenses.

Euclid dichroic mirror is coated with a stack of thin layers, enabling it to perform an optical bandpass function. These optical properties are the result of interference from the electromagnetic signal transmitted and reflected at each interface of this stack of almost 200 layers (See Chapter 3, part 3.2).

The signal reflected by the dichroic induces a phase shift that is highly dependent on the wavelength and thicknesses of the layers in the stack. As a result, even the smallest thickness error within the layers stack is likely to cause irregular and non-linear chromatic spatial variations in the WFE. The PSF(x, y, λ) function thus inherits these complex variations, making its characterization and calibration more complex. This will be detailed in the next chapter.

3.3. CCD sensor effects

The detection system of the VIS instrument, located at the image plane of the telescope, is made up of 36 CCD detectors which can also introduce a bias on the PSF. CCD pixels produce electrons by photoelectric effect. These electrons are then transferred from pixel to pixel to the readout system at the ends of the sensor. However, this transfer is not perfect, with a certain probability of failure in the passage of electrons from one pixel to another. This is the Charge Transfer Inefficiency (CTI) effect [50]. If this effect is too pronounced, it translates visually into a unidirectional blurring of the entire image. Figure 22 shows a simulation of this effect. CCD pixels produce electrons which are transferred laterally from right to left. Objects on the right-hand side of the field, i.e. further away from the readout electronics, undergo lateral spreading. This spread generates PSF, which is non-convolutive because it depends on the point in the field considered, and for which Eq. 16 is therefore not applicable.

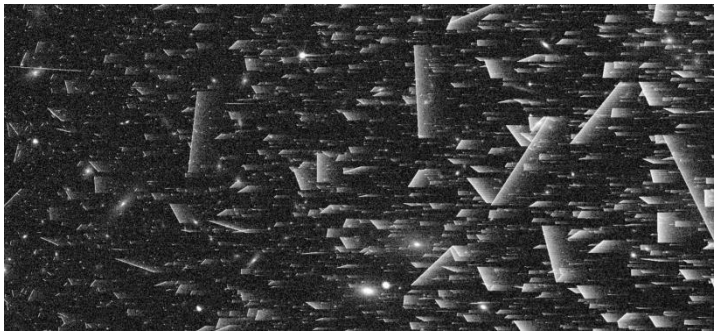

Figure 22: Simulation of the CTI effect in Euclid (Image credit: P. Hudelot and S. Serrano for OU-SIR).

These effects are compounded by other detector faults. For example, high-energy cosmic rays [51], present in the space environment, strike the detector. Their traces are visible in the simulation shown in Figure 22, in the form of segments in all directions. Here again, we speak of a non-convolutive PSF. These effects have been the subject of extensive simulation work for *Euclid* [51], in order to predict their consequences on the instrument's performance. Regular in-flight calibration using a dark or flat signal, and dithers [28], will reduce the impact of defects.

3.4. Spacecraft stability

The stability of the PSF is required to ensure the same image quality along *Euclid* survey which means to ensure an unchanged PSF over time. Several factors contribute to the stability of the PSF in a space-based mission as a precise pointing, a control of the temperature and of vibrations.
The telescope is embarked on a satellite that will move to point at various regions of the sky over a period of 6 years. To ensure the same image quality, the satellite must remain stable throughout the observation period, which is around 500s. The displacements also induce possible modifications of the PSF linked to the stability over time of the telescope's pointing.
It is required that during the 500s of VIS observation, telescope pointing variations remain below $25 * 10^{-3}$ arcsec RMS [28]. To achieve such positioning accuracy, the satellite features an excellent Attitude and Orbit Control System (AOCS), consisting of a "star tracker" and cold gas thrusters, which are more stable and precise than a reaction wheel [28].

To ensure the telescope's thermomechanical stability in the space environment, Airbus Defense and Space (ADS), in charge of *Euclid*'s telescope design, chose to use silicon carbide (SiC) for the telescope's mirrors, a material with very stable thermomechanical properties for an operating temperature of 150 K. Such a material enables athermal modeling of the mirrors for the VIS PSF [28]. Thermomechanical constraints also affect the choice of materials for the mirror supports (ceramic: Si_3N_4) and the optical bench (reinforced carbon fiber: CRFP). Finally, regular calibrations are necessary to correct any drift or degradation in the telescope's PSF performance. This is conducted through a comprehensive ground and in-flight characterization and calibration program.

4. *EUCLID* PSF CHARACTERIZATION

Characterizing the PSF is a complex problem for any astronomical project. In this section, we will see how *Euclid*'s PSF is characterized and how the images obtained by the telescope are processed.

A characterization of *Euclid*'s PSF on the ground is necessary before the start of the space mission, in order to have an excellent prior knowledge of the telescope's physics, and also to enable an in-flight calibration strategy to be established. For example, if end-to-end simulations carried out on the ground predict non-linear, chromatic, temporal or field-dependent effects, in-flight calibration will be affected. The number and diversity of objects used for calibration, or the number of revisits of each calibration field, will need to be adjusted.

4.1. Ground PSF characterization

The PSF model can be parametric or non-parametric. A parametric model is based on the finest possible knowledge of the physics of the optical system and its defaults. A non-parametric model is purely mathematical and data-driven. It is not based on the physics of the telescope. There is a wide variety of such models (shape interpolation, Principal Components Analysis, etc.). Of course, a parametric model is fitted realistically from measurement data, such as knowledge of a mirror's Surface Figure Error.

For *Euclid*'s Science Ground Segment (SGS) processing, the baseline consists of a parametric model [43, 46] adjusted from a **Phase Diversity**[1] measurements, which results may be supported by a data-driven model fitted from data taken in flight at point L2. The dichroic mirror analysis is thus a building block of this parametric model. Chapter 3 presents a part of the theory used to understand and describe the chromaticity of the WFE and PSF induced by this dielectric mirror. A realistic physical model of this mirror was then established and calibrated on the basis of a campaign of measurements of its optical response. Parameterization of the dichroic mirror's chromatic WFE was thus added to *Euclid*'s global PSF pipeline, designed by SGS.
Of course, the dichroic mirror is not the only Euclid optical component to have required such characterization work. The surface irregularities of the other mirrors were also measured. VIS detectors were characterized to determine pixel effects, such as pixel persistence or CTI. These sensor defects were then modeled and then numerically tested on pre-existing sky maps similar to those *Euclid* will observe during its mission.

Another area for consideration concerns environmental conditions. These differ between the ground and the space environment, so that the PSF of the telescope on ground differs from that which would have been measured in flight. Earth's gravity, atmospheric pressure, ambient temperature and radiation level all impact the PSF in one way or another. Another example is ice, which creates a thin film layer on the telescope mirrors [53] during the first few months after launch. The thickness of this ice layer depends on time, surrounding materials and sunlight exposition.

4.2. In-flight PSF calibration

As mentioned above, ground-based characterization of the PSF allows setting up in-flight calibration strategy. We have seen that the PSF is the telescope's impulse response (including the dichroic

[1] Phase diversity is a technique that consists in measuring the PSF of an optical system by deliberately adding aberrations such as defocus. These defocused acquisitions are then used to apply phase retrieval algorithms, such as the Gerchberg-Saxton algorithm [52]. This enables the PSF to be identified with better precision than with in-focus measurements only.

mirror). To adjust the in-flight PSF, *Euclid* will therefore observe calibration stars, which are consider as point light sources. Observing these stars will allow the application of Phase Diversity algorithms to adjust the PSF parametric model. However, this calibration remains highly complex. Firstly, the resolution of VIS channel is limited by pixel size. In addition, the PSF itself is a physical quantity that depends on several parameters such as:

- **Position in the field of view**. The PSF is a quantity that depends on the position in the observed field of view. To calibrate these spatial variations, simulations [28] showed that 1800 stars in each field are needed for calibration.
- **Wavelength**. The chromaticity of the PSF poses challenges to be characterized at each wavelength from a stellar image integrated across the entire visible spectrum (VIS), making estimation of the polychromatic PSF complex. This necessitates knowledge of the spectral energy distribution (SED) of each star and demands that *Euclid*'s parametric PSF model realistically considers this chromaticity.
- **Time**. We have seen several examples where the PSF is time-dependent (ice formation on optics, thermomechanical stability of materials, etc.), requiring regular observations of calibration stars (every 3 or 6 months).

The fitted PSF model can then be propagated to the galaxies used for the WL probe, which are at different locations in the field, and with different spectral emissions. Non-linearity phenomena may also exist, and must be supported by the model.

5. CONCLUSION

This chapter defined firstly how PSF parameters were constrained to respect the performance of *Euclid*'s WL probe. Next, we presented PSF formalism and its dependence to WFE. The elements contributing to *Euclid*'s PSF were then listed, in particular the dichroic mirror. Finally, the issue of PSF model calibration with Phase Diversity on the ground and in flight was addressed, the effectiveness of which depends on knowledge of the telescope defects and physics as a whole. This chapter provides an overview of the environment in which we are working to characterize *Euclid*'s dichroic mirror, which adds chromaticity to the PSF.

The next chapter is dedicated to the dichroic mirror itself. We will look at its precise function in the telescope and how it complies with the specs. After explaining the origin of the optical properties of this dielectric mirror, we will move on to its complex chromaticity.

6. REFERENCES

35 M. Cropper, H. Hoekstra, T. Kitching et al., Defining a weak lensing experiment in space, Monthly Notices of the Royal Astronomical Society, Volume 431, Issue 4, 1 June 2013, Pages 3103–3126, https://doi.org/10.1093/mnras/stt384

36 T. D. Kitching, A. N. Taylor, A. F. Heavens, Systematic effects on dark energy from 3D weak shear, Monthly Notices of the Royal Astronomical Society, Volume 389, Issue 1, September 2008, Pages 173–190, https://doi.org/10.1111/j.1365-2966.2008.13419.x

37 S. Paulin-Henriksson, A. Amara, L. Voigt, A. Réfrégier, S. Bridle, "Point spread function calibration requirements for dark energy from cosmic shear" L. 2008, A&A, 484, 67, DOI: 10.1051/0004-6361:20079150

38 S. Bridle et al. "Handbook for the GREAT08 Challenge: An image analysis competition for cosmological lensing". Ann. Appl. Stat. 3(1): 6-37 (March 2009). DOI: 10.1214/08-AOAS222

39 F. Vidal. « Calibrations et reconstruction tomographique en optique adaptative multi-objet pour l'astronomie : Application au démonstrateur CANARY ». (2009) tel-00559962

40 E. Hecht (1987). "Optics" (2nd Ed.). Addison Wesley. ISBN 0-201-11609-X. Sect. 5.7.1

41 Image Credit: SiriusB, from https://en.wikipedia.org/wiki/Airy_disk

42 L. M. Gaspar Venancio, L. Carminati, J. Amiaux, Luciana Bonino, Giuseppe Racca, Roland Vavrek, René Laureijs, Alex Short, Tobias Boenke, and Paolo Strada "Status of the performance of the *Euclid* spacecraft", Proc. SPIE 11443, Space Telescopes and Instrumentation 2020: Optical, Infrared, and Millimeter Wave, 114430G (15 December 2020); https://doi.org/10.1117/12.2562490

43 M. A. Schmitz et al. *Euclid*: "Nonparametric point spread function field recovery through interpolation on a graph Laplacian". A&A, 636 (2020) A78, https://doi.org/10.1051/0004-6361/201936094

44 F-C. Huang, B. Barsky. (2011). "A Framework for Aberration Compensated Displays."

45 T. Liaudat, J-L. Starck, M. Kilbinger, P-A. Frugier (2022), "Rethinking data-driven point spread function modeling with a differentiable optical model." Front. Astron. Inverse Problems 39 035008. doi: 10.1088/1361-6420/acb664

46 M. A. Schmitz. "*Euclid* weak lensing: PSF field estimation". Cosmology and Extra-Galactic Astrophysics [astro-ph.CO]. Université Paris Saclay (COmUE), 2019. English. NNT: 2019SACLS359

47 T. Liaudat, J-L. Starck and M. Kilbinger (2023), "Point spread function modelling for astronomical telescopes: a review focused on weak gravitational lensing studies". Front. Astron. Space Sci. 10:1158213. doi: 10.3389/fspas.2023.1158213

48 T. Begou, H. Krol, D. Stojcevski, F. Lemarchand, M. Lequime, C. Grezes-Besset, J. Lumeau "Complex optical interference filter with stress compensation", Proc. of SPIE Vol. 9627 96270R-1 (2015)

49 R. Laureijs et al. (2011) "*Euclid* Assessment Study Report for the ESA Cosmic Visions." ESA/SRE(2009)12

50 J. Rhodes, A. Leauthaud, C. Stoughton, R. Massey, K. Dawson, W. Kolbe, N. Roe (2010). The Effects of Charge Transfer Inefficiency (CTI) on Galaxy Shape Measurements. Publications of the Astronomical Society of the Pacific, 122(890), 439–450. https://doi.org/10.1086/651675

51 M. Niedźwiecki, K. Rzecki, M. Marek et al. (2019). "Recognition and classification of the cosmic-ray events in images captured by CMOS/CCD cameras." [astro-ph.IM], arXiv:2207.10411v1

52 R. W. Gerchberg, "A practical algorithm for the determination of phase from image and diffraction plane pictures." Optik 35 (1972): 237-246.

53 *Euclid* Collaboration, "*Euclid* preparation. XXIX. Water ice in spacecraft. Part I: The physics of ice formation and contamination" A&A 675, A142 (2023).

Chapter 3

Euclid dichroic mirror

This chapter gives a comprehensive introduction of the dichroic mirror itself. Commencing with a physical description, we will subsequently explain its role and integration within the telescope system. The latter part of the chapter will be dedicated to the tolerances and initial specifications encompassing aspects such as reflectivity, transmission, and surface quality.

An unexpected aspect that emerged in the later stages of the project is the chromaticity of the WFE emitted by the dichroic mirror. Initially, the mirror's reflected WFE was subject only to achromatic requirements. However, more evaluation indicates the need to also consider chromatic aberrations. This section will therefore explain how the stack of thin layers, which determines the optical properties of the dichroic mirror, introduces chromatic WFE thereby increasing the complexity of its definition and characterization. This characterization will be the subject of the following chapters.

1. DESCRIPTION OF THE COMPONENT IN THE PAYLOAD MODULE

The dichroic mirror divides the telescope's collected beam into two channels: infrared light is directed to the NISP spectro-photometer, while visible light is reflected to the VIS channel for visible imaging. As introduced earlier, this section focuses on the dichroic mirror as an optical component within *Euclid*. It provides detailed descriptions of its geometry, construction, technology, function within *Euclid*, and position within the telescope's opto-mechanical assembly.

1.1. Dimensions, composition and aspect

The dichroic mirror consists of a transparent fused silica substrate, polished by Amos [54], and coated with a stack of thin layers to give it the right reflective properties. This stack was created by Optical Balzers Jena (OBJ) [55]. The dichroic mirror is a cylinder 119 mm in diameter and 20 mm thick. Figure 23 is a picture of the Flight Spare (FS) model of the mirror, received at LMA for characterization.

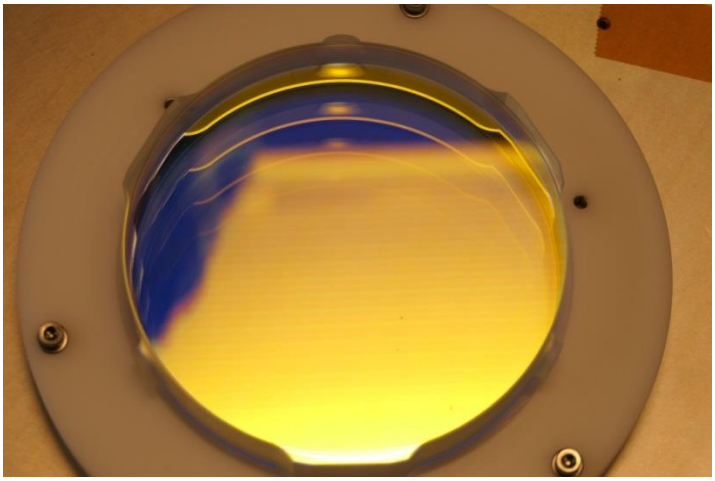

Figure 23: The Euclid dichroic mirror (Flight Spare), after reception at the LMA clean room.

The "front" face of the substrate is coated with a "dichroic" thin-film stack, consisting of 182 alternated thin layers of niobium oxide Nb_2O_5 and SiO_2. The total thickness of the stack is 9.8 µm. The "back" side of the substrate is coated with an anti-reflective stack, consisting of 205 layers of the same materials as the dichroic stack. Its total thickness is 10 µm. There is a wedge between both faces of 0.0425° to prevent stray rays from returning to VIS. The mirror reflects visible light from 550 to 900 nm. Its appearance is therefore yellow or violet, depending on the tilt.

On Figure 23 are also visible the protuberances located around the circumference of the cylinder. These are 3 cylindrical supports and 3 flat supports, each at 120°. They allow the mirror to be attached to its *Euclid* support. The cylinder and supports are machined directly in the SiO2 blank.

1.2. Integration in the opto-mechanical assembly

Position at VIS exit pupil

The dichroic mirror is attached to the rest of *Euclid*'s optical platform by means of a 3-point attachment and a triple planar support using protuberances on the barrel of the mirror. The entire optical platform under operating temperature of 150K, in the vacuum of space, and its covering limits any stray rays towards the instruments.

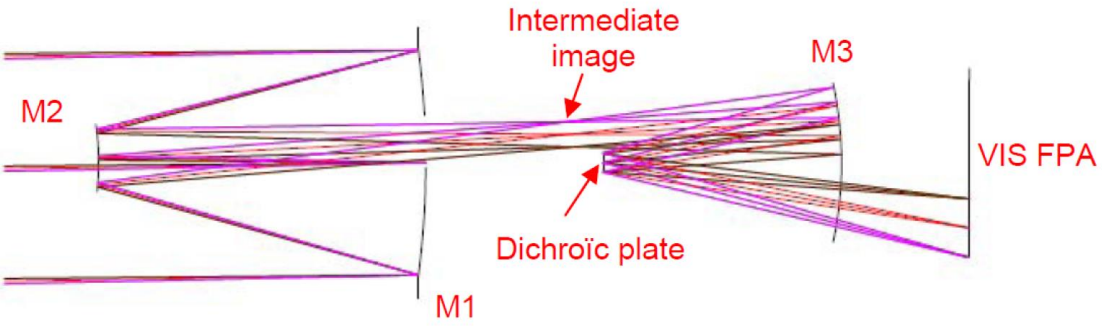

Figure 24: Unfolded view of the optical path of Euclid's VIS chain [28].

The dichroic mirror is positioned at the exit pupil plane[2] of the VIS channel between the M3 spherical mirror and the FoM3 plane mirror. This positioning is shown in Figure 24, showing an unfolded view of the VIS channel. For simplicity's issue, the folding mirrors FoM1, 2 and 3 are not shown here. Their function is to fold the beam in three dimensions, making the telescope more compact.

The most obvious example of pupil plane is the human eye pupil. Even if narrowed, the pupil does not vignette the perceived image, but rather adjusts the received brightness level uniformly. In the same way, surface defects in the dichroic mirror have uniform repercussions on the whole image, rather than being localized.

Dichroic mirror illumination

The front of the mirror is illuminated on a 103 mm diameter disk centered on the optic. Each point on this disk is reached by a non-collimated beam from the M3 mirror with an angular aperture of between 2.5° and 3.5° around the main beam (depending on the position on the mirror). The mirror is illuminated by a beam whose angle of incidence is between 4.1° and 17.1°. Figure 25 illustrates this illumination.

[2] The exit pupil is the image of the optical system's aperture, which is the entrance pupil. These two pupils form a corridor through which all rays passing through the optical system must pass. A point source, imaged by the system, produces a beam that uniformly illuminates the planes where the pupils are located. By adjusting the size of these pupils, for example with an iris, it is possible to adjust the flux collected by the system, without vignetting the image from this source point [56].

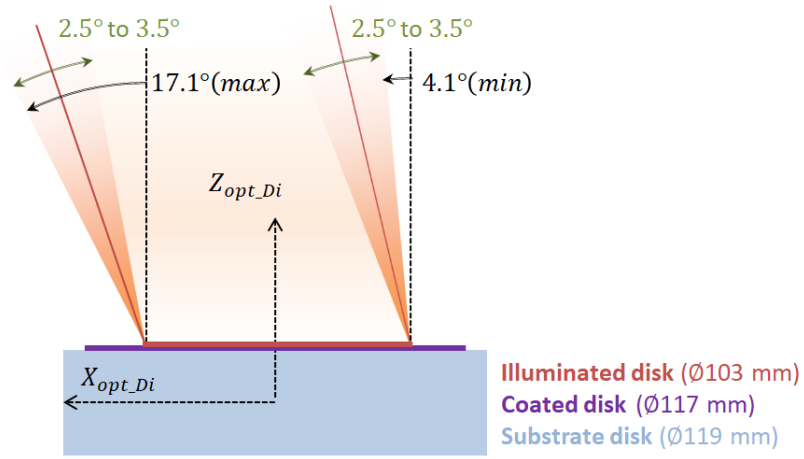

Figure 25: Illustration of dichroic mirror illumination at variable incidence. Each point on the illumination disk (horizontal line in red) is reached by a light cone (shown in orange).

The following section presents the specifications and tolerances of the dichroic mirror that led to the design proposed by OBJ. The chromaticity of the mirror's WFE was only identified afterwards, resulting in outdated constraints.

2. SPECIFICATIONS ON *EUCLID* DICHROIC MIRROR

In this section, the dichroic mirror reflectivity requirements will be presented. Subsequently, specifications for surface and WFE will be outlined. These specifications are established before the discovery of the chromatic nature of WFE. The necessity to characterize chromatic WFE is elaborated in section 4.2 of this chapter, as well as in the subsequent chapter.

2.1. Reflectance and transmittance requirements

Figure 26 shows the corridors that the reflection and transmission of the dichroic mirror and its anti-reflective coating must respect. These corridors should be valid for any angle of incidence between 4.1° and 17.1°, and for any polarization state.

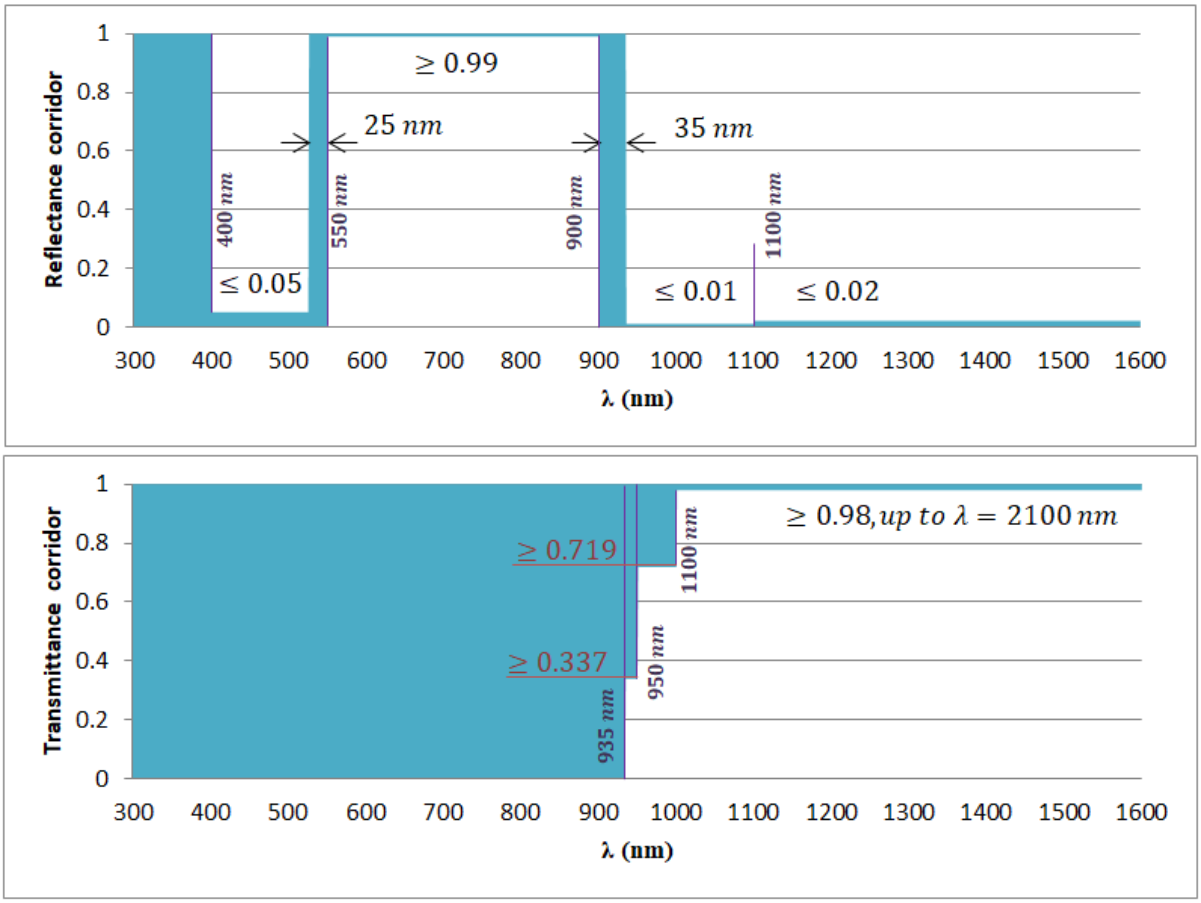

Figure 26: Tolerances on reflectance (top) and transmittance (bottom) of the Euclid dichroic mirror [55, 57].

The study presented here concerns the mirror's reflection (towards VIS instrument) only. The tolerances shown in Figure 26 apply to the mirror under space environmental conditions. Reflectance is severely constrained between 525 and 900 nm, with a minimum value specified at 99%. This plateau is delimited by two very narrow corridors: a blue edge, 25 nm wide, and a red edge, 35 nm wide. Reflectance then drops sharply from 99% minimum to 5% maximum at the blue side or 1% at the red side.

Dichroic mirror reflectance

Figure 27 presents the measured and theoretical reflectance curves on the dichroic mirror demonstrator produced by OBJ.

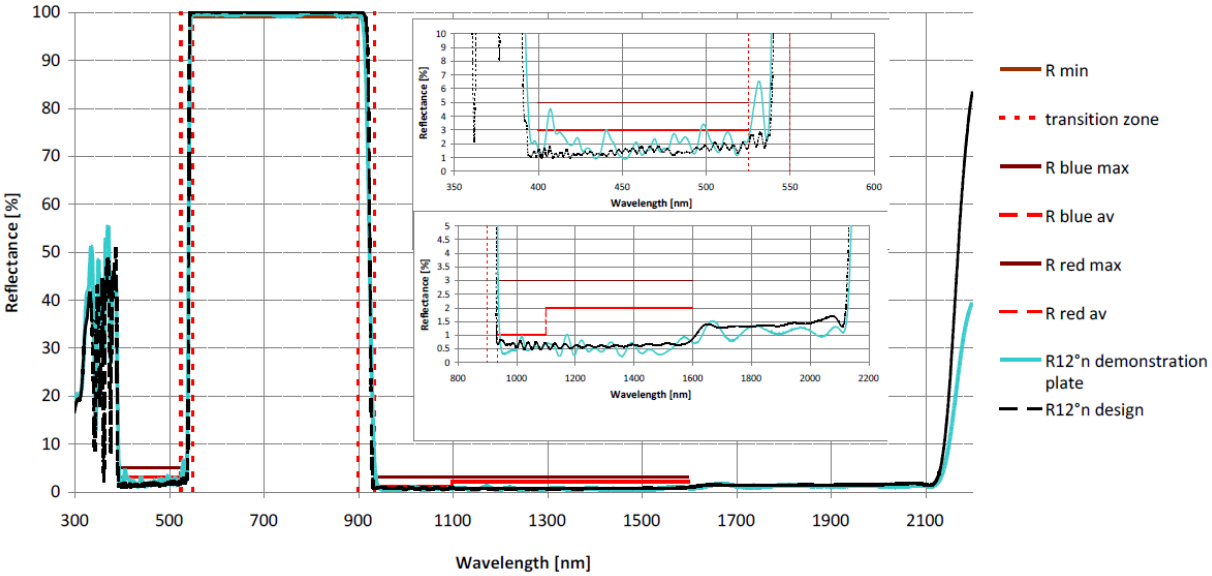

Figure 27: Measured (cyan line) and theoretical (black dotted line) reflectance curves of the dichroic mirror, at 12° incidence, in unpolarized light. Tolerances are indicated by the 6 red, dotted and solid lines. [55]

OBJ's design meets the tolerances perfectly, always staying within the corridors. We can notice strong variations of the reflectance below 400nm, which correspond to wavelengths already filtered by other upstream optics. Here, the comparison is at 12° incidence. A lower incidence results in a shift of the reflectance spectrum towards higher wavelengths [58], and blue-shifted for a higher incidence. Further OBJ measurements, focusing more specifically on the edges of the bandpass with varying incidence and polarization, show that the optical design of the dichroic mirror meets specifications in all cases.

2.2. Surface and achromatic wavefront requirements

The mirror surface specifications that were initially applied were established by considering the mirror as a purely reflective mirror. In other words, the phase shift is linearly dependent on wavelength, and the reflected WFE is twice the SFE of the component at normal incidence.

Requirement	1 atm, 298 K, 0 g.	0 atm, 150 K, 0 g
WFE without piston, tilt	$< 20\ nm\ RMS$	$< 20\ nm\ RMS$
WFE without piston, tilt, defocus	$< 10\ nm\ RMS$	$< 12\ nm\ RMS$
Measured WFE accuracy	$< 5\ nm\ RMS$	$< 7\ nm\ RMS$

Table 13: Achromatic WFE requirements for Euclid dichroic mirror (ambient and cryogenic conditions). Reference: Euclid Consortium internal documentation.

The achromatic WFE specifications for the dichroic mirror are shown in Table 13. In the first row, the piston and tilt terms have been removed. These terms are only related to the imperfect alignment of the mirror and are not relevant here. For the second line, we have also removed the defocus term, which corresponds to the residual with respect to the best sphere. Figure 28 illustrates this

representation. Defocus is related to the physical deformation of the component. This can occur as a result of thermal or mechanical stress. Removing the defocus term reveals the defects associated with polishing and deposit non-uniformity, which are the cause of phase deviations.

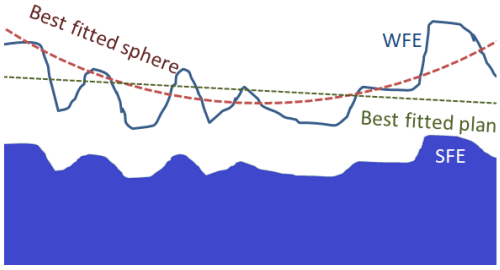

Figure 28: Illustration of WFE fitted with the best plane or best sphere.

Achromatic WFE must be measured to an accuracy of less than 5 nm RMS under ambient conditions.

3. CHROMATIC PROPERTIES OF THE DICHROIC COATING

In this section, we will show how the optical response of the dichroic mirror is intricately related to the coating used to provide high reflectivity in the visible range and high transmission in the infrared range. This coating can potentially induce chromatic effects.

The dichroic mirror is coated with a stack of thin layers. The physical principles governing the adjustment of the stack's reflective properties will be presented. Then, the concept of chromatic WFE induced by the stack's thickness figure errors will be explain to illustrate the chromatic properties of a thin-film stack. The *Euclid* dichroic case will be then reviewed.

3.1. Thin films coating principle

The whole principle of optical thin-film filters is based on interference between the multiple primary and secondary rays created at each interface between layers. As these interferences depend on wavelengths and layer properties (thickness, refractive index), the chromatic optical response is also correlated to the stack properties.

Case of a monolayer coating

Figure 29 shows a simple example of a substrate with a single-layer stack. The substrate is made up of a material with index n_s, while the layer with thickness e_1 is made up of a material with refractive index n_1. The assembly is illuminated by an electromagnetic beam of wavelength λ, with angle of incidence θ_0, and with polarization state. The thickness of the substrate is pointless, as it is considered semi-infinite here and no ray is reflected from its back side. The external medium index is $n_0 = 1$.

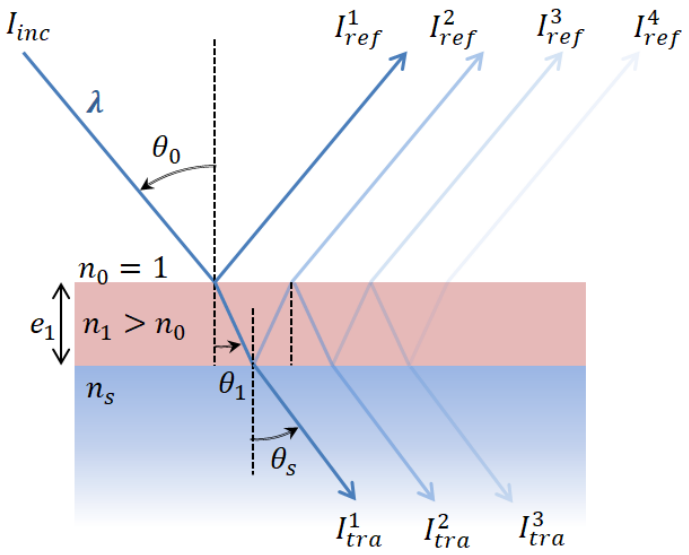

Figure 29: Illustration of rays from multiple reflections and transmissions on a monolayer stack (red) applied to a substrate (blue).

Figure 29 illustrates the first few rays reflected and transmitted in the layer. Superimposing these secondary rays gives the total reflected electromagnetic field, with amplitude E_R and phase φ_R with respect to the incident electromagnetic field:

$$E_R\, sin(\varphi_R) = \sum_{j=1}^{\infty}\left[E_{ref}^j\, sin\left(\varphi_{ref}^j\right)\right] \tag{17}$$

In Eq. 17, E_{ref}^j corresponds to the amplitude of each reflected field and φ_{ref}^j their phase with respect to the incident electromagnetic field. The value of the amplitude E_R depends on how the reflected beams will interfere with each other. The phase shift between two reflected beams I_{ref}^j and I_{ref}^{j-1} can easily be calculated by geometry, giving [56]:

$$\varphi_{ref}^j - \varphi_{ref}^{j-1} = \frac{4\pi}{\lambda} e_1 n_1 \cos(\theta_1)\ \ \forall j > 1 \tag{18}$$

With the refraction angle θ_1 in Eq. 18 expressed from the Fresnel-Descartes law:

$$n_1\, sin(\theta_1) = n_0\, sin(\theta_0)$$

Constructive interference corresponds to a phase shift equal to $k\pi$ for any even integer k, resulting in perfect superposition of the electromagnetic waves. With k odd, the two waves are in phase opposition, and therefore cancel each other out.

The amplitude E_R of the reflected beam thus depends strongly on the wavelength, the angle of incidence, the layer thickness, and its refractive index. By fixing the angle of incidence θ_0, this thus leads to a reflectance $R(\lambda)$ that is specific to the properties of the chosen layer. The phase $\varphi_R(\lambda)$ of the reflected beam can be identified from Eq. 17 and 18. This depends on the intensity and phase of each reflected beam. Consequently, $\varphi_R(\lambda)$ is also defined by the properties of the layer.

Examples of multilayer coatings

A stack of several thin layers is based on the same principle of interference between secondary rays, although this interaction is far more complex. Here, the reflected ray now depends on the characteristics of all the layers applied. Thin-film theory, presented in Chapter 6, part 1.2, allows $R(\lambda)$

and $\varphi(\lambda)$ to be calculated directly for any stack, without having to consider each ray reflected at each interface individually. By optimizing the number of layers and their thickness in this way, $R(\lambda)$ can be adjusted ever more finely, and there are various techniques [58] for identifying or defining the best optical stack formula (list of thicknesses and indices) for obtaining a specific reflectance curve. In most cases, including that of the *Euclid* dichroic mirror, the stacks are made up of only two different materials, with "high" index n_H and "low" index n_L. This simplifies, among other things, manufacturing methods, and the identification of optimal optical formulas. It also satisfies the "maximum principle" [58] which states that the optimum solution will be achieved by using the materials with the lowest and highest refractive indices available.

Two examples are shown below: the Bragg mirror [60], on the left of Figure 30, and the high-pass mirror [61], on the right.

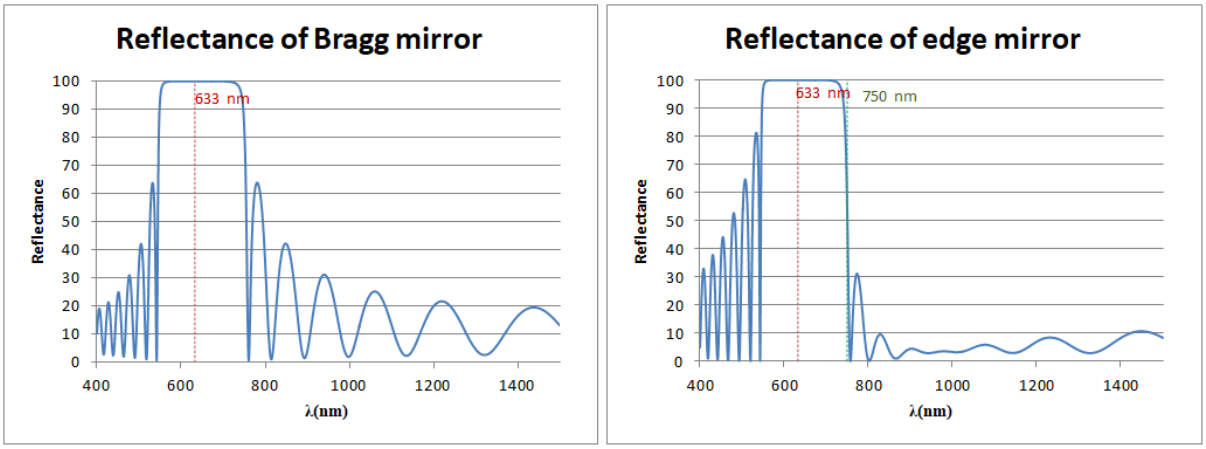

Figure 30: Reflectivity curves for Bragg (left) and high-pass (right) mirrors, obtained with Optilayer software. Both stacks are adjusted to $\lambda = 633\ nm$.

The idea of the Bragg mirror is to maximize total reflection around a specific wavelength λ_{Bragg}. This is created with a stack of N quarter-wave layers, i.e. with a physical thickness $e = \lambda_{Bragg}/4n$, with n the layer index, which is either n_L or n_H. For normal incidence ($\theta_0 = 0°$), the rays reflected outwards from the mirror all undergo constructive interference with a phase shift of π for $\lambda = \lambda_{Bragg}$. In the example shown in Figure 30, λ_{Bragg} is 633 nm, for a stack of 24 alternated L and H layers, such as $n_L = 1.46$ (SiO_2) and $n_H = 2.31$ (Nb_2O_5).

The second example is the high-pass mirror. Reflectivity is maximized up to a limit wavelength λ_{cut}, from which $R(\lambda)$ drops sharply. The stack is similar to the Bragg mirror, but two H layers of thickness $e = \lambda_{Bragg}/8n_H$ are added to the ends of the stack. The result is a mirror whose reflectance follows a plateau and then abruptly becomes minimal after a certain threshold. In the example shown here, this cut-off is around 750 nm. The materials used are the same as in the previous example, with a total of 24 layers.

Consequences of layers thickness variations

It was seen in the previous section that the reflectance $R(\lambda)$ of a mirror with a coating depends strongly on the layers thickness in the stack, but also the phase φ_R of the beam reflected by the mirror. Phase is generally not a significant criterion in comparison with $R(\lambda)$ or $T(\lambda)$ but it will be explained here how it plays a major role when a coating admits thickness errors.

Figure 31 shows the reflectance (panel A) and phase (panel C) curves of a Bragg mirror with 24 layers. This time, thickness errors of 1% and 3% have been added uniformly to all layers, giving a

new value for $R(\lambda)$ and $\varphi_R(\lambda)$. The difference between these new optical properties and the nominal properties, $\Delta R(\lambda)$ and $\Delta\varphi_R(\lambda)$, can be seen in panels B and D.

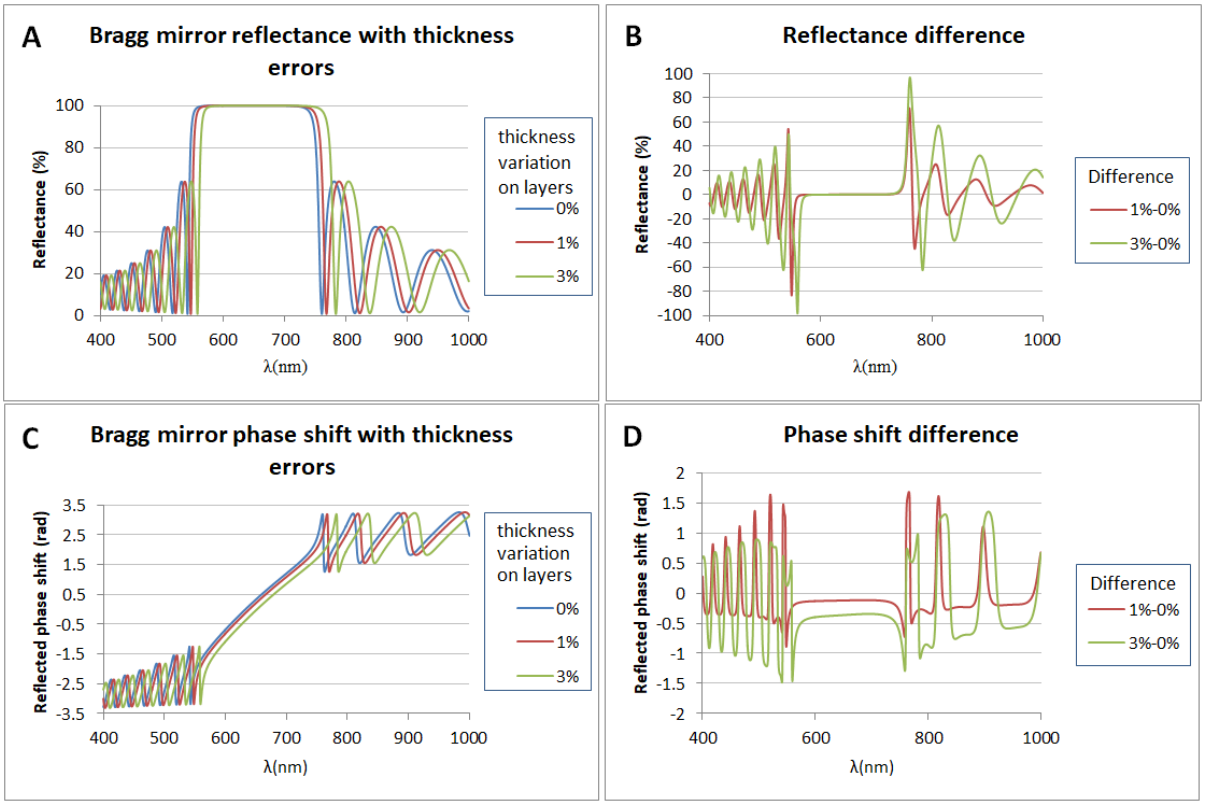

Figure 31: Reflectivity (A) and phase (C) curves of a Bragg mirror with thickness errors added to the coating. (B, D): Difference from the theoretical case without thickness error.

It thus appears that a systematic thickness error over the entire stack results in a shift in $R(\lambda)$ and $\varphi_R(\lambda)$. We then observe a shift in λ_{Bragg} proportional to the thickness variation. Such a spectral shift is not specific to the Bragg mirror [62]. The shifts $(\Delta R(\lambda), \Delta\varphi_R(\lambda))$ are therefore proportional to the slopes of $R(\lambda)$ and $\varphi_R(\lambda)$ depending on the level of thickness variation. Near λ_{Bragg}, $R(\lambda)$ has a zero slope, resulting in zero $\Delta R(\lambda)$ regardless of thickness variation. However, $\varphi_R(\lambda)$ does not admit a zero slope, in which case, $\Delta\varphi_R(\lambda)$ is not zero, even at λ_{Bragg}.

A coating with different thickness variations at each point (x, y) on its surface will therefore generate phase errors $\Delta\varphi_R(x, y, \lambda)$ locally. The coating-induced reflected WFE ($\mathrm{WFE_c}$) is defined from $\Delta\varphi_R(x, y, \lambda)$ via Eq. 19:

$$\mathrm{WFE_c}(x, y, \lambda) = \frac{\lambda}{2\pi}\Delta\varphi_R(x, y, \lambda) \tag{19}$$

From the above observation, it is easy to understand that a coating with a profile of thickness errors in all its layers results in a WFE with complex chromaticity.

3.2. The Euclid dichroic coating thickness errors evaluation

Euclid's dichroic coating is made up of 182 thin-layers producing the reflectance $R(\lambda)$ presented in part 2.1 but also a phase shift in reflection $\varphi_R(\lambda)$ with respect to the incident ray. The Bragg mirror example showed that the phase shift is very sensitive to the thickness of the layers in the stack. The

same conclusion can be drawn for the *Euclid*'s dichroic coating. Here in Figure 32 is a simulation of $\varphi_R(\lambda)$ of the dichroic mirror, with several cases of layer thickness errors.

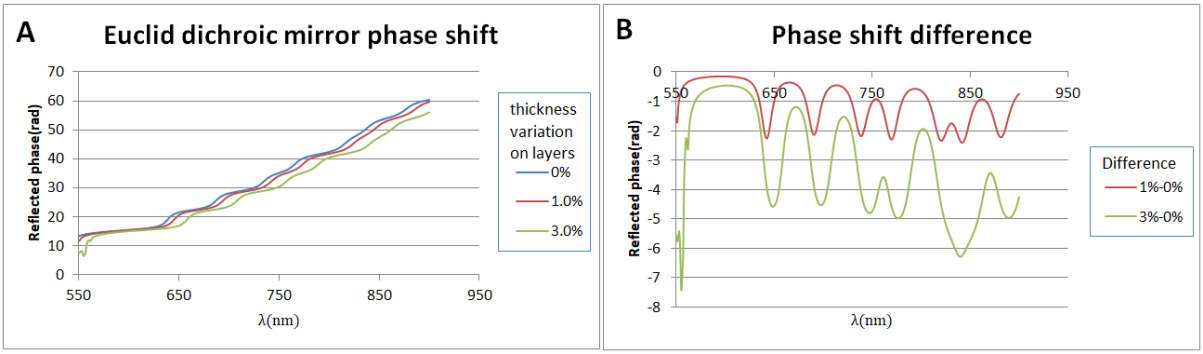

Figure 32: (A) Simulation of reflection phase on the dichroic mirror with the addition of thickness errors in the coating. (B): Difference from the theoretical case without thickness error.

As already shown with the Bragg mirror, the phase deviation obtained (right) for different cases of systematic thickness error is correlated to the local Group Delay [62]. However, this slope is highly irregular, leading once again to phase deviations that are highly wavelength-dependent.

OBJ carried out reflectance measurements on the dichroic mirror Demonstration Model[3] (DM) near the red edge of the bandpass. For each point (x, y) onto the mirror, OBJ sought the wavelength $\lambda_{R50\%}^{mes}(x, y)$ for which the measured reflectance is 50%. Figure 33 shows the deviation expressed with $\left(\lambda_{R50\%}^{mes}(x, y) - \lambda_{R50\%}^{theo}\right) / \lambda_{R50\%}^{theo}$.

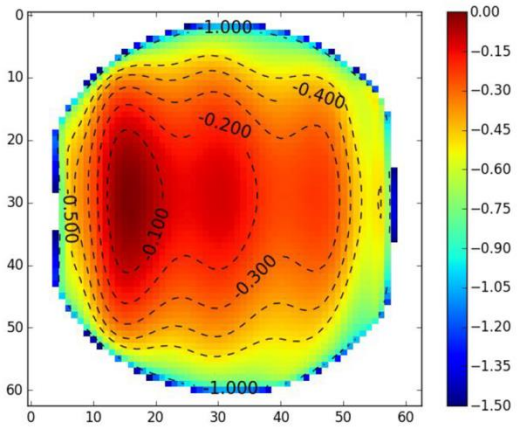

Figure 33: Spectral reflectance shift homogeneity in percentage of λ for R=50%, measured on DM. [59].

Subject to certain conditions (see 4.1 and Chapter 6, part 3.4) we can assume that this reflectance deviation at each point is equivalent to a homogeneous deviation of the stack thickness from the theoretical one. Figure 33 is therefore an equivalent of a SFE map of the mirror coating. If the DM mirror was achromatic, the WFE induced by this SFE would be within the tolerances expressed in Table 13.

[3] The reflected phase function of the "**demonstration"** mirror is not the same as that shown in Figure 32, but also features phase variations leading to chromatic WFE.

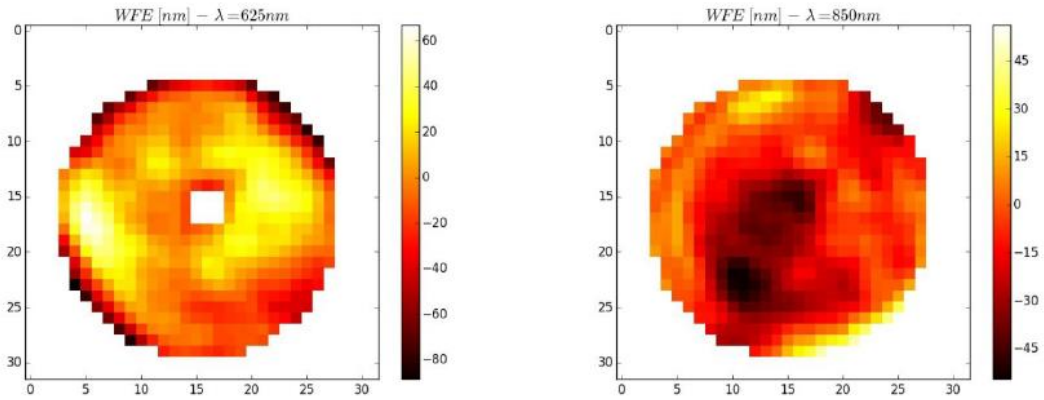

Figure 34: Measurement of the WFE (nm) of Euclid's dichroic mirror (DM) at 625 and 850 nm wavelengths [59].

Figure 34 shows the WFE measured on the dichroic mirror by Sodern (ArianeGroup company subsidiary) at two wavelengths. These measurements were carried out under the initiative of L.Venancio (ESA) in 2016 [59], who suspected for the first time a chromatic contribution from the dichroic mirror to the WFE of the *Euclid* telescope. The WFE at λ = 625 nm has a RMS value of 26.19 nm which is therefore out of tolerance (20 nm RMS). Conversely, for λ = 850 nm, the map RMS value is 18.03, then within tolerance. These measurements thus mark the starting point for the whole issue addressed in this thesis.

If the WFEs were achromatic or linearly chromatic, the two maps in Figure 34 would be identical with a different scale. Here, there seems to be no clear correlation. These measurements provide the first proof that the WFE induced by the dichroic mirror is chromatic, and requires special attention and fine characterization.

As a result, a new coating design was optimized by OBJ, in order to have the lowest possible GD and WFE. OBJ has also improved significantly the thickness uniformity. The **Flight Model (FM)** and **Spare Model (FS)** were then produced according to this new process. Figure 35 shows the non-uniformity map of the FS coating, which will be characterized at the LMA.

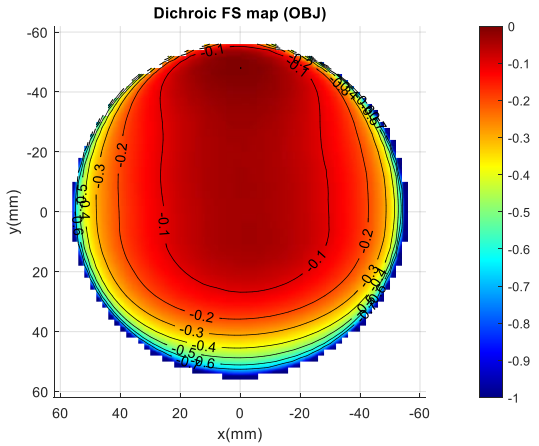

*Figure 35: Spectral reflectance shift homogeneity in percentage of λ for R=50%, measured on dichroic mirror **Flight Spare**.*

The previous WFE measurements have been done at few wavelengths only and with a limited accuracy but have justified a full characterization campaign which is the subject of this thesis.

4. NEED OF CHROMATIC WFE CHARACTERIZATION

When the chromatic nature of reflected WFE on the dichroic mirror was identified, the WFE specifications that were initially imposed became obsolete. They were based on the assumption that dichroic treatment behaved in the same way as metallic treatment. From now on, the WFE cannot be considered as twice the SFE anymore but its chromatic dependency must be known over the entire visible spectrum, with a precision that we will be justified in this section.

4.1. Consequence on PSF metrics

To update the requirements and define the level of precision needed to characterize the WFE chromaticity, a full set of simulations (J. Amiaux and P.A. Frugier (CEA) [63]) has been set. The authors began by comparing by simulation the consequences of a chromatic and achromatic WFE on the PSF parameters (e_1, e_2, R^2). Figure 36 shows *Euclid*'s PSF parameters in the case of an achromatic WFE induced by the dichroic mirror, i.e. linked only to its SFE.

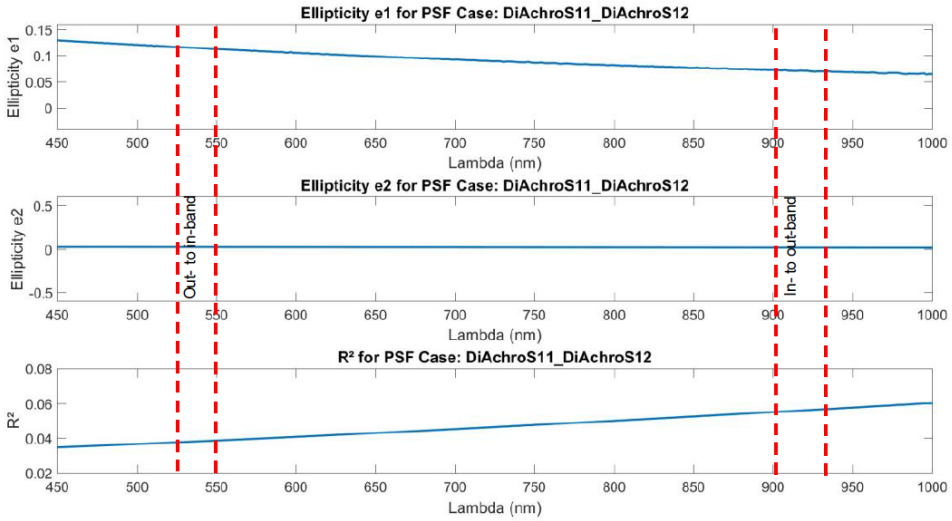

Figure 36: Simulation to overall Euclid PSF metrics (e_1, e_2, R^2) where the dichroic mirror is achromatic.

The same simulation has been carried out in Figure 37, this time with a chromatic WFE. On each of the three plots, the red and blue curves show the PSF parameters calculated for different fields of view "F2" and "F9". The exact location of these fields is irrelevant, as these graphs are intended here to illustrate the chromatic behavior of the PSF.

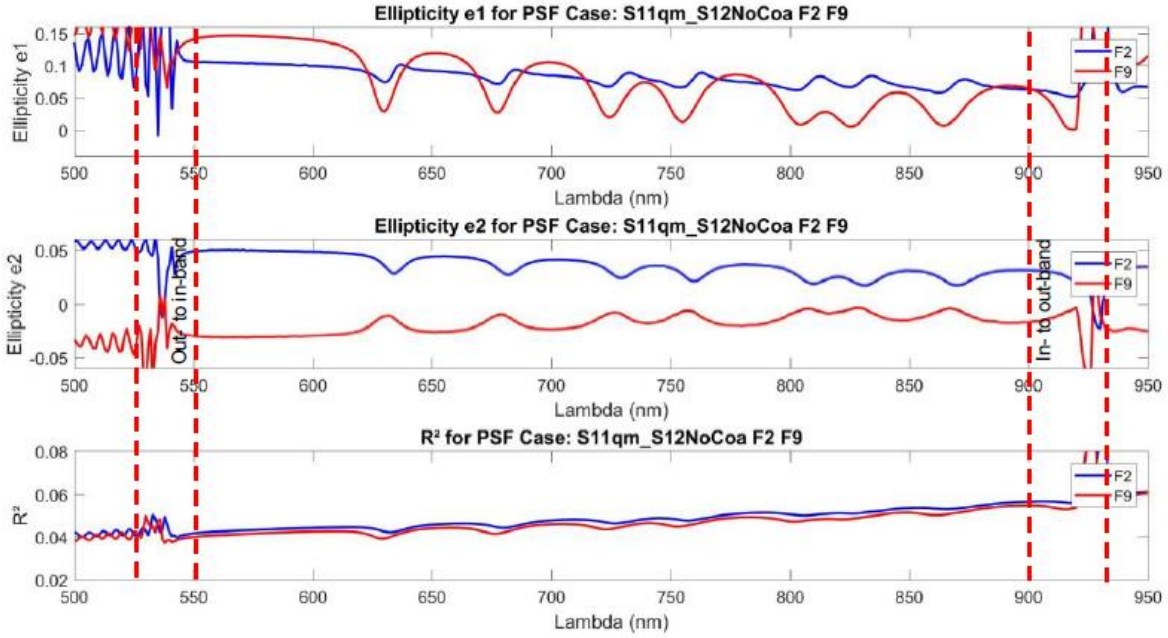

Figure 37: Simulation to overall Euclid PSF metrics (e_1, e_2, R^2) *where the dichroic mirror is supposed chromatic.*

To rebuild this simulated WFE, the authors used the reflection phase of the dichroic mirror as presented in Figure 32, as well as thickness non-uniformity maps presented in section 3.2. Assuming homothetic thickness errors[4], it is possible to establish a relationship between WFE(x, y, λ), SFE(x, y) and the reflection phase $\varphi_R(\lambda)$. Even in this simplified case (see Chapter 6, part 3.4) the consequences for the PSF are immediate.

Unlike the case shown in Figure 36, the PSF parameters are no longer chromatically monotonic, and are now field-dependent. We can also recognize the chromatic pattern of the phase reflected by the dichroic mirror observed in Figure 32. This has justified a change in the requirement.

4.2. Chromatic WFE characterization requirement

The second part of the work was then to quantify the precision required to characterize the actual WFE of the dichroic mirror.
The authors have considered a scenario in which *Euclid*'s polychromatic PSF reconstructed by the data pipeline corresponds to that shown in Figure 37. The data required related to the dichroic mirror are therefore the surface error map and the theoretical phase-shift function. In this work, the authors have considered a homothetic distribution of thickness errors in the mirror coating. The polychromatic PSF is thus predicted, as presented in Chapter 2, from the SEDs of stars and the telescope's theoretical Photon Conversion Efficiency (PCE).

[4] A homothetic distribution is the simplest case for describing the distribution of layers thickness non-uniformities within a stack. It is assumed that all layers have the same non-uniformity profile, and this same profile is thus reflected in the stack's surface error map (SFE).

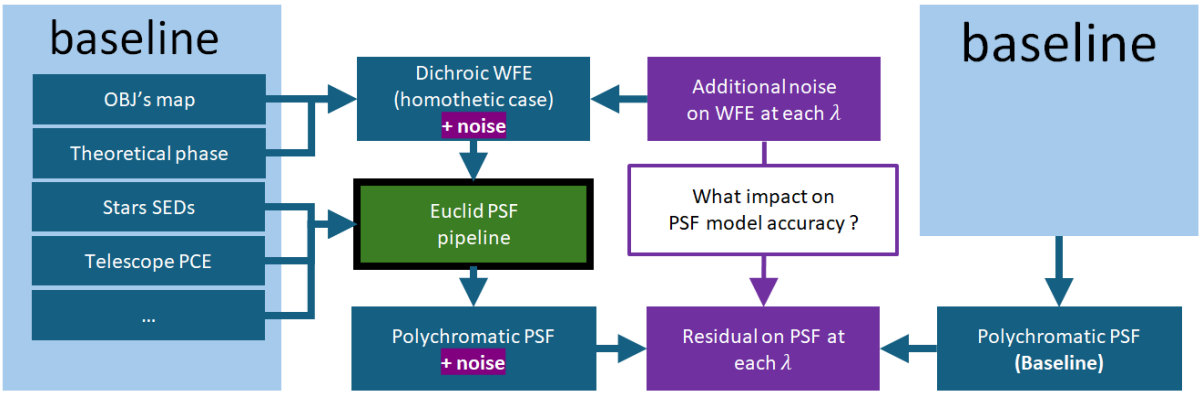

Figure 38: Schema of the Monte-Carlo simulation carried out in [63] to evaluate the PSF metrics (chromatic) residuals as a function of a deviation of the WFE (purple) from the baseline (light blue blocks).

A Monte-Carlo simulation was therefore carried out, adding a random bias to the "real" WFE. This bias on the knowledge of WFE(x, y, λ), applied to each wavelength, is quantified by its spatial standard deviation, in nm RMS. Figure 38 is a schema of the process used to carry out the Monte-Carlo simulation. The authors have thus sought the maximum noise where the polychromatic PSF parameters are identified with sufficient accuracy. Figure 39 shows the results of this Monte Carlo simulation for WFE noise with a standard deviation of 2 nm RMS.

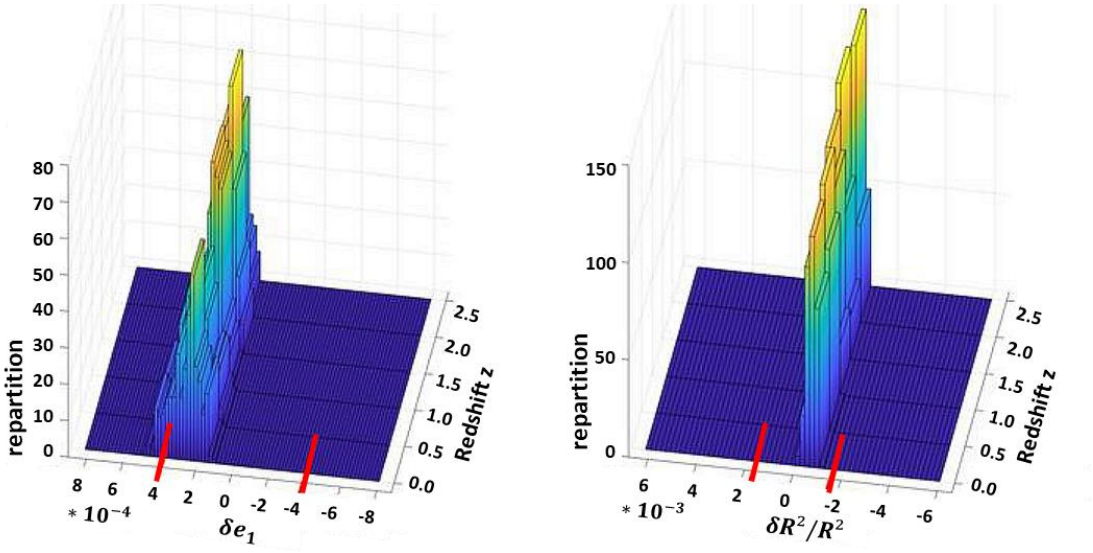

*Figure 39: Monte-Carlo simulation of PSF metrics error (right: e_1 and left: $R^2/R^2{}_{ref}$) where the **WFE perturbation is 2 nm RMS** at each wavelength.*

The simulation involves 100 runs reconstructing the PSF on the basis of the galaxies $SED(\lambda)$ at different redshifts, used to generate a polychromatic PSF. The error on the reconstruction of this PSF is therefore materialized by the deviation $\delta e_1, \delta e_2$ and δR^2. The standard deviation of this reconstruction error, proportional to the noise added to the WFE, must respect the PSF stability constraints presented in Chapter 2, part 1.3, namely $\sigma^2(e_{1,2PSF}) \leq 2 * 10^{-4}$ and $\sigma^2(R^2{}_{PSF})/R^2{}_{PSF} < 10^{-3}$. It would thus appear that the maximum permissible noise on the WFE is 2 nm RMS. Higher noise would induce too much residual bias for the reconstructed PSF parameters.

The conclusion of this simulation is therefore that the WFE of the dichroic mirror must be identified with accuracy better than 2 nm RMS for every wavelength between 550 and 900 nm, for every angle of incidence between 4.1° and 17.1°, and for every polarization state of the light.

5. CONCLUSION

In conclusion, in this chapter, we review and highlighted the properties of the Euclid dichroic mirror, coated with a stack of thin layers by OBJ, endowing it with a unique optical function. We review how the chromaticity of the WFE exhibited by this mirror will significantly influence the telescope's PSF.

It was then shown that the WFE should be accurately known with a precision of 2 nm RMS across all conditions of component illumination, including Angle of Incidence (AoI), wavelength, and polarization. This understanding is crucial for ensuring the dichroic mirror's optimal performance within the broader telescope system.

It was then decided to fund a full campaign to characterize the WFE of the dichroic mirror. ESA has then funded the development of a dedicated metrology bench. This innovative bench, designed and built by Imagine Optic, is suitable for multi-spectral, multi-incidence and multi-polarization coverage. This metrology work is presented in the following chapter.

6. REFERENCES

54 *Euclid Consortium* Internal document (EUCL-OBJ-TR-3-240)

55 M. Lappschies, T. Weber, L. Venancio, S. Jakobs, "Advanced dielectric coatings for the *Euclid* mission telescope manufactured by the PARMS process", Optical Interference Coatings (2016)

56 E. Hecht (1987). "Optics" (4th Ed.). 2003 Addison Wesley. ISBN 0-321-18878-0

57 T. Weber, M. Lappschies, S. Jakobs, "Manufacturing of high performance VIS-NIR beam splitters by plasma assisted thin film deposition technologies", Proc. SPIE 10691, Advances in Optical Thin Films VI, 106911A (2018); doi: 10.1117/12.2313459

58 Sh. A. Furnam, A.V. Tickhonravov, "Basics of optics of multilayer systems", 1st ed. (Editions Frontières, 1992), Chap. 1

59 L. Venancio, L. Carminati, J. L. Alvarez, J. Amiaux, L. Bonino, J.-C. Salvignol, R. Vavrek, R. Laureijs, A. Short, T. Boenke, P. Strada, "Coating induced phase shift and impact on *Euclid* imaging performance", (2016), Proc. of SPIE Vol. 9904

60 F. Réveret. « Etude du couplage fort par spectroscopie optique dans des microcavités GaN élaborées sur silicium ». Matière Condensée [cond-mat]. Université Blaise Pascal - Clermont-Ferrand II, 2008. Français. tel-00412515f

61 B. Haj Ibrahim. "The deposition of multilayer and gradient index thin films by Matrix Distributed Electron Cyclotron Resonance Plasma Enhanced Chemical Vapor Deposition" MDECR-PECVD. Physics [physics]. Ecole Polytechnique X, 2007. English. Pastel-00002930

62 G. Carlow, J-M. Guay, A. Christou, C. Montcalm, A. Badeen, and B. T. Sullivan, "Optical filter wavefront distortion: out-of-band to in-band predictions and the effect of the illumination source bandwidth", Appl. Opt. 62, B133-B140 (2023)

63 *Euclid Consortium* Internal document (EUCL-SAP-TN-1-005)

Chapter 4

OBSERVE metrology bench

In the preceding chapters, we explored the critical role of the *Euclid* dichroic mirror in the Weak Lensing probe, emphasizing the chromatic effects it introduces to PSF. Consequently, it becomes imperative to meticulously characterize this mirror. This chapter is starting the experimental part of the thesis, focusing on the optical metrology bench and the characterization plan for *Euclid*'s dichroic mirror.

We detail the bench specifications mandated by the European Space Agency (ESA), crucial for accurate measurements of WFE, PSF, and light intensity after reflection on the dichroic mirror under diverse illumination configurations.
Subsequently, we introduce the "OBSERVE" bench, a technical solution designed and developed by the French company Imagine Optic to meet the expectations of both ESA and the *Euclid Consortium*. We will then describe the procedure for acquiring measurements with OBSERVE.

1. TEST BENCH AND METROLOGY SPECIFICATIONS

This first part is dedicated to the specifications of the metrology bench needed to characterize *Euclid*'s dichroic mirror. Most of the information presented here has been listed in the technical document "Dichroic FS test bench technical specifications" [64], written by ESA-ESTEC in April 2020. These specifications are directly related to the conclusions of the previous chapters, which quantified the need to characterize the optical (chromatic) properties of the mirror enable PSF models to be calibrated.

The top level requirements for the bench specifications are that the WFE, PSF, and reflected intensity of the dichroic mirror must be identified with accuracy better than 2 nm RMS for every wavelength between 550 and 900 nm, for every angle of incidence between 4.1° and 17.1°, and for every polarization state of the light.

Firstly, we will discuss the diagnostic requirements which are to cover three measurement channels such as WFE, PSF, and intensity. Secondly, we outline the requirements related to the illumination conditions of the incident light source, encompassing aspects like spectral range, spectral resolution, angle of incidence, polarization etc. Lastly, we detail the environmental requirements, requiring the bench installation in the clean room at IP2I LMA in Villeurbanne.

1.1. The WFE, PSF, and Intensity channels.

The metrology bench shall measure:

- The WFE after reflection of a collimated beam on the dichroic mirror.
- The uniformity of light intensity induced by the dichroic mirror on this same beam.
- The PSF induced by the dichroic mirror, which can be detected directly by focusing the reflected beam on a camera placed at the focal plane.

However, it is not necessary to conduct all measurements on the same mirror diameter. Certain measurements must encompass the entire coating diameter, whereas others, like the PSF, only cover a smaller diameter. Figure 1 illustrates the three designated areas in the specifications. Please note that the areas are not to scale for better readability. Table 1 provides the diameters and positioning tolerances for these three areas.

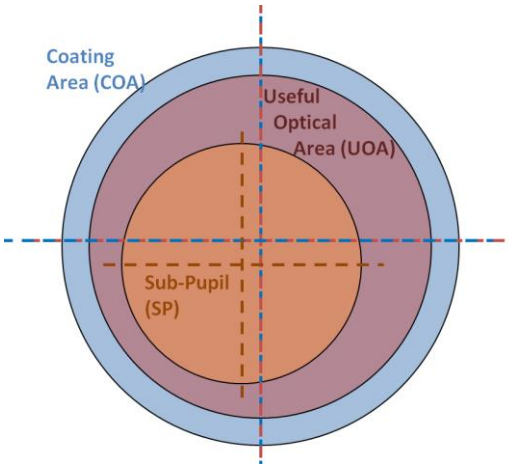

Figure 40: Illustration and name of each considered area on Euclid Dichroic Mirror specifications document.

Area name	Diameter (mm) and tolerance	Centering accuracy (mm)
COA	$116.75^{+0.00}_{-0.25}$	$\pm$ 0.25
UOA	$108.00^{+0.10}_{-0.10}$	$\pm$ 0.10
SP	$103.00^{+0.10}_{-0.10}$	$\pm$ 0.10

Table 14: Name, diameter, and centering accuracy of each considered area on Euclid Dichroic Mirror specifications document.

The **COA** corresponds to the area of the mirror covered by the coating. The **UOA**, centered on the COA, corresponds to the illuminated area in *Euclid*, as shown in the Figure 25 in Chapter 3. The SP is a specific area used for PSF measurements. The **SP** has several possible positions and is not necessarily centered on the COA. It is only defined as being contained within the UOA, with a centering accuracy of $\pm$0.25 mm.

WFE channel

The primary function of the bench is to measure the WFE reflected by the dichroic mirror. We will not go inside an exhaustive technical specifications found in the document, but we will focus on highlighting the key specifications that significantly influenced the technical solution put forth by Imagine Optic. Refer to Table 2 for a listing of these specifications.

Spec. ID	Description
WFE-040	The bench shall record the WFE over the **COA** without any vignetting.
WFE-050	The WFE (**UOA**) measured **at λ_{ref}** is under **1 nm RMS** accuracy without tilt and focus.
WFE-060	The WFE (**UOA**) measured **between λ and λ_{ref}** is under **1.5 nm RMS** accuracy, with tilt, focus.
WFE-080	The WFE channel shall detect a WFE (UOA) with a PTV value between **300 nm (typical) and 900 nm (maximum)**, and a maximum slope of **75 nm by mm**.
WFE-090	The spatial resolution on WFE channel allows **55 Noll Zernike** decomposition of WFE over any **SP** within the UOA.
WFE-100	The WFE (**UOA**) maps orientation along dichroic mirror perpendicular axis is known with under **0.25° accuracy.**

Table 15: WFE channel main requirements for Euclid DC test bench.

All specifications on the WFE channel (as well as the other channels) are valid for all bench illumination configurations, i.e. for any incidence, wavelength and polarization.

The bench shall therefore be designed to measure the WFE over the entire COA (WFE-040), without vignetting. Vignetting is an edge effect that occurs when the entrance and exit pupils of the optical system are not properly conjugated. Specifications WFE-050 and WFE-060 concern the accuracy of the WFE measurement over the "UOA" area. The strategy proposed by ESA is to determine with 1 nm RMS accuracy excluding tilts and focus[5] (WFE-050), the reflected WFE at a wavelength λ_{ref}, which will be chosen as a reference wavelength. The second step is to measure the deviation between the WFE at λ_{ref} and the WFE at any wavelength λ (WFE-060), with 1.5 nm RMS accuracy. The

[5] Bench settings intrinsically induce a tilt and defocus parameter on the measurement, and it is irrelevant to retain them in the processing. On the other hand, tilt and defocus deviations between λ and λ_{ref} are important as they are a manifestation of the chromatic WFE of the dichroic mirror. This is why WFE-050 excludes tilt and focus, but WFE-060 does not.

quadratic sum of these two measurements gives an estimate of WFE at λ with an accuracy better than 2 nm RMS. For a better understanding of the measurement strategy, see section 2.3 of this chapter.

Specification WFE-080 stipulates that the WFE detector shall be calibrated to measure a WFE with a typical PTV value of 300 nm, and a maximum of 900 nm. This specification is based on the expected WFE behavior of the dichroic mirror. The Zernike modes referenced in WFE-090 are a set of polynomials used for surface decomposition on a unit disk, detailed in Chapter 5, part 1.1. Knowing the first 55 Zernike modes serves as a criterion for spatially sampling the WFE maps. The final specification, WFE-100, concerns the orientation of the maps, which can be determined from marks etched onto the surface of the dichroic mirror. Precise knowledge of the orientation of WFE maps within 0.25° is crucial for effectively processing WFE data, particularly when combining multiple maps.

Intensity channel

The second main function of the test bench is to measure light intensity after reflection from the dichroic mirror. To do this, the bench shall measure the level of light intensity before and after reflection on the mirror. By dividing both maps, the contribution of the bench and the spatial intensity inhomogeneity of the source are removed, giving the spatial inhomogeneity of the light intensity during reflection on the dichroic mirror.

Spec. ID	Description
INC-060	The beam intensity profile **incident** on the component shall be known with an accuracy of **0.1%** with a spatial resolution of **1024*1024 pixels** over the UOA and this for WFE and PSF channels.
INC-070	The beam intensity profile **reflected** by the component shall be known with an accuracy of **0.1%** with a spatial resolution of **1024*1024 pixels** over the UOA and this for WFE and PSF channels.
INC-080	The spatial uniformity of the beam is greater than **90%** over the UOA.

Table 16: Intensity channel main requirements for Euclid DC test bench.

The main specifications for measuring the intensity of the incident and reflected beams on the dichroic mirror are listed in Table 16, and remain valid for any illumination condition. Intensity must be measured with 0.1% in accuracy over the entire UOA, with a sampling of 1024x1024 pixels. This resolution is sufficient to estimate the PSF contribution of heterogeneity in the dichroic mirror aperture function. Specification INC-080 stipulates a highly uniform incident beam with only 10% uniformity error, thus guaranteeing sufficient SNR over the entire surface.

PSF channel

The test bench should finally incorporate a PSF channel featuring various defocus values. This inclusion serves a dual purpose: firstly, it offers additional insights into the characteristics of both the dichroic mirror and the bench itself, and secondly, it provides a way to measure both the PSF and the WFE of the same component using the same instrument and configuration to conduct PSF calibrations using phase diversity algorithms (PD), as discussed in the PSF chapter.

The detection system effects degrade the PSF, making it difficult to fit the WFE when λ exceeds 850 nm. The method to calibrate PSF and WFE is based on Phase Diversity calibration and consists in measuring the PSF with a small defocus applied, around $\lambda/3$. Varying the defocus spread the PSF spot over a larger number of pixels, enabling more information on the PSF and thus facilitating the WFE

fitting process. A tool (developed by CNES) for WFE fitting from defocused PSFs will therefore be cross-validated in all the optical configurations that the bench can offer and will allow a better verification process.

This PSF channel is not a bench prior. The decision to incorporate a PSF channel was more an opportunity to have an accurate WFE measurement bench. The integration of the PSF channel was strategically approached to ensure minimal disruption to the bench design and measurement campaigns. The priorities for ESA and the *Euclid Consortium* are therefore WFE and intensity measurements. Table 17 summarizes some of the main specifications of the PSF channel.

Spec. ID	Description
PSF-020	The PSF shall be measured over the UOA.
PSF-030	The PSF shall be measured over the SP centered on the UOA.
PSF-040	The PSF imagery SNR shall be over 500.
PSF-110	The diameter of the beam in the PSF channel shall be adjustable between 80 and 117 mm.

Table 17: PSF-PD channel main requirements for Euclid DC test bench.

Most of these specifications concern the diameter of the collimated beam entering the PSF channel, which shall be adjustable between 80 and 117 mm in diameter. This beam must then be focused on a point on the camera (CCD or CMOS). The camera shall have an SNR of at least 500, and shall be movable along the optical axis to create a controlled defocus on the PSF. All PSF specifications remain valid regardless of illumination conditions.

1.2. Needs in terms of illumination configurations.

The metrology bench should cover a very wide range of illumination configurations. In this part, we list most of the requirements expressed in terms of wavelength selection, accessible angle of incidence and polarization. These needs alone justify the design of this new bench, as no existing metrological tool at that time was capable of achieving such a wide range of possibilities while guaranteeing accuracy on the WFE measured better than 2 nm RMS.

Spectral requirements

The bench's main spectral specifications are listed in Table 18. SPE-010 and SPE-030, define the spectral range accessible by the bench. This ranges from 510 to 950 nm with a sampling of 1 nm, corresponding to a spectral interval slightly wider than the reflection band of the dichroic mirror. SPE-040 and SPE-050 define accuracy (0.1 nm) and resolution (0.4 nm FWHM) of the selected wavelength obtained from a polychromatic tunable source.

Spec. ID	Description
SPE-010	The bench shall measure the WFE or PSF for a spectral range comprised between **510 and 950 nm**.
SPE-030	The bench can measure the WFE or PSF for each nm between **510 and 950 nm**.
SPE-040	The selected λ resolution shall be below **0.4 nm FWHM.**
SPE-050	Each central λ is known with accuracy better than **0.1 nm.**

Table 18: Main spectral requirements for Euclid DC test bench.

Angle of incidence requirements

The bench shall also offer possibilities for adjusting the angle of incidence (AOI), and for which specifications are given in Table 19. The specified AOI, between 4° and 20°, and identified with 0.005° in accuracy, correspond to the dichroic mirror illumination conditions in *Euclid* PLM. INC-030 adds, however, the possibility of measuring the bench at normal incidence, allowing a WFE measurement in a case that is "simpler" to analyze: at normal incidence, and assuming that the mirror has no optical activity, the polarization of the incident beam has no impact on the properties (WFE, Intensity) of the reflected beam. Moreover, geometric phenomena such as beam elliptisation on the component no longer need to be considered.

Spec. ID	Description
INC-010	The bench shall measure the WFE or PSF for any AOI between **4 and 20°**
INC-030	The bench shall measure the WFE at **normal AOI.**
INC-050	Each selected chief ray AOI shall be known with an accuracy better than $\pm$ **0.005°**

Table 19: Main requirements on Angle of Incidence for Euclid DC test bench.

Polarization requirements

The last illumination parameter specified for the bench is the polarization of the light, which shall be controlled. The bench must have two linear polarizers positioned before and after the dichroic mirror, to control the polarization of the beam before and after reflection. Specification POL-070 (not listed here) stipulates that the polarization axis of these polarizers must be known to within 0.5°. Other specifications include knowledge of the polarization induced by the bench itself, and knowledge of the S and P polarization directions on the dichroic mirror reference frame.

It is important to understand that the complexity of the bench lies in the inter-compatibility of all requirements in terms of wavelengths, AOIs and polarizations. Each measurement is made at a chosen wavelength, for a given AOI and two polarization angles "before" and "after" the dichroic mirror. As mentioned above, these "illumination configurations" are also compatible with the needs of the WFE, Intensity and PSF channels.

There are many other optical specifications which have not been mentioned here, but which nevertheless have a strong impact on the design of the bench. These include the stray light that appear in each channel, and which shall remain below a certain intensity level on the detectors. There are also

functional requirements involving automatic control of all illumination parameters and measurement channels.

1.3. Needs in terms of environment and hardware.

This last section is about the hardware used and the environment in which the bench and *Euclid*'s dichroic mirror are installed.

Spec. ID	Description
ENV-010	The bench operating temperature range is **21±0.1 °C.**
ENV-020	The bench is operated within a vertical laminar air flux of **0.2 m/s.**
ENV-030	The whole bench (material and process) is compatible with an installation in an ISO-3 class clean room.
ENV-040	The bench will be placed on an optical table with vibration isolation supports.
HAR-030	The maximal dimensions of the optical bench are **2.4 m x 1.5 m.**
HAR-040	The maximum height of the optical bench is **1 m.**
HAR-050	The maximum mass of the optical bench is **1000 kg.**
HAR-060	The bench shall be compatible with an optical table "TMC anti-vibration Clean Top series 780"
HOL-020	The holder shall safety maintain the dichroic mirror in a static position for any test configuration.
HOL-030	The holder shall safety maintain the dichroic mirror in a static position for any configuration changes.
HOL-050	The repositioning repeatability of the dichroic mirror in the holder shall be better than **0.2°** around the mirror perpendicular axis and **±0.1 mm** in decentering.

Table 20: Main requirements on environment and hardware for Euclid dichroic mirror test bench.

Environmental and hardware specifications are listed in Table 20. The required environment corresponds to that found in the ISO-3 [65] clean room at the LMA in Villeurbanne (France), where temperature, laminar air flow and, above all, the quantity of particles in the air are controlled. Such an environment guarantees the bench's thermal and mechanical stability, as well as extreme cleanliness: very little dust in the air and no contamination of mirrors, which would affect the measurements. This environment choice creates constraints on the materials used to build the bench, as well as the electronic equipment (control computers, cables, screens, etc.), which must be compatible with the cleanroom. Finally, the bench is installed on an optical table, mentioned in HAR-060, which limits its size (2.4*1.5*1.0 m) and weight (1000 kg). This table isolates high-frequency vibrations in the vertical direction.

The final aspect we will focus on is the dichroic mirror holder that must support, protect and stabilize the mirror both **on** the bench (HOL-020) and **off** the bench (HOL-030). It also ensures excellent repeatability in positioning the dichroic mirror on the bench. The dichroic mirror shall also be removable and reinstalled in the holder with the repeatability specified with HOL-050: 0.2° in orientation, and 0.1 mm in lateral offset. The holder is one of the most sensitive parts of the bench, being the only one in physical contact with the dichroic mirror. It must not damage the dichroic mirror by impact or scratching, or exert excessive mechanical stress, as this could lead to residual achromatic WFE.

The specifications considered as the most important for the metrological bench have been reviewed in this section. The descriptions of most of these specifications have been summarized with respect to the official ESA technical document, in order to give a better overview of the performance to be achieved. As already mentioned, many other specifications have been imposed on other technical aspects, such as software which is a fully integrated package. In the following section, we will present the bench as it was proposed by Imagine Optic.

2. "OBSERVE" METROLOGY BENCH

The "**O**ptical **B**ench for **S**p**e**ctrally **R**esolved Wa**v**efront of ***Euclid*** Dichroic" (**OBSERVE**) bench has been entirely designed and manufactured by the French company Imagine Optic (IO) [66] based in Orsay, near Paris. Founded in 1996, IO specialized in the design of optical metrology and adaptive optics systems.

The OBSERVE project, carried out by IO for ESA, began in July 2021. The bench design phase lasted until February 2022, when ESA validated the concept proposed by IO, marking the start of the OBSERVE manufacturing phase. The bench was assembled by the IO team directly in the LMA's clean room, in parallel with the procurement of some elements, software development and a series of tests. The integration and final validation of OBSERVE were validated by ESA the following year, in July 2023, after numerous interactions between ESA, IO, the *Euclid Consortium* (CEA and CNES), and the LMA.

In this section, we will begin by a presentation of the OBSERVE test bench and its general operating principle. Next, we will look in detail the main sub-assemblies, such as the diagnostic block comprising the three measurement channels, or the source block comprising the tunable source and the reference source.

2.1. General principle of OBSERVE bench.

Before the detailed presentation of the bench installed in the LMA clean room, we will first explain its operating principle. Figure 41 shows a scheme of OBSERVE in top view, in a configuration suitable for an "AOI≠0" measurement. On the left is shown the case of an AOI adjusted to a value of γ_1. On the right appears a partial view of the bench, for an AOI of $\gamma_2 > \gamma_1$.

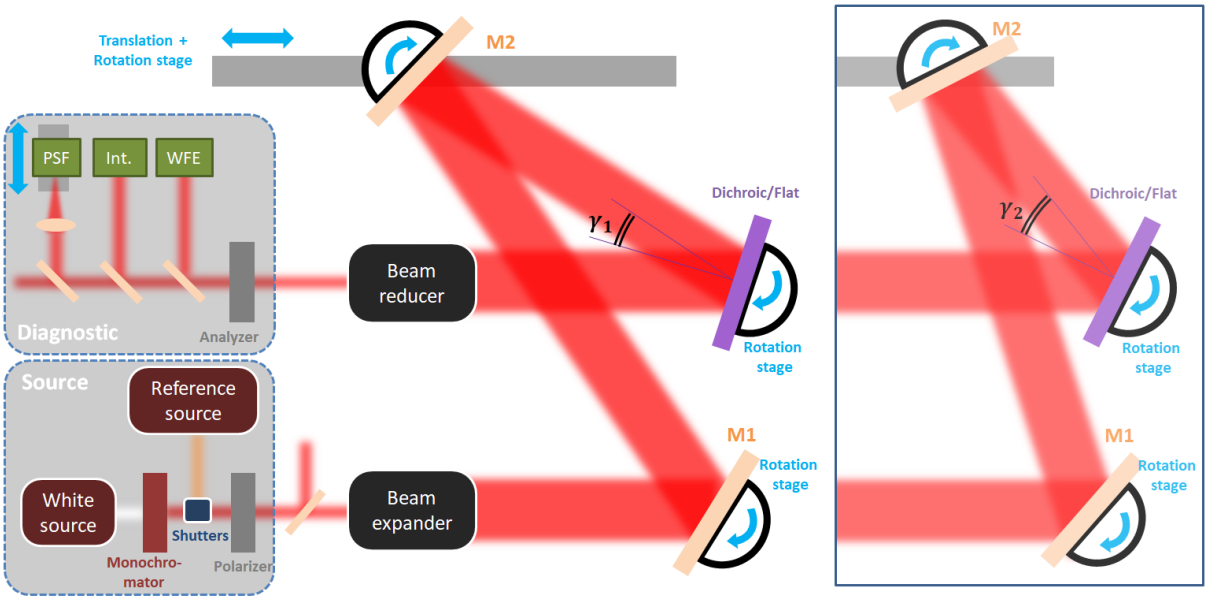

Figure 41: Simplified schema of OBSERVE bench in AOI≠0 configuration, top view. Two AOI adjustments (γ_1, γ_2) are showed.

"Source" block

We will start step by step with the OBSERVE "source" block, bottom left. This block includes two laser sources: the first is the reference source (orange), and the second one is the tunable polychromatic source (white). The latter is followed by a monochromator, which selects a wavelength (in this example, red). A system of "ultra-fast" shutters then selects the source to be injected into the bench. Finally, the injected laser passes through a polarizer, which applies a linear polarization state to the light before exiting the source block.

Beam expander and beam reducer

The beam expander is made up of a system of spherical and flat mirrors, enabling the beam diameter to be enlarged by a factor of 12, to illuminate the entire dichroic mirror. The beam thus expands from a diameter of 10 mm to 120 mm. The beam reducer, located after the dichroic mirror in the optical path, is the exact replica of the beam expander. Composed of the same mirrors, it turns the beam reflected by the dichroic mirror into a beam 10 mm in diameter, adapted to the size of the sensors in the three measurement channels.

"Diagnostic" block

The diagnostic block is a platform comprising the three measurement channels: WFE, Intensity and PSF. After passing through the output polarizer, also labelled as **"analyzer"**, the beam passes through a series of two intensity beamsplitter cubes and a compensator plate, which successively separate the beam towards each channel.

- The WFE channel is a Wavefront Sensor (WFS) designed by IO.
- The Intensity channel features a high-resolution CMOS camera. It measures light intensity after reflection on the dichroic mirror.
- The "PSF" channel is a second high-resolution camera, mounted on a translation stage that enables a slight defocus to be applied. For this channel, the collimated beam is reflected on a concave spherical mirror to be focused on a point.

AOI management

IO's strategy is to have a minimum of moving parts on the bench to ensure simplicity, stability and repeatability of measurements. The source block and diagnostic block are therefore immobile and fixed to the optical table, regardless of the AOI (non-zero). This is also the case for the beam expander and beam reducer, which are fixed to the table in all circumstances. The moving parts of the bench used to adjust the AOI are:

- A rotating stage supporting a plane mirror "M1", at the beam expander output.
- The "rail" stage, which is another flat mirror "M2" that rotates as well as M1 but can be also translated along the rail.
- The dichroic mirror rotating stage, shown in purple in Figure 41 (or reference plane mirror, discussed later).

The first two movable stages (M1 and M2) are called the "trombone" of OBSERVE. Figure 41 representation shows how the IO design makes the AOI adjustment on the dichroic mirror between 4° and 20° without moving the source block, diagnostic block, beam-expander and beam-reducer mirrors.

Besides, the M1 and M2 stages also each feature a rotation plate for adjusting the vertical tilt on each mirror. This additional degree of freedom is used to compensate the mechanical errors in the bench, for example a pitch induced on M2 during the translation along the rail.

Finally, here is a simplified diagram of the OBSERVE bench in "AOI=0" configuration, on Figure 42.

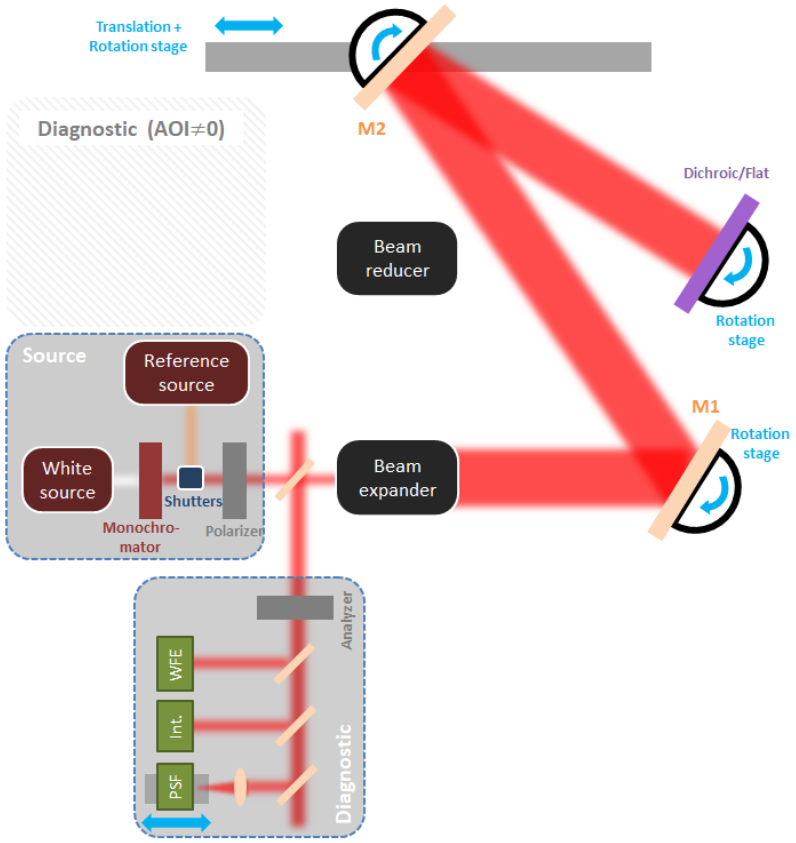

Figure 42: Simplified schema of OBSERVE bench in AOI=0 configuration, top view.

In this configuration, the incident beam is perpendicular to the dichroic mirror, and is therefore reflected in the opposite direction and goes back through the beam expander. The reflected beam is

then separated from the incident beam by a beamsplitter towards the diagnostic unit. In this configuration, the platform of the diagnostic block must be moved manually from its "AOI≠0" position to the "AOI=0" position (see Figure 52). No other bench components need to be moved during the configuration change.

Now that the general principle of the OBSERVE bench has been presented, we will go into detail and illustrate most of the bench's components in the following part.

2.2. Detailed description of OBSERVE bench.

Overview

Figure 43 is a picture of the entire OBSERVE bench, in "AOI=0" configuration. The scale has been added in yellow in the middle of the image. The bench thus fills almost the entire 2.4 m long and 1.5 m wide optical table.

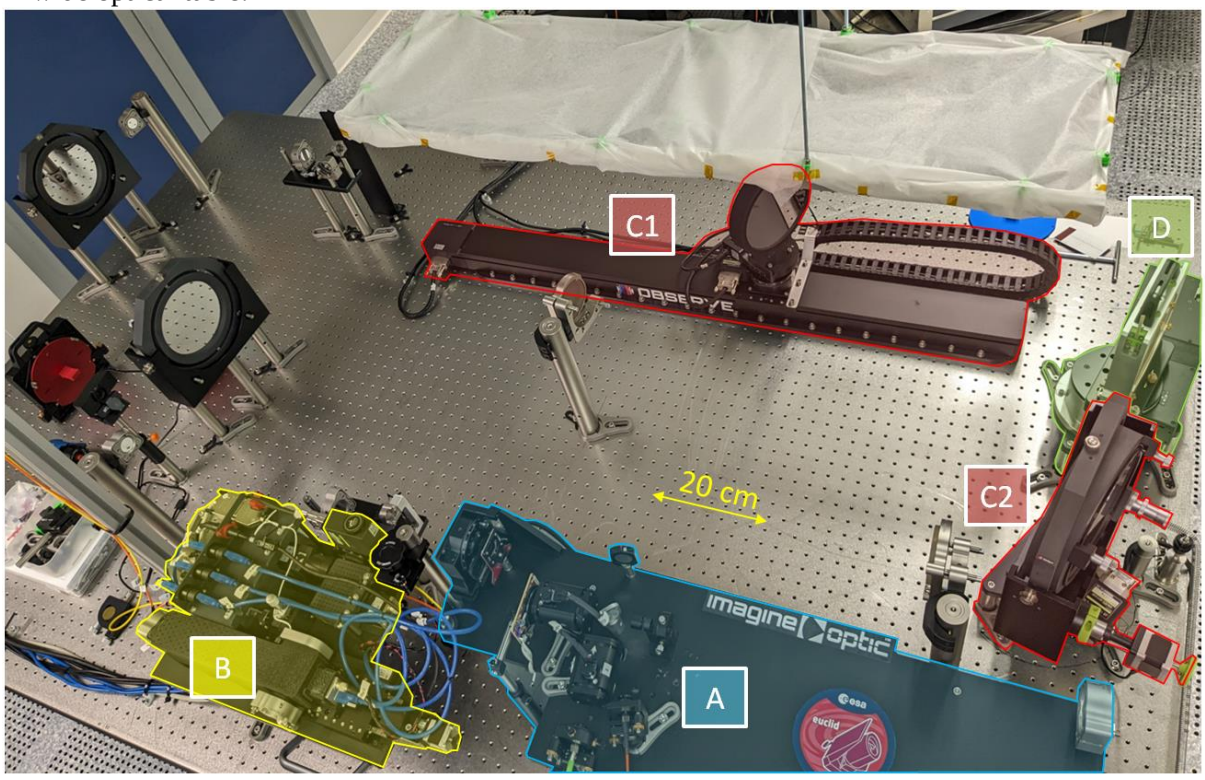

Figure 43: Overview of OBSERVE bench in LMA clean room, from top view.

The source block (A) is highlighted in blue. The diagnostic block (B) is highlighted in yellow, and the two parts of the trombone (C) are highlighted in red. This includes the large translation/rotation rail (C1), visible at the top of the image (above which is a white sail reducing the vertical airflow), and the M1 rotation stage shown in Figure 41. These are best seen from the side view in Figure 48. The stage supporting the dichroic or reference mirror (D) is shown in green. The other mirrors on either side of the optical table are those of the beam expander and beam reducer.

Source block

Newport's "MKS N-LYP-173" reference source is shown in Figure 44, left (A). This is a helium-neon laser with a wavelength of 594.1 nm. This orange laser is then guided towards the source block, located behind the vertical aluminum heat shield, using a periscope.

Figure 44: (Left) Reference source. (Right) Polychromatic source and monochromator.

The polychromatic source (Figure 44, right) (A) and monochromator (B) are located outside the optical table, in the OBSERVE control room. A white Gaussian beam is produced by the "SuperK Fianium FIU 15" source (NKT photonics), in the 390-2400 nm band. This source is directly coupled to a "SuperK LLTF" monochromator (NKT photonics) equipped with 5 gratings (510-575nm; 575-650nm; 650-735nm; 735-835nm; 835-950nm) enabling wavelength selection with a spectral resolution of 0.4 nm FWHM and with an accuracy of 0.1 nm. At the output of the monochromator, the beam is injected into a single-mode optical fiber via a "SuperK Connect" connector (NKT photonics), which then guides the laser towards the source block, pictured in top view in Figure 45.

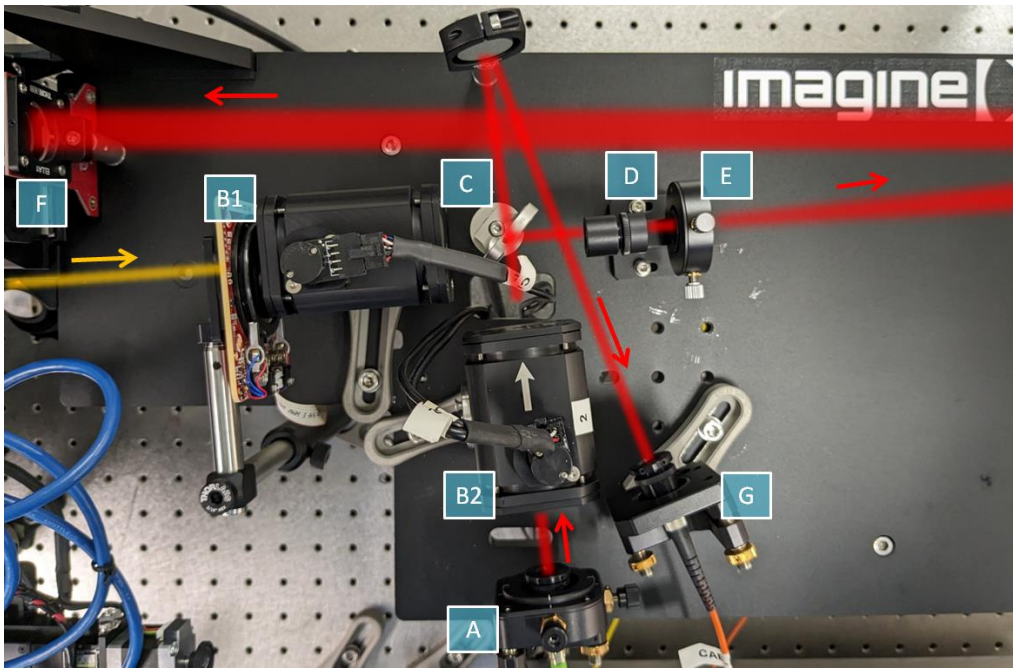

Figure 45: Source bloc of OBSERVE.

The optical paths are shown in red for the tunable laser, and in orange for the reference source. The tunable beam exits the green optical fiber and is then collimated with a collimating lens (A). The selection of the beam injected into the bench is made using two "ultra-fast" synchronized shutters (B1), (B2) designed by Optogama and which can be clocked up to 500 Hz. In the case illustrated here, the tunable beam is injected. After a beam splitter (C), the beam passes through an achromatic doublet (D), making it achromatically focused on a diffraction hole (E). This hole has several functions:

- Ensuring alignment of the beams from B1 and B2.
- Clean up aberrations in the beams, caused by injection into the fibers, or the various optics located upstream of the optical path.
- Create a Gaussian beam whose the central part (highly uniform) is selected by an iris (F) to meet ESA specifications on illumination uniformity.

The divergent beam, diffracted by the hole, is then re-collimated by a 2-inch diameter concave spherical mirror located outside the image, on the right. The central part of the collimated beam is thus truncated by a 10 mm diameter iris (F), and then injected into the source polarizer (more visible on Figure 46 (A)). This is a broadband polarizer: 300 to 2700 nm, (Edmund Optics) whose linear polarization angle is remotely controlled. Finally, Figure 45 (G) shows the fiber optic input towards the lambda-meter (WS5 series, Optonlasers) for active wavelength monitoring with 0.1 nm accuracy. The latter recovers the beam transmitted by the beam splitter (C).

Beam expander elevator block

The beam expander was not shown in Figure 42. The beam expander entrance is via an elevator, which raises the beam, whose diameter will be increased later. Figure 46 shows this elevator, made up of three optical elements. The collimated beam exits the polarizer (A) of the source block (here masked in yellow). It passes through a 50/50 beamsplitter cube (B), whose function is described in the "diagnostic block" section. The beam is then made convergent by a concave spherical mirror (1 inch, f=250 mm) (C), and folded back with a small 0.5-inch plane mirror. The beam, still convergent, is now 3 cm higher than the polarizer axis (A). The chief ray is now 27 cm above the optical table surface.

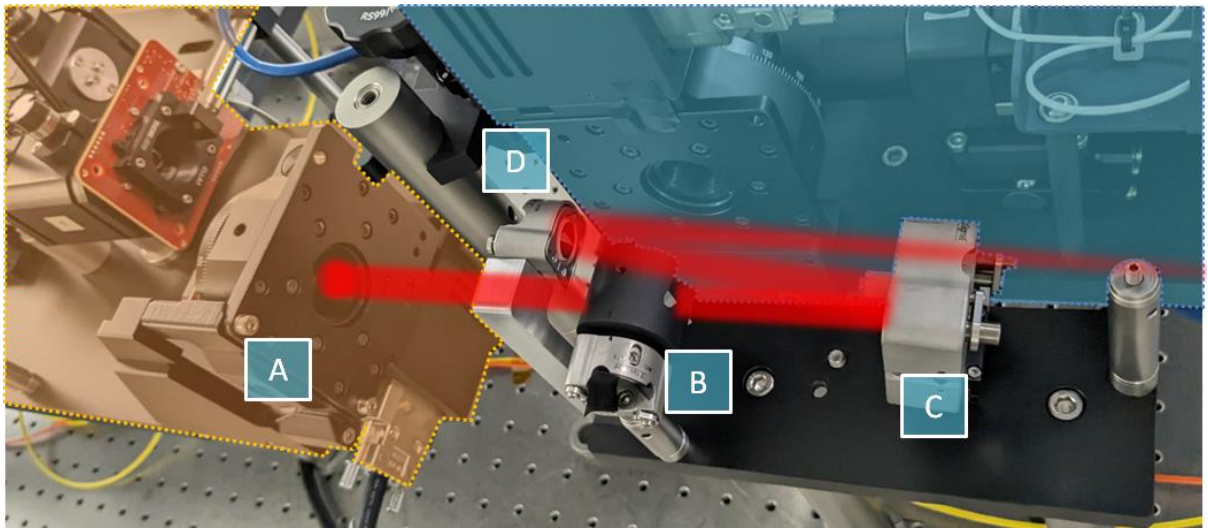

Figure 46: Elevator block of OBSERVE Beam Expander.

Beam Expander Arm

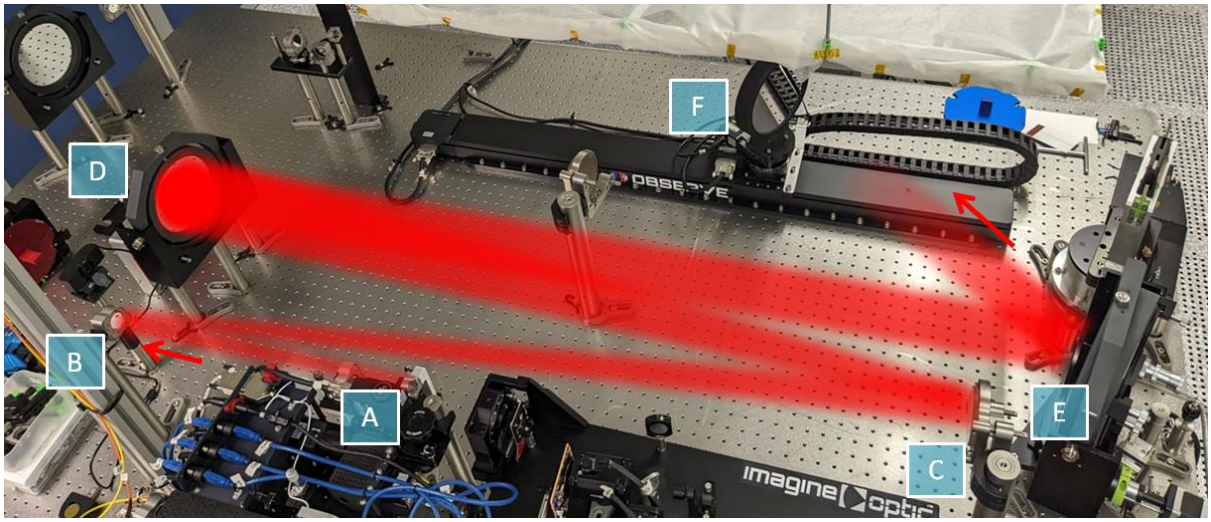

Figure 47: Beam Expander of OBSERVE bench.

The optical assembly of the Beam expander arm is shown in Figure 47. After leaving the elevator (A), the beam is reflected by three mirrors on either side of the optical table. The characteristics of these mirrors are given in Table 21. After (D), the beam is collimated and has a diameter of 120 mm. The beam expander applies then a magnification of 12 to the beam. The choice of this "Galilean" configuration with only spherical and flat mirrors avoids inducing a residual WFE with excessively steep local slopes. The optical solution identified by IO does not create astigmatism or defocus, and only a coma aberration. After the beam expander, the beam reaches the flat mirrors M1 (E) and M2 (F) of the trombone.

Label on Figure 47	Diameter	Surface and focal length
B	1 in.	plane
C	3 in.	plane
D	150 mm	Spherical, concave (f = 3 m)

Table 21: Characteristics of OBSERVE Beam Expander mirrors.

Trombone

As presented in Part 2.1, the trombone has two moving stages on the bench. The first two moving parts are shown in Figure 48. On the left, we first see the large 200 mm-diameter "M1" plane mirror (A), which collects the collimated beam at the beam expander exit. This mirror is housed in a gimbal mount that allows rotation on two axes. The "pitch" axis, shown in purple, is controlled by the stepper motor (B), also highlighted in purple. This actuates a screw fixed on the mount and tilts it around its horizontal axis. The entire mount is positioned on a rotation plate (C), highlighted in orange, which controls rotation around the vertical axis.

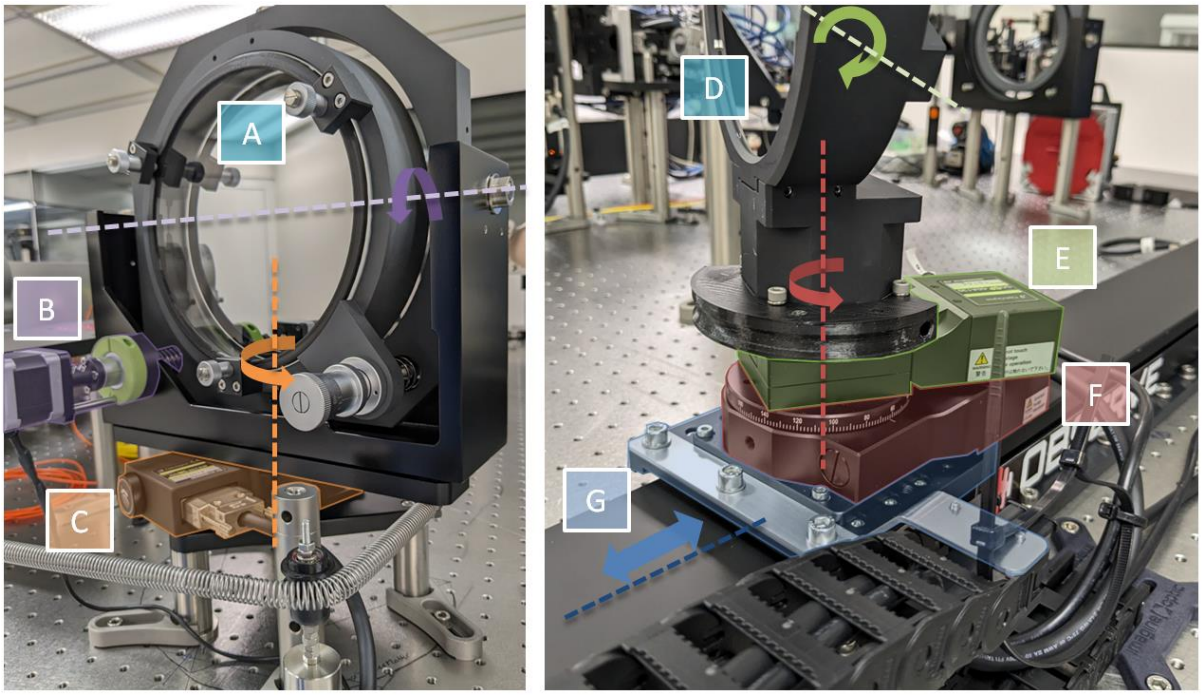

Figure 48: (Left) Trombone mirror M1 mounted on double-rotation stage. (Right) Trombone mirror M2 mounted on double rotation and horizontal translation stage.

On the right of Figure 48 appears the 150 mm-diameter M2 plane mirror (D), which receives the beam reflected by M1. M2's mount is positioned on a first rotation plate (E), highlighted in green, allowing a rotation of the mirror around the pitch axis in green. The lower rotation plate (F), highlighted in red, controls the rotation around the vertical axis, as for M1. The whole assembly is placed on the platform (G) of the 1 m long motorized translation rail. Table 22 summarizes the trombone's motorized components, with the accuracy and repeatability of adjustment on the rotation and translation axes.

Label	Description	Adjustment	**Accur.**	Repeat.
B	Stepper motor (Sanyo Denki) with 1.8 step	M1 pitch	**Not quantifiable**	Not quantifiable
C	Stepping motor driven rotation stage (Optosigma)	M1 yaw	**0.5 mdeg**	20 mdeg
E	Motorized goniometer (Optosigma)	M2 pitch	**0.5 mdeg**	4 mdeg
F	Stepping motor driven rotation stage (Optosigma)	M2 yaw	**0.5 mdeg**	20 mdeg
G	Custom 1-m stepper motor linear stage (Optosigma)	M2 translation	**1 µm**	-

Table 22: Characteristics of trombone motorized elements

For the M1 step motor (B), it is difficult to quantify the increment around the pitch axis. Trombone motors are especially chosen for their **accuracy (resolution)**, and not necessarily their repeatability. The position increment must be as small as possible to make very fine adjustments to the beam on the WFE camera. In practice, the increments of the M1 and M2 motors enable the beam adjustment on the WFE with a resolution of **0.4 mrad in vertical and horizontal tilt**.

Dichroic or reference mirror stage

After the trombone's M2 mirror, the incident beam finally reaches the rotation stage supporting the holder of the dichroic mirror (Figure 49, left) or the holder of the reference plane mirror (right).

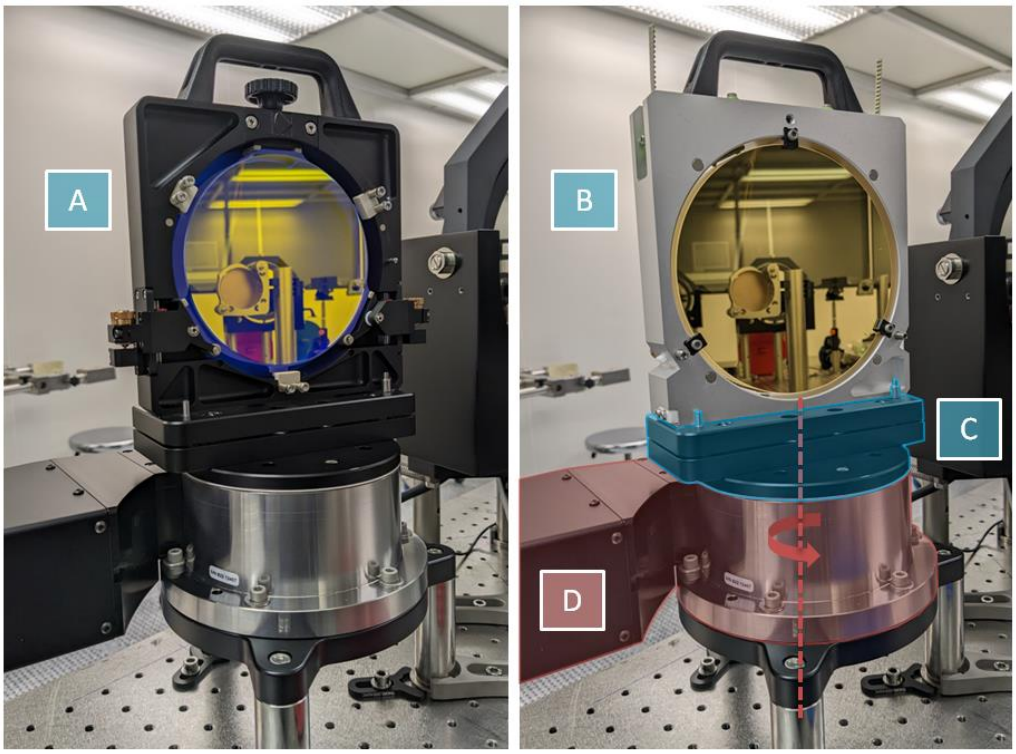

Figure 49: (Left) Euclid Dichroic mirror holder mounted on the rotation stage. (Right) Reference mirror holder mounted on the rotation stage.

Each holder is positioned on the platform (C), highlighted in blue. This platform includes a threaded hole (not visible) and three stop pins (2 of which are visible in the foreground) to position the holder with excellent repeatability. The adjustment between each holder and the platform is made without tightening, using a single safety screw. The platform is mounted on the last rotation plate (Newport RV120 PE), highlighted in red, which enables very fine control of the angle around the vertical axis with an accuracy of 4 mdeg, and a **repeatability of 0.7 mdeg.**

Unlike the trombone, the most important criterion in the choice of this Newport stage is repositioning repeatability, as the latter is the master of all bench alignment. In fact, the highly accurate M1 and M2 motors are adjusted in function of the Newport turntable, and not the contrary. It is therefore essential that the Newport rotation plate has excellent repeatability, for adjusting the entire bench towards the correct AOI.
The two mirrors are each held in a holder, as shown in Figure 49. IO was responsible for the entire mechanical design and manufacture of these holders. Each mirror is held differently in its respective holder, due to the particular geometry of the dichroic mirror. The dichroic mirror, shown in Figure 50 (A), is maintained by 3 flat PEEK supports at its three protuberances (represented by orange lines). Stops (shown in green) are also provided to prevent the mirror from falling when the holder is moved. This secure holding of the dichroic mirror ensures compliance with all the "HOL" constraints of Table 20.

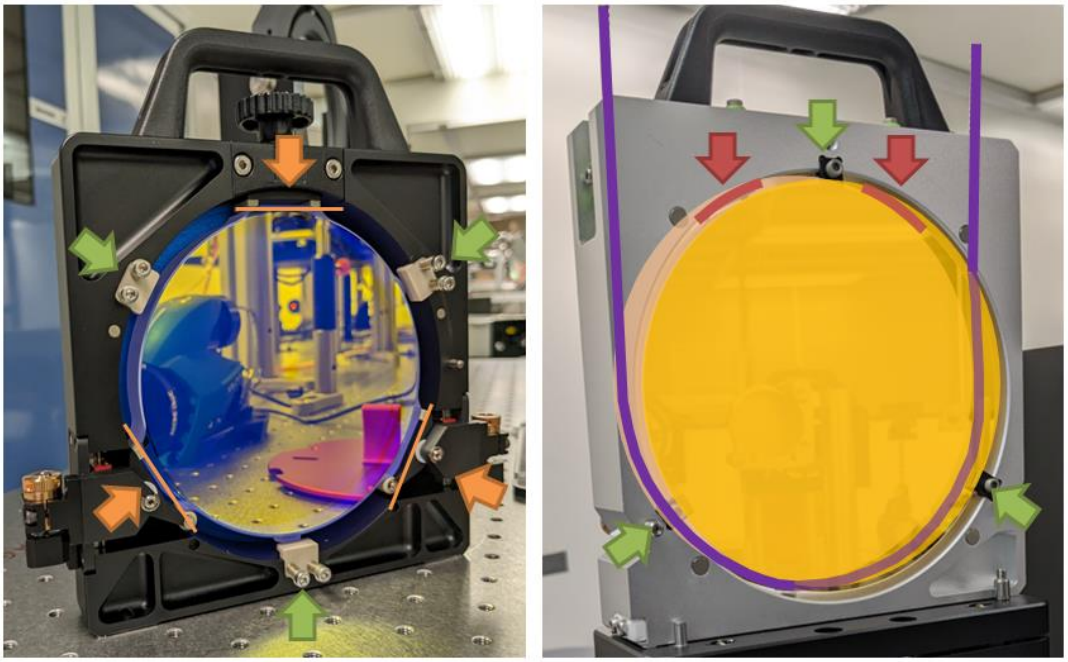

Figure 50: (Left) Dichroic mirror (Right) and reference mirror (B) mounted in its holder.

Unlike the dichroic mirror, the reference mirror is completely cylindrical and has no lateral supports. This is why it is held differently in its own holder (Figure 50, right). Instead of a 3-point support, it is fixed with a belt, shown in purple, and a double cylindrical PEEK support, shown in red. This holder also features safety stops, shown in green, similar to those on the dichroic mirror holder.

Beam Reducer

In the case of an oblique incidence measurement, the beam is then directed towards the beam reducer. The latter is made up of the same mirrors as the beam expander, and an elevator almost identical to the one shown in Figure 46. The beam reducer arm is shown at the top of Figure 51. The collimated beam returns from the dichroic mirror/reference flat to the right of the image, passes through the beam reducer and, after reflection on the small 1inch plane mirror (A), and then reaches the elevator (B). The bottom of Figure 51 is a zoom on this elevator. The only difference with the previous one is that the beamsplitter cube is replaced by a 1-inch oblique plane mirror (C). After reflection on this plane mirror, the beam is collimated, with a diameter of 10 mm, equivalent to that of the input iris (see Figure 45, (F)).

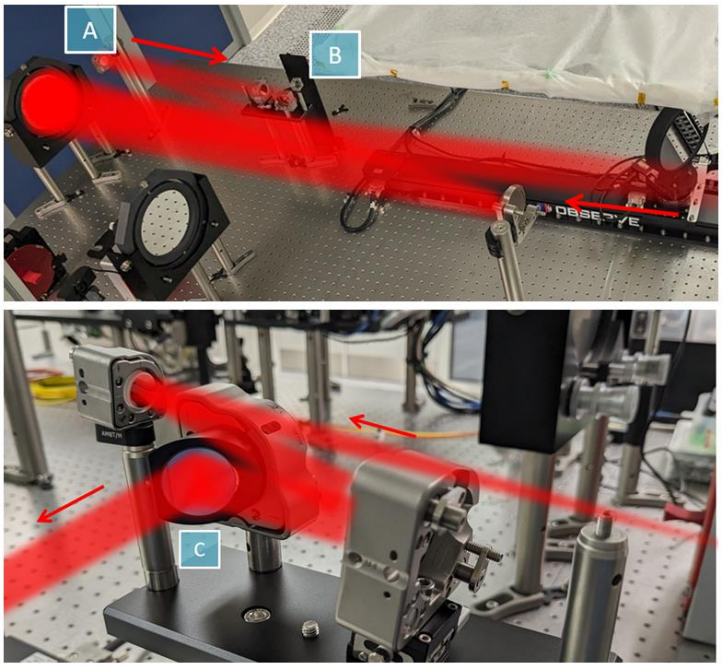

Figure 51: (Up) Beam reducer arm. (Down) Beam reducer elevator.

Diagnostic block

In section 2.1, we saw that the diagnostic block must be positioned either in a configuration suitable for measurement at normal or oblique incidence. Figure 52 shows the two possible positions of the diagnostic block, with the "AOI≠0" position in blue (behind the beam reducer elevator), and the "AOI=0" position in yellow (behind the beam expander elevator).

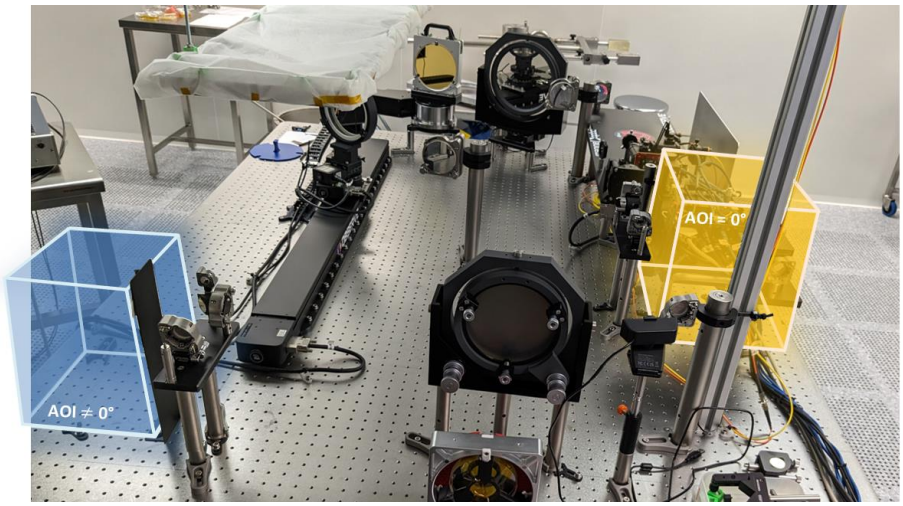

Figure 52: Illustration of diagnostic block position in bench configuration "zero AOI" or "non-zero AOI".

Figure 53 shows the entire OBSERVE diagnostic block, viewed from above and in its "AOI=0" position. It is partly enclosed to limit the stray light that can reach the various cameras it contains. The optical path has been drawn for better understanding.

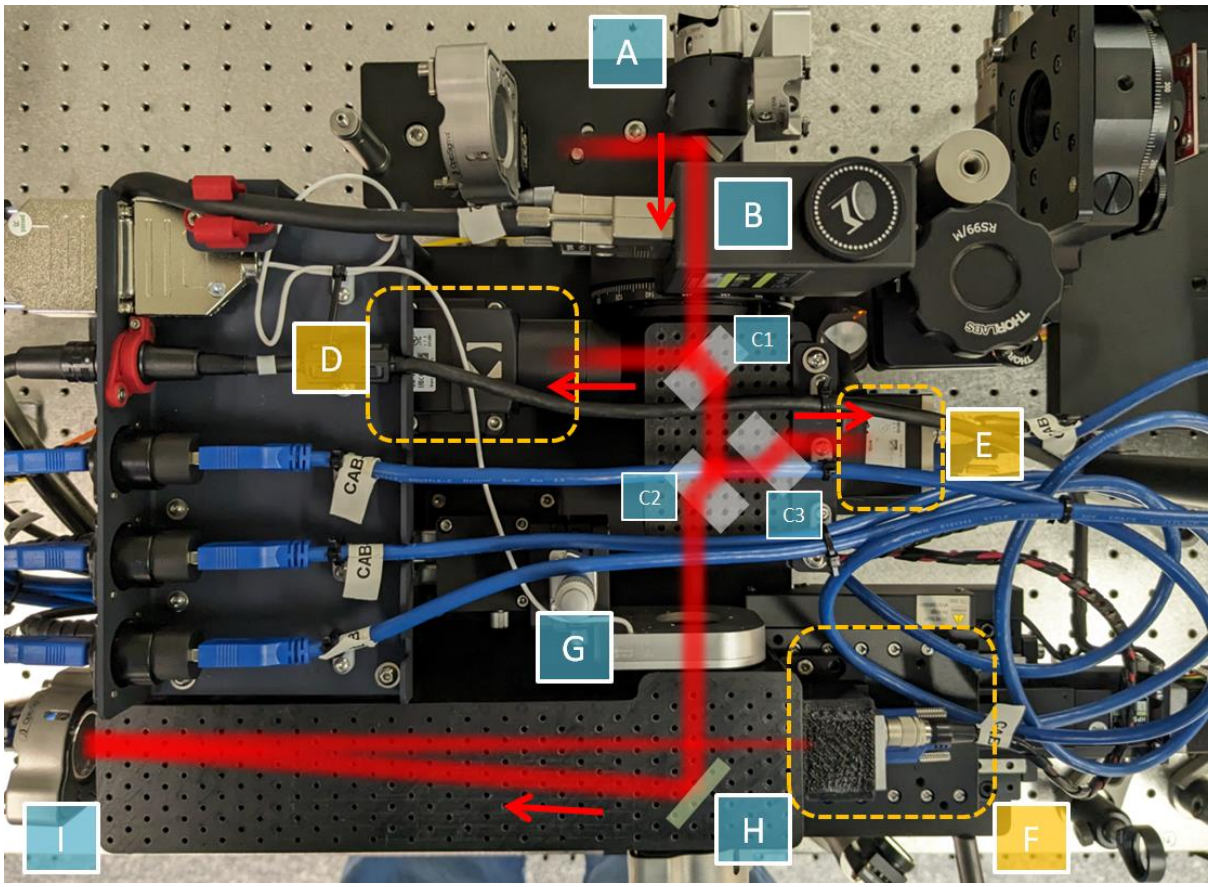

Figure 53: Top view of OBSERVE Diagnostic block ("AOI=0" configuration).

After reflection on the elevator's beamsplitter cube (A), the beam is collimated and sized to its original diameter of 10 mm. It then passes through the analyzer (B) (output polarizer, identical to the source polarizer), then through three CHROMA cubes: 2 beamsplitter cubes (C1, C2), and a compensator cube (C3). Reflections of the cubes separate the beam towards the three channels (D, E, and F), which have been circled in yellow. IO's optical simulations have shown that no parasitic light from secondary reflections on the cubes rear faces reach the cameras. The reflectivity of the two beamsplitter cubes was optimized according to the flux required for each channel.

Note that the refraction angle of light rays through each cube is chromatic, due to the prism effect. The configuration of the optical path through the two beamsplitter cubes and the compensator cube lead to a complete auto-compensation of these aberrations, so that the trajectory of the outgoing rays (directed towards the three channels) is entirely achromatic.

The last beam, directed towards the PSF channel (F), has its diameter adjusted by a motorized iris (G) between 6.67 and 9.75 mm, enabling a smaller area of the illuminated surface to be selected and thus complying with the PSF-100 constraint (Table 17). After a 1-inch oblique plane mirror (H), the beam is then focused on the PSF camera (F) using a final 1-inch concave spherical mirror (I), with a focal length of 300 mm. Finally, here are details of the detectors in the three channels.

- The WFE (D) channel consists of a Shack-Hartmann Wavefront Sensor (SHWFS), with a matrix of 48*48 microlenses. This number makes it possible to meet the WFE-090 specification (Table 15), which concerns the decomposition of the WFE into 55 Zernike modes. IO, which is specialized in this type of technology, designed this custom SHWFS, including the design of the microlens array, the camera, and the whole development of the software used to calculate the WFE maps.

- The Intensity (E) channel contains a Basler CMOS camera with a resolution of 4096x3000 pixels. After a discussion between IO and ESA, supported by a deep study of OBSERVE photometry, the INC-080 specification on beam intensity uniformity has been relaxed. The collimated beam detected by the CMOS camera has homogeneity of 50% instead of the initial 90%.
  IO, ESA, and the *Consortium* have also agreed to modify the method used to measure the reflected beam intensity. Instead of measuring intensity before (INC-060) and after (INC-070) the dichroic mirror, the "intensity" channel will measure intensity after reflection only. By comparing the intensity maps for the dichroic mirror and the reference mirror, the bench will calculate the **relative** non-uniformity of the intensity reflected by the mirror (and not the reflectance $R(x, y, \lambda)$, which is an **absolute** quantity). This is not a blocking point for the *Consortium*, because the spatial variations of reflected intensity at each λ are very important for PSF computing, more than their absolute value.

- The PSF (F) channel contains another CMOS camera (Basler) with a resolution of 1140x1080 pixels. It is mounted on an Optosigma motorized translation platform with 50 mm range. The latter moves the camera around the focus point in the direction collinear with the optical axis, then creating the defocusing required for Phase Diversity studies with an accuracy of 1 µm.

Shack-Hartmann WaveFront Sensor

Before we finish describing the detailed description of OBSERVE, we make a parenthesis on the detection system used to measure the WFE, which is very different from a simple camera. Wavefront detection can be achieved using a number of different technologies, and in the case of OBSERVE, the choice is the widely-used "Shack-Hartmann" technology, illustrated in Figure 54 [67]. This system takes the form of a microlenses array with the same focal length f and diameter d, followed by a camera positioned at the focal plane of the microlenses. Each microlens focuses part of the collimated incident beam onto the image plane, producing a matrix of spots detected by the camera.

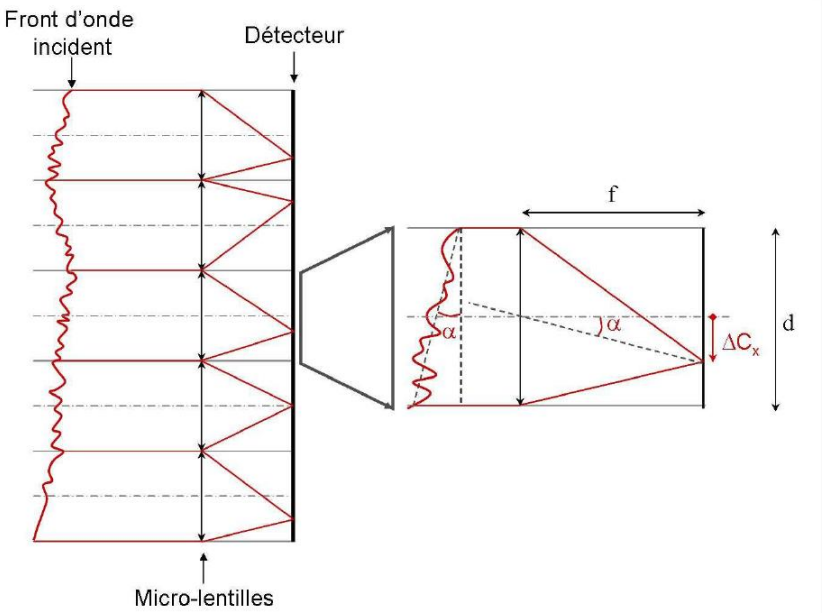

Figure 54: Shack-Hartmann WaveFront Sensor (SHWFS) Principle. [67]

Without WFE, the beam is focused along the optical axis of each lens. In the case of a non-zero WFE, the image obtained by each lens, or sub-aperture, will be a small PSF spot. At the scale of a single

lens, we can consider that the local WFE (shown on the right in Figure 54) is dominated by a mean tilt. The local wave plane is thus tilted by an average angle α. On the detector, the barycenter of the focused spot is now at a distance ΔC_X from the reference position, which is geometrically:

$$\Delta C_X = f tan(\alpha) \tag{20}$$

The Eq. 20 can be rewritten by introducing the edge-to-edge phase difference $\Delta\varphi_X$ of the pupil, caused by the inclination α of the wave plane:

$$\Delta C_X = \frac{\lambda}{2\pi d}\Delta\varphi_X \tag{21}$$

By precisely identifying the position of the focused spot, on a sub-pixel scale, we can use Eq. 21 to determine the local phase shift. By proceeding in this way for X and Y, and for each lens, we can reconstruct the whole WFE.

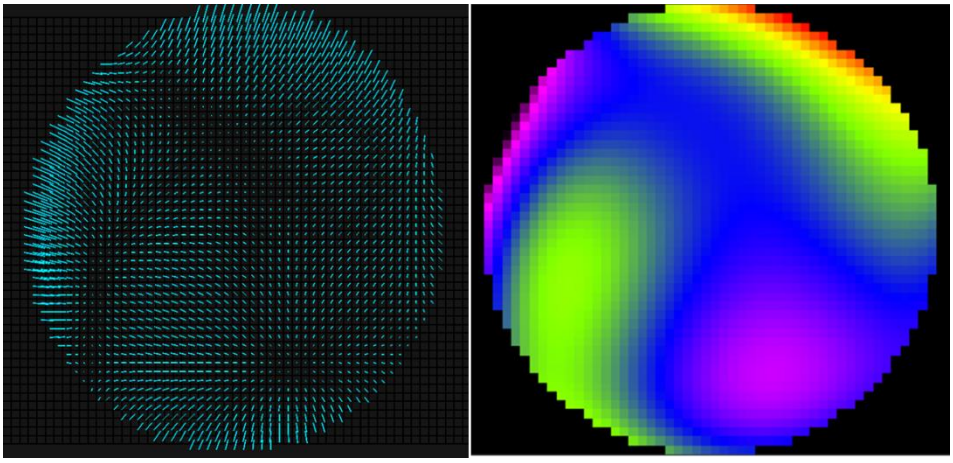

Figure 55: ***WaveView*** *Simulation of some WFE measured with a SHWFS.* ***(Left)****: Displacement vectors of each microlens spots barycenters from their reference position.* ***(Right)*** *WFE computed.*

Figure 55 shows a simulation of a WFE detected by a SHWFS. The camera records the actual position of each spot. The left image corresponds to the displacement of each spot barycenter relatively to its reference position (without WFE). The local slope of the WFE is calculated, and then the full WFE map is then constructed (right).

2.3. Operating mode

We will now present the operational procedure necessary to acquire a dataset essential for calculating the WFE of the *Euclid* Dichroic mirror.

Chromatic data acquisition

We will first present how the bench is operated to obtain a correct WFE measurement. The principle is essentially the same for intensity and PSF measurements.

A simple acquisition of the **WFE of the dichroic mirror** $\boldsymbol{WFE_{DC}^{true}(\lambda)}$ at a given wavelength, and at a given instant t_0 includes chromatic aberrations of the bench $WFE_{bench}(\lambda, t_0)$ and temporal achromatic aberrations due to air turbulence on the optical path $WFE_{air}(t_0)$. We therefore have:

$$WFE_{DC}^{meas}(\lambda, t_0) = \boldsymbol{WFE_{DC}^{true}(\lambda)} + WFE_{bench}(\lambda, t_0) + WFE_{air}(t_0) \tag{22}$$

To remove the temporal aberrations due to air turbulence in Eq. 22, IO has implemented an automated "tic-toc" measurement strategy. The latter consists of alternating between measurements at λ and λ_{ref} = 594.1 nm in a very short time, typically 20 ms, considering that the air flow on the bench does not evolve on this time scale. Subtraction can be performed, to obtain a WFE measurement referenced at λ_{ref}, excluding air-related aberrations:

$$WFE_{DC/ref}^{meas}(\lambda, t_0) = \boldsymbol{WFE_{DC}^{true}(\lambda)} - WFE_{DC}^{true}(\lambda_{ref}) + WFE_{bench/ref}(\lambda, t_0) \quad (23)$$

From now, a static term $WFE_{DC}^{true}(\lambda_{ref})$ appears in Eq. 23, along with bench aberrations referenced to λ_{ref}, $WFE_{bench/ref}(\lambda, t_0)$. IO then proposes to make a second measurement only at λ_{ref} and averaged over a long time to remove air effects (typically >30 min). Assuming that the air aberrations have an average value of zero:

$$WFE_{DC}^{meas}(\lambda, t_0) = WFE_{DC}^{true}(\lambda_{ref}) + WFE_{bench}(\lambda_{ref}, t_0) \quad (24)$$

This static measurement gives thus the sum of the actual WFE of the dichroic mirror at λ_{ref}, $WFE_{DC}^{true}(\lambda_{ref})$ and that of the bench $WFE_{bench}(\lambda_{ref}, t_0)$. By adding the referenced chromatic measurement (Eq. 23) and the averaged static measurement (Eq. 24), the reference is removed and the chromatic **WFE of the dichroic mirror** is then isolated:

$$WFE_{DC/ref}^{meas}(\lambda, t_0) + WFE_{DC}^{meas}(\lambda_{ref}) = \boldsymbol{WFE_{DC}^{true}(\lambda)} + WFE_{bench}(\lambda, t_0) \quad (25)$$

To identify the chromatic aberrations of the bench in Eq. 25, IO suggests making the same "tic-toc" measurement on a metal reference mirror (whose WFE is already known), for which the aberrations of the bench will be the same and can be subtracted.

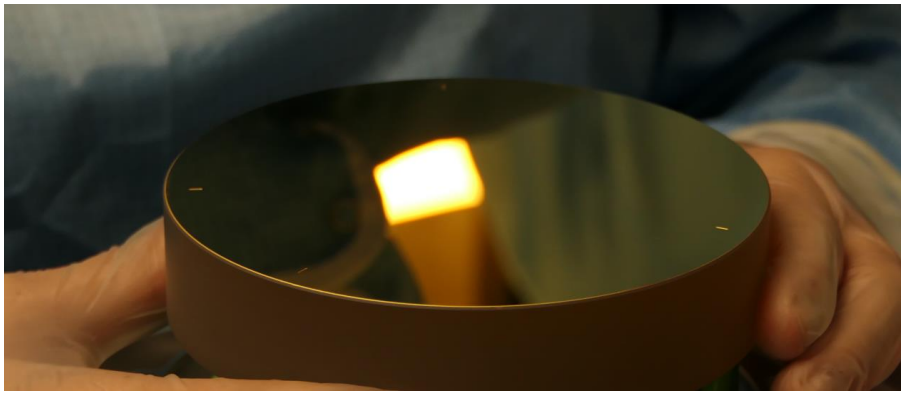

Figure 56: OBSERVE reference mirror (Zeiss)

This metallic reference mirror, shown in Figure 56, was manufactured by Zeiss and features excellent flatness and achromatic WFE. It is coated with a layer of gold, 150 nm thick. Its own WFE was measured using the LMA's ZYGO interferometer at $\lambda_{zygo} = 1064\ nm$, and with an accuracy of 0.2 nm RMS. Figure 57 shows this WFE before and after installation in the holder, without tilt and focus aberrations. The WFE of the Zeiss mirror is thus 1.44 nm RMS after installation in the holder, and includes mostly low-frequency aberrations, mainly astigmatism. Figure 57 also proves that the holder designed by IO induces very few aberrations on the reference mirror.

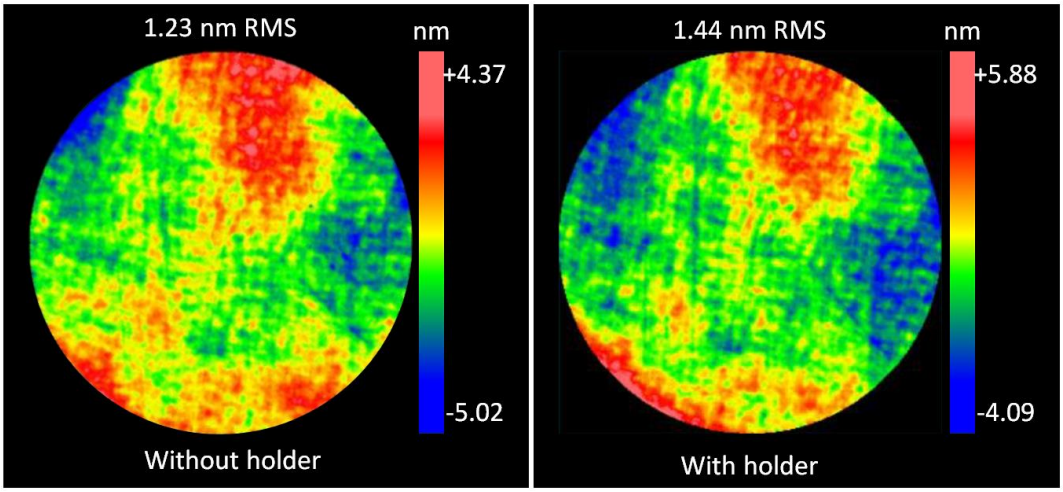

Figure 57: Reference mirror WFE, measured at λ=1064 nm, on a 120 mm diameter (centered), with LMA Zygo interferometer, without its holder (left) and with its holder (right). For both, tilts and defocus are removed.

By making a tic-toc measurement on the reference plane mirror, we obtain a second referenced measurement equivalent to Eq. 23:

$$WFE_{plan/ref}^{meas}(\lambda, t_1) = \boldsymbol{WFE_{plan}^{true}(\lambda)} - WFE_{plan}^{true}(\lambda_{ref}) + WFE_{bench/ref}(\lambda, t_1) \quad (26)$$

In Eq. 26 therefore appears the **actual WFE of the plane mirror** at λ, $\boldsymbol{WFE_{plan}^{true}(\lambda)}$, and at λ_{ref}, $WFE_{plan}^{true}(\lambda_{ref})$. The last term is the bench-referenced WFE, equivalent to that appearing in Eq. 23. Again, adding an averaged static measurement to λ_{ref} (identical to Eq. 24),

$$WFE_{plan/ref}^{meas}(\lambda, t_1) + WFE_{plan}^{meas}(\lambda_{ref}) = \boldsymbol{WFE_{plan}^{true}(\lambda)} + WFE_{bench}(\lambda, t_1) \quad (27)$$

Assuming that the contributions of the bench are equivalent at t_0 and t_1, we have, by subtraction of Eq. 25 and 27,

$$\left[WFE_{DC/ref}^{meas}(\lambda) + WFE_{DC}^{meas}(\lambda_{ref})\right] - \left[WFE_{plan/ref}^{meas}(\lambda) + WFE_{plan}^{meas}(\lambda_{ref})\right] = \boldsymbol{WFE_{DC}^{true}(\lambda)} - \boldsymbol{WFE_{plan}^{true}(\lambda)} \quad (28)$$

This time, the term $\boldsymbol{WFE_{plan}^{true}(\lambda)}$ in Eq. 28 is known, as it corresponds to the interferometric measurement of the plane mirror by the Zygo interferometer. By adding it to Eq. 28, we then access the chromatic contribution of the dichroic mirror $\boldsymbol{WFE_{DC}^{true}(\lambda)}$**.** The whole process thus requires four measurements in total:

- A referenced chromatic measurement of the dichroic mirror: $\boldsymbol{WFE_{DC/ref}^{meas}(\lambda)}$
- A static measurement of the dichroic mirror: $\boldsymbol{WFE_{DC}^{meas}(\lambda_{ref})}$
- A referenced chromatic measurement of the Zeiss plane mirror: $\boldsymbol{WFE_{plan/ref}^{meas}(\lambda)}$
- A static measurement of the Zeiss plane mirror: $\boldsymbol{WFE_{plan}^{meas}(\lambda_{ref})}$

Such a process involves a number of conditions. Naturally, the maps must be perfectly aligned and oriented so that the various subtractions can be made without residuals. Secondly, the exposure time, number of images averaged, and tic-toc speed must be optimized to eliminate any air contributions. Finally, successful subtraction of the maps from the reference mirror and dichroic mirror measurements assumes that there was no drift of the bench between the two acquisitions, hence a different $WFE_{bench}(\lambda)$.

The time required to obtain these data depends on the spectral range needed and is directly related to the photometric needs of the bench. It takes around 60 seconds to obtain a measurement at one wavelength. To cover the 550-950 nm wavelength range with 1 nm step, 7 hours are required. It will therefore take 15h of measurements to complete the four acquisitions, not counting the set-up time for the dichroic mirror and the reference mirror on the bench. We will now describe the bench's operating mode.

OBSERVE acquisition running mode.

The OBSERVE bench has been designed to be highly automatic. Changes in wavelength over a given interval, incidence, and polarization (input and output) are made automatically via the control software, based on user-defined values. In addition, the dark subtractions, the exposure time, and number of images for averaging (to obtain the right SNR) are managed directly by the software developed by IO.

However, several key steps remain the responsibility of the operator. A set of four measurements $WFE^{mes}_{DC/ref}(\lambda), WFE^{mes}_{plan/ref}(\lambda), WFE^{mes}_{DC}(\lambda_{ref}), WFE^{mes}_{plan}(\lambda_{ref})$, is obtained with the 10 "Operator" actions listed in Figure 58.

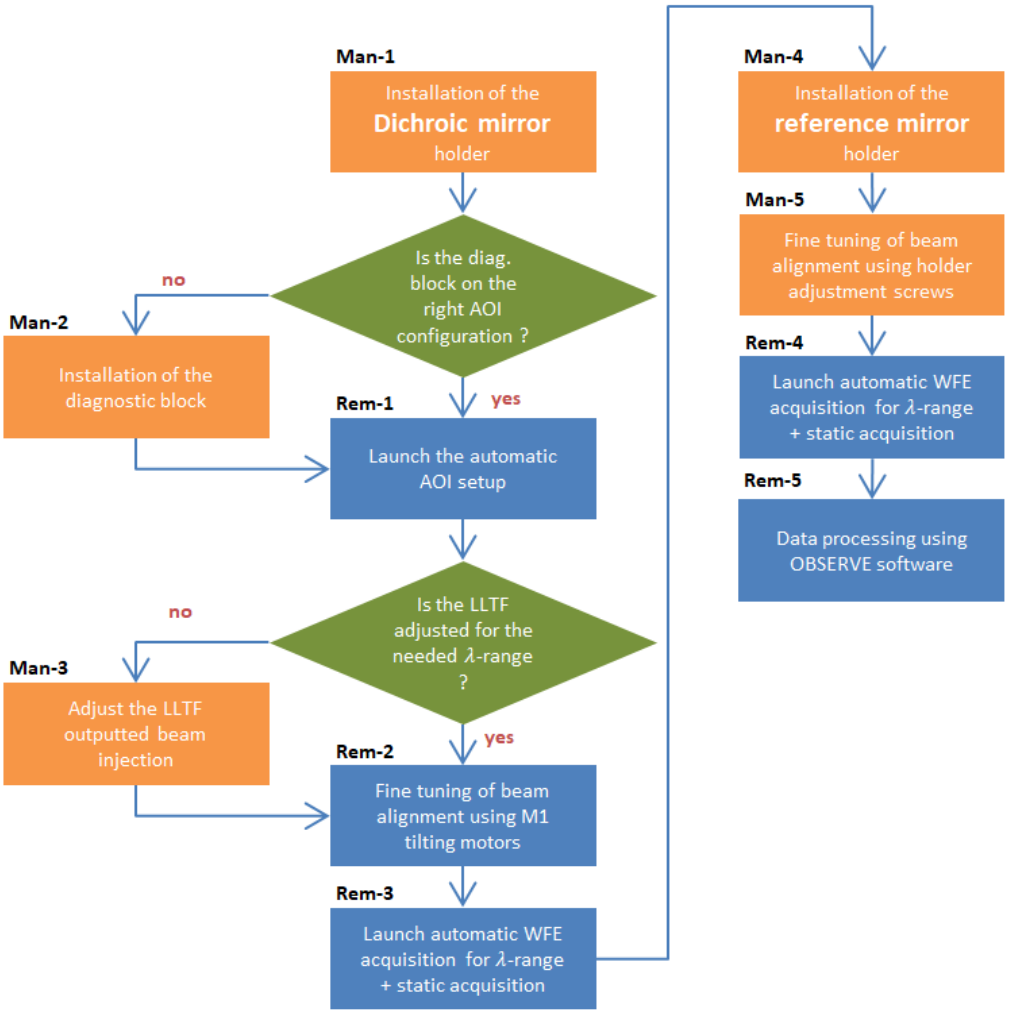

Figure 58: Sequence of manual and remote user actions on OBSERVE.

First, we detail the manual actions shown in orange in Figure 58.

- **(Man-1)** Dichroic mirror installation on OBSERVE. This action does not require direct contact with the mirror. The mirror is integrated into the holder designed by IO.
  The user places the holder on the platform (Figure 49), which is designed for setting the holder always in the same position. The area covered by the holder on the platform is shown in yellow in Figure 59. The 3-point contact on the cylindrical stops is represented by the orange lines. The holder's safety screw is positioned without tightening in the hole indicated in blue.

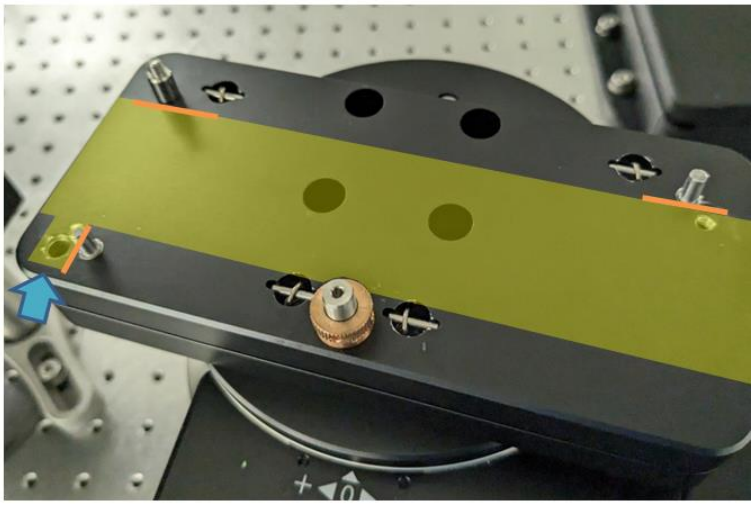

Figure 59: Mounting area for dichroic/reference holders.

- **(Man-2)** Switch to "AOI=0" or "AOI≠0" configuration (if required). This action consists in moving the diagnostic block to the right position on the bench. This is done by touching the supports on the optical table. These two positions are illustrated in Figure 52.

- **(Man-3)** LLTF monochromator output beam injection adjustment (if required). Although wavelength selection is automatic, a manual operation is required to maximize the flux over the 650-735 nm spectral range. This manual operation is very simple, but it implies that a direct measurement over the complete 550-900 nm range is not possible. The chosen range must therefore either contain exclusively wavelengths between 650 and 735 nm or be excluded altogether. This subdivision of accessible intervals naturally has consequences for the organization of measurement campaigns.

- **(Man-4)** Installation of the reference mirror on the bench. Like the dichroic mirror, the plane mirror is mounted in its secure holder. Installation on the bench is identical.

- **(Man-5)** Reference mirror alignment. The reference mirror holder has three adjustment screws on the rear side, shown in Figure 60 with three blue arrows, enabling fine adjustment of the surface orientation without changing the settings of the bench itself. IO calculated that a horizontal and vertical beam tilt setting of 0 ± 0.5 mrad (in the SHWFS reference frame) is required to meet the WFE accuracy specifications. For comparison, a tilt of 0.5 mrad in SHWFS space corresponds to a tilt of 42 µrad in the mirror reference frame. Finally, the safety screw, identical for both holders, is circled in orange.

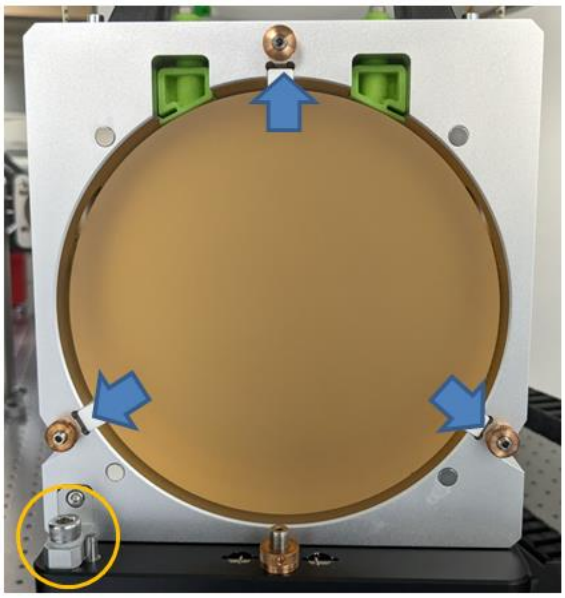

*Figure 60: (**Blue**) fine-tuning screws of reference mirror holder (rear view).*

Next, we detail the "remote" actions shown in blue in Figure 58.

- **(Rem-1)** AOI setting. The AOI is specified by the user in the OBSERVE interface. The Newport rotation plate supporting the dichroic mirror is then automatically set to an angular position available in a look-up table, and the trombone mirrors are roughly preset to this AOI.

- **(Rem-2)** Beam alignment after dichroic mirror installation. It is not possible to launch an acquisition directly, as the motors of M1 and M2 are not repeatable enough to be adjusted automatically during Rem-1, and the inaccuracy of positioning the holder on the platform must be compensated. This is why fine-tuning of the inclination (horizontal and vertical) of the M2 mirror is required for beam fine alignment. The user then controls the motors of the M2 rotation plates via the bench interface to align the beam on the dichroic surface with a residual tilt of 0 ± 0.5 mrad in both directions (always in "WFE camera" reference frame).

- **(Rem-3)** Launch chromatic or static acquisition. The user specifies the acquisition type, spectral range and polarizations, and then launches the acquisition, which is fully automated.

- **(Rem-4)** Idem, for an acquisition launch on the reference mirror.

- **(Rem-5)** Data processing. Once the four data sets have been obtained, the user post-processes them with the software supplied by IO. This software automatically manages the alignment and overlay of the maps, and also calculates the WFE maps from the SHWFS data, for each wavelength.

An essential aspect to remember from these "operator" manipulations is the alignment process: the reference mirror is aligned with the bench, and the bench is aligned with the dichroic mirror. This explains why the dichroic mirror is measured first, using a bench motor adjustment (Rem-2), rather than a manual holder adjustment, as done with the reference mirror.

During the calibration phase, IO aligned some of OBSERVE's optics, using the dichroic mirror holder as a reference. Consequently, the bench must always be aligned with the dichroic mirror holder when the latter is repositioned on its platform, and not the contrary. Changing the settings of this holder would involve a realignment of some of OBERVE's optics, which could be a complex operation.

Finally, it is essential that the bench settings remain unchanged for measurements on both mirrors. In this way, the contribution from the bench is identical for both measurements, making possible to eliminate it thanks to Eq. 28.

In conclusion, we have presented all the necessary steps to use the OBSERVE bench, concluding the section by detailing the bench's operational procedure. While many of the bench's functions are automated, some manual or remote interventions are still necessary. At this point, it is clear that four acquisitions are necessary to generate WFE maps of the dichroic mirror, catering to a specified spectral range and fixed illumination conditions.

Output WFE files

During an acquisition with the OBSERVE bench, we obtain raw files containing the position of all spot barycenters from the SHWFS camera. This raw data from the four acquisitions (two static, and two chromatic) are then loaded into the dedicated analysis software supplied by Imagine Optic. This post-processing software automatically manages among others:

- Time-averaging for the static acquisitions, and chromatic referencing for the "tic toc" (chromatic) acquisitions.
- Maps combination: centering, alignment, rotation, cropping to a specified diameter.
- Switching between the different reference frames (SHWFS, dichroic mirror), taking into account of the obliquity and orientation.
- WFE calculation from barycenter files. This also takes into account phenomena such as obliquity.

The result is then a folder containing all pupil WFE maps at each wavelength in the dichroic mirror reference frame and all metadata. Each map is a text file always comprising 128 x 128 points matrix, whatever the pupillary diameter we specify. These circular WFE maps are directly usable and no additional post-processing is required on our part. For the work presented in this thesis, we do not need to go further into details of the WFE maps computing and treatment from the raw data obtained from the SHWFS.

3. CONCLUSION

In this chapter, we presented in detail the "OBSERVE" optical metrology bench, entirely designed by IO, and validated by ESA and the *Euclid Consortium*. The bench's overall operating principle for acquiring highly accurate measurements of WFE, intensity and PSF in a wide range of optical configurations has been described. The bench's main components (mirrors, motors, cameras, etc.) and the operating procedure for obtaining the various chromatic data sets were also presented.
The "user" tasks for operating with the bench have now been established. Many of the bench's functions are automated, but some manual adjustments are still necessary: changing the components to be characterized, realigning the beam, etc. We will see in the following chapter how these settings are a crucial factor for the measurement repeatability and reproducibility.

4. REFERENCES

64 *Euclid Consortium* internal document (EUCL-EST-TN-3-013)
65 ISO-classification ; https://www.americancleanrooms.com/cleanroom-classifications/
66 Imagine Optic website: https://www.imagine-optic.com/imagine-us/
67 M. Nicolle. « Analyse de front d'onde pour les optiques adaptatives de nouvelle génération. » Astrophysique [astro-ph]. Université Paris Sud - Paris XI, 2006. Français. ⟨tel-00137288⟩
68 *Euclid Consortium* internal document (EUCL-CEA-TN-8-006)

Part B

Euclid dichroic mirror characterization

The Chapter 4, as well the previous ones set the context for this thesis: the dichroic mirror takes part to the *Euclid* PSF complexity which is a crucial criterion for WL observations with VIS instrument. This problem comes from the chromaticity of the WFE reflected by the mirror, and we have seen that this chromaticity is linked to the thin-films stack of the dichroic coating. ESA therefore expressed a need to characterize the WFE of this mirror. For this purpose, a characterization plan has been drawn up by the *Euclid Consortium* [68] comprising four campaigns of varying duration and with different objectives, to be carried out during and following this thesis. We will focus on the first of these, which contains all the tests required to characterize the mirror in this thesis.

This first compaign, labelled "**Dry-Run**" is followed by the "**Preliminary Compaign"**, which focuses on specific spectral bands under specific illumination conditions, such as cross-polarization. The aim will be to identify or not the optical activity of the mirror, such as birefringence effects. Such an effect would mean redefining the rest of the campaign. The work presented in this thesis does not take into account the results of the Preliminary Compaign. After the Preliminary compaign it will be the "**Core compaign"**. This long campaign includes WFE, Intensity and PSF measurements in the entire visible band, over a wide range of incidence angles and polarizations. This volume of highly detailed measurement data will be adjusted according to the findings of previous campaigns. Finally, there is the "**Extra compaign**", which has not yet been fully defined. It will mainly contain PSF measures in Phase Diversity.

The aim of this thesis is twofold: firstly, to correctly measure the WFE of the dichroic mirror using the brand-new OBSERVE bench, which involves working on the commissioning, validation and calibration of the bench in order to understand its actual performances. Next, a measurement campaign will be carried out, and these measurements will allow the accurate modeling of the dichroic mirror and all its layers. This model, which is the second objective of the thesis, should enable us to predict the optical behavior of the mirror under flight conditions.

The work of this thesis, devoted to the characterization of the dichroic mirror, begins then with the following chapter, which presents the OBSERVE bench commissioning and validation.

Chapter 5

Bench commissioning and validation

This chapter is the beginning of *Euclid* dichroic mirror characterization work. For this purpose, measurements will be made on OBSERVE bench, which was introduced in the previous chapter, and which has been available at LMA since July 2023, after a year of development.

We will begin by presenting the bench commissioning phase, which lasted until December 2023. This included a set of stability, repeatability, and reproducibility tests, which led to a redefinition of the experimental protocol and some modifications to the bench itself. Next, we will present the bench validation tests, using a dummy mirror to identify any possible experimental biases coming from the bench.

1. OBSERVE BENCH COMMISSIONING WITH SPECIFIC TESTS

This section is devoted to the commissioning of the bench with an analysis of the initial results, particularly in terms of repeatability and reproducibility.

The goal of this part was to estimate the sensitivity of the OBSERVE bench to the environmental conditions (clean room, temperature, alignment etc.) and to estimate their impact on the results. From this work, the data campaign can be adjusted and corrections can be applied.

This has been done from July until December 2023. The bench proved to be much more sensitive than expected to ambient conditions in the cleanroom and to optical alignment and corrections were applied that improved greatly the measurement accuracy.

1.1. Zernike polynomials

To do the analysis, WFE will be decomposed in Zernike polynomials which are a tool to understand and describe the different optical contributions in the WFE or SFE maps.

In this part, we will present the Zernike polynomials [69]. They were first introduced in the description on the specification WFE-090 (see Table 15 in Chapter 4) in order to define the spatial frequency components of the WFE. Previous works have concluded that the knowledge of the 55 first Zernike modes of the dichroic WFE is sufficient to meet the requirements on the PSF reconstruction. Here, we present the formalism of these polynomials and the chosen conventions. Zernike polynomials, formalized by Fritz Zernike in 1935 [70], are widely used in optical imagery to define and classify the aberrations of any circular surface, such as a pupillary WFE.

This is an infinite sequence of polynomials in polar coordinates (ρ, θ), defined on the unit disk. The polynomials $Z_n^m(\rho, \theta)$ are defined by their radial degree n and azimuthal degree m, with $n > m$ and $m \geq 0$. For each n and m, we thus obtain two polynomials, one of which is even:

$$Z_n^m(\rho, \theta) = R_n^m(\rho)\cos(m\theta)$$

And the second is odd:

$$Z_n^{-m}(\rho, \theta) = R_n^m(\rho)\sin(m\theta)$$

With $R_n^m(\rho)$ the radial function:

$$R_n^m(\rho) = \sum_{s=0}^{(n-m)/2} \left[\frac{(-1)^s (n-s)!}{s!\left(\frac{n+m}{2}-s\right)!\left(\frac{n-m}{2}-s\right)!} \rho^{n-2s} \right]$$

Figure 61 shows the first Zernike polynomials for m and n from 0 to 4, represented in the form of a pyramid. The vertical axis of the pyramid corresponds to radial polynomials such that $m = 0$. The left side of the pyramid contains all odd polynomials, while the right side contains all even polynomials.

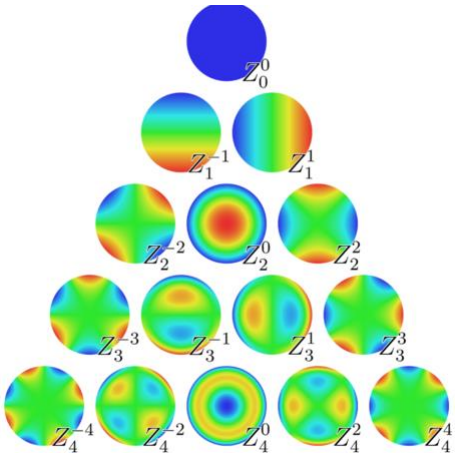

Figure 61: Visual representation of the 15 first Zernike polynomials [71]

Noll Index	*n*	*m*	Equation in polar coordinates	Aberration
1	0	0	$Z_0^{+0} = 1$	Piston
2	1	+1	$Z_1^{+1} = 2\rho\cos(\theta)$	Horizontal tilt
3	1	-1	$Z_1^{-1} = 2\rho\sin(\theta)$	Vertical tilt
4	2	0	$Z_2^{+0} = \sqrt{3}(2\rho^2 - 1)$	Defocus
5	2	-2	$Z_2^{-2} = \sqrt{6}\rho^2\sin(2\theta)$	Oblique astigmatism
6	2	+2	$Z_2^{+2} = \sqrt{6}\rho^2\cos(2\theta)$	Vertical astigmatism
7	3	-1	$Z_3^{-1} = \sqrt{8}(3\rho^3 - 2\rho)\sin(\theta)$	Vertical coma
8	3	+1	$Z_3^{+1} = \sqrt{8}(3\rho^3 - 2\rho)\cos(\theta)$	Horizontal coma
9	3	-3	$Z_3^{-3} = \sqrt{8}\rho^3\sin(3\theta)$	Vertical trefoil
10	3	+3	$Z_3^{+3} = \sqrt{8}\rho^3\cos(3\theta)$	Horizontal trefoil
11	4	0	$Z_4^{+0} = \sqrt{8}(6\rho^4 - 6\rho^2 + 1)$	Spherical
12	4	+2	$Z_4^{+2} = \sqrt{10}(4\rho^4 - 3\rho^2)\cos(2\theta)$	2nd vertical astigmatism
13	4	-2	$Z_4^{+2} = \sqrt{10}(4\rho^4 - 3\rho^2)\sin(2\theta)$	2nd oblique astigmatism
14	4	+4	$Z_4^{+2} = \sqrt{10}\rho^4\cos(4\theta)$	Vertical quadrafoil
15	4	-4	$Z_4^{-4} = \sqrt{10}\rho^4\sin(4\theta)$	Oblique quadrafoil

Table 23: Name, label (Noll convention), and expression of the 15 first Zernike polynomials.

Table 23 lists the equations of the 15 first Zernike polynomials illustrated in Figure 61, together with the name of the corresponding aberration. These are listed according to their Noll index [72], which will be used as a convention throughout the manuscript. Even if the 55 first modes are needed to comply with the PSF requirements, the most interesting part of information is included in the low orders. The 15 first modes will be a useful tool for diagnosis in order to have a better insight of the bench. They will be used to understand any malfunctioning of the bench.

Zernike polynomials constitute an orthogonal basis over the unit disc. This means that a pure aberration onto the unit disc can only be characterized by a single polynomial. Indeed, the scalar product between two different polynomials is given by:

$$\langle Z_k, Z_m \rangle \equiv \iint [Z_k(x,y) Z_m(x,y) dxdy] = 0 \; \forall \; k \neq m$$

A pupillary WFE$(\rho, \theta, \lambda_i)$, for example, could thus be projected onto the first *N* Zernike polynomials independently.

1.2. Temporal stability of OBSERVE bench

The aim of this section is to study the stability of the bench during time and to correct any temporal evolution of the measurements if needed. The temporal evolution of the bench can be due to any evolution of external conditions, as for example the cleanroom. To achieve this, we will carry out **raw acquisitions** over several hours at the reference wavelength λ_{ref} = 594.1 nm, with a sample every **38 seconds**.

Temporal tilts measurements

We have chosen to present here the results on the tilts only, which corresponds to the Zernike modes Z2 and Z3. It turns out that the other Zernike modes undergo variations several orders of magnitude smaller than those observed here. Figure 62 shows a time measurement made over a full night, at 19° incidence, P/N, on the reference mirror. The results are smoothed by a sliding window average on 20 samples (i.e. 12 minutes). After 6 hours (transition between the green and magenta zones in Figure 62), the entire cleanroom then switches to a "reduced" mode, where the airflow is reduced (by half), for energy-saving reasons. Every day, the cleanroom is in reduced mode between midnight and 6:30 a.m., as well as during weekends.

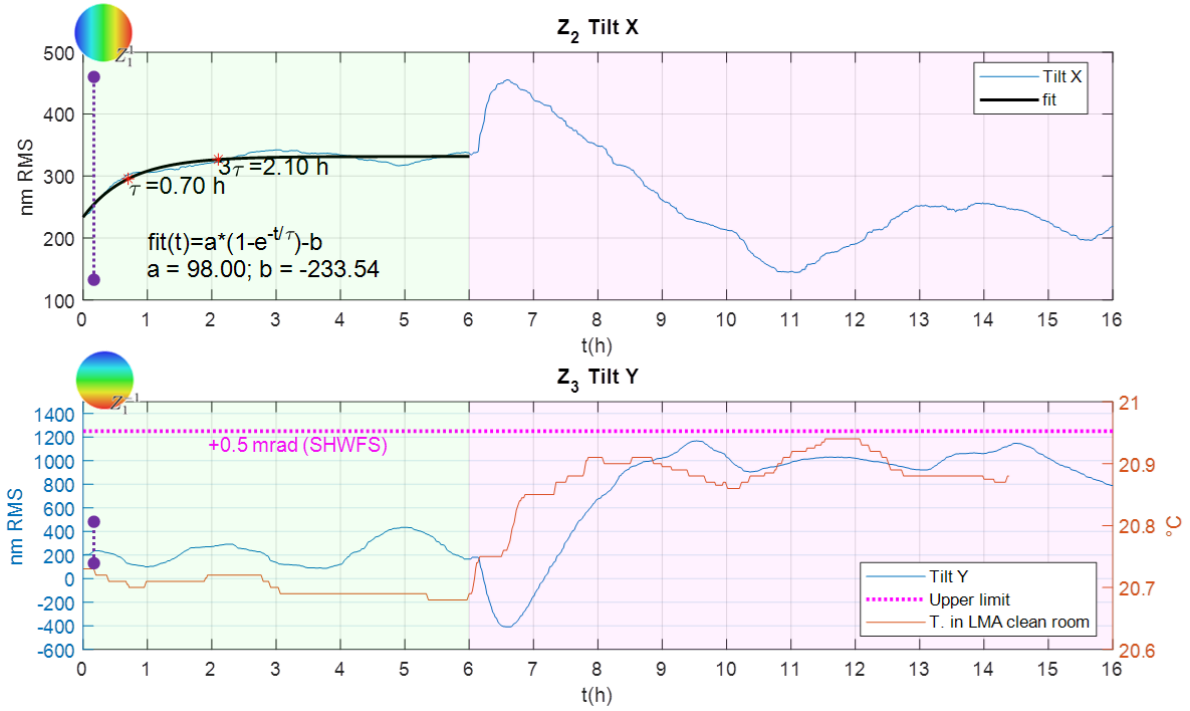

Figure 62: ***(Up)*** ***Blue****: Temporal measurements (sliding window average) of Tilt X on reference mirror at* λ_{ref}*=594.1 nm 19° AOI, P/N.* ***Black****: exponential decay fit over the first 6 hours.* ***(Down)*** ***Blue****: Temporal Tilt Y, same conditions.* ***Pink****: Upper limit of 1250 nm RMS (0.5 mrad in SHWFS space).* ***Red****: temperature of LMA clean room air conditioning. Area color represent the clean room air regime (****green*** *= nominal,* ***magenta*** *= reduced).*

- Nominal LMA clean room conditions

We will start by focusing on the first 6 hours. At this point, the cleanroom is operating in nominal mode, with a vertical laminar airflow of 0.12 m/s. The time value of the tilts has been plotted in blue on each graph. The tilt X appears to stabilize following an exponential decay (black curve), with an amplitude of 98 nm RMS and a mean lifetime of $\boldsymbol{\tau}$ **= 40 minutes**. By definition, stabilization at 95% is reached at t = 3τ, i.e. after around two hours, from the instant when the settings are made (t = 0). This evolution seems to correspond to a mechanical stabilization of the bench or reference mirror holder.

Tilt Y, on the other hand, appears to be dominated by a periodic oscillation with a period of 2.5 hours and an amplitude of around 250 nm RMS. It is worth mentioning that such an oscillation also appears in the Tilt X data but with amplitude **4-5 times lower**. On Figure 62 are plotted vertical dashed lines (purple) to highlight the different scales between the tilts variations.

- "Reduced" LMA clean room conditions

Let us observe now the behavior of tilts after the regime change in the clean room. Unsurprisingly, both tilts undergo sharp variations (t = 6h), without reaching a new level of stabilization. It is difficult to explain the behavior of the tilts during the period when the cleanroom is changing regime, but we suspect a change of the thermal balance because of the change of the airflow. Moreover, we can see a correlation between the oscillations of tilt Y and the temperature measured in the cleanroom, which was measured and plotted in red on the lower graph in Figure 62. However, the temperature is regulated to within ± 0.1°C. Tilt Y is therefore highly sensitive to cleanroom conditions (temperature, pressure etc). Tilt X, on the other hand, admits also non-negligible variations of 300 nm PTV RMS after the cleanroom switches into reduced mode. These variations are, however, well below those of tilt Y, which is critically close to the maximum tolerance: **1250 nm RMS**, which corresponds to **0.5 mrad** in SHWFS coordinates (plotted in pink in Figure 62).

Conclusion on bench temporal stability

The long time measurements presented here has shown that the bench is very sensitive to external conditions. We have seen the very fine sensitivity of tilts to various factors. We have mentioned the air conditions in the cleanroom and the mechanical stabilization of the bench as the main factors. Numerous other temporal measurements were made on the bench, in other optical configurations, with other settings, and at other times. Our conclusions are then as follows:

- It is essential to wait at least two hours between any physical intervention on the bench and the beginning of any acquisition, to allow the (mechanical) stabilization of the bench and the surrounding air flow.
- No measurements should be carried out when the cleanroom is in reduced mode, because the tilts X and especially Y are particularly sensitive during this period.
- If any tilt exceeds the value of ± 0.5 mrad (SHWFS coordinates), the entire corresponding dataset is cancelled.

Despite all these precautions, the fact remains that tilt Y is difficult to stabilize, as it is not possible to completely eliminate the vertical airflow by, for example, completely covering it. Further strategies will be put in place to reduce the variability of tilt Y.

1.3. Reproducibility and repeatability tests

In this section, we present a series of tests designed to assess the bench's repeatability and reproducibility, and deduce possible errors linked to the bench itself, the acquisition software, the environment or the protocol used.

- **The repeatability** corresponds to the dispersion of results without changing bench adjustments. To measure it, we will repeat some measurements several times during each day, without tuning the bench in the meantime.
- **The reproducibility** is the global dispersion of the results including any bench re-settings in the same configuration. The reproducibility of the bench will be then evaluated by comparing the data from one day to another day.

To isolate the various sources of measurement error as easily as possible, we carried out only tests at 0° incidence, in P/P polarization, and only in the "green/IR" band, which excludes the 650-735 nm range. No adjustment was made to the monochromator, angle of incidence or polarizers during this period. In addition, we chose to increase the wavelength sampling to 10 nm instead of 1 nm, enabling us to perform a chromatic measurement over the visible band in around half an hour instead of 7 hours. In this way, measurements can be repeated many times. The aim here is to study the differences between measurements and not the chromatic variations of a single measurement, so increasing the sampling step is not a problem.

Repeatability

The aim is to highlight stability over one day, which can be correlated with the dispersion. We will use the dichroic and the reference mirror. We repeated measurements over three days. No bench adjustment is made during the whole day, except the reference mirror holder that is adjusted during its installation. We expect than only the cleanroom environment and the drift of the bench can generate dispersion in the results on a given day.

Each day, we start by setting up the dichroic mirror, then, after waiting a few hours, we make four identical chromatic $\mathbf{WFE}_{DC/ref}^{meas(i)}$ measurements, followed by a single static $\mathbf{WFE}_{DC}^{meas}(\boldsymbol{\lambda_{ref}})$ measurement. The labels of the acquisitions were introduced in Chapter 4, part 2.3. We then take the corresponding measurements on the reference mirror ($\mathbf{WFE}_{plan/ref}^{meas(j)}$ and $\mathbf{WFE}_{plan/ref}^{meas}$). The sequence over one day is then as follows:

$$\mathbf{WFE}_{DC/ref}^{meas(1)} \rightarrow \mathbf{WFE}_{DC/ref}^{meas(2)} \rightarrow \mathbf{WFE}_{DC/ref}^{meas(3)} \rightarrow \mathbf{WFE}_{DC/ref}^{meas(4)} \rightarrow \mathbf{WFE}_{DC}^{meas}(\boldsymbol{\lambda_{ref}}) \rightarrow$$
$$\rightarrow \mathbf{WFE}_{plan/ref}^{meas(1)} \rightarrow \mathbf{WFE}_{plan/ref}^{meas(2)} \rightarrow \mathbf{WFE}_{plan/ref}^{meas(3)} \rightarrow \mathbf{WFE}_{plan/ref}^{meas(4)} \rightarrow \mathbf{WFE}_{plan}^{meas}(\boldsymbol{\lambda_{ref}})$$

Next, we compute the chromatic WFE of the dichroic mirror in accordance with the standard procedure in Chapter 4, part 2.3, crossing the four $\mathbf{WFE}_{DC/ref}^{meas(i)}$ with the four $\mathbf{WFE}_{plan/ref}^{meas(j)}$. This gives 16 possible computed WFE combinations. Static measurements $\mathbf{WFE}_{DC}^{meas}(\boldsymbol{\lambda_{ref}})$ and $\mathbf{WFE}_{plan}^{meas}(\boldsymbol{\lambda_{ref}})$ are common to all 16 combinations.
Figure 63 (top) shows the results obtained on three different days, each represented by one color. Each day therefore includes 16 WFEs calculated. For clarity, we choose to represent the WFE projected on three Zernike modes: Z6, Z10, and Z12 where chromatic variations between the three days appear clearly.

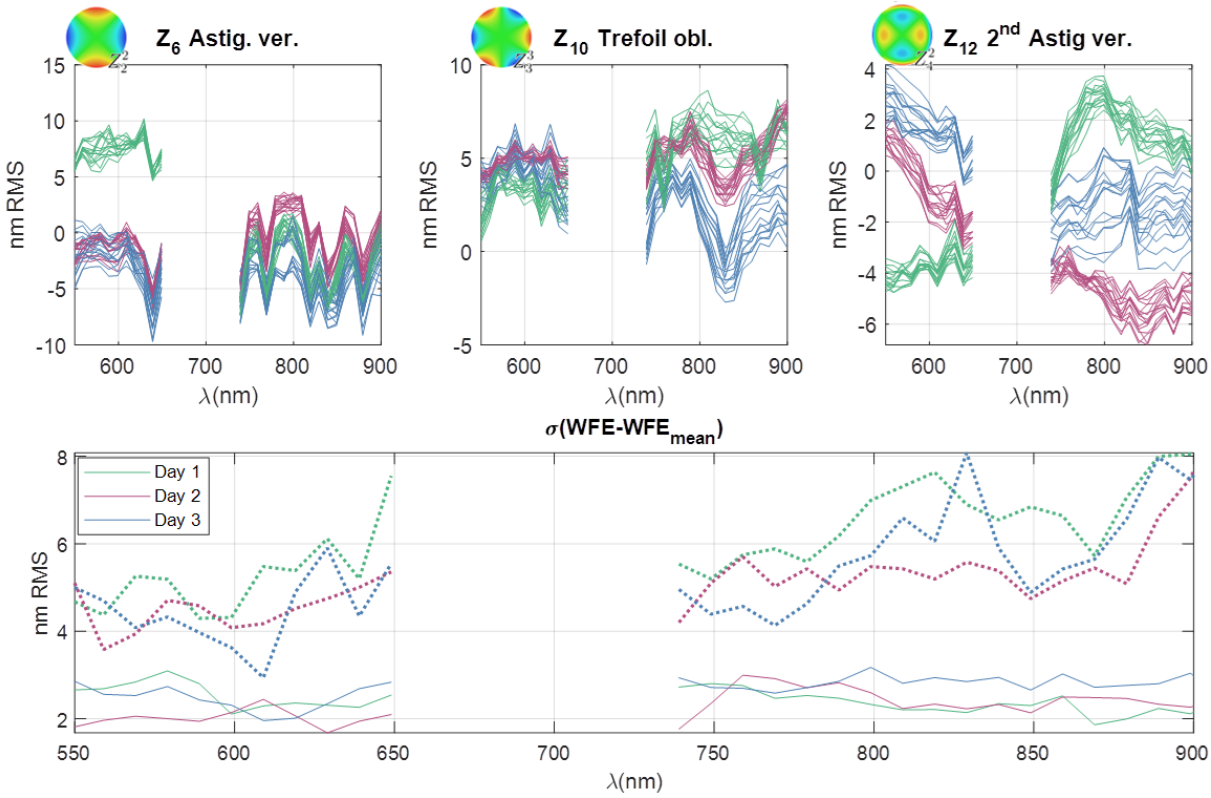

*Figure 63: (**Top**) Projection of measured WFE on few first Zernike polynomials. Data from 2023, September **18th**, **19th**, and **25th**, zero AOI, P/P polarization. For each day, 16 WFEs are computed from 4 chromatic measurements on DC and 4 others on plane mirror. (**Down**) Standard deviation of these 3*16 WFE datasets with respect to the average "daily" WFE (Dotted lines = tilts included)*

The standard deviation within each daily dataset with respect to its average WFE does not show any relevant feature (Figure 63, down). Repeatability appears to be good for the three Zernike modes. Figure 63 (down) shows the standard deviation from the mean WFE for each wavelength on each day. **The repeatability (excluding tilts) is then between 2 and 3 nm RMS**, which is quite encouraging. This proves that, over one day, the bench did not drift significantly. This result is supported by the low standard deviation within each daily dataset (Figure 63, down)

- Reproducibility

The reproducibility of the bench can be evaluated by comparing the data from one day to the other days (Figure 63, top). Each day, the bench is set up in the same configuration as the previous day. The results shown on the standard deviation of the WFE for the 3 days (Figure 63, down) are quite consistent between each other and can suggest that the measurements are pretty reproducible. However, the variations of Z6, Z10 and Z12 (Figure 63, top) seem to be day-dependent. Several nanometers of difference appear on almost all the Zernike modes (not only the three ones showed here).

The stability of the bench over one day does not seem to be the cause of these glitches, for two reasons. Firstly, this stability would have an impact on the repeatability of one-day measurements, and we have seen that the bench's repeatability is much lower than the variations observed here. Secondly, the stability of the bench would have an impact on the static measurements, which consist of an

acquisition at λ_{ref} = 594.1 nm averaged over half an hour. If these static measurements were affected by the bench stability, this would result in achromatic deviations on all Zernike modes from one day to the next, therefore constant whatever λ. However, the differences are clearly chromatic, as shown on mode Z12.

Our hypothesis is that the results are much more sensitive to bench settings than expected. Depending on the optical alignments that are made, a chromatic bias appears and impacts the measurement reproducibility. In the following section, we will investigate this hypothesis by studying the effect of a controlled misalignment.

Tests with controlled misalignment

In this series of measurements, we try to isolate the cause of the (chromatic) differences in the results when the bench is reset. The procedure is as follows: we install the dichroic mirror on the bench and align the M2 mirror following the usual procedure described in Chapter 4, part 2.3. We then carry out 6 chromatic measurements on the dichroic mirror $\mathbf{WFE}_{DC/ref}^{meas(i)}$, introducing deliberately horizontal tilt by slightly detuning the dichroic/plane mirror rotation stage (see Figure 49) for each measurement. In addition, **the plane mirror data and static measurements data are identical for the 6 WFEs calculated**. Thus, the differences between the results can therefore only come from $\mathbf{WFE}_{DC/ref}^{meas(i)}$.

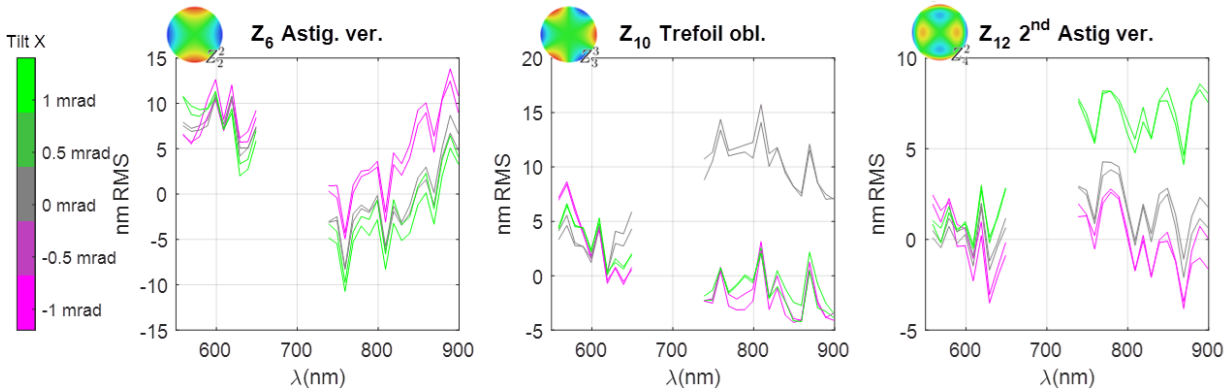

Figure 64: Zernike projection of 6 WFE computed with M2 mirror tuning error in X tilt.

Figure 64 shows the results of this series of 6 measurements, for the same Zernike modes used again as examples. The color of each curve corresponds to the tilt on the dichroic mirror induced by the M2 mirror. According to the procedure, the tilt X setting shall be tuned to 0 ± 0.5 mrad. Here, a tilt of approx. 1.2 mrad is added for two acquisitions (green) and approx. -1.2 mrad for two others (pink). Since curves of the same tilt value (same color) are superimposed, and variations between curves of different tilts are highly chromatic, it becomes obvious that a change in the tilt causes a variation in results.

By investigating the optical components that could be sensitive to a beam pointing variation, the suspicions were inclining towards **the output polarizer**, which is located in the diagnostic block (see Chapter 4, Figure 53). Indeed, microbubbles were detected inside the polarizer that has a laminated structure. The beam propagation through these bubbles causes chromatic phase effects. Depending on the tilt (even within the tolerances of $\pm$ 0.5 mrad), the optical path varies slightly through the polarizer and the bubbles pattern sensed by the beam is then different. Since the optical alignment is not strictly identical for the *Euclid* dichroic mirror and the reference flat, the effect of the output polarizer in the WFE is not canceled, and that can give rise to a significant chromatic contribution. On Figure 65 we compare intensity measurements on dichroic mirror for λ = 800 nm, normal incidence, before and

after removing the output polarizer. The microbubbles create the circular “granules” that appear on the left map (some of which are marked with yellow arrows).

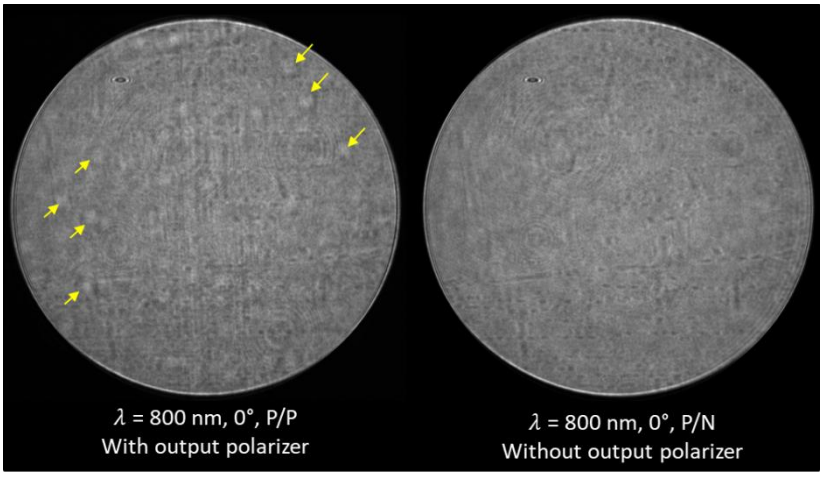

Figure 65: Comparison of intensity measurements on dichroic mirror at 0° in incidence, with (left) and without (right) output polarizer.

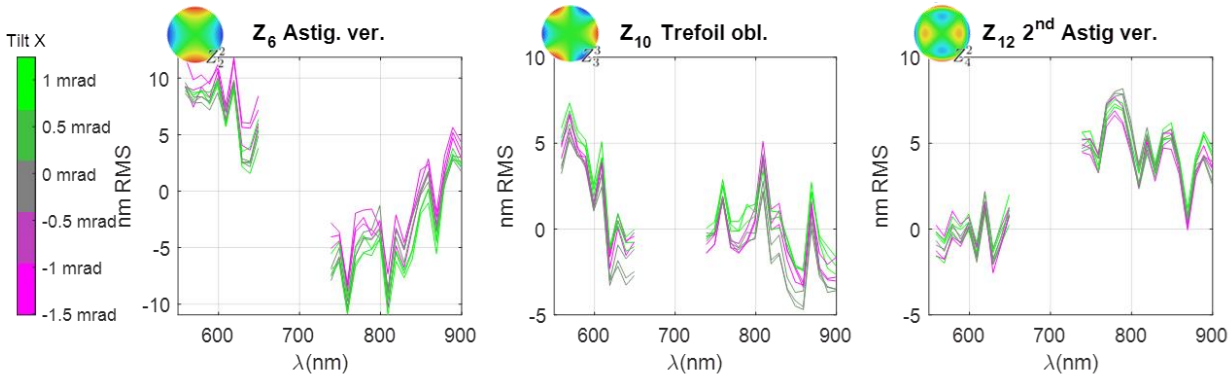

Figure 66: Zernike projection of 9 WFE computed with M2 mirror tuning error in X Tilt, after removing the output polarizer.

Consequently, the output polarizer was removed from OBSERVE bench, as its use is not crucial for the thesis measurement campaign. Figure 66 shows 9 acquisitions following the same protocol as in Figure 64, but without the output polarizer. This time, measurement reproducibility is greatly improved.

This study has helped us to understand the sources of chromatic dispersion in the OBSERVE results. It appears that the bench’s drift over a single day is not very significant based on measurement repeatability. However, measurement reproducibility was affected by the output polarizer, causing the results to be unusually sensitive to bench tuning.

These led to changes on the bench itself, with for this campaign, the removal of the output polarizer. This has led also to a redefinition of the experimental protocol. At the time of writing (February 2024), we estimate that the bench has **reproducibility of 6 nm RMS without tilts**, based on a few data sets that could be compared.

1.4. Measurement sequence

After this campaign of commissioning and verification, we present now the final protocol for the acquisition of one WFE dataset on the visible band, without the output polarizer and with new adjustments on the bench. This new protocol takes 2 days, and allows four acquisitions: $\mathbf{WFE}_{DC/ref}^{meas}, \mathbf{WFE}_{DC}^{meas}(\lambda_{ref}), \mathbf{WFE}_{plan/ref}^{meas}, \mathbf{WFE}_{plan}^{meas}(\lambda_{ref})$.

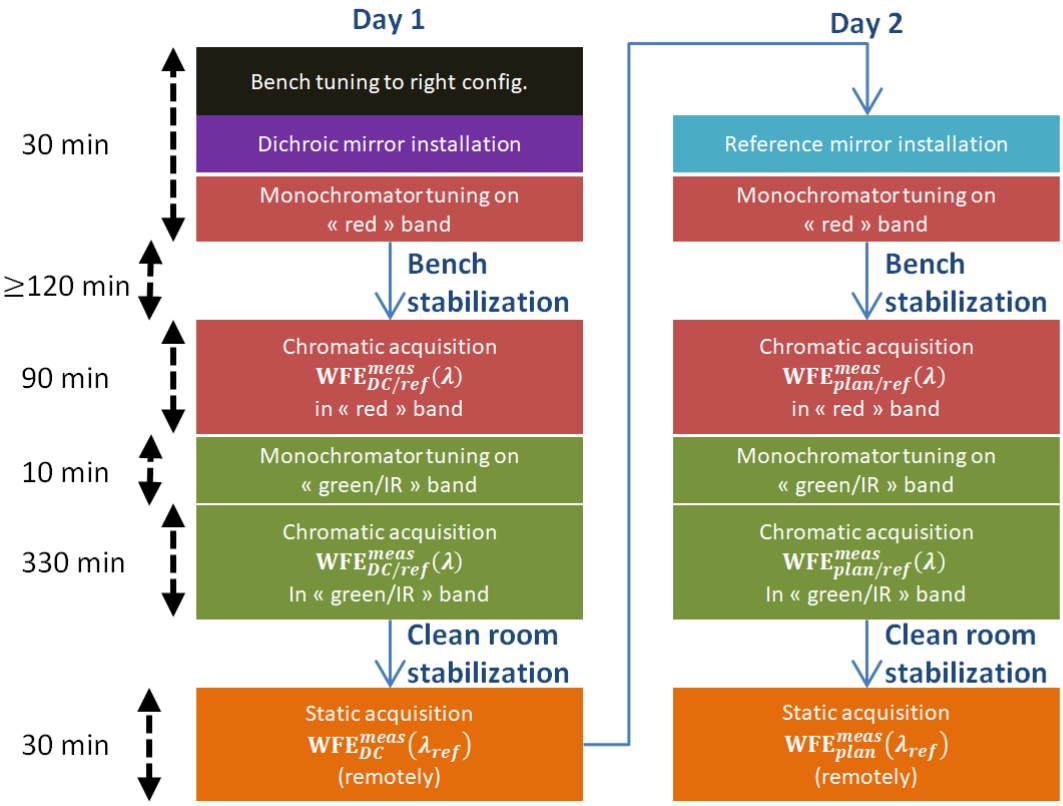

Figure 67: Sequence for obtaining a full WFE dataset on Visible Band at one AOI and polarization.

Figure 67 shows the complete sequence for obtaining a WFE dataset of the same angle of incidence and polarization state, established from conclusions in part 1.2. The bench is set up in the morning (black block), and then the dichroic mirror is installed (purple block). After stabilizing for at least two hours, chromatic measurement starts in the red band (650 to 735 nm), then in the green/infrared band (rest of the visible band). The static measurement starts in the evening, when the cleanroom is empty, and the air flow over the bench is stable. The next day, without changing the bench settings, the same operation is done with the reference mirror. In this way, it takes two days to obtain a dataset for the whole visible band.

2. OBSERVE BENCH VALIDATION

In this section, we present a set of validation tests to estimate the overall accuracy of the OBSERVE bench. To this end, we propose to use a dummy reference mirror. This mirror is metallic, and therefore induces theoretically an achromatic WFE. Its WFE was measured at λ_{zygo} = 1064 nm by the Zygo interferometer available at LMA. This facility has an accuracy of 0.2 nm RMS that offers a very precise knowledge of the WFE of the dummy mirror. We acquired then different datasets with this mirror from OBSERVE in several optical configurations

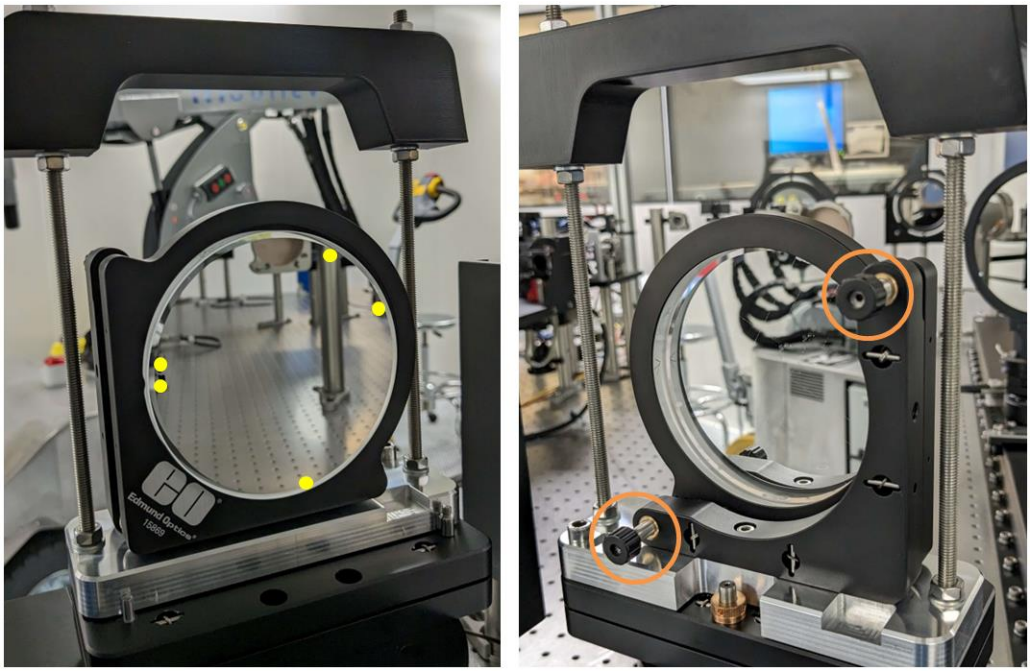

*Figure 68: Dummy mirror mounted in its holder. (**Left**) Front face, with five markers (yellow). (**Right**) Rear face, with holder adjustment screws circled in orange.*

The mirror is installed in a dedicated holder, adapted to its 100 mm diameter (i.e. smaller than that of the dichroic mirror). Figure 68 shows the dummy mirror in its holder. On the front of the mirror (left), markers have been placed, highlighted in yellow. These are used to check the orientation of the maps obtained with the OBSERVE bench and the interferometric bench. On the rear face (right) are the two screws of the Edmund Optics mount, used for fine alignment of the mirror. The dummy mirror holder is attached and adjusted in the same way as the dichroic mirror (see Chapter 4, part 2.3).

2.1. Measurements on Dummy Mirror

We carried out measurements on this mirror, at the beginning of February 2024, on the 549-929 nm wavelength range, with two AoI and S, P polarizations. The protocol used to perform these measurements is identical to that shown in Figure 67.

WFE calculated from Zygo interferometric map

The LMA's Zygo bench was already used to characterize the WFE of the Zeiss reference mirror (see Chapter 4, part 2.3). Figure 69 shows the interferometric measurement of Dummy mirror WFE on 85 mm in diameter, with black dots indicating markers positions. The WFE is presented according to the orientation as achieved with the OBSERVE bench.

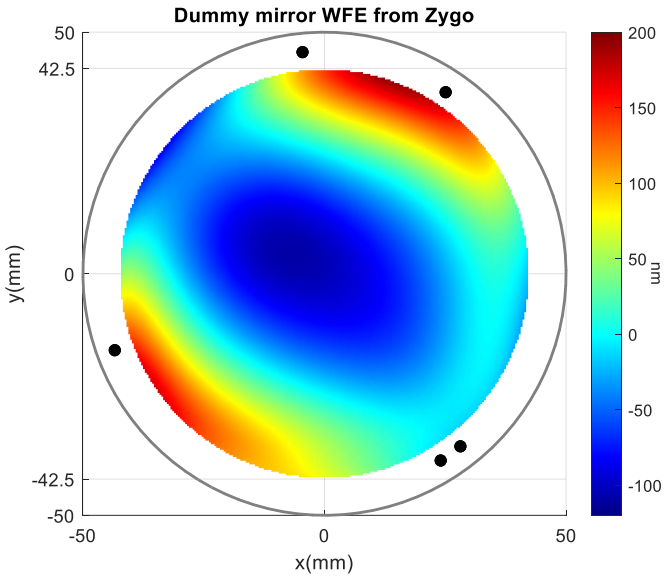

Figure 69: Dummy mirror WFE measured by the Zygo interferometer. Gray circle corresponds to the actual diameter of the mirror.

Comparison with OBSERVE measurements in the Visible Band

A WFE dataset was produced with the dummy mirror. To compare the data between Zygo and OBSERVE, we project the maps onto 55 Zernike modes and display the first 16 in Figure 70 (without tilts, which are not comparable for both instruments). At the top of Figure 70 are displayed the chromatic dispersion of the **difference between OBSERVE and Zygo measurements** at normal incidence. The median value in a Whisker plot represents then the median difference between OBSERVE WFE and Zygo WFE (for a given Zernike coefficient, in S and P polarization).

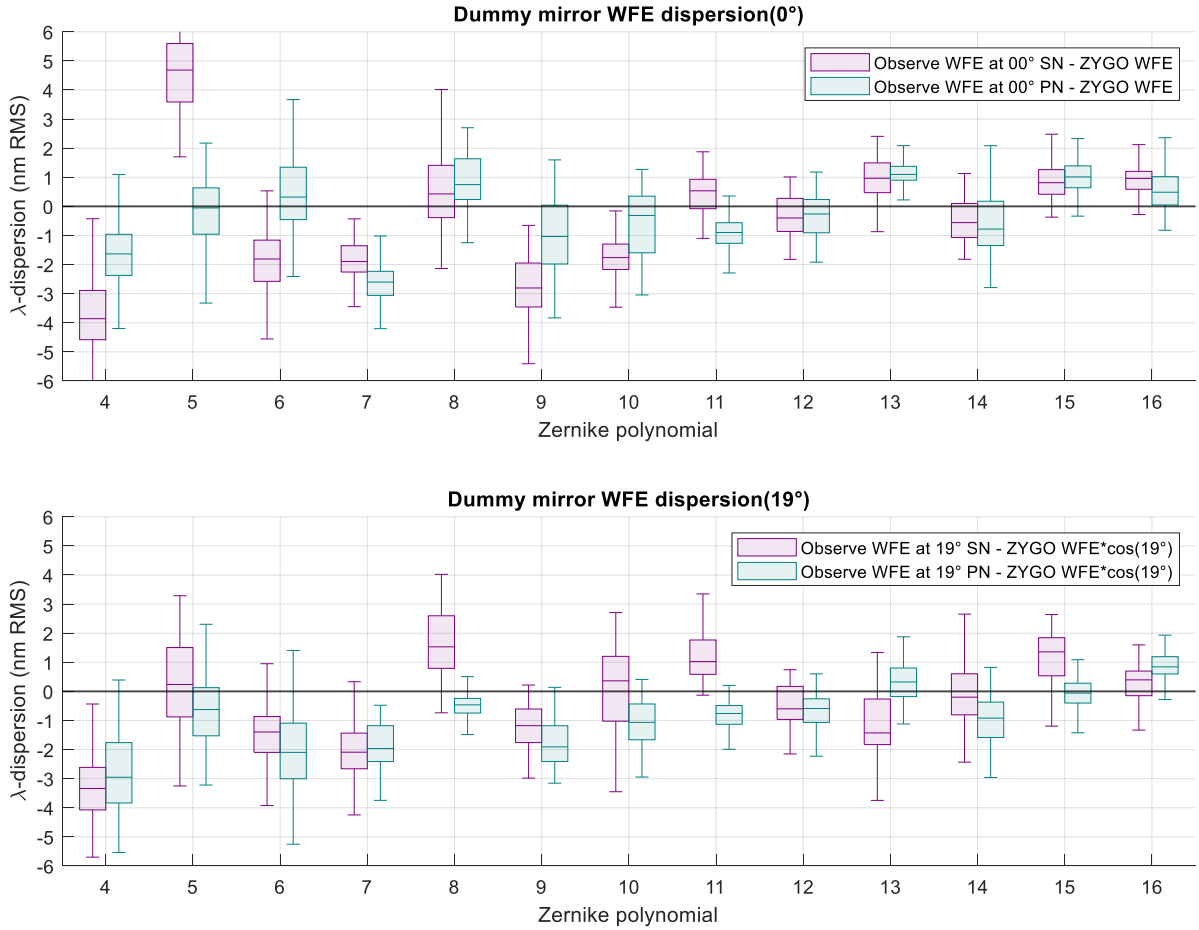

*Figure 70: Chromatic dispersion of OBSERVE WFE between 549 and 939 nm **with respect to Zygo WFE** represented with colored Whisker plots for each Zernike coefficient. The boxes edges indicate 25% (bottom) and 75% (top) quantiles.*

As the Dummy mirror is achromatic, a perfect measurement should result in zero dispersion for each Zernike, with OBSERVE and Zygo results superimposed. With the exception of tilts, we see that the dispersion of OBSERVE measurements is very low, as shown in Figure 70. First-order aberrations ($3 < Z < 10$) are globally within confidence intervals [25%; 75%] 2 nm wide at maximum. For higher-order aberrations, this dispersion is often less than 1 nm RMS. These results are in line with the conclusions of section 1.3, where we estimated measurement repeatability at 3 nm RMS for the dichroic mirror. Indeed, as the dummy mirror is achromatic, measuring its WFE over 350 wavelengths (550 to 900 nm, every 1 nm) is equivalent to repeating the same measurement 350 times. However, there is a gap between the "Zygo" Zernike coefficients and the median of the "OBSERVE" Zernike coefficients. On Z4 and Z5, for example, this deviation exceeds 4 nm RMS at 0°, S/N. We observe a similar dispersion for measurements at 19° of incidence, at the bottom of Figure 70. Here, the WFE obtained with Zygo is corrected by a factor $cos(19°)$ to take into account the obliquity of the measurements. In the following part, we compute the WFE residual corresponding to the achromatic gap for each case.

2.2. Achromatic bias

The difference between the Zygo measurements and the median of the OBSERVE measurements on each Zernike is used to compute the residual map for each dataset, in Figure 71. In each case, the achromatic residual is around 30 nm PTV. The RMS of these maps is between 4.7 nm RMS (P/N, 00°) and 8.11 nm RMS (S/N, 00°).

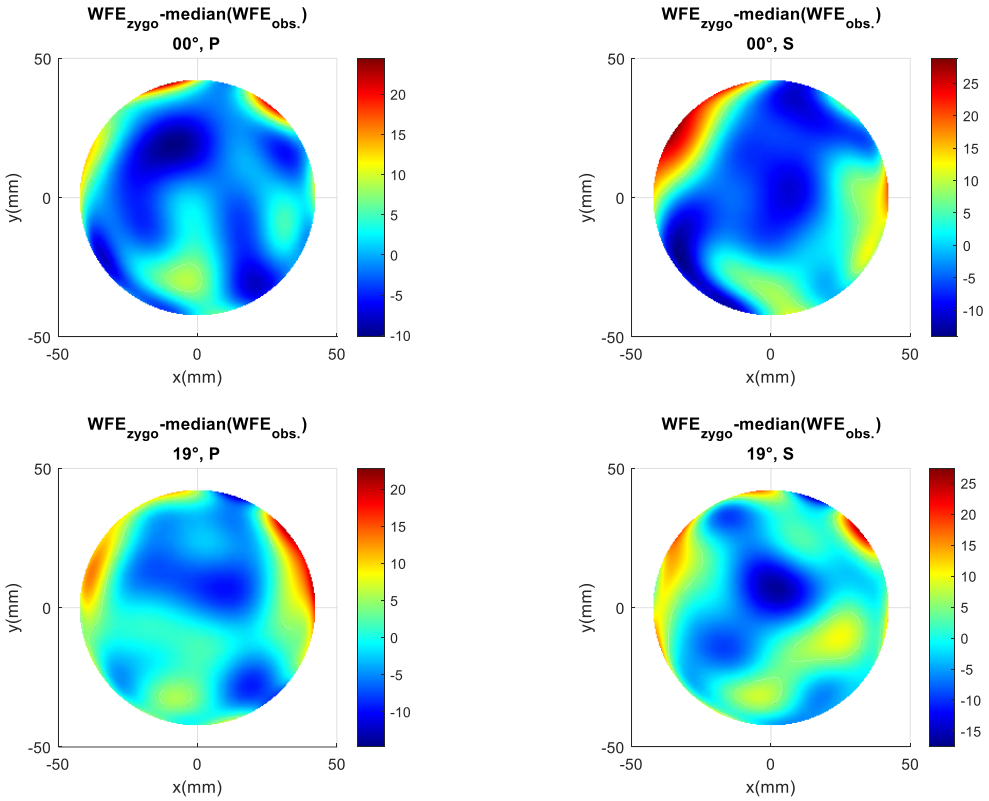

Figure 71: Residual maps (in nm) on Dummy mirror between $WFE * cos(AoI)$ computed from Zygo interferometer, and the median map obtained from OBSERVE at four bench optical configurations.

This residual may be due to a number of factors, for example:

- The **reproducibility** of the OBSERVE bench, which is of the same order of magnitude.
- The use of a different mirror and holder than the dichroic mirror, which can lead to slight unanticipated offsets in data processing.
- An actual achromatic bias induced by the bench.

After this thesis, further analysis will enable us to assess the actual achromatic bias induced by the bench (at each incidence and polarization) and, if needed, the latter will eventually be subtracted from all the measurements obtained with OBSERVE.

3. CONCLUSION

In this chapter, we present the initial findings from the bench testing. To commission it, we conducted stability, repeatability, and reproducibility tests to establish the optimal procedure for using the OBSERVE bench. This procedure involves two working days to gather a complete dataset across the visible spectrum. Each dataset comprises two acquisitions (static and chromatic) for both the dichroic and reference mirrors. We have also enhanced the bench's accuracy, including the resolution of issues with the **output polarizer,** which had to be removed from the bench.

Measurements on the Dummy Mirror were used to estimate the bench's current performance. The bench was used in the best conditions currently possible at the LMA, following the protocol defined during the commissioning phase. As the Dummy Mirror is achromatic and the Zygo interferometer is repeatable to 0.2 nm RMS, the only variations between the two measurements can only come from the bench. These measurements showed high repeatability (**3 nm RMS**), consistent with our initial observations during commissioning.

However, the current reproducibility of OBSERVE is approximately **6-7 nm RMS**. According to Figure 71, the remaining residual seems to be achromatic and random; suggesting that averaging multiple measurements could reduce this residual which will naturally increase the time needed to obtain a data set.

4. REFERENCES

69 V. Lakshminarayanan, A. Fleck, "Zernike polynomials: a guide" (2011), Journal of Modern Optics, 58:18, 1678, DOI: 10.1080/09500340.2011.633763

70 F. Zernike, "Beugungstheorie des schneidenver-fahrens und seiner verbesserten form, der phasenkontrastmethode", Physica, Vol. 1, Issues 7–12, 1934, pp. 689-704, https://doi.org/10.1016/S0031-8914(34)80259-5

71 J. H. Castillo, R. Hanna, E. Berkowitz, B. Tiosano, "Wavefront Analysis for Keratoconus." Int J Kerat Ect Cor Dis 2014;3(2):76-83

72 R.J. Noll, "Zernike polynomials and atmospheric turbulence", J. Opt. Soc. Am., Vol. 66, No. 3, March 1976

Chapter 6

Dichroic coating modeling

In this chapter, we will describe a parametric model of the dichroic mirror, adjusted on the basis of measurements made on the Flight Spare mirror. The parameters of this model should enable a realistic description of the mirror's physical properties (layer thickness figure error) to predict the resulting chromatic properties, under optical flight conditions. This is different from the parametric model developed by the *Euclid consortium* and presented in Chapter 2 that is based on the *Euclid* telescope to take into account spatial, chromatic and temporal variations coming from the sensors and the optical path of the telescope.

The first method to be presented here was published in **Optic Express, September 2023** [73], and is applicable to any dielectric stack. This chapter takes up the definitions, formalism and conclusions presented in that article, but the details of the mathematical development will not be rewritten here. First, we will look at the methodology of this analytical method, i.e. the assumptions and mathematical formalism on which it is based. We will then introduce the general principles of thin-film theory, to understand how a WFE can be calculated from a stack with thickness errors. In a second part, we will describe the key equations of the analytical method, which allow WFE measurements to be used to identify thickness variations in dichroic mirror layers. In sections 3 and 4, the method will be tested in different cases, concluding with sensitivity analysis to random errors.
The results obtained in this section justify the development of a second method, which has a different philosophy, albeit based on the same mathematical development. This new method, based on iterative optimization, was initiated to overcome some shortcomings of the analytical method. Concrete application to OBSERVE data will then be made, in the next chapter.

1. METHODOLOGY

This first section presents the methodology used to build the analytical method. We begin by presenting the basic idea, which is inspired by knowledge of the manufacturing process for thin-film stacks, and in particular the *Euclid* dichroic mirror. Next, we detail the physics of thin films, which enables us to compute the optical properties of the stack, and on which the mathematical development of the method is based. Finally, we will formalize the concept of WFE based on properties derived from thin films physics.

1.1. The analytical method strategy

We present here an analytic method that allows the identification of the chromatic properties of the dichroic mirror or any other stack, from a reduced number of information, and realistic simplifying assumptions. This approach allows the stack reconstruction, including the entire layer's Thickness Figure Error (TFE) which quantifies the spatial non uniformity of the stack. With such a reconstruction, it is possible to regenerate the optical properties (including the chromatic variations of the wavefront) of the stack, for any illumination conditions.

Manufacturing process inspiration

Physical Vapor Deposition (PVD) Technology [74] is widely used to create high performance coating. The latter is available in several vacuum deposition techniques generally based on plasma sputtering or controlled evaporation, with the possible assistance of an ion beam. The sputtering/evaporation process leads to a thin layer deposited on a substrate and whose thickness must be precisely controlled. In first approximation, a spatial non-uniformity in the film deposition leads to a TFE whose amplitude should be only thickness-dependent. Nevertheless, that remains valid for only one given material. The layer growth depends on the plume of sputtered/evaporated materials that is specific to the material and/or the plasma parameters. The thickness uniformity is then specific to the material as well.

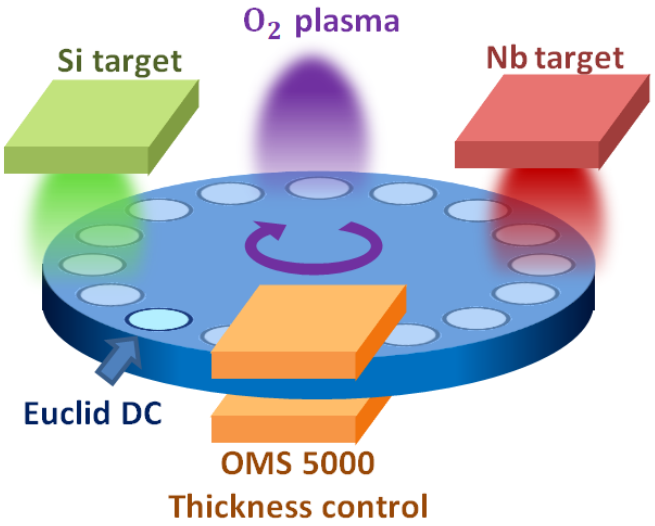

Figure 72: Schematic representation of PARMS process applied to Euclid dichroic with OBJ's Helios machine [75].

Euclid's dichroic mirror was manufactured [57, 76] by OBJ using the HELIOS800 deposition machine [76] with the PARMS (Plasma Assisted Reaction Magnetron Sputtering) process [76] and the OMS 5000 active thickness control. The dichroic mirror substrate is placed on a turntable in a vacuum chamber. The simplified deposition process is illustrated in Figure 72.

The principle [76] to create a SiO_2 layer is as follows: Argon (Ar) plasma is generated into the chamber and confined by a magnetic field near the target. The ionized Ar particles reach the target and pull-out Si particles. These particles are therefore deposited on mirror substrate surface during its passage under the Si target. A flow of pure dioxygen O_2 creates a non-stoichiometric SiO_x layer on the substrate. Still in the same rotation, the thin SiO_x layer is then oxidized using a reactive radio-frequency (RF) O_2 plasma source, in order to fill the remaining free Si-O bonds. The result is then a stoichiometric SiO_2 layer of a few Å thick.

This operation is repeated at each rotation, until the layer grows up to the required thickness. Next, the same process is repeated, this time with a pure niobium (Nb) target. Figure 73 illustrates how the stack thus created will grow, layer by layer, as will the TFE induced at each layer, proportional to thickness.

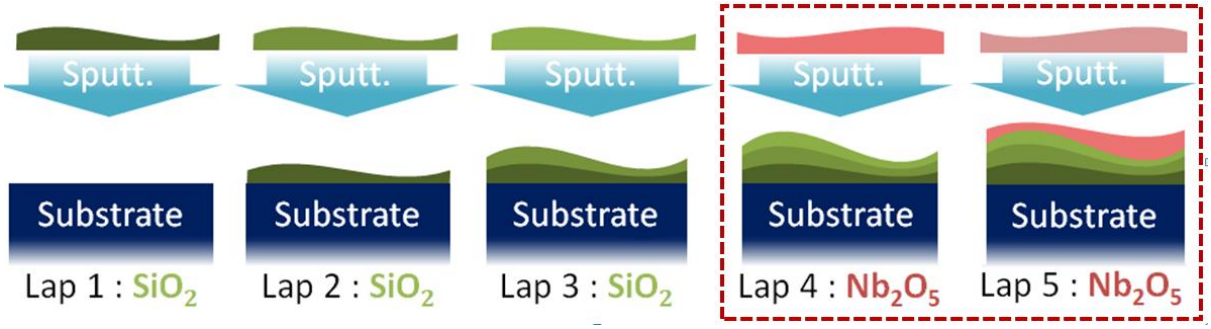

Figure 73: Illustration of the double-SFE profile (material-dependent) assumption. The non-uniformity profile is different for each sputter [75].

The approach proposed here to build the model is to consider a relative non-uniformity profile identical for all layers made of each material within a bi-material (H, L) stack, where the low

refractive index is denoted “L” and the high refractive index is denoted “H”. In the case of the *Euclid* dichroic mirror, L corresponds to SiO_2 and H corresponds to Nb_2O_5.

Required data

The analytical method (Opt. Express [73]) has been developed in such a way that it can be applied to any stack of thin layers, and not only the *Euclid* dichroic mirror. To use it, it is necessary to know the theoretical thicknesses of the layers stack, as well as their refractive indexes (which correspond to the optical formula). This information can be difficult to obtain, as it may constitute the manufacturer’s intellectual property and know-how. In the case of the dichroic mirror, OBJ has agreed to share this information with ESA and LMA **under a non-disclosure agreement**.

1.2. Thin films theory

In this section, we will present the key equations of thin-film theory, which enable us to calculate the reflectance and phase in reflection of a stack of thin films.

Each layer, denoted, “*j*”, has a thickness “d_j” and a complex refractive index “n_j” (see Figure 74). The stack is illuminated at a wavelength λ and at an angle of incidence of γ. The polarization state is also determined. The thin films theory [58] gives for each layer its phase shift δ_j and admittance q_j as follows:

$$\delta_j(\lambda, \gamma_j, d_j, n_j) = \frac{2\pi}{\lambda} d_j n_j \cos(\gamma_j) \tag{29}$$

$$q_j(\lambda, \gamma_j, n_j) = \begin{cases} n_j \cos(\gamma_j)^1, \mathrm{S-polarization\ state} \\ n_j \cos(\gamma_j)^{-1}, \mathrm{P-polarization\ state} \end{cases} \tag{30}$$

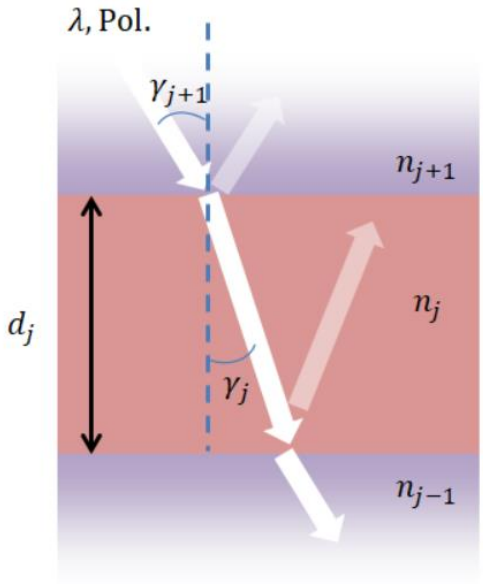

Figure 74: Illustration of a layer within a stack, crossed by an incident electromagnetic beam [73].

The propagation angle γ_j through layer "*j*" is calculated from γ according to the Snell-Descartes relation:

$$n_j \sin(\gamma_j) = n_{\mathrm{a}} \sin(\gamma) \tag{31}$$

With n_a the refractive index of the external media, often air or vacuum. The characteristic matrix M_j, expressed with Eq. 29, 30, and 31 establish the link between the input and output electromagnetic fields through the layer:

$$M_j(\lambda, \gamma_j) = \begin{bmatrix} \cos(\delta_j) & \frac{i}{q_j}\sin(\delta_j) \\ iq_j \sin(\delta_j) & \cos(\delta_j) \end{bmatrix} \tag{32}$$

The overall stack characteristic matrix M_c, making thus the link between the input and output electromagnetic fields through the stack, is then the cumulative product, from the top layer "*N*" to the bottom layer "1".

$$M_c(\lambda, \gamma) = \prod_{j=N}^{1} M_j(\lambda, \gamma) = \begin{bmatrix} m_{11} & m_{12} \\ m_{21} & m_{22} \end{bmatrix} \tag{33}$$

In that follows, the characteristic matrix will be simply denoted $M_c(\lambda)$. All the presented mathematical approach in this document remain valid whatever the polarization state and the incidence. This matrix $M_c(\lambda)$ takes into account the stack material properties and the illumination conditions, it thus leads to amplitude transmittance "$t(\lambda)$" and reflectance "$r(\lambda)$":

$$t(\lambda) = \frac{2q_a}{q_a m_{11} + q_s m_{22} + q_a q_s m_{12} + m_{21}} \tag{34}$$

$$r(\lambda) = \frac{q_a m_{11} - q_s m_{22} + q_a q_s m_{12} - m_{21}}{q_a m_{11} + q_s m_{22} + q_a q_s m_{12} + m_{21}} \tag{35}$$

The terms $q_{\mathrm{a}}(\lambda)$ and $q_{\mathrm{s}}(\lambda)$ are the admittances of the ambient media "a" and substrate "s" respectively. The energy reflectance $R(\lambda)$ and the phase shift $\varphi_R(\lambda)$ between incident and reflected electromagnetic fields are then:

$$R(\lambda) = |r|^2 \tag{36}$$

$$\varphi_R(\lambda) = \arg(r) \tag{37}$$

1.3. Wavefront and surface errors from coating properties

The quantity SFE is the coating's surface non-uniformity error. The coating "nominal" thickness is denoted D_{nom} (see Figure 75 for illustration). The actual total thickness $D(x, y)$ of the coating is then:

$$D(x, y) = D_{\mathrm{nom}} + \mathrm{SFE}(x, y) \tag{38}$$

The small air gap induced by the SFE on the mirror leads to a small phase difference after reflection. This phase shift corresponds then to a WFE in reflection, equivalent to a round trip through the air gap and it depends on the angle of incidence γ:

$$\mathrm{WFE}_{\mathrm{air}}(x, y, \lambda, \gamma) = 2\, n_a \cos(\gamma)\, \mathrm{SFE}(x, y) \tag{39}$$

In addition, local variations in the thickness of the coating layers lead to a variation in the phase shift in reflection. Indeed, φ_R depend on the M_c terms, which depend themselves on the layers thicknesses at position (x, y). The resulting WFE related to the coating optical properties is denoted as WFE_c:

$$\mathrm{WFE}_{\mathrm{c}}(x, y, \lambda) = \frac{\lambda}{2\pi}\left[\varphi_R(x, y, \lambda) - \varphi_{R,\mathrm{nom}}(\lambda)\right] \tag{40}$$

Here, $\varphi_{R,nom}(\lambda)$ is the phase shift induced by the nominal (i.e. theoretical) layers thicknesses. In what follows, the γ-dependence of WFE is implicit. Still illustrated in Figure 75, the resulting total WFE is then:

$$\mathrm{WFE}(x,y,\lambda) = \mathrm{WFE}_{\mathrm{air}}(x,y,\lambda) + \mathrm{WFE}_{\mathrm{c}}(x,y,\lambda) \tag{41}$$

Furthermore, SFE corresponds to the sum of the whole TFE_j. The actual thickness of each layer is then expressed with:

$$d_j(x,y) = d_{j,nom} + \mathrm{TFE}_j(x,y) \tag{42}$$

The total WFE depends then on the value of each TFE_j:

$$\mathrm{WFE}(x,y,\lambda) \equiv \mathrm{WFE}(\mathrm{TFE}_1, \mathrm{TFE}_2, \ldots \mathrm{TFE}_{\mathrm{N}}, \lambda) \tag{43}$$

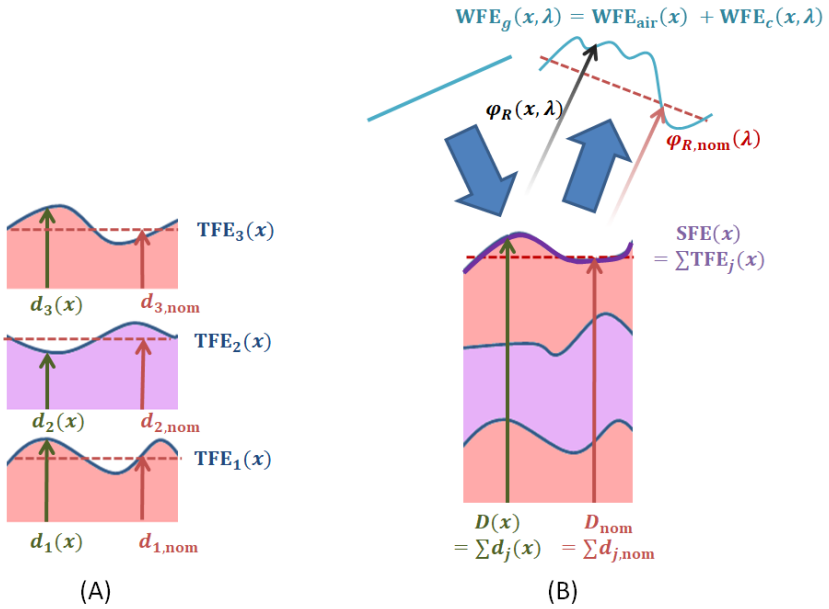

Figure 75: (A) Illustration of three layers having their own TFE (B) The coating is the stack of these layers and its SFE is the sum of the layers TFEs [73].

2. MATHEMATICAL DESCRIPTION OF ANALYTICAL METHOD

In this section, we will derive from realistic mathematical assumptions, the identification of each TFE from sample WFE in a controlled environment. The knowledge of these TFEs enables the prediction of the WFE for any illumination conditions. We will start by detailing the method approach, in which TFEs follow a particular distribution. Next, the mathematical and physical assumptions will be listed. Thanks to these assumptions, a linear relationship between WFE and SFE will be obtained.

2.1. Approach of the bi-SFE method

The approach proposed here is to consider a relative non-uniformity profile identical for all layers made of each material within a common bi-material (L, H) stack. For any "*j*" layer made of L material, the ratio $\mathrm{TFE}_j/d_{j,nom}$ is constant, similarly for H-layers. The resulting TFE_j for each layer will generate two different SFEs, one per material. The Figure 76 illustrates the principle of splitting into the contributions of both materials. As a result, these two quantities are sufficient to determine the whole stack geometry.

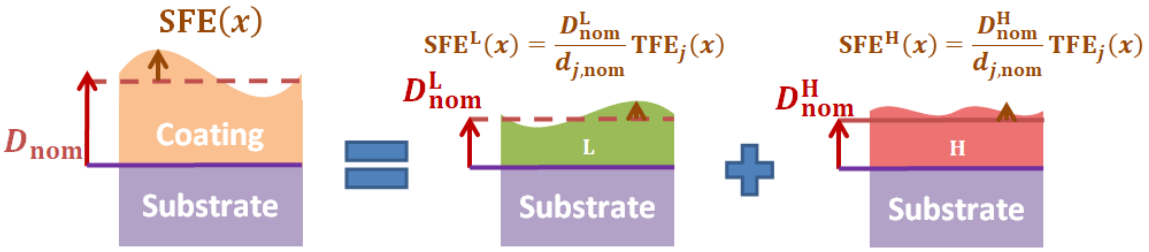

Figure 76: Illustration of the coating splitting into two materials (L, H) contributions [73].

The objective of the method is to get $\mathrm{WFE}_{meas}(x,y,\lambda)$, that is a measurable quantity, directly expressed with the sought $\mathrm{SFE}^{\mathrm{L}}(x,y)$ and $\mathrm{SFE}^{\mathrm{H}}(x,y)$ that are the measurands. Such an expression involves a linearization of the chromatic and spatial dependence of $\mathrm{WFE}_{meas}(x,y,\lambda)$, according to the L and H contributions.

We will then consider a thin-film stack with an even number of layers and the first layer, closest to the substrate, has index n_{H}. The generalization of the following developments would be straightforward. For each layer, the TFE can be expressed in function of two scale factors, $\alpha(x,y)$ for L-layers, and $\beta(x,y)$ for H-layers given by:

$$\frac{\mathrm{TFE}_j(x,y)}{d_{j,\mathrm{nom}}} = \begin{cases} \alpha(x,y) - 1, j \text{ even} \\ \beta(x,y) - 1, j \text{ odd} \end{cases} \tag{44}$$

As the non-uniformities amplitudes are thickness-dependent within each material, the equivalent $\mathrm{SFE}^{\mathrm{L}}$ $^{(\mathrm{H})}$ for L (H) layers only is expressed by:

$$\frac{\mathrm{SFE}^{\mathrm{L(H)}}(x,y)}{D_{\mathrm{nom}}^{\mathrm{L(H)}}} = \frac{\mathrm{TFE}_j(x,y)}{d_{j,\mathrm{nom}}} \tag{45}$$

With $D_{nom}^{\mathrm{L(H)}}$ is the total theoretical thickness of L (H) material.

2.2. Mathematical and physical hypothesis

In what follows, the thickness variations are considered very small. Then, for the layer "*j*", with nominal thickness $d_{j,nom}$:

$$d_j(x,y)/d_{j,\text{nom}} = \begin{cases} \alpha(x,y) \approx 1, j \text{ even} \\ \beta(x,y) \approx 1, j \text{ odd} \end{cases} \forall\, x,y$$

The deviations α and β being extremely close to 1, the following mathematical assumptions are then considered for the whole development:

Factors with power: $(1-\alpha)^n = 0 \;= 0 \;\forall\, n \in \mathbb{N}_{>1}$

Product of factors: $(1-\alpha)^{n_1}(1-\beta)^{n_2} = 0 \;\forall\, n_1, n_2 \in \mathbb{N}^*_{\geq 1}$

Trigonometric functions: $\cos[(1-\alpha)z] = 1;\ \sin[(1-\alpha)z] = (1-\alpha)z, \forall z \in \mathbb{R}$

The same considerations apply for β. All the mathematical approach is valid for any polarization and angle of incidence without restriction. In addition, chromatic dependence of refractive indices is here neglected.

2.3. Coating TFEs retrieval from sample WFE

To find the value of $\text{SFE}^{\text{L}}(x,y)$ and $\text{SFE}^{\text{H}}(x,y)$, we propose to set a linear system linking the two SFEs with two sample WFEs, each at two wavelengths.

To obtain such a system, we need to linearize the optical parameters that were introduced in section 1.2, as functions of the thickness deviations $\alpha(x,y)$ for the L layers and $\beta(x,y)$ for the H layers. The first step is to linearize the stack characteristic matrix. Full details of the calculations are available in open access [73].

The **characteristic matrix of the stack** "with thickness deviations", denoted M'_c, can be expressed from α, β, the matrix "without deviations" M_c and two chromatic quantities A_M and B_M :

$$M'_c(x,y,\lambda) = M_c(\lambda) + [\alpha(x,y) - 1]A_M(\lambda) + [\beta(x,y) - 1]B_M(\lambda) \tag{46}$$

With

$$A_M(\lambda) = -\lambda\left[\left(M_N * M_{N-1} \ldots \frac{\partial M_2}{\partial \lambda} * M_1\right) + \cdots + \left(M_N * M_{N-1} \ldots \left.\frac{\partial M_j}{\partial \lambda}\right|_{j\ even} \ldots M_2 * M_1\right)\ldots\right]$$

$$B_M(\lambda) = -\lambda\left[\left(M_N * M_{N-1} \ldots * M_2 * \frac{\partial M_1}{\partial \lambda}\right) + \cdots + \left(M_N * M_{N-1} \ldots \left.\frac{\partial M_j}{\partial \lambda}\right|_{j\ odd} \ldots M_2 * M_1\right)\ldots\right]$$

And, for each derived matrix,

$$\frac{\partial M_j}{\partial \lambda} = -\frac{\delta_j}{\lambda}\begin{bmatrix} -\sin(\delta_j) & \dfrac{i}{q_j}\cos(\delta_j) \\ iq_j\cos(\delta_j) & -\sin(\delta_j) \end{bmatrix}$$

With Eq. 46, the spatial dependence and chromatic dependence of the characteristic matrix are separated, along with the contribution of each material.

Thanks to this linearized expression of the stack characteristic matrix, the same work can be done for the **complex reflectance amplitude**. As with M'_c, the complex reflectance amplitude "with thickness deviations" r' is expressed as a function of α, β, and two other quantities A_r, and B_r :

$$r'(x,y,\lambda) = r(x,y) + [\alpha(x,y) - 1]A_r(\lambda) + [\beta(x,y) - 1]B_r(\lambda) \quad (47)$$

With

$$A_r(\lambda) = \frac{t}{2q_a}[q_a(1-r)A_{M11} - q_s(1+r)A_{M22} + q_a q_s(1-r)A_{M12} - (1+r)A_{M21}]$$

$$B_r(\lambda) = \frac{t}{2q_a}[q_a(1-r)B_{M11} - q_s(1+r)B_{M22} + q_a q_s(1-r)B_{M12} - (1+r)B_{M21}]$$

$$A_M(\lambda) = \begin{bmatrix} A_{M11} & A_{M12} \\ A_{M21} & A_{M22} \end{bmatrix}; B_M(\lambda) = \begin{bmatrix} B_{M11} & B_{M12} \\ B_{M21} & B_{M22} \end{bmatrix}$$

Once again, spatial, and chromatic dependencies have been separated in Eq. 47. From r can be expressed the **reflected phase $\boldsymbol{\varphi_R}$.** Following the same notation, we obtain:

$$\varphi'_R(x,y,\lambda) = \varphi_R(\lambda) + [\alpha(x,y) - 1]A_\varphi(\lambda) + [\beta(x,y) - 1]B_\varphi(\lambda) \quad (48)$$

With

$$A_\varphi(\lambda) = \frac{\mathrm{Im}(A_r)\mathrm{Re}(r) - \mathrm{Im}(r)\mathrm{Re}(A_r)}{|r|^2};\ B_\varphi(\lambda) = \frac{\mathrm{Im}(B_r)\mathrm{Re}(r) - \mathrm{Im}(r)\mathrm{Re}(B_r)}{|r|^2}$$

The WFE created by the coating, $\mathrm{WFE_c}(x,y,\lambda)$ can easily be computed from $\varphi'_R(x,y,\lambda)$. Similarly, $\mathrm{SFE^L}(x,y)$ and $\mathrm{SFE^H}(x,y)$ can easily be expressed from $\alpha(x,y)$ and $\beta(x,y)$. Again, full details of the calculations are in [73]. We then obtain the linearized expression for the **total WFE (coating + air)**, which corresponds to the measured WFE:

$$\mathrm{WFE}(x,y,\lambda) = F_\mathrm{L}(\lambda)\mathrm{SFE^L}(x,y) + F_\mathrm{H}(\lambda)\mathrm{SFE^H}(x,y) \quad (49)$$

With the functions F_L and F_H defined with:

$$F_\mathrm{L}(\lambda) = \left[\frac{\lambda A_\varphi(\lambda)}{2\pi D^\mathrm{L}_\mathrm{nom}} + 2n_a\right]\cos(\gamma);\ F_\mathrm{H}(\lambda) = \left[\frac{\lambda B_\varphi(\lambda)}{2\pi D^\mathrm{H}_\mathrm{nom}} + 2n_a\right]\cos(\gamma)$$

Using two $\mathrm{WFE}^{meas}(x,y,\lambda)$, at different wavelengths, we can set an invertible linear system that leads to the identification of $\mathrm{SFE^L}$ and $\mathrm{SFE^H}$.

$$\begin{bmatrix} \mathrm{SFE^L}(x,y) \\ \mathrm{SFE^H}(x,y) \end{bmatrix} = \begin{bmatrix} F_\mathrm{L}(\lambda_1) & F_\mathrm{H}(\lambda_1) \\ F_\mathrm{L}(\lambda_2) & F_\mathrm{H}(\lambda_2) \end{bmatrix}^{-1} \begin{bmatrix} \mathrm{WFE}_{meas}(x,y,\lambda_1) \\ \mathrm{WFE}_{meas}(x,y,\lambda_2) \end{bmatrix} \quad (50)$$

From Eq. 45, and 50, all the $\mathrm{TFE}_j(x,y)$ can be computed. The fit quality depends on the selection of λ_1 and λ_2 (see Section 3.1 for more details). Also, this choice must not induce a zero determinant for the central matrix of Eq. 50. This implies, for example, $\lambda_1 \neq \lambda_2$ or $F_\mathrm{L} \neq F_\mathrm{H}$. In addition, Eq. 50 is valid at any angle of incidence γ and polarization state.

The main steps in the mathematical development leading to Eq. 50, as well as the expressions for F_L and F_H, have been presented here. These are the main results, and the rest of the calculation can be found in [73]. The WFE shown here corresponds to a WFE that could be measured experimentally.

3. SIMULATIONS ON SPECIFIC CASES

In this section, based on realistic mathematical assumptions, we deduce the identification of each TFE from the WFE measured in a controlled environment. Knowing these TFEs enables us to predict the WFE for all illumination conditions.

3.1. Identification on linearization errors

The purpose of the simulations presented here is to show that Eq. 50 is effective in recovering the geometry of a sample stack, whose TFEs perfectly respect the assumptions established in part 2.2, i.e., for each material, TFE proportional to layer thickness. We therefore generate the WFE induced by this "sample" stack, assumed unknown, and apply Eq. 50 using the "sample" WFE at two wavelengths λ_1 and λ_2.

Linearization errors and wavelength choice

This first simulation already introduces an intrinsic limit to the analytical method. The method is only effective if the matrix terms in Eq. 50 are correct. Indeed, their analytical expression is obtained from assumptions, such as constant refractive indices, and also involves several mathematical simplifications. These include, for example, first-order Taylor series expansions on trigonometric functions, or non-linear terms that have been neglected.

However, the equations need not to be correct at all wavelengths. It is sufficient that there are two optimal wavelengths λ_{opt1} and λ_{opt2} such that these errors are very small. The solution proposed in [73] to identify these optimal wavelengths is a three-step process:

- We consider the nominal dichroic coating stack, to which we apply a scale factor α to the L layers, and β to the H layers. We also consider the actual refractive indices, which are tabulated by OBJ.

- The theoretical phase $\varphi_{R,theo}(\alpha,\beta,\lambda)$ is calculated directly from thin-film theory, introduced in part 1.2. It is considered to be the "actual" phase, which does not need approximations to be calculated.

- For this same coating, we compute the "linearized" phase $\varphi_{R,lin}(\alpha,\beta,\lambda)$ whose expression is found in 2.3 (Eq. 48) and from which the terms $F_{\mathrm{L}}(\lambda)$ and $F_{\mathrm{H}}(\lambda)$ in Eq. 50 are directly derived. The error $\delta\varphi_R(\alpha,\beta,\lambda)$ between $\varphi_{R,lin}(\alpha,\beta,\lambda)$ and $\varphi_{R,theo}(\alpha,\beta,\lambda)$ corresponds to the total error induced on the phase φ_R due to the linearization of the thin-film theory equations, and thus quantifies the error on the analytical method. In the end, we identify two wavelengths such that the value of $\delta\varphi_R(\alpha,\beta,\lambda)$ is as small as possible.

Application 1: Computing of linearization errors

The value of the deviation $\delta\varphi_R(\alpha,\beta,\lambda)$ was calculated in the case of the *Euclid* dichroic mirror for α,β = [0.995; 1.005], λ = 510 to 950 nm, normal incidence. This corresponds to maximum thickness variations of $\pm$ 0.5% for each material. We observe in Figure 77 spectral zones of interest where the median value of $\delta\varphi_R(\alpha,\beta,\lambda)$ are minimal, approaching 10^{-4} deg, for example around λ = 593 nm, and λ = 662 nm.

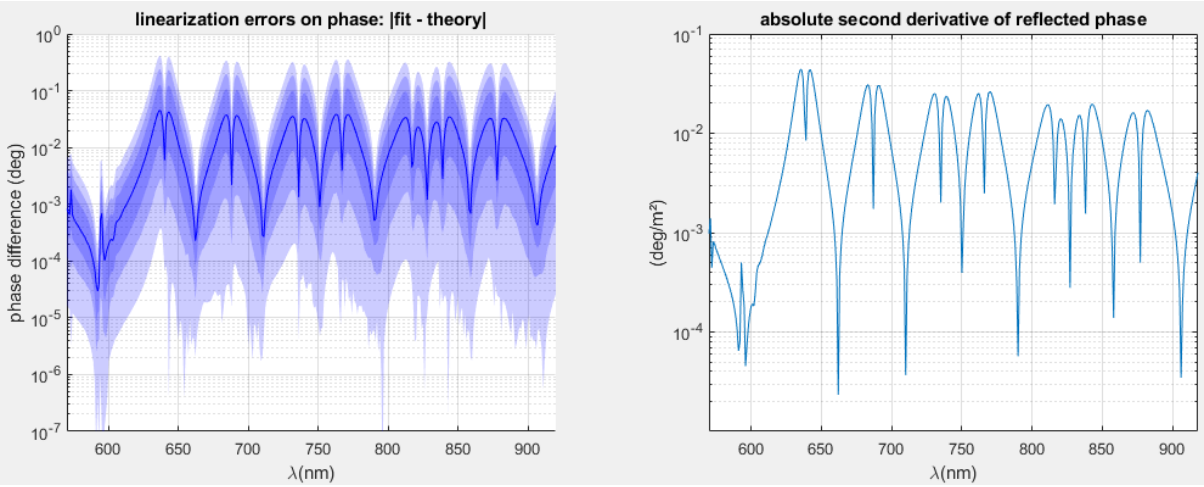

Figure 77: (Right) Median value (blue line) of $\delta\varphi_R(\alpha,\beta,\lambda)$ and quantile corridors [25% to 75%], [10% to 90%], and [1% to 99%], for α,β = [0.995; 1.005]. (Left) Absolute value of second derivative $\partial^2\varphi_R(\lambda)/\partial\lambda^2$.

Linearization errors appear to be highly correlated with the second derivative of the phase in reflection $\partial^2\varphi_R(\lambda)/\partial\lambda^2$, whose absolute value has been plotted on the right side of Figure 77. Indeed, the linearized phase expression (Eq. 48) can be compared to a first-order Taylor expansion, in which only the first phase derivative terms appear. The second derivatives terms are thus the first higher-order terms neglected in the Eq. 48.

Application 2: Comparison between good and bad choices of λ_1 and λ_2.

A simulation was carried out to identify the impact of incorrect wavelength selection λ_1 and λ_2. Figure 78 shows the results of this simulation. Initially, a *Euclid* dichroic-type stack is created with SFEs (Figure 78: A, B). The SFEs are randomly generated using Zernike polynomials (see Chapter 5, part 1.1) up to 55th order, on a surface sized 108 mm in diameter and sampled with 62*62 points. The PTV value of these maps was adjusted to **0.5% of the thickness of each material**, which is the order of magnitude of the actual PTV measured on the component by OBJ [55]. For the moment, SFEs are considered to have a zero-mean value.

The WFE induced by this "sample" stack is then calculated using thin-film theory at 0° AOI, and acts as the "measured WFE". The analytical method (Eq. 48) is then applied at two wavelengths **λ_1 = 593 nm and λ_2 = 662 nm**, yielding two modeled WFE (Figure 78: C, D). These wavelengths correspond to very low linearization errors, as shown in Figure 77. Indeed, we observe very low residuals on the reconstruction of the SFEs (Figure 78: E, F), of the order of 0.02 nm RMS.

The same simulation (Figure 78: G, H, I, J, K, L) was done choosing wavelengths where linearization errors are worse. We thus choose **λ_1 = 635 nm and λ_2 = 680 nm**, and we observe that the residuals on the reconstruction (K, L) are quite high this time. They are two orders of magnitude above the residuals obtained for optimal λ_1 and λ_2 (**λ_1 = 593 nm and λ_2 = 662 nm)**.

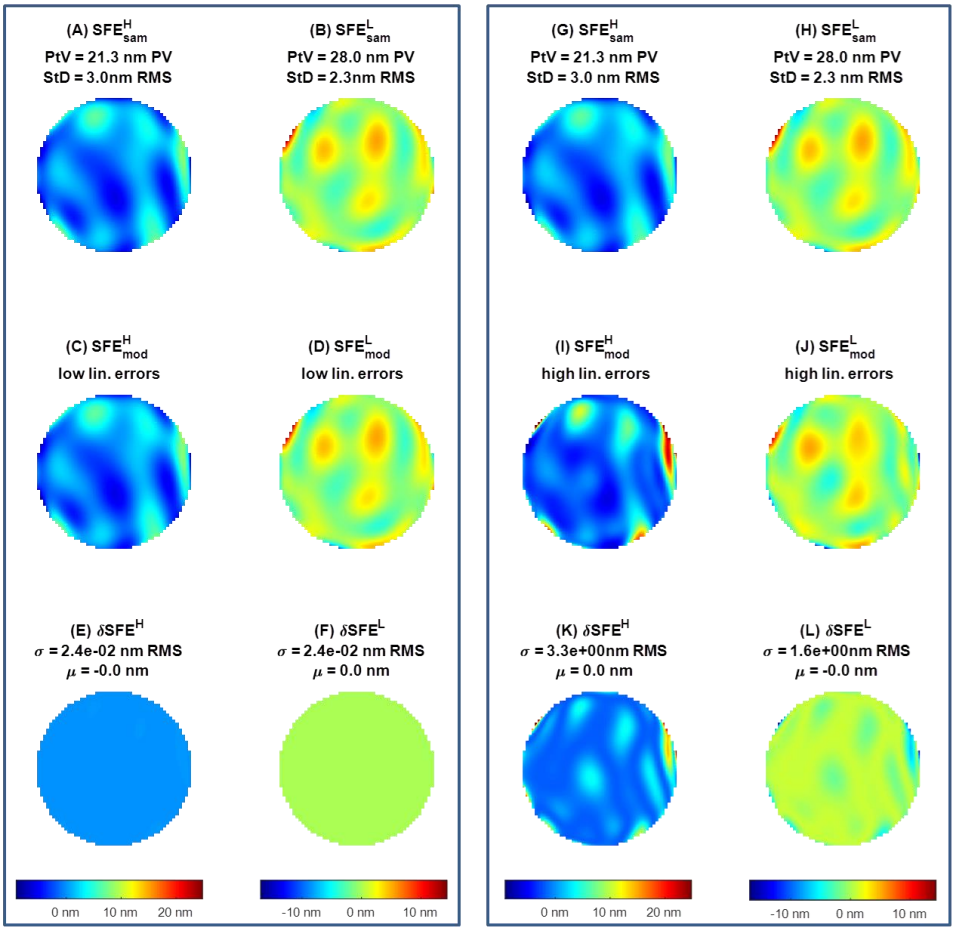

Figure 78: Simulation of modeled SFEs on dichroic mirror coating. (A, B): Relative SFE^H and SFE^L used as sample. (C, D) Modeled SFEs with the analytic method (Eq. 50), using λ_1 and λ_2 such linearization errors are low. (E, F): residuals, in nm RMS. (G, H, I, J, K, and L) Equivalent simulation with high linearization errors.

We can retain from these simulations that the selection of wavelengths used to apply the analytic method is crucial. It is important to first determine the linearization errors at all accessible wavelengths and under the same illumination conditions as the measurement conditions. In Figure 77, we observe between 5 and 8 wavelengths where the linearization errors are extremely low and lead to results similar to those observed in Figure 78. With other wavelengths, the residuals that can be of the same order of magnitude as the RMS of the SFE map themselves. We have reminded here in a very simple case in order to understand the importance of the choice of λ_1 and λ_2. In the simulations that follow, this optimal choice is implicit.

3.2. Identification of SFEs means values.

Impact of unknown WFE mean value

One of the limitations of Eq. 50 is that it does not allow us to find the average WFE value. Indeed, measurement of the WFE, for example by interferometry, or with a SHWFS as in the case of the *Euclid* dichroic mirror, gives no information on the sample WFE, which means that the average spatial value of WFE (in other words, the "piston" Zernike term) at each wavelength, $\overline{\mathrm{WFE}(x, y, \lambda_i)}$, is not accessible, or meaningless. As a result, Eq. 50 assumes that the spatial average of the WFE (and therefore the SFE) is zero. This means that the average thickness of a layer corresponds to its

theoretical thickness. Unfortunately, there's no physical reason to assume that this is true. Without optimization, the stack is thus poorly reconstructed, with a bias on each material. Here, we will detail a method for recovering the average SFE value.

Optimization process for SFEs means values identification.

We will assume that the stack has $\overline{\mathrm{TFE}_j(x,y)} \neq 0$. We have assumed that the amplitude of $\mathrm{TFE}_j(x,y)$ is proportional to the theoretical thickness $d_{j,theo}$ of the layer. Logically, this is also true for the value of $\overline{\mathrm{TFE}_j(x,y)}$. We will call a_j the ratio between the actual and theoretical thicknesses of a layer:

$$a_j = \frac{\overline{d_j(x,y)}}{d_{j,\mathrm{theo}}}$$

The term a_j has only two possible values: one for the layers of L, denoted a_L, and a_H for the layers of H. Thus,

$$\frac{d_{j,\mathrm{theo}}+\overline{\mathrm{TFE}_j(x,y)}}{d_{j,\mathrm{theo}}} = \begin{cases} a_\mathrm{L}, j \equiv \mathrm{L}-layer \\ a_\mathrm{H}, j \equiv \mathrm{H}-layer \end{cases} \quad (51)$$

The values of a_L and a_H cannot be identified analytically. To compute them, we implemented a two-variable optimization. Figure 79 is a simplified diagram of this optimization, with 6 steps listed.

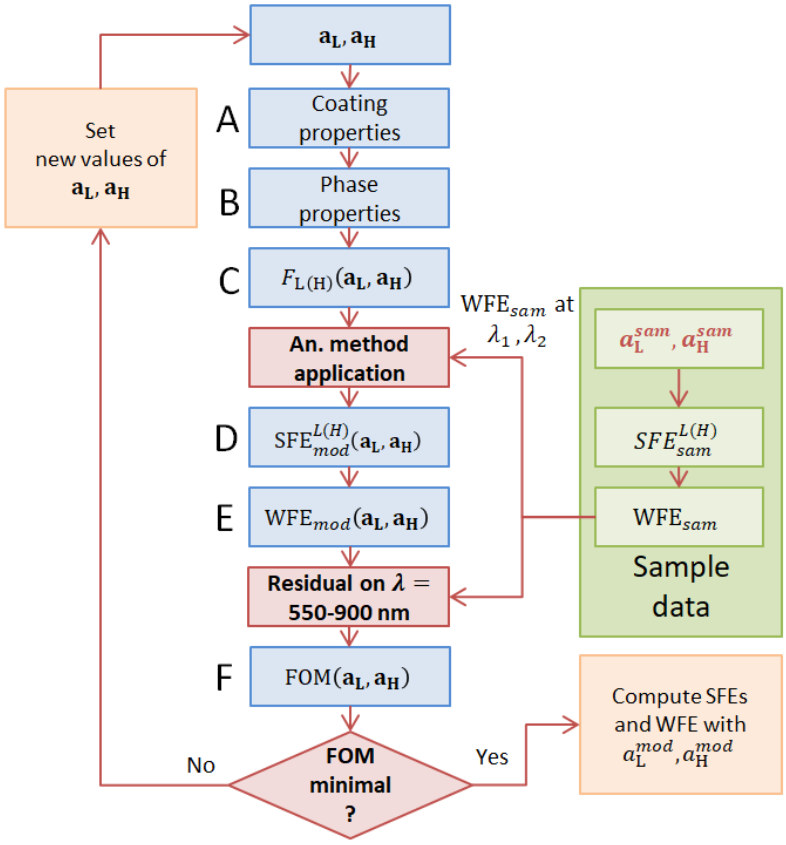

Figure 79: Schema of the optimization process used to identify a_L and a_H. The green blocks correspond to the sample, and the blue ones correspond to the modeled quantities. The values of a_L^{sam} and a_H^{sam} are the sample offsets, that are sought.

The functions $F_\mathrm{L}(\lambda)$ and $F_\mathrm{H}(\lambda)$ in Eq. 50 depend on the stack characteristic matrix value $M_c(\lambda)$, at each wavelength and which depends itself on the optical formula (theoretical thicknesses, theoretical

refractive indices: see Eq. 33). By applying an arbitrary scale factor a_{L} and a_{H}, we obtain a new value for $M_c(\lambda, a_{\mathrm{L}}, a_{\mathrm{H}})$, leading to $F_{\mathrm{L}}(\lambda, a_{\mathrm{L}}, a_{\mathrm{H}})$ and $F_{\mathrm{H}}(\lambda, a_{\mathrm{L}}, a_{\mathrm{H}})$. This corresponds to steps A, B, and C in Figure 79.

With the same $\mathrm{WFE}_{sam}\left(x, y, \lambda_{1(2)}\right)$ we thus obtain with Eq. 50 different values of $\mathrm{SFE}^{\mathrm{L}}(x, y, a_{\mathrm{L}}, a_{\mathrm{H}})$ and $\mathrm{SFE}^{\mathrm{H}}(x, y, a_{\mathrm{L}}, a_{\mathrm{H}})$ (step D). These different SFEs lead to a differently reconstructed stack. Using thin-film theory, the WFE of this stack can be modeled, giving $\mathrm{WFE}_{mod}(x, y, \lambda, a_{\mathrm{L}}, a_{\mathrm{H}})$ (step E), which is then compared with the sample: WFE_{sam},

We can then create a two-variable Figure of Merit (FOM) function of a_L and a_H (step F), expressed for example as the maximum RMS between $\mathrm{WFE}_{mod}(x, y, \lambda)$ and $\mathrm{WFE}_{sam}(x, y, \lambda, a_{\mathrm{L}}, a_{\mathrm{H}})$ via:

$$\mathrm{FOM}(a_{\mathrm{L}}, a_{\mathrm{H}}) = \max_{\lambda}\left\{\mathrm{std}_{x,y}[\mathrm{WFE}_{mod}(x, y, \lambda) - \mathrm{WFE}_{sal}(x, y, \lambda, a_{\mathrm{L}}, a_{\mathrm{H}})]\right\} \qquad (52)$$

Minimizing FOM allows us to identify a_{L}^{mod} and a_{H}^{mod} which thus approach their actual value defined by Eq. 51. The $F_{\mathrm{L(H)}}\left(\lambda, a_{\mathrm{L}}^{mod}, a_{\mathrm{H}}^{mod}\right)$ terms of Eq. 50 are then calculated from the average stack thicknesses, rather than the theoretical ones. Now that the average stack has been identified, it is possible to compute each $\overline{\mathrm{TFE}_j(x, y)}$ with Eq. 51.

Application

In this new simulation, we have generated a new *Euclid* dichroic-type stack featuring other SFE, again with random coefficient for the 55 first Noll Zernike polynomials. This time, the average SFEs are non-zero. We arbitrarily set $\boldsymbol{a_{\mathrm{H}} = 0.998}$ **and** $\boldsymbol{a_{\mathrm{L}} = 1.004}$, which, as a reminder, correspond to the ratio between average layer thickness and theoretical thickness. Figure 80 compares the two results, presented in the same way as Figure 78. On the left side (Figure 80: A to F), we apply the analytic method with Eq. 50 without optimization. We observe in E that the RMS between the sample and reconstructed SFE maps is acceptable (less than 0.1 nm RMS), but that the mean difference between the two maps is significant: 8.5 nm. Since $\overline{\mathrm{SFE}_{mod}^{\mathrm{H}}} = 0$, we have $\overline{\mathrm{SFE}_{mod}^{\mathrm{H}}} - 0 = -8{,}5\ nm$. Insofar as the total H-thickness is 4.25 µm, this corresponds well to a thickness variation of -0.2% of D^{H}. The same applies to $\mathrm{SFE}^{\mathrm{L}}$ where an average difference of 22.4 µm appears between the two maps (i.e. $+0.4\%$ of D^{L}).

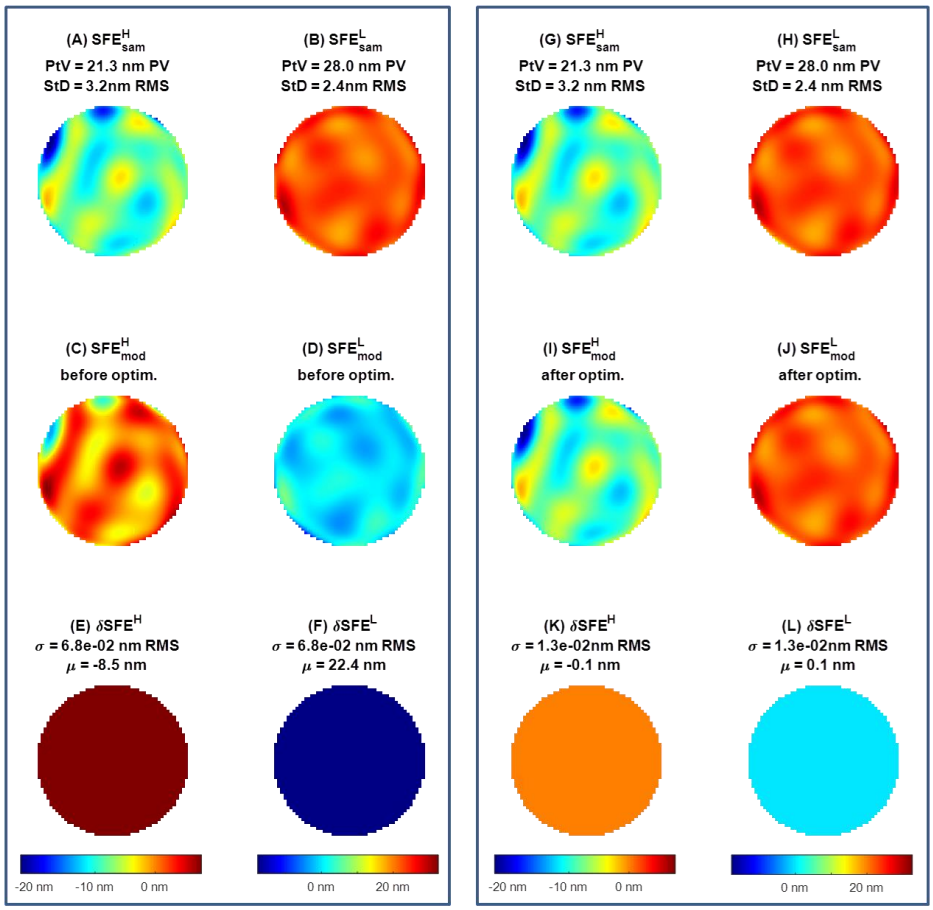

Figure 80: Simulation of modeled SFEs on dichroic mirror coating, with $\overline{SFE(x,y)} \neq 0$. *(A, B): Relative* SFE^H *and* SFE^L *used as sample. (C, D): Modeled SFEs with the analytic method (Eq. 50), without piston identification. (E, F): Residuals, in nm RMS. (G, H, I, J, K, and L) Equivalent simulation after identification.*

Applying the optimization algorithm presented earlier produces much better results (Figure 80: G to L). On the one hand, the residual RMS is about 0.01 nm RMS for both SFE, but we also note that the mean value of these SFEs has been correctly identified. The average deviation between the "sample" and "optimized" maps is about 0.1 nm for each material.

To achieve this optimization, we have set a $\mathrm{FOM}(a_\mathrm{H}, a_\mathrm{L})$ function equivalent to Eq. 52, which we aim to minimize over the 550-900 nm spectral range. Figure 81 shows the successive iterations. The starting point is $\mathrm{FOM}(1,1)$ = 0.64 nm RMS which is equivalent to applying the analytic method without optimization (Figure 80, C and D). This value of 0.64 nm RMS thus corresponds to the worst-case deviation between the sample WFE and the modeled WFE, and is therefore linked to the residual on the map reconstruction (E, F).

Using MATLAB's optimization functions, a two-variable optimization was performed, resulting in a value of $\mathrm{FOM}\left(a_\mathrm{H}^{mod} \approx 0.998, a_\mathrm{L}^{mod} \approx 1.004\right)$ = 0.02 nm RMS with just a few dozen iterations. This value is associated with the SFEs calculated in Figure 80, I and J. Optimization has therefore made it possible both to recover a_L, a_H and to divide the FOM by a factor of 30, which is equivalent to the residual on the WFE fit.

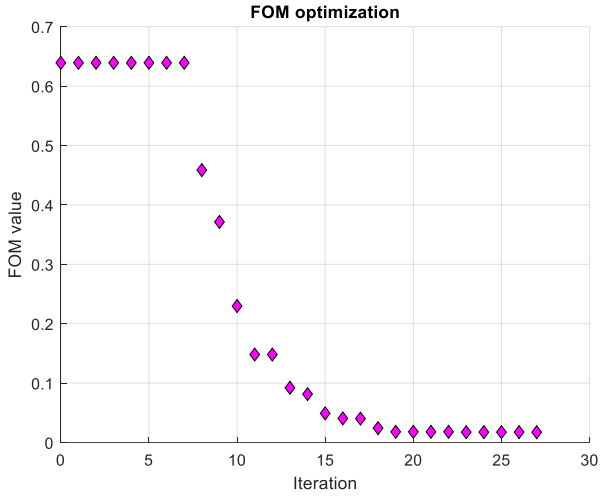

Figure 81: 27 iteration process using MATLAB's optimization toolbox [77].

Of course, we are still in an ideal case, assuming "perfect" WFE measurements, which are generated from a stack that perfectly respects the specifications introduced in part 2.1. We are not yet considering measurement errors, or random errors in the stack. This optimization will certainly be more complex once applied to real data. The aim of the work presented here is solely to show that it is theoretically possible to identify the mean stack deviation, using the theoretical stack as the knowledge base and with WFE measurements that have no relevant mean value.

There are several ways in which this optimization process could be improved, for example on the FOM, which could be expressed from the 95% percentile instead of the maximum, selecting a specific spectral band to apply the FOM, or identifying a more suitable optimization solver. In particular, this work would make it possible to better guarantee optimization convergence by avoiding local minima.

3.3. Identification of substrate SFE

Analytic method modification

Eq. 50 allows us to find the SFE for each material, L and H but not the SFE of the substrate, which we will denote $\mathrm{SFE}^{\mathrm{S}}(x,y)$ here. The substrate-induced WFE is achromatic and simply corresponds to the air gap created by $\mathrm{SFE}^{\mathrm{S}}(x,y)$. We can therefore modify Eq. 50 to include a third parameter:

$$\begin{bmatrix} \mathrm{SFE}^{\mathrm{L}}(x,y) \\ \mathrm{SFE}^{\mathrm{H}}(x,y) \\ \mathrm{SFE}^{\mathrm{S}}(x,y) \end{bmatrix} = \begin{bmatrix} F_{\mathrm{L}}(\lambda_1) & F_{\mathrm{H}}(\lambda_1) & 2\,n_a\cos(\gamma) \\ F_{\mathrm{L}}(\lambda_2) & F_{\mathrm{H}}(\lambda_2) & 2n_a\cos(\gamma) \\ F_{\mathrm{L}}(\lambda_3) & F_{\mathrm{H}}(\lambda_3) & 2n_a\cos(\gamma) \end{bmatrix}^{-1} \begin{bmatrix} \mathrm{WFE}_{meas}(x,y,\lambda_1) \\ \mathrm{WFE}_{meas}(x,y,\lambda_2) \\ \mathrm{WFE}_{meas}(x,y,\lambda_3) \end{bmatrix} \quad (53)$$

In this new equation, $F_{\mathrm{L}}(\lambda)$ and $F_{\mathrm{H}}(\lambda)$ are identical to those present in Eq. 50. Henceforth, three wavelengths are required to calculate the three SFEs with Eq. 53.

The $\mathrm{SFE}^{\mathrm{S}}(x,y)$ term obtained with Eq. 53 corresponds more generally to all achromatic contributions to the WFE. This includes the contribution of the substrate, whose polishing is not perfect, but also mechanical stresses on the mirror: clamping in the holder or residual bending [48, 78] due to the coating application.

Application

We have generated a stack with three SFE, including the one of the substrate. The simulation parameters are identical to those tested in section 3.2. Both SFE^L and SFE^H are assumed to have zero mean values. The variant of the analytical method presented here is well compatible with the two-variable optimization discussed above: unlike SFE^L and SFE^H, the WFE does not depend on the mean value of SFE^S. In fact, it is assumed that no ray returns from the rear face of the dichroic mirror substrate, which is coated with an anti-reflective stack and has a wedge. The substrate SFE was randomly generated as SFE^L and SFE^H, from the 55 first Noll Zernike modes. The PTV value of SFE^S was arbitrarily set at 25 nm PTV, corresponding to the order of magnitude of the PTV values of the other SFE.

The simulation results are shown in Figure 82. In the same way, a stack is generated. The WFE of this stack is calculated using thin-film theory, then used as the sample WFE. On panels D, E, and F in Figure 82 appear the SFE calculated with Eq. 53, using three wavelengths **λ_1 = 593 nm, λ_2 = 662 nm and λ_3 = 710 nm**. The three SFEs are reconstructed faithfully to the sample, with very low residuals (Figure 82: G, H, and I), between 0.01 and 0.02 nm RMS for each SFE.

For comparison, we applied Eq. 50 to this same sample stack (thus the method ignoring SFE^S), and at wavelengths λ_1 = 593 nm and λ_2 = 662 nm. Unsurprisingly, the modeled SFE (Figure 82: J, K, and L) do not match those of sample. The standard deviation of the residuals for each SFE (Figure 82: M, N, and O) is between 2.3 and 5 nm RMS, despite the optimal choice of wavelengths for analytic method application. In conclusion, it is essential to consider the substrate SFE, and therefore to favor a method with 3 unknowns, using Eq. 53.

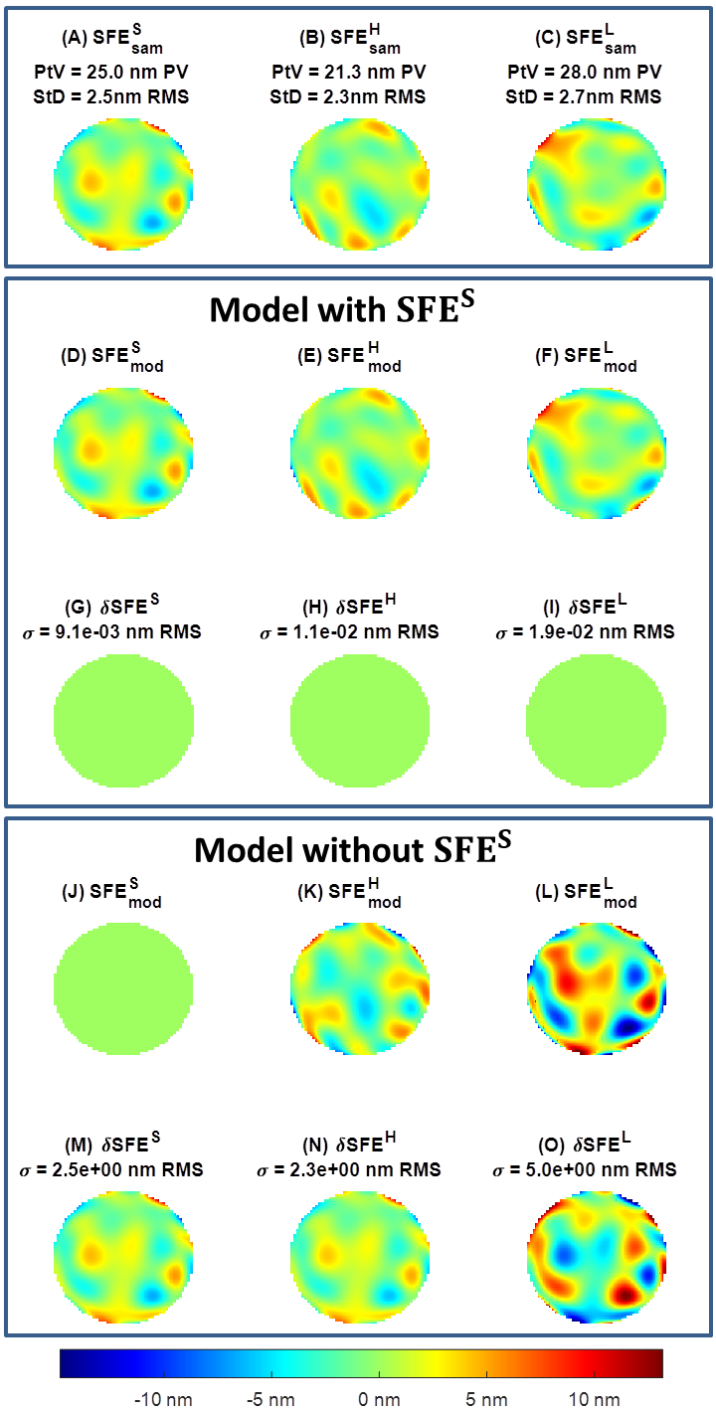

Figure 82: Comparison of "3-SFE" and "2-SFE" analytic methods. (A, B, C): Sample coating (and substrate) SFEs. (D, E, F): Modeled SFEs using the "3-SFE" method. (G, H, I): Residuals. (J, K, L, M, N, and O): Equivalent simulation using the "2-SFE" method.

3.4. Homothetic case

The homothetic case is a special situation where SFE^L and SFE^H are assumed to be proportional, so $\alpha(x,y) = \beta(x,y)$. All the layers in the stack have identical TFE, within a scale factor. This case has been presented in [73, 75], and it can be shown that Eq. 50 can be turned into a system with a single unknown:

$$\mathrm{SFE}(x,y) = \left[2n_a\, cos(\gamma) - \frac{{\lambda_1}^2}{2\pi D_{nom}} \frac{\partial \varphi_R(\lambda_1)}{\partial \lambda}\right]^{-1} \mathrm{WFE}_{meas}(x,y,\lambda_1) \tag{54}$$

A mathematical approach of the stack with a homothetic behavior has been firstly proposed by Giacomo [79]. Further works [62, 80] have been presented on this homothetic basis, to point out the optical sensibility of coatings. The WFE/SFEs interaction is similar to Eq. 54, but the optical dispersion is taken into account.

A visualization of a stack with homothetic TFEs distribution is represented on Figure 83. On panel (A), one layer "j" is shown whose nominal thickness is $d_{j,nom}$ and actual thickness is $d_{j,nom}$ plus an additional $\mathrm{TFE}_j(x)$. The ratio $\mathrm{TFE}_j(x)/d_{j,nom}$ is a constant scale factor that does not depend on the considered layer. Each layer of the stack in panel (B) admits then the same relative TFE leading to a straightforward characterization of the whole stack. Indeed, the stack SFE can be directly retrieved from one chromatic WFE measurement with this approach. In any case, Eq. 50 (double-SFE method) and Eq. 53 (three-SFE method) remain applicable for the homothetic case.

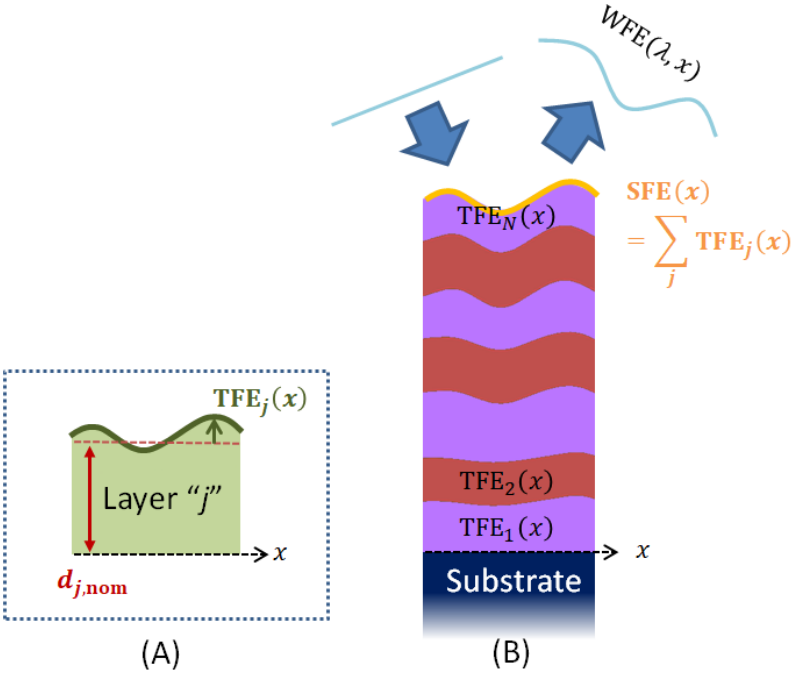

Figure 83 (A): Illustration of a layer with a TFE. (B) Multilayer stack with TFEs distribution matching the "homothetic" assumption [73].

However, in most of the cases there is no technical reason that the layers have the same non-uniformity profile whatever the material [81]. The homothetic variation is then quite a strong assumption especially for large optics. In contrary, it seems that layers of different materials have likely different thickness variation.

Of course, the homothetic method is confronted with the same issues as those discussed for the double SFE method: linearization errors, mean SFE value and substrate contribution. Similar concerns have been encountered for the wavefront reconstruction at arbitrary wavelength developed by Venancio [82]. A work published in Proc. of SPIE in 2022 [75] furthermore presents a comparison of the two analytical methods for reconstructing *Euclid* dichroic-type stacks that contain SFE^L and SFE^H with several levels of correlation[6]. Unsurprisingly, the "double-SFE" method is efficient in all cases, except where the "reference" stack is truly homothetic: in such a case, both methods perform equally well.

In conclusion, even though the homothetic method has the advantage of being much simpler to apply, in our opinion it is still more interesting to favor the double SFE approach. However, it is possible that the accuracy of the data used by OBSERVE, the actual TFEs of the dichroic stack, and all the other sources of experimental error could make one method drastically more efficient than the other. In the next chapter, we will apply both analytical methods to Dry-Run data acquired with OBSERVE bench and compare their performance in terms of WFE reconstruction.

The four situations presented here demonstrate that it is possible to apply the analytical method to retrieve the TFEs of the dichroic mirror layers (or any other stack) with accuracy, using the knowledge available at the LMA, i.e. the WFE measurements and the optical stack formula. By applying the right optimizations, it is possible to retrieve the SFEs with a fit that is of the order of a hundredth of nm RMS, which is more than sufficient to reproduce the WFE numerically via the thin-film theory. Nevertheless, the simulations presented here remain an ideal case, with no errors in the actual SFE distribution, or in the WFE measurements themselves, which may be noisy or biased. In the following section, we will test the method's sensitivity to different cases of random errors. This will give an idea of the method's robustness when applied to actual OBSERVE data. Even if they are applied in "ideal" situations, the simulations presented here highlight the importance of some choices that will be useful later. We are thinking in particular of the choice of wavelengths λ_1 and λ_2, which is crucial.

[6] Three situations were tested. First case: perfectly identical SFEs (homothetic case). Second case: Almost identical SFEs, with 10% (RMS) deviations added on each Zernike aberration up to Noll 55 order. Third case: completely decorrelated SFEs generated independently.

4. ANALYTIC METHOD SENSIBILITY ANALYSIS FROM MONTE-CARLO SIMULATIONS

In this section, we will present several Monte-Carlo simulations designed to test the sensitivity of the analytical method to different types of error sources. We will start by testing the method robustness with a simulation in which the sample stack differs to the theoretical stack with random thickness errors. The second simulation will test the impact of error on measurements, by adding a noise to the WFE map. The order of magnitude of this noise is comparable to the uncertainty of the measurements acquired by OBSERVE. These two simulations are similar to those presented in [73], but which were then applied to a Bragg-type mirror stack. We reproduce this work here, but this time with the *Euclid* dichroic thin-films stack.

4.1. Analytic method sensitivity to random thickness errors

As mentioned in the introduction, we present here a Monte-Carlo simulation, where we add random errors in the thickness of the stack layers in order to reproduce the limited accuracy of film thickness monitoring during the deposition.

The error model we have chosen to introduce is as follows: we assume that the deviation Δ_j between the mean thickness of each of the 182 layers and their theoretical thickness $d_{j,theo}$ follows a normal distribution with standard deviation σ_{rand} and mean zero, in proportion to the theoretical layer thickness:

$$\sigma_{rand} = RMS\left(\left\{\frac{d_{j,theo} + \Delta_j}{d_{j,theo}}\right\}_{N\ layers}\right)$$

The simulation includes 50 virtual dichroic coatings, for which we obtain a stack with thickness errors added to the theoretical stack with a fixed σ_{rand}, e.g. 1% RMS. Next, one TFE per material is generated randomly and added to the stack. These TFEs are identical for each run and retain the same parameters as for the simulations in part 3.1. We do not add substrate SFE or non-zero spatial averages to the TFEs. The aim is to identify the sensitivity of the analytical method to random thickness errors only.

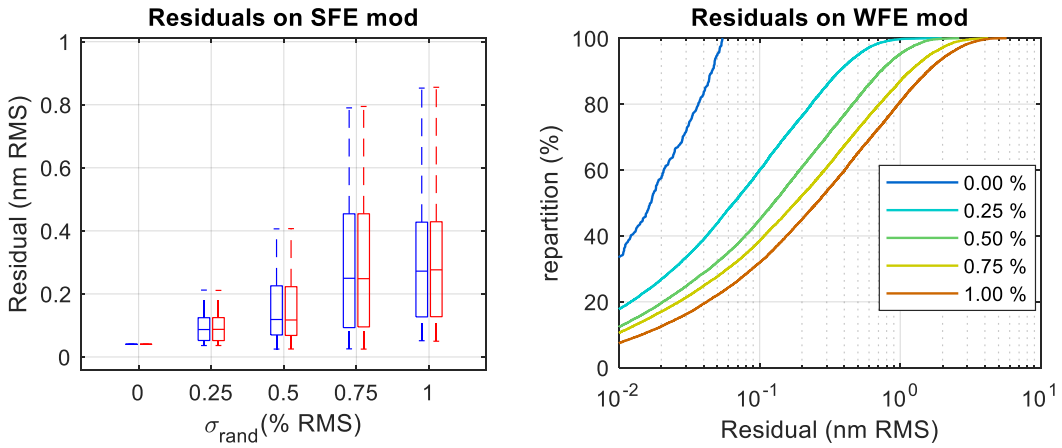

*Figure 84: Monte-Carlo simulation of analytic method sensibility to random thickness errors. The mean thickness of layers is noised with a specific standard deviation. (Left) The residuals on SFEs reconstruction are plotted with Whisker plots (**H**, **L**). (Right) Residuals on WFE reconstruction represented as cumulative distribution for each σ_{rand}.*

Figure 84 shows the simulation results. For each of the 5 specified standard deviations, 50 tests are performed. On the left are the residuals obtained on the SFEs (L and H), presented as a Whisker plot. With σ_{rand} = 1% RMS, the median error on δSFE is around 0.3 nm RMS. On the right of Figure 84 are plotted the residuals on the WFE fit for λ between 550 and 900 nm (1 nm step), from these SFEs. Each curve represents the cumulative distribution of all δWFE(λ_i) from the whole 50 runs of a specific σ_{rand} (see legend). The median value (at 50%) is between 0.01 nm RMS (best case) and 0.2 nm RMS (worst case), which is very encouraging regarding the 2 nm RMS goal. On the other hand, the 95% quantile is above 1 nm RMS when σ_{rand} exceeds 0.75 % RMS. Such errors are unlikely, given the mirror's photometric performance. Indeed, control errors of this order of magnitude would degrade dramatically the response at the reflection band edges, which is not the case, as shown in Figure 27 (Chapter 3).

In this simulation, we kept the same set of $\mathrm{SFE}_{sam}^{\mathrm{L(H)}}$, and changing only the thickness errors distribution. It is therefore interesting to check whether the results depend on the $\mathrm{SFE}_{sam}^{\mathrm{L(H)}}$ or not. In Figure 85 we have tested 10 different $\mathrm{SFE}_{sam}^{\mathrm{L(H)}}$ sets. For each set, 50 reconstruction trials are carried out, this time setting σ_{rand} = 0.5%. It thus appears that neither residuals on $\mathrm{SFE}_{mod}^{\mathrm{L(H)}}$ nor on WFE_{mod} depend significantly on $\mathrm{SFE}_{sam}^{\mathrm{L(H)}}$.

In conclusion, random thickness errors alone do not significantly affect the analytical fit convergence, but there are still specific wavelengths where the error on the WFE fit can exceed 1 nm RMS.

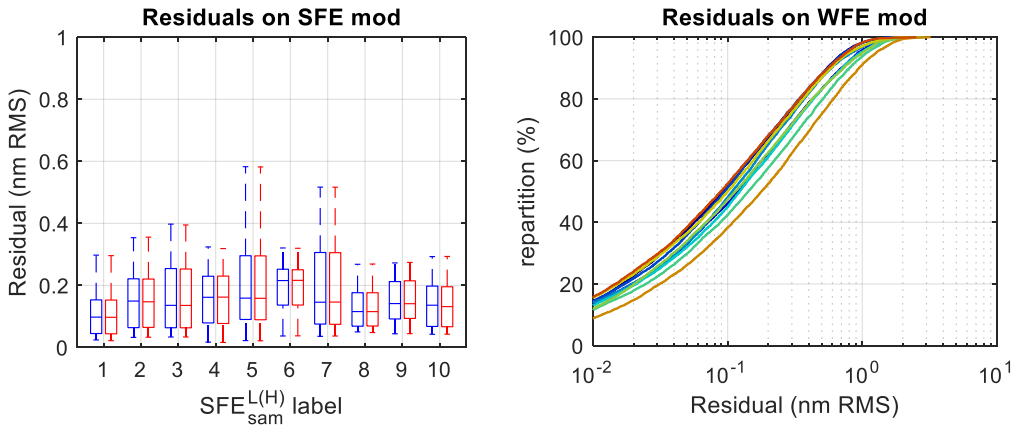

*Figure 85: Monte-Carlo simulation of analytic method sensibility to random thickness errors = **0.5%,** with 10 sets of $SFE_{sam}^{L(H)}$ tested. (Left) The residuals on SFEs reconstruction are plotted with Whisker plots (H, L). (Right) Residuals on WFE reconstruction represented as cumulative distribution for each set of $SFE_{sam}^{L(H)}$.*

4.2. Analytic method sensitivity to noise on sample WFE

In this new section, we test the method's sensitivity to the presence of noise in the sample WFEs. To generate this noise realistically, we proceed as follows for each run:

1) The SFEs of the theoretical stack are created and the reflected WFE is computed, likewise the work described in section 3.1. For each run of the simulation, we use the same SFE maps as for part 4.1, so that the results can be compared. Once again, we ignore the substrate SFE and the average SFEs values.

2) Noise is then generated at each wavelength as an additional WFE. This additional WFE is created from the first 10 Zernike modes, with random amplitude. The noise maps are then all normalized so that their spatial RMS $\sigma_{noise}(\lambda)$ is identical at all wavelengths, for example 1 nm RMS:

$$\mathrm{RMS}\big(Noise(x,y,\lambda_i)\big) = \sigma_{noise}\ \forall\lambda_i$$

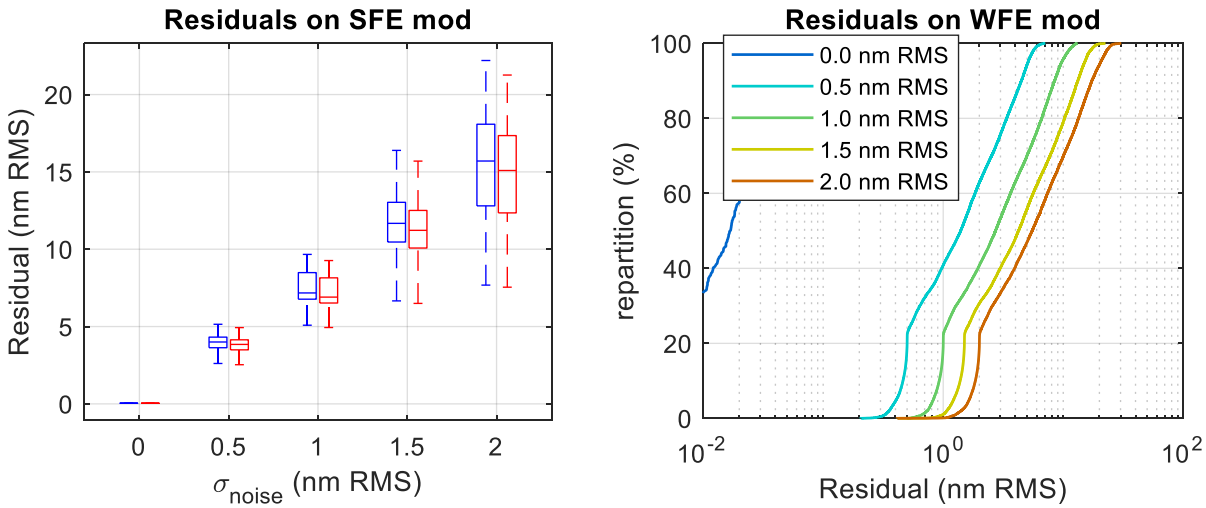

*Figure 86: Monte-Carlo simulation of analytic method sensibility to WFE noise. (Left) The residuals on SFEs reconstruction are plotted with Whisker plots (**H**, **L**). (Right) Residuals on WFE reconstruction represented as cumulative distribution for each σ_{noise}.*

The results are shown in Figure 86 in a similar way as previously, and for 5*50 runs. This time, the results are more questionable. An induced WFE measurement error of 2 nm RMS, similar to the expected performance of the OBSERVE bench, results in SFEs residuals exceeding 15 nm RMS (Figure 86, left). Such errors in SFEs have then a strong impact on the computed WFE (Figure 86, right), with median residuals exceeding several nanometers RMS.

To overcome this lack of accuracy, we can attempt to artificially reduce the noise by reproducing the measurement N times. The analytic method requires only two WFE measurements at two wavelengths. It needs then to repeat these two measurements as many times as necessary to significantly reduce the noise.

Keeping the same sample SFEs, we therefore reproduce the same Monte Carlo simulation with 5*50 runs, simulating for each of them a WFE averaged from N = 100 “samples”. The comparison between simulations with and without averaging is shown in Figure 87. As expected, averaging several measurements reduces the residual on the modeled SFE and WFE. Moreover, this reduction is constant regardless of $\sigma_{noise} \neq 0$ and is equivalent to a division by $\sqrt{N} = 10$.

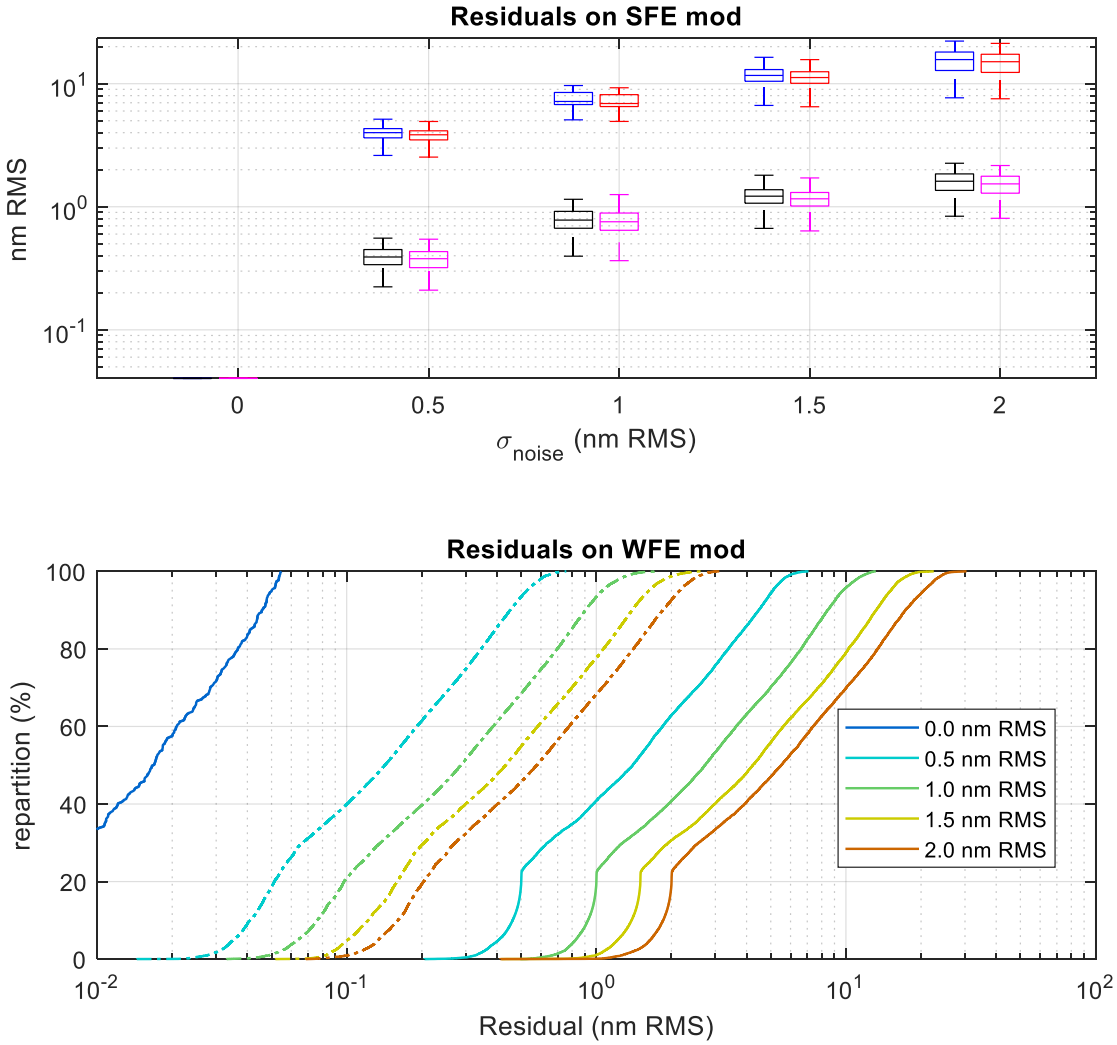

*Figure 87: (Up) Comparison between SFE modeled without averaging WFE noise (**H**, **L**) and with an averaging of 100 measurements (**H**, **L**). (Down) Residuals on WFE fit reconstruction represented as cumulative distribution for each σ_{noise}. The dashed lines correspond to the simulation with averaging.*

Based on the Variance Sum Law [83] the variance σ_{ave}^2 of a Gaussian signal averaged *N* times can be expressed as:

$$\sigma_{ave}^2 = \frac{1}{N}\sum_{k=1}^{N}\sigma_k^2$$

Where σ_k^2 corresponds to the signal variance at the k^{th} measurement. Here, ${\sigma_k}^2 = \sigma_{noise}^2 \forall k$, the standard deviation of the averaged signal is then $\sigma_{ave} = \sigma_{noise}\sqrt{1/N}$. The noise on the WFE, of standard deviation σ_{noise} = 1 nm RMS for example, will be of 0.1 nm RMS after averaging over 100 samples. Nevertheless, the residuals on WFE (Figure 87, down) are still high, of the order of 1 nm RMS (median) in the case where the noise on the measurement is 2 nm RMS (red dashed curve). If we aimed at a more reasonable median residual of 0.1 nm RMS on the WFE for this same noise level, it would have to reduce it by a further factor of 10, and therefore perform the same measurement 10,000 times. Even with only two wavelengths of interest, it is unlikely that the OBSERVE bench could perform so many repetitions without drifting with the time (estimated at almost 150 hours by wavelength).

4.3. Conclusion

We have seen that the analytic method is a linear application between the SFEs and two WFE measurements only. This was achieved by developing the equations derived from thin-film theory. The analytical method can be used to identify the layer thickness variations of any thin-films stack, and is not specific to the *Euclid* dichroic mirror coating. Various cases have been tested in this chapter and involve strategies for successfully computing SFEs.
The robustness of the analytic method to random errors has been tested, and it appears that noise on the WFE measurement induces non-negligible residuals on the reconstructed SFEs and WFEs. This is due to the very philosophy of the analytical method: to be applied, it requires very little experimental data (two measurements at two different wavelengths). To reduce the impact of noise, it is necessary to increase the amount of experimental data. This can be done in two main ways: repeat the measurements $N \approx 10{,}000$ times to reduce the SFE and WFE residuals by two orders of magnitude, as demonstrated on the previous section, or use more measurement data to apply the method, for example by using all the WFE measurements made over a wider spectral range, instead of selecting only two. However, this latter would mean redefining the very philosophy of the method. Finally, we have shown in Figure 85 that the residuals on SFE and WFE depend very little on the SFEs used to build the “sample” stack and WFE.

5. ZERNIKE-WISE METHOD

In the previous section, we saw that the analytic SFEs identification method, based on a linear system, is quite robust with respect to random layer thickness errors, but is too sensitive to noise in the WFE measurement, and for good reason: the method relies solely on two WFE measurements at two different wavelengths.

In this section, we present an alternative version of the method, this time based on a least-square fit of the SFEs using not only two WFE measurements, but all the WFEs acquired over a given spectral range.

5.1. Approach of the "Zernike-wise" method

The alternative method proposed here is based on the same mathematical assumptions as the previous one: we consider that the stack contains only one SFE for the L material, and another for the H material. These SFEs will be then estimated by fitting the WFE measurements. Of course, the natural problem is the difficulty to optimize many parameters at once. Convergence issues can occur with an excessive number of parameters. If we consider that the SFEs are defined by 55 Zernike coefficients, then the optimization induces 110 free parameters or even 165 if we also include the substrate SFE.
There are, of course, advanced methods for optimization with numerous parameters, applied in a wide range of scientific disciplines. Few examples are the Dimension-wise Particle Swarm Optimization (DPSO) method [84], or genetic algorithms [85]. However, we have chosen to select a simple, intuitive solving method based on gradient descent, rather than brute-force solving, but this implies to keep a reduced number of free parameters.

To get around the problem of the number of parameters, the idea is to consider, for example, that astigmatism on the SFEs can only lead to astigmatism on the WFE. If this is true for each aberration (or each Zernike mode), then we can simply divide the optimization into 55 successive, independent steps. At each step "*k*", we simply optimize the k^{th} Zernike mode on the L and H SFE, focusing only on the same k^{th} Zernike mode on the modeled and sample WFEs.

5.2. Mathematical and physical hypothesis

We propose here to give a demonstration that justifies the Zernike-wise method. The Zernike polynomials were introduced in Chapter 5, part 1.1 and, as a reminder, form an orthogonal basis. In this section, the k^{th} Noll Zernike polynomial (see Figure 61) is denoted $Z_k(x,y)$ and defined on the unit disk. As all Zernike polynomials form an orthogonal basis, the scalar product between two different polynomials is given by:

$$\langle Z_k, Z_m \rangle \equiv \iint [Z_k(x,y) Z_m(x,y) dxdy] = 0 \;\forall\; k \neq m$$

The orthogonal projections of SFEs or WFE onto the k^{th} polynomial of the basis is denoted here with an index *k*, and expressed from their scalar product:

$$\mathrm{SFE}_k^{\mathrm{L(H)}}(x,y) = \frac{\langle \mathrm{SFE}, Z_k \rangle}{\langle Z_k, Z_k \rangle} Z_k(x,y)$$

$$\mathrm{WFE}_k^{\mathrm{L(H)}}(x,y,\lambda_i) = \frac{\langle \mathrm{WFE}(\lambda_i), Z_k \rangle}{\langle Z_k, Z_k \rangle} Z_k(x,y)$$

By convention, we choose here to define the "RMS" normalization for each Zernike polynomial, so that the normalized scalar product between a surface and a Zernike polynomial is equivalent to the standard deviation of the projected surface:

$$std\left[\mathrm{SFE}_k^{\mathrm{L(H)}}(x,y)\right] \equiv \frac{\langle \mathrm{SFE}_k^{\mathrm{L(H)}}, Z_k\rangle}{\langle Z_k, Z_k\rangle};\ \forall k > 1 \tag{55}$$

Eq. 55 remains valid for any Zernike polynomial except for the piston Z_1, for which the standard deviation is necessarily zero. By definition, the sum of all projected SFEs or WFEs leads to the complete SFE/WFE:

$$\mathrm{SFE}^{\mathrm{L(H)}}(x,y) = \sum_{k=1}^{+\infty} \mathrm{SFE}_k^{\mathrm{L(H)}}(x,y)$$

$$\mathrm{WFE}^{\mathrm{L(H)}}(x,) = \sum_{k=1}^{+\infty} \mathrm{WFE}_k^{\mathrm{L(H)}}(x,y)$$

Similarly, the RMS convention allows the quadratic sum of standard deviations:

$$std\left[\mathrm{SFE}^{\mathrm{L(H)}}(x,y)\right] = \sqrt{\sum_{k=1}^{+\infty}\left\{std\left[\mathrm{SFE}_k^{\mathrm{L(H)}}(x,y)\right]^2\right\}}$$

Let us take Eq. 49 again, considering SFEs uniquely composed of a single Zernike mode "*k*":

$$\mathrm{WFE}(x,y,\lambda) = F_{\mathrm{L}}(\lambda)\mathrm{SFE}_k^{\mathrm{L}}(x,y) + F_{\mathrm{H}}(\lambda)\mathrm{SFE}_k^{\mathrm{H}}(x,y)$$

Or:

$$\mathrm{WFE}(x,y,\lambda) = \mathrm{WFE}(x,y,\lambda).Z_k$$

This result implies that $\mathrm{WFE}(x,y,\lambda)$ is uniquely composed of the same Zernike mode "*k*" as the SFEs. We thus deduce that if Eq. 49 is valid, a Zernike mode on the SFEs only modifies the WFE projected onto that same mode. We can therefore evaluate $\mathrm{WFE}_k^{sam}(x,y,\lambda)$ by projection onto the first 55 Zernike modes, and successively optimize $\mathrm{SFE}_k^{L(H)}(x,y)$. The Z_1 piston is excluded here. The case of this particular polynomial is detailed in section 5.3.

Based on this conclusion, we can generalize Eq. 49 into a matrix form:

$$\begin{bmatrix} WFE_2(x,y,\lambda) \\ \vdots \\ WFE_{55}(x,y,\lambda) \end{bmatrix} = M_L(\lambda) * \begin{bmatrix} SFE_2^L(x,y) \\ \vdots \\ SFE_{55}^L(x,y) \end{bmatrix} + M_H(\lambda) * \begin{bmatrix} SFE_2^H(x,y) \\ \vdots \\ SFE_{55}^H(x,y) \end{bmatrix} \tag{56}$$

With $M_L(\lambda)$, $M_H(\lambda)$ two diagonal matrices such that:

$$M_{\mathrm{L}}(\lambda) = F_{\mathrm{L}}(\lambda) * I;\ M_{\mathrm{H}}(\lambda) = F_{\mathrm{H}}(\lambda) * I$$

We have computed M_{L} and M_{H} matrices by simulation, successively calculating the $\mathrm{WFE}(x,y,\lambda)$ induced by a single $\mathrm{SFE}_k(x,y)$, and this for the first 55 Zernike Noll modes. The result of the calculation is shown in Figure 88. At the top appear $M_{\mathrm{L}}(\lambda = 630\,nm)$ and $M_{\mathrm{H}}(\lambda = 630\,nm)$ a wavelength for which linearization errors are high (see Figure 77). At the bottom are shown the same matrices without the diagonal terms. It thus appears that these two matrices are almost diagonal, as predicted by Eq. 56.

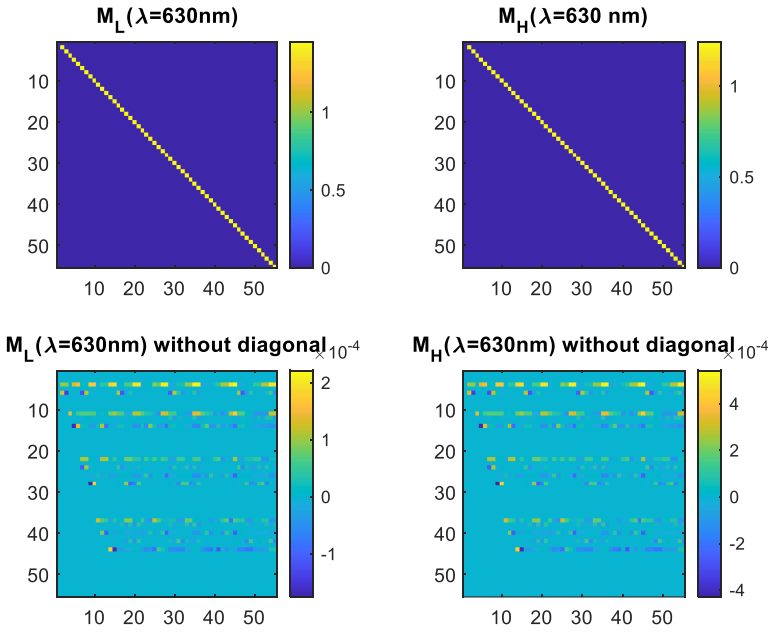

Figure 88: (Up): Simulation of M_L and M_H at $\lambda = 630\,nm$ and for 55 Noll Zernike modes computed. (Down): Simulation of: M_L and M_H with the diagonal terms removed.

Non-diagonal terms reflect how a $\mathrm{SFE}_k(x,y)$ will induce a coupling with $\mathrm{WFE}_{p\neq k}(x,y,\lambda)$ terms. Their value depends on two main factors:

- The accuracy on the Zernike polynomial decomposition: despite the addition of a Gram-Schmidt ortho-normalization [86], the Zernike polynomial decomposition cannot be perfect, due to the spatial sampling of the maps.
- Linearization errors.

Despite these two sources of error, the non-diagonal terms remain four orders of magnitude below the value of the diagonal terms. We can reasonably conclude that it is possible to fit each $\mathrm{SFE}_k(x,y)$ independently, from the Zernike decomposition of the $\mathrm{WFE}_{sam}(x,y,\lambda)$.

5.3. Test on some specific cases

We saw that the analytic method presented in sections 2 and 0 was purely mathematical, using Eq. 50 and 53 to analytically find the two (or three) SFEs. For the Zernike-wise method presented here, there is no longer about using a direct analytical expression, but rather of proceeding by an iterative fit. In this section, we will test this approach in a few cases. We will then reproduce the same sensitivity analysis as for the analytical method (Section 4).

Identification of two SFEs

As before, a "sample" WFE is generated from a sample stack, between **550 and 900 nm wavelengths, in 1 nm steps**. The aim is still to identify SFEs from the sample stack with the lowest possible residual. For the time being, the SFEs have zero mean value and generated in a similar way to that presented in section 3.1.

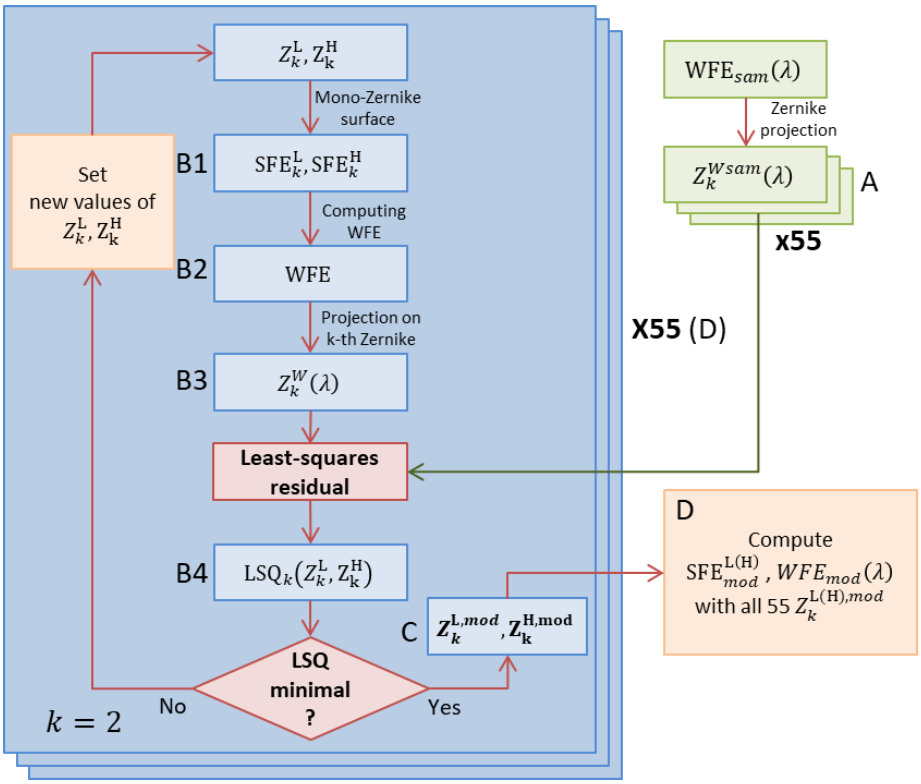

Figure 89: Schema of the optimization process used to identify the whole $Z_k^{L,mod}$ and $Z_k^{H,mod}$. The green blocks correspond to the sample, and the blue ones correspond to the modeled quantities.

Figure 89 depicts a simplified diagram of the process used to apply the Zernike-wise method. The latter is divided in the following steps:

Step A: The sample WFE is projected into 55 Noll-Zernike, giving 55 $WFE_k(x, y, \lambda)$. The standard deviation of the projected maps $\boldsymbol{Z_k^{Wsam}(\lambda) = std[WFE_k(x, y, \lambda)]}$ is then calculated for each wavelength.

Step B:

- **B1**: Creation of two mono-Zernike surfaces $SFE_{k=2}^{L(H)}(x, y)$ for k = 2 with standard deviation $Z_{k=2}^L$(and $Z_{k=2}^H$) arbitrarily defined.
- **B2**: A dichroic stack is then modeled with these SFEs mono-Zernike.
- **B3**: The WFE of this stack is computed.
- **B4**: The value of the coefficient $Z_{k=2}^{Wmod}(\lambda)$ is calculated.
- **B5**: The least-squares residual $\boldsymbol{LSQ_{k=2}(Z_{k=2}^L, Z_{k=2}^H)}$ is then calculated:

$$\mathrm{LSQ}_{k=2} = \sum_{\lambda_{min}}^{\lambda_{max}} [Z_2^{Wmod}(\lambda_i) - Z_2^{Wsam}(\lambda_i)]^2$$

Step C: A bivariate optimization algorithm is applied to identify $Z_{k=2}^{L,mod}, Z_{k=2}^{H,mod}$ that minimize LSQ_2 calculated in step 2.

Step D: Once $Z_{k=2}^{L,mod}, Z_{k=2}^{H,mod}$ have been identified, steps 2 and 3 are repeated for k ranging from 3 to 55. We then obtain the 2*55 parameters needed to compute $SFE_{mod}^L(x, y)$ and $SFE_{mod}^H(x, y)$.

From the two SFEs, the stack is reconstructed and the WFE is modeled. Figure 90 compares the sample (A, B) and modeled (C, D) SFEs. The residuals (E, F) on the SFEs reconstruction are less than 0.01 nm RMS. The process presented here is therefore highly efficient in recovering the SFEs, with residuals of the same order of magnitude as those presented in part 3.1 with the previous method.

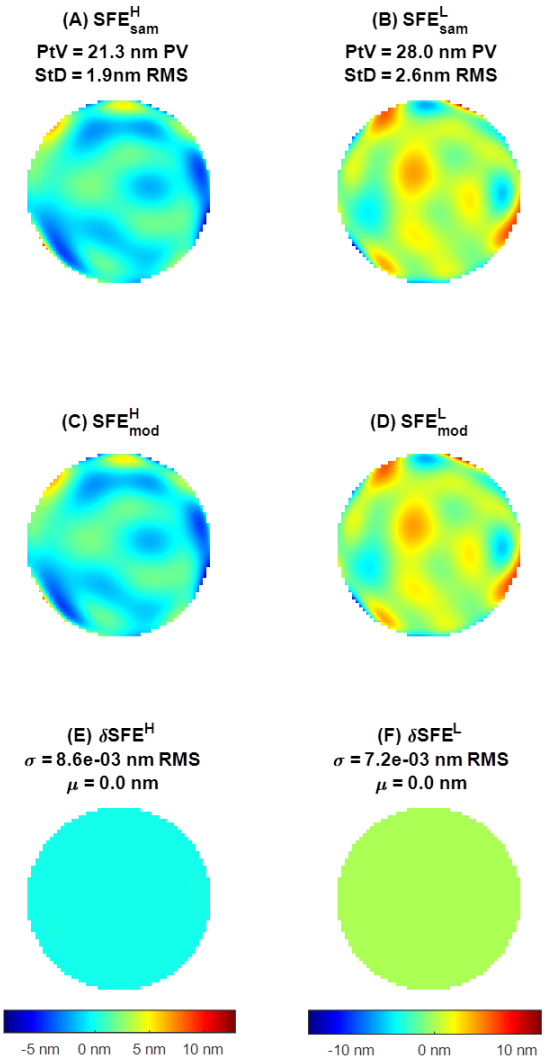

Figure 90: (A, B) Sample SFE used to generate the "sample WFE". (C, D): Modeled SFE. (E, F): Residuals.

Identification of SFEs means values

The average SFEs value corresponds to the projection onto the Zernike "Piston": Z_1^{L} and Z_1^{H}. The piston case is different from other Zernike polynomials for two reasons. Firstly, we have seen that the average of a sample WFE has no physical meaning, in which case Z_1^{Wech} is not an accessible data (see section 3.2). The process presented in the previous paragraph is therefore not applicable to the piston. Secondly, unlike other Zernike modes, the addition of terms Z_1^{L} and Z_1^{H} will impact the value of all $Z_k^W(\lambda)$. By definition, Z_1^{L} and Z_1^{H} are related to the average thicknesses of the stack, and therefore to its spectral response [58]. With a new spectral response, $Z_k^W(\lambda)$ then differs. An example is shown in Figure 91, where several $Z_{k=5}^W(\lambda)$ are compared with the only difference being the value of Z_1^{L} and Z_1^{H} in SFEs. We mainly observe a spectral shift of about 1 nm, which is related to Z_1^{L} and Z_1^{H} values, -17 nm and 11.2 nm respectively.

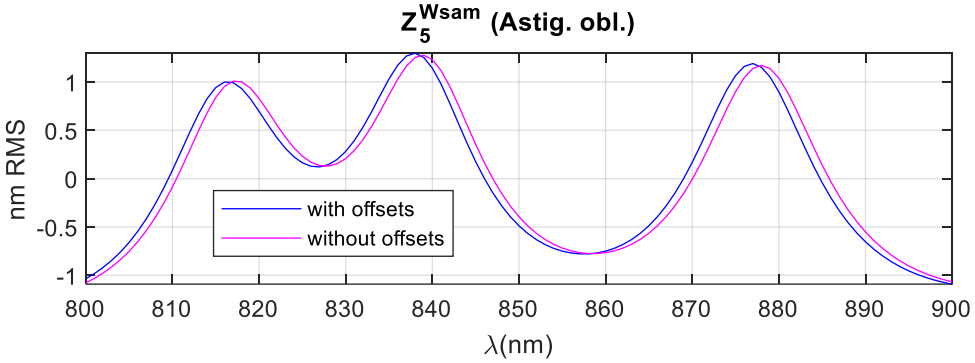

Figure 91: Sample $Z_5^{Wsam}(\lambda)$ computed from SFEs with piston (blue) and without piston (pink). The piston values are: Z_1^L=-17.0 nm and Z_1^H=11.2 nm.

The values of Z_1^L and Z_1^H can thus be identified during the fit of any $Z_k^{\mathrm{W}sam}(\lambda)$. Here, we will take $Z_{k=5}^{\mathrm{W}sam}(\lambda)$ as an example, by considering SFEs composed of oblique astigmatism and piston. The aim is to minimize the 4-variable function $\mathrm{LSQ}_5(\boldsymbol{Z_1^L}, \boldsymbol{Z_1^H}, Z_5^{\mathrm{L}}, Z_5^{\mathrm{H}})$. For all other Zernike modes, it is sufficient to take into account the fitted values for $Z_1^{\mathrm{L}}, Z_1^{\mathrm{H}}$ and proceed as described in the previous section.

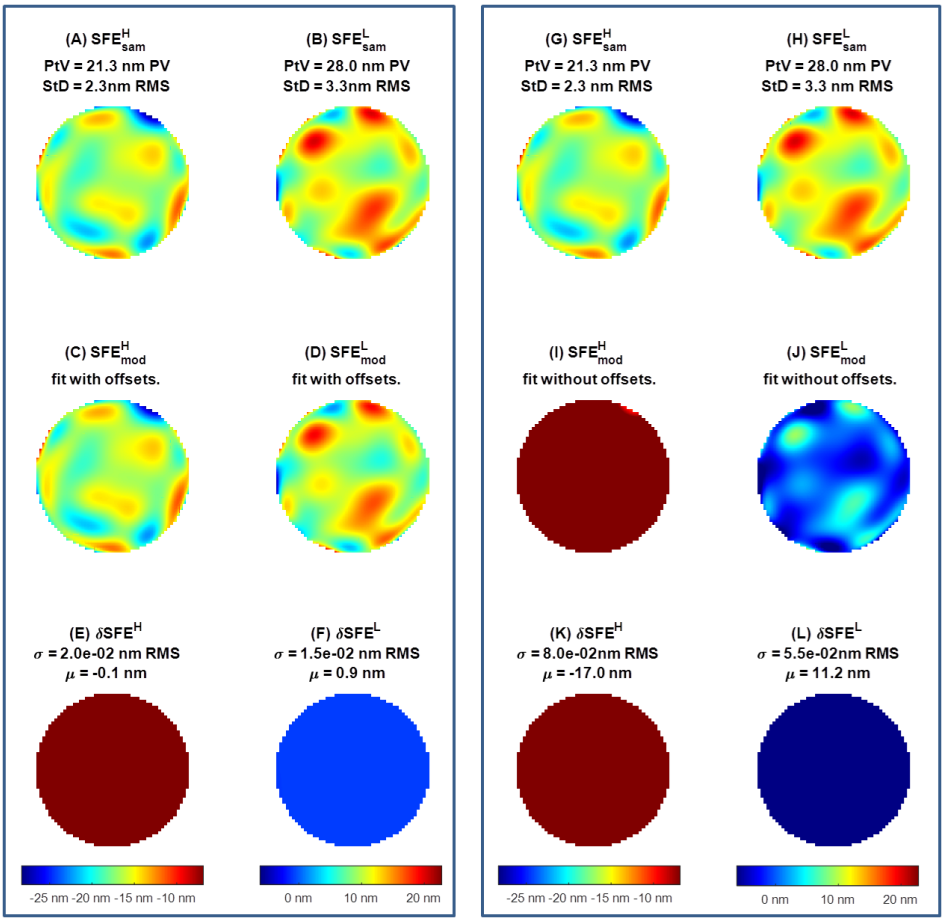

Figure 92: Simulation of modeled SFE on dichroic mirror coating, with $\overline{SFE(x,y)} \neq 0$. (A, B): Relative SFE^H and SFE^L used as sample. (C, D): Modeled SFE with the Zernike-wise method with piston identification. (E, F): residuals, in nm RMS. (G, H, I, J, K, and L) Equivalent simulation without piston identification.

On the left of Figure 92 are the SFEs used as samples (A, B), then the SFEs obtained with the Zernike-wise method (Figure 92: C, D), including the pistons. The residuals (Figure 92; E, F) show that the new method retrieves SFEs with a standard deviation of less than 0.1 nm. The pistons on the SFEs are -17 nm for L, and 11 nm for H, and the fit also recovers these pistons, with an error of less than 1 nm. Simulation parameters are identical to those in Part 3.2.

On the right side of Figure 92, the same sample SFEs (Figure 92: G, H) appear, but this time applied without considering the pistons of the SFEs (Figure 92: I, J). Unsurprisingly, the mean error (Figure 92: K, L) on the fit corresponds well to the value of Z_1^{L} and Z_1^{H}. The standard deviation on the SFEs reconstruction is still correct, being less than 0.1 nm RMS too. However, ignoring Z_1^{L} and Z_1^{H} leads to an error between the sample WFE and the reconstructed WFE. Indeed, ignoring the pistons of the SFEs leads to residuals on the WFE that can reach almost 1 nm RMS (Figure 93, in orange). In contrary, taking these pistons into account leads to residuals on the WFE that rarely reach 0.05 nm RMS.

In conclusion, even if the fit is not as good as with the analytical method (section 3.2, Figure 80: residual on both SFE = 0.013 nm), we can conclude that the residuals on the WFE remain acceptable, and that it is possible to identify Z_1^{L} and Z_1^{H} with an error of less than 1 nm (Figure 92: E, L).

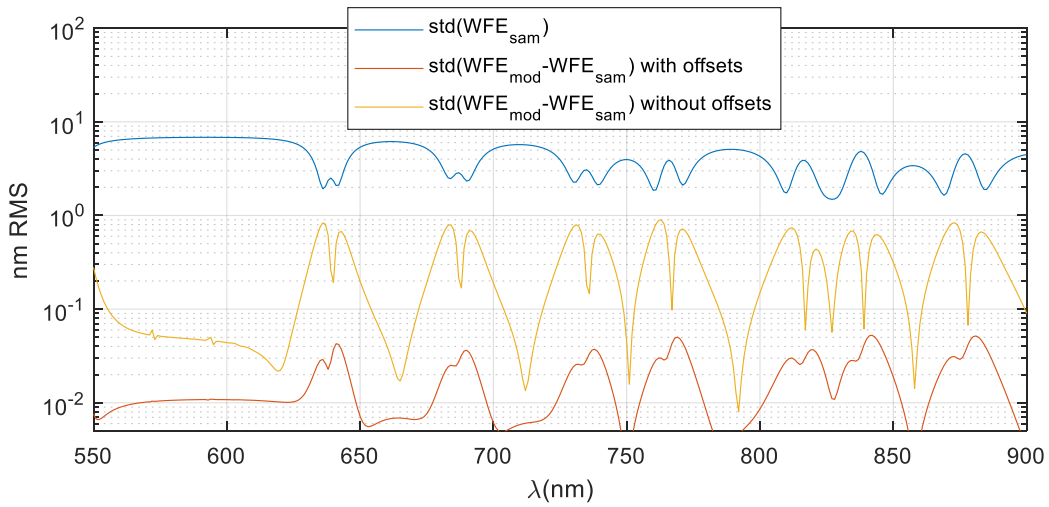

Figure 93: Residuals on modeled WFE at each λ with respect to sample WFE (blue).

Identification of the substrate SFE

It is easy to modify the analytic method to include identification of the substrate SFE, labeled $\mathrm{SFE}^{\mathrm{S}}(x, y)$. In section 3.3, we established that $\mathrm{SFE}^{\mathrm{S}}(x, y)$ induces an achromatic WFE due to the air gap:

$$\mathrm{WFE}_{sub}(x, y, \lambda) = 2\, n_a \cos(\gamma)\, \mathrm{SFE}^{\mathrm{S}}(x, y)$$

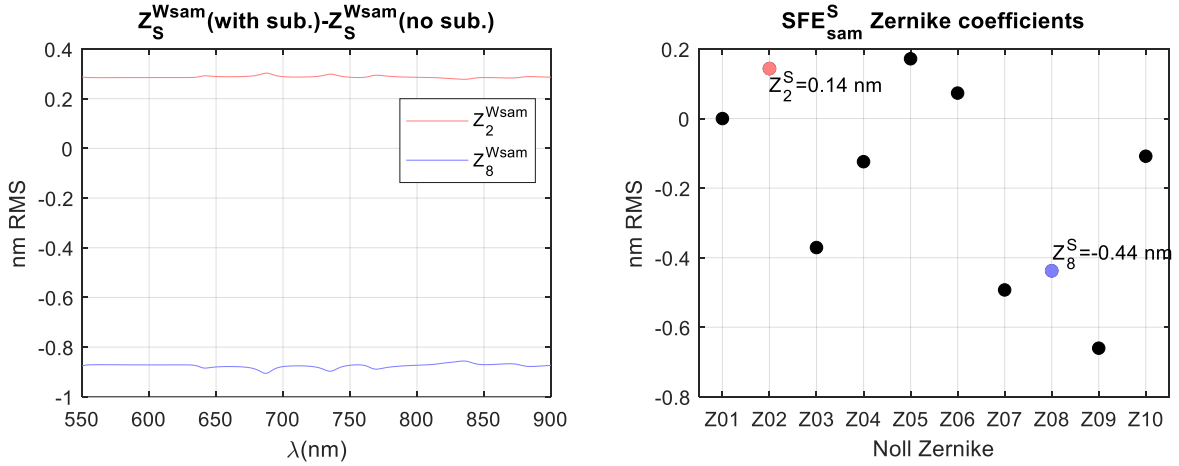

*Figure 94: (**Left**) Difference between WFE sample with" and "without" substrate contribution (projection on Z2 and Z8 only). (**Right**): Projection of sample substrate SFE on 10 first Noll Zernike (Z2 and Z8 are highlighted).*

This additional WFE manifests itself as a vertical offset of each $Z_k^{\mathrm{W}sam}(\lambda)$. This is clearly shown in Figure 94 (left), where the difference between WFE with or without SFE_S is computed for two Zernike modes (Z2 and Z8). On right of Figure 94 are plotted the 10 first Zernike coefficients of the corresponding substrate map Z_k^{S}. The achromatic offset (colored curves) corresponds then to $2n_a\cos(\gamma)\,Z_k^{\mathrm{S}}$, with γ = 0°, and n_a = 1.

Consequently, the aim is to minimize the deviation $\mathrm{LSQ}_k\left(Z_k^{\mathrm{L}}, Z_k^{\mathrm{H}}, \boldsymbol{Z_k^{\mathrm{S}}}\right)$ for each value of k, which is now a 3-variable function (apart from LSQ_5, which will be a 5-variable function if we also search for the piston terms of the SFEs: Z_1^{L} and Z_1^{H}). In Figure 95 are compared the results of a reconstruction of a sample stack (A, B, C) featuring 3 SFEs, generated identically to part 3.3. The iterative fit is applied to the first 55 Zernike modes, first taking into account the SFE of the substrate (Figure 95: D, E, F), then the residuals are calculated (Figure 95: G, H, I). Next, the same stack is modeled without taking substrate the SFE into account, giving J, K, L, M, N, and O.

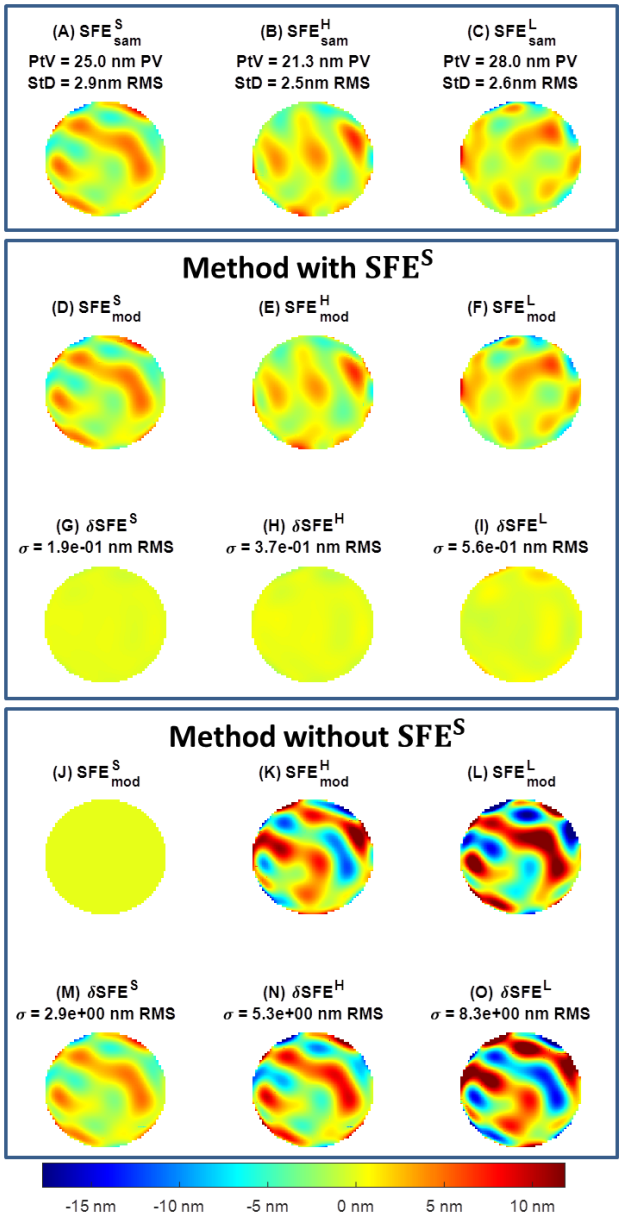

Figure 95: Comparison of "3-SFE" and "2-SFE" Zernike-wise methods. (A, B, C): Sample coating (and substrate) SFE. (D, E, F): Modeled SFE using the "3-SFE" method. (G, H, I): Residuals. (J, K, L, M, N, O): Equivalent simulation using the "2-SFE" method.

As observed in section 3.3 with the analytical method, it is clear that the SFE of the substrate must be considered. The three SFEs reconstructed have residuals between 0.2 and 0.6 nm RMS when the substrate is included, while the deviations are of several nanometers RMS without. With the triple SFE Analytical method presented in part 3.3, residuals were of the order of 0.01 nm RMS, so better than presented here. Nevertheless, the Zernike-wise method gives sufficiently accurate results for our study, and there are several ways for improvement that could not all be investigated here, such as the use of a more accurate solver.

It is also interesting to note the anti-correlation that appears in the residual maps with the fit ignoring the SFE^S (Figure 95: N, O). We have shown that substrate SFE^S causes achromatic WFE, which translates into a vertical shift of each $Z_k^{Wsam}(\lambda)$ (see Figure 94). It seems that the fitting method "without SFE^S" is unable to reproduce this vertical shift, except by introducing, for example,

excessively high values of Z_k^L and Z_k^H compared to their actual values, and with $Z_k^L \approx -Z_k^H$. The combination of these two parameters results in $Z_k^{Wmod}(\lambda)$ closest to $Z_k^{Wsam}(\lambda)$ but naturally makes no physical sense. As this mathematical artifact appears for each Zernike, the result is then anti-correlated SFEs maps (Figure 95: K, L).

The simulations presented here demonstrate that the Zernike-wise method gives equivalent results to the method based on an analytical calculation of SFEs. In addition, both methods can take into account thickness offsets as well as substrate SFE. In the following section, we will compare the results of the two methods when random thickness and measurement errors are considered.

5.4. Sensibility analysis and comparison with analytic method

In this section, we reproduce the same sensitivity analyses as presented in section 4. A comparison with the results obtained with the analytical method will be shown in order to assess the improvement with this new approach.

Zernike-wise method sensibility to random thickness errors

Figure 96 compares the two Monte Carlo simulations carried out with the two methods in relation to the thickness errors introduced according to the procedure described in section 4.1. The SFE considered here are identical to those used in the simulations presented in 4.1 and 4.2. The Zernike-wise method seems equivalent to the previous one in terms of WFE residuals (Figure 96 down, dashed lines) with a maximum median value of 0.2 nm RMS, and 95% quantiles are around 1 nm RMS when σ_{rand} exceeds the – pessimistic – value of 0.75 % RMS. We can therefore consider that thickness errors are not a showstopper for either method.

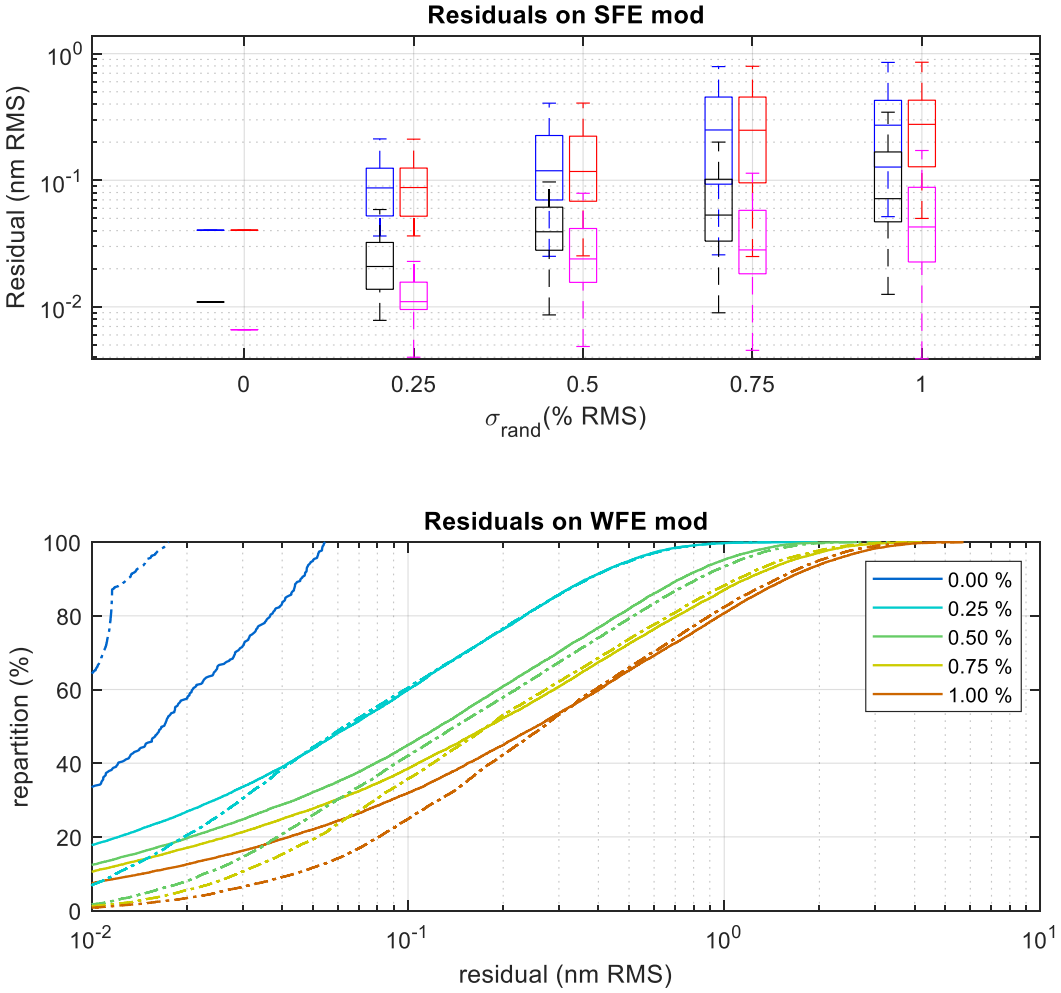

*Figure 96: (Top) Comparison between: "Analytical" fit with random thickness error on layers (**H**, **L**) versus "Zernike-wise" fit (**H**, **L**). (Down) Residuals on WFE fit for both methods represented as cumulative distribution for each σ_{rand}. The dashed lines correspond to the simulation with Zernike-wise fit.*

Zernike-wise method sensibility to noise on sample WFE

The differences between the two methods will be seen mainly in their robustness to measurement noise. A Monte-Carlo simulation identical to that in section 4.2 was carried out. The results are shown in Figure 97.

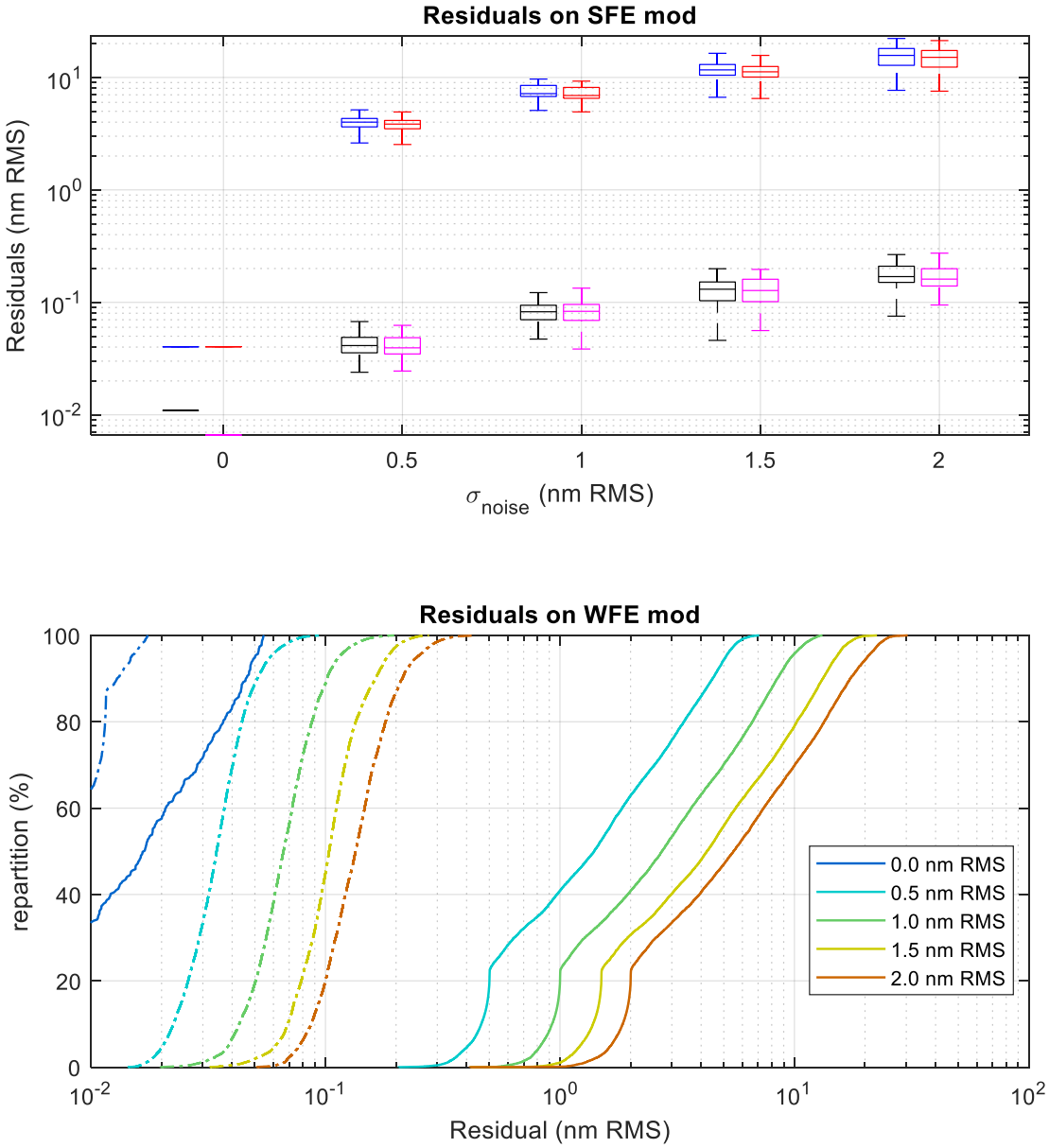

*Figure 97: (Up) Comparison between: "analytical" fit application with WFE noise (**H**, **L**) versus "Zernike-wise" fit (**H**, **L**). (Down) Residuals on WFE fit for both methods represented as cumulative distribution for each σ_{noise}. The dashed lines correspond to the simulation with Zernike-wise fit.*

This time, the Zernike-wise method provides clearly much better results, with residuals on the SFEs of the order of 0.2 nm RMS with σ_{noise} = 2 nm RMS. With this new strategy, we have therefore reduced the residuals by two orders of magnitude on the SFEs. In terms of WFE reconstruction (Figure 97, down, dashed curves), the residuals are also very low: with σ_{noise} = 2 nm RMS (red), no residual exceeds 0.3 nm RMS, and the median value is under 0.2 nm RMS.

To achieve the same performance with the analytical method, we would have had repeated the measurements several thousand times at two WFEs. Assuming that the modelled noise on the sample WFEs is realistic, we can estimate that this new method recovers properly the SFEs (and TFEs) of the dichroic stack. Of course, it is possible to multiply measurements over the 550-900 nm bands to further reduce residuals on the WFE.

6. CONCLUSION

In this chapter, we presented the two methods for recovering the SFEs, which describe the non-uniformity of the layers of the entire dichroic coating, from stack optical formula data and WFE measurements with the OBSERVE bench. The first method is established by making the realistic assumption that the TFEs of the layers are unique for each material of the stack. Using the equations of thin-film theory, we were able to set a linear system that enables to recover the SFEs of each material, as well as the SFE of the substrate, from two WFE measurements at different wavelengths. Simulations were then carried out, proving the analytic method's effectiveness in a variety of situations. One limitation of this method is the introduction of noise to the WFE measurement, resulting in WFE residuals exceeding 15 nm RMS (maximum) when the noise on sample WFE exceeds 2 nm RMS (Figure 84). Consequently, this has led us to develop a second method.

The second method is based on an iterative fit. The idea is to describe SFEs and WFE with Zernike polynomials, and we have seen that it is possible to progressively rebuild SFEs from WFE measurements over a wide spectral range. Although based on the same mathematical approach as the former and taking the development a step further, the strategy used, and the resources required to apply it are different. As a result, this Zernike-wise turns out to offer very encouraging results, particularly in the case of noisy WFE, where the residuals on WFE reconstruction are 0.3 nm RMS at maximum when σ_{noise} = 2 nm RMS.

In the following chapter, both methods will be applied to data acquired by OBSERVE. The results of both will be compared under various illumination conditions.

7. REFERENCES

73 M. Baron, B. Sassolas, L. Pinard, and A. Ealet, "Numerical modelling for retrieval of the coating thickness variations from wavefront errors measurements" Opt. Express 31, 32968-32986 (2023)

74 Tien, C.-L. Special Issue "Advanced Coating Technology by Physical Vapor Deposition and Applications". Coatings 2023, 13, 467. https://doi.org/10.3390/coatings13020467

75 Baron, B. Sassolas, P.-A. Frugier, L. M. Gaspar Venancio, J. Amiaux, M. Castelnau, F. Keller, G. Dovillaire, P. Treimany, R. Juvénal, L. Miller, L. Pinard, and A. Ealet, "Measurement and modelling of the chromatic dependence of a reflected wavefront on the *Euclid* space telescope dichroic mirror", Proc. SPIE 12180, Space Telescopes and Instrumentation 2022: Optical, Infrared, and Millimeter Wave, 121804V (2022); https://doi.org/10.1117/12.2630072

76 M. Scherer, H. Hagedorn, W. Lehnert, J. Pistner, "Innovative production of thin film laser components" Proc. SPIE 5963, Advances in Optical Thin Films II, 596319 (2005); doi: 10.1117/12.625226

77 https://fr.mathworks.com/help/optim/

78 A. Brenner, S. Senderoff, "Calculation of Stress in Electrodeposits from the Curvature of a Plated Strip" J. Res. Natl. Bur. Stand., Vol. 42, No. 2, p. 105 (1949)

79 Giacomo. P. Giacomo, « Propriétés chromatiques des couches réfléchissantes multi-diélectriques. » J. Phys. Radium, (1958), 19 (3), pp.307-311. 10.1051/jphysrad: 01958001903030700. jpa-00235839

80 G. Carlow, B. T. Sullivan, C. Montcalm, and A. Miles, "Effect of an optical coating on in-band and out-of-band transmitted and reflected wavefront error measurements", Appl. Opt. 59, A135-A142 (2020)

81 Wang B, Fu X, Song S, Chu HO, Gibson D, Li C, Shi Y, Wu Z. "Simulation and Optimization of Film Thickness Uniformity in Physical Vapor Deposition". Coatings. 8(9):325. (2018).

82 L.M Gaspar Venancio, (European Space Agency), 2020, "Wave front reconstruction for dielectric coatings at arbitrary wavelength" (patent: US 2020/0348228 A1). UPSTO, https://pubchem.ncbi.nlm.nih.gov/patent/US-2020348228-A1

83 P-O. Caron, L. Lemardelet "The Variance Sum Law and Its Implications for Modelling". Université d' Ottawa (2021)

84 J. Schlauwitz, P. Musilek. "Dimension-Wise Particle Swarm Optimization: Evaluation and Comparative Analysis". Applied Sciences. 2021; 1113:6201.

85 V. Magnin, « Contribution à l'étude et à l'optimisation de composants optoélectroniques. Modélisation et simulation. » Université des Sciences et Technologie de Lille – Lille I, 1998. Français.

86 D.Gatinel. « Une nouvelle méthode de décomposition polynomiale d'un front d'onde oculaire ». Organes des sens. Université Paris Saclay (COmUE), 2017. Français. NNT: 2017SACLV042

Chapter 7

Dichroic model validation with OBSERVE data

In this last chapter we will use the OBSERVE bench dataset to test the methods to model the stack and predict WFE, as presented in Chapter 6. Our aim is to validate a model of the dichroic stack that can predict its WFE and reflectivity for any illumination condition: wavelength, incidence and polarization. To do this, we will attempt to identify as precisely as possible the thickness non-uniformities of all the layers in the stack. This will enable us to calculate the optical properties of the stack at any point on the mirror

First, we outline the experimental data requirements necessary for accurately creating the models. Then, we present and analyze the data obtained within the timeframe of this thesis. Next, we apply the Zernike-wise method, as discussed in the previous chapter, to these data, generating models of the dichroic coating. These models will then discussed and different tests in different conditions will be presented using other datasets from OBSERVE and simulated data.

1. WFE MEASUREMENTS COMPAIGN WITH OBSERVE

We would like to provide a model of the dichroic stack that can predict its WFE and reflectivity for any illumination condition: wavelength, incidence and polarization. To do this, we have established two possible methods for identifying variations in the thickness of mirror layers, which are presented in the last chapter.

In this first part, we will present the experimental data requirements for characterizing the dichroic mirror. This campaign is part of a wider test plan drawn up by the *Consortium*, due to be completed after the end of this thesis.

1.1. Needs in terms of WFE measurements

We have established in previous chapter two possible methods for identifying variations in the thickness of mirror layers:

- To be applied, the first method requires at least two WFE measurements at two very specific wavelengths λ_1 = 593 and λ_1 = 662 nm (see Chapter 6, part 3.1), at a single angle of incidence and at a single incident polarization state.

- The second method uses more experimental data (see Chapter 6, part 5). It requires WFE measurements over the entire reflection band of the mirror, at a single angle of incidence and a single incident polarization state too.

Only WFE measurements at one angle of incidence/polarization are then required to compute the dichroic coating SFE. Of course, this excludes possible cross-validation of models by, for example, applying both methods to WFEs at a different angle of incidence, or data used to compare actual reflectivity with that calculated via the models.

Consequently, for a given spectral band, we have chosen to record the WFE and reflected intensity at least 0° and 19° incidence, which represent the greatest angle difference available on the bench. Finally, all measurements are made in pure S and pure P polarization, i.e. with input and output polarizers both set to "S" and the same for P. This multiplicity of measurements will therefore be useful for confirming the model results.
Naturally, these measurements require knowledge of the actual accuracy of the OBSERVE bench. This has been assessed during the commissioning and calibration phases, used to validate the bench. Depending on the level of final accuracy, repeated measurements may be required.

1.2. Required data for the thesis

Here, we present the various measurements that make up the campaign. Table 24 lists the four tests, labelled "**VB" for Visible Band**, such R > 25% in the dichroic mirror. We also define the polarization states as X/Y where X and Y are the polarization states in the dichroic mirror reference frame of the incident and reflected beam respectively. They correspond to a specific tuning of input and output polarizers (see Chapter 4, Figure 46 and Figure 52). X and Y can have the following labels:

- S for S-polarized light
- P for P-polarized light
- N for unpolarized light

Label	Band (nm)	Step (nm)	AOI(°)	Polarization state
VB 00° S/N	539 to 928	1	0	Pure S
VB 00° P/N	539 to 928	1	0	Pure P
VB 19° S/N	539 to 928	1	19	Pure S
VB 19° P/N	539 to 928	1	19	Pure P

Table 24: LMA's Euclid dichroic mirror WFE characterization tests

The various operations required on the bench have already been described in Chapter 4, part 2.3. As a reminder, 4 series of measurements are required to obtain a dichroic mirror WFE dataset, for example the dataset "VB 00° S/N" needs:

- $\mathbf{WFE}_{DC/ref}^{meas}\mathbf{(VB)}$: Referenced measurement on *Euclid* dichroic mirror.
- $\mathbf{WFE}_{DC}^{meas}(\boldsymbol{\lambda_{ref}})$: Static measurement on the dichroic mirror at λ_{ref} = 594.1 nm.
- $\mathbf{WFE}_{plan/ref}^{meas}\mathbf{(VB)}$: Referenced measurement on the Zeiss plane mirror.
- $\mathbf{WFE}_{plan}^{meas}(\boldsymbol{\lambda_{ref}})$**:** Static measurement on the plane mirror at λ_{ref} = 594.1 nm.

Of course, the four acquisitions are all carried out with the bench tuned at normal incidence, with source polarizer tuned in order to have pure S-polarized light before reflection on the dichroic mirror and the reference mirror.

1.3. Obtained WFE measurements

As the output polarizer has been removed from the bench, all data presented in this thesis will be in P/N or S/N polarization. The interest of the second polarizer is mainly to investigate cross-polarization effects, which is not the topic of this thesis.

WFE measured at normal incidence

We present first at the top of Figure 100 some examples of WFE from the VB-19°-P/N dataset, at three wavelengths: **600, 755, and 850 nm**, for 19° in incidence and P/N polarization. As it was expected, the WFE appears to be highly wavelength-dependent.

The middle of Figure 100 shows the RMS values of the maps for the 549-929 nm range, at 0° in incidence and in S/N and P/N polarizations. The RMS values of the three maps at 600, 725 and 850 nm have been indicated with colored markers.

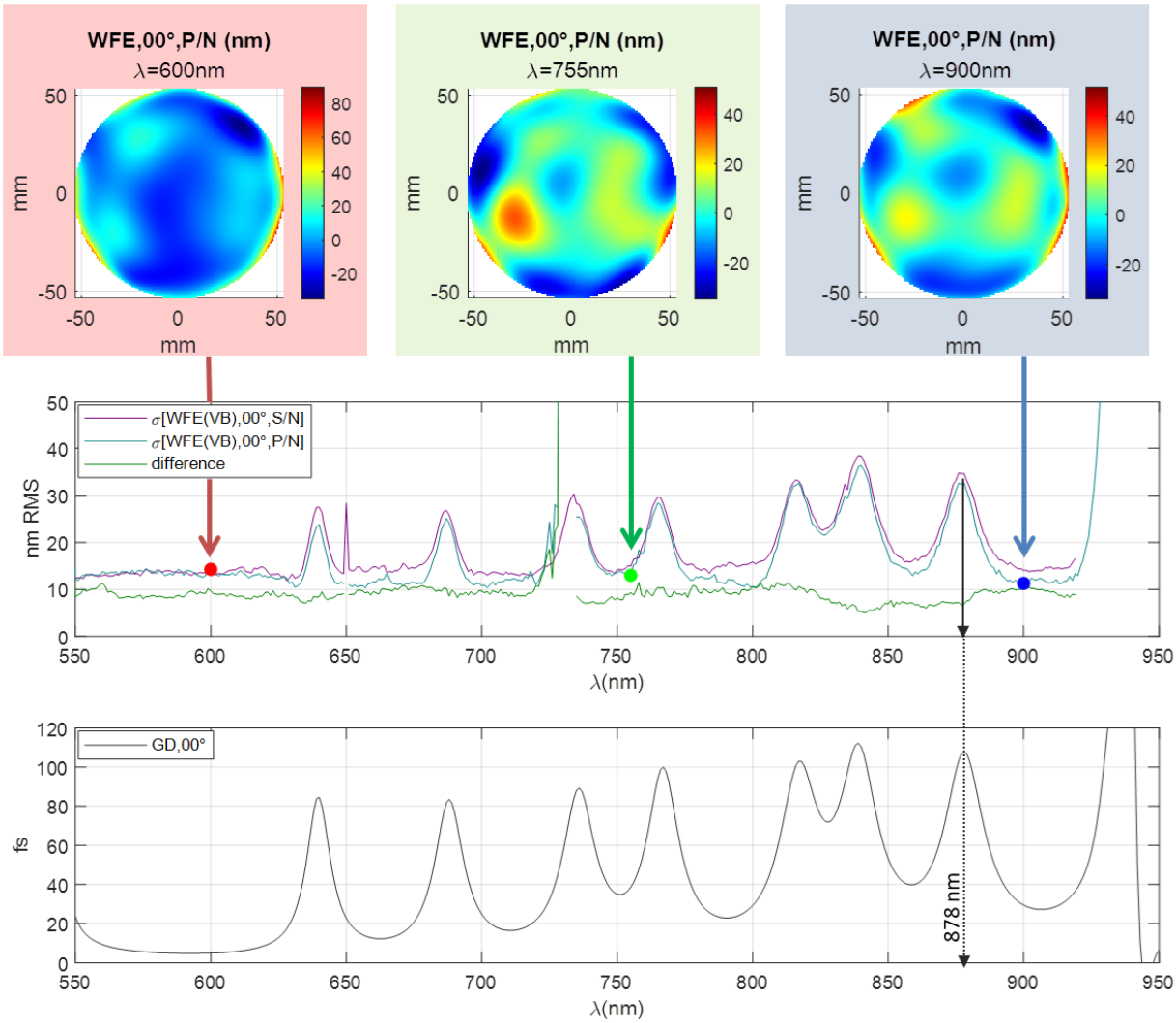

*Figure 98: (**Top**) WFE maps at three wavelengths, normal incidence and P/N. Tilts are removed. (**Middle**) Standard deviation of WFE is computed at 0° (P/N, S/N, and difference). (**Down**) Theoretical Group Delay in reflection on Euclid dichroic mirror at normal incidence.*

The RMS value of the WFE maps also appears to vary with wavelength, with oscillations correlated to the Group Delay (GD) presented at the bottom of Figure 98. See the example with the GD peak at λ = 878 nm. For a dielectric mirror as the dichroic mirror of *Euclid*, the GD is defined as the (reflected) theoretical phase derivative with respect to the angular optical frequency, and is commonly used in optics to characterize the chromaticity of optical components. Its unit is the femtosecond (fs).

$$\mathrm{GD}(\lambda) = \frac{\partial \varphi_R}{\partial \omega}(\lambda)$$

This correlation between GD and WFE is expected, as the WFE materializes phase differences between different points on the mirror. The higher the phase sensitivity (high GD) is, the more deviations in thickness on the mirror will result in increased phase differences, leading to higher WFE.

Theoretically, at normal incidence, the RMS in P/N and S/N should be strictly equal, as the GD is. However, the RMS of the difference between the two WFE maps at each wavelength, shown in green, is around 9 nm RMS. This difference may have several origins:

- Errors due to the bench reproducibility, which is 6 nm RMS
- Some bench's biases
- An optical activity of the dichroic mirror, such as birefringence.

The differences between S and P are also visible in the Zernike projection. Figure 99 shows the 16 first modes. This figure also shows that the chromaticity due to the dichroic coating does not manifest in the same way on all aberrations. We see clearly in some Zernike modes the GD and WFE variations structures that contain **oscillations between 30 and 80 nm (wavelength) periods**. The most pronounced manifestations are on radially symmetrical Zernike modes such as Z4 and Z7. In contrast, the chromaticity due to the dichroic coating seems negligible on Z5 and Z10. Based on the assumptions of the Zernike-wise method, this means that the SFEs of the stack mainly contain radial aberrations such as defocus. This seems to match the observations made by OBJ [59], who assume that the stack has a highly domed profile.

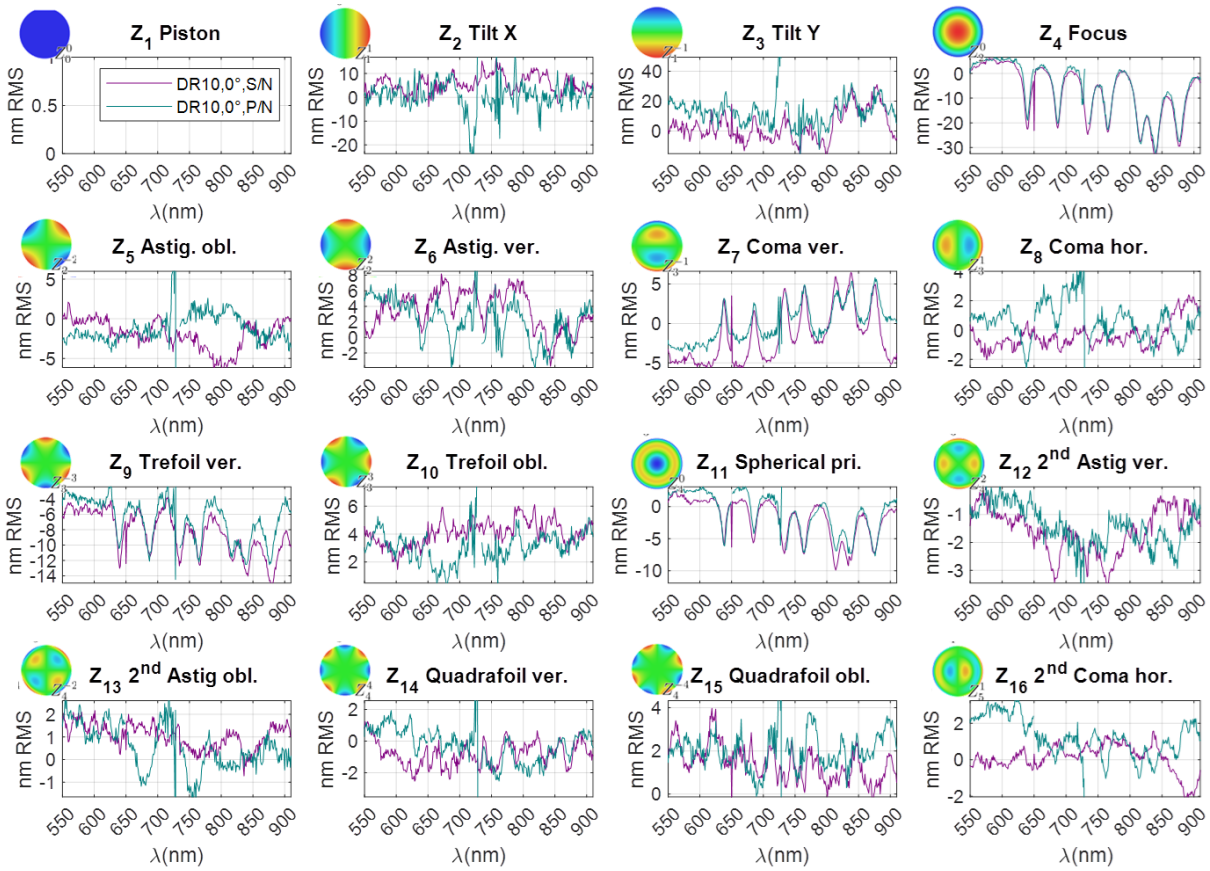

Figure 99: Zernike projection of WFE on 16 first modes (normal incidence, S/N and P/N).

In addition, it seems that the WFEs (and therefore the SFEs) are dominated by low-order aberrations. From Z11 to Z55, the amplitude of WFE's Zernike modes rarely exceeds 3 nm RMS. These high-order aberrations are probably mostly dominated by measurement noise. In section 2.2 we will evaluate the noise level for each aberration, which will show whether or not it is possible to extract interesting information about the coating.

Finally, the case of oblique trefoil (Z10, Figure 99) is interesting. The dichroic coating's chromaticity does not appear, meaning that the SFEs do not contain trefoil (or else, very little). However, if the measurement on Z10 was dominated by noise, the latter should have a zero mean value. In contrary, the Z10 average value is about 4 nm RMS in both polarizations. Since bench aberrations are

suppressed during the acquisition procedure, this residual trefoil could be related to the dichroic mirror substrate. The substrate-related WFE is indeed achromatic (see Chapter 6, part 3.3); however Amos measurements of the substrate after polishing and before deposition [54] do not reveal significant trefoil aberration. But it is worth mentioning that the dichroic mirror holder can add an additional trefoil on the substrate. Indeed, the holder supports the dichroic mirror by a 3 point support at 120° each that could produce a strain field consistent with the trefoil deformation (see Chapter 4, Figure 50). That is then outstanding example of the effectiveness of the Zernike-wise method (see Chapter 6, part 5) that must allow identifying a maximum number of chromatic aberrations (related to the coating SFEs) and achromatic aberrations related to the substrate SFE and residual bending.

WFE measured at oblique incidence (19°)

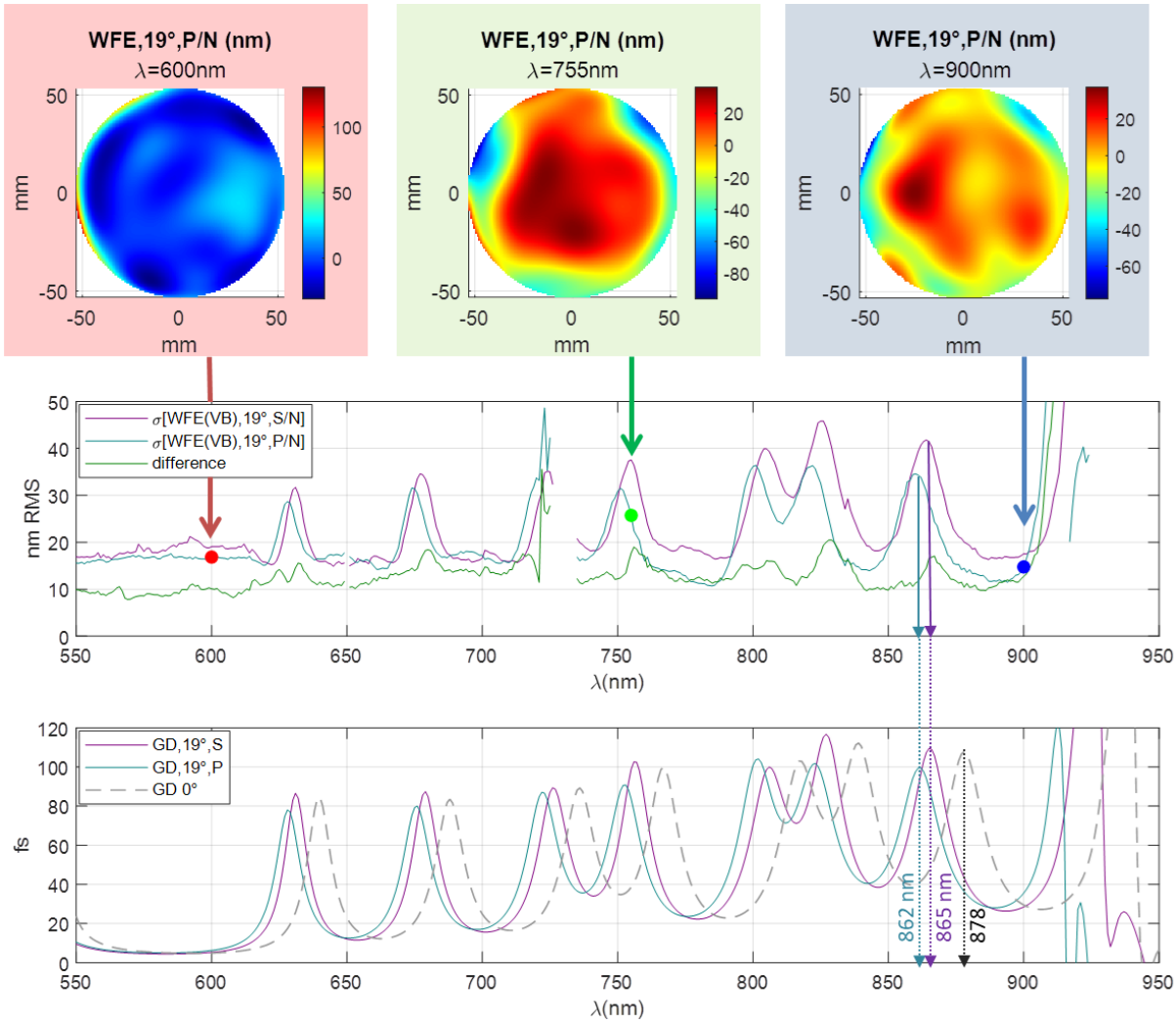

*Figure 100: (**Top**) WFE maps at three wavelengths, 19° AOI, P/N. Tilts are removed. (**Middle**) Standard deviation of WFE is computed at 19° (P/N, S/N, and difference). (**Down**) Theoretical Group Delay (GD) in reflection on Euclid dichroic mirror (19°, S and P).*

At the top of Figure 100 are showed some examples of WFE from the VB-19°-P/N dataset, at three wavelengths: **600, 725, and 850 nm**, for 19° in incidence and P/N polarization. The data representation is the same way as the previous figure. The visible deviations between S/N and P/N at 19° match also the thin-film theory predictions. We see a spectral shift of around 3 nm in wavelength, and amplitude shift up to 10 nm RMS between both polarizations. Indeed, the optical responses of

dichroic mirror between S and P are different, and will appear on the GD. See the example of the RMS on Figure 100 that is in close agreement with the GD peaks near 862 nm.

There is also a spectral shift from the result achieved at normal incidence. The peak observed at 878 nm at normal incidence is shifted by -16 nm for P (19°) and -13 nm for S (Figure 100, down) at 19° angle. This is due to the difference in the optical path through the stack layers. Indeed, the phase thickness δ of the layer (and consequently the interference phenomena through the layers) depends on the angle of incidence (see Chapter 6, part 1.2). In a first approximation, increasing the incidence is equivalent to reducing the thickness of all the layers, and thus shifting the spectral response towards shorter wavelengths.

2. DICHROIC MIRROR MODELING WITH ZERNIKE-WISE METHOD

In this section, we apply the Zernike-wise method to measurements obtained with OBSERVE. We will first use data at normal incidence, S/N polarization. We will apply the method in several cases: Homothetic case ($SFE_L \propto SFE_H$), nonhomothetic case ($SFE_L \neq SFE_H$), with also the substrate's SFE: SFE_S. From the models obtained, we will compute any WFE and compare it with the measured WFEs, at normal incidence, but also at oblique incidence.

2.1. Fit at normal incidence, S/N.

At normal incidence, the thin-film physics equations used by the Zernike-wise method are independent of the polarization. We have chosen to present the results obtained with the S/N polarization measurement.

Homothetic case, with substrate

Figure 101 shows the three SFE obtained when applying the Zernike-wise method to the first 55 Noll Zernike modes, with the homothetic hypothesis, and on a diameter of 108 mm. Tilts are ignored. As a reminder, according to this assumption, the SFE is independent of the considered material (see Chapter 6, part 3.4).

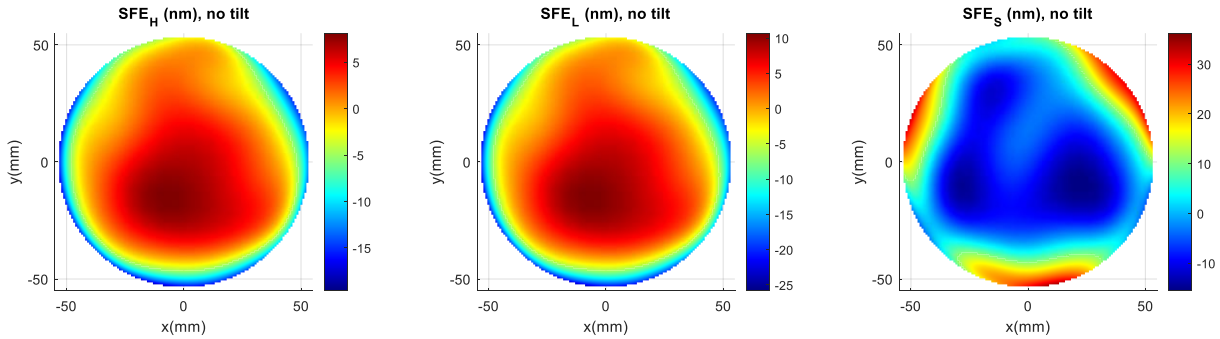

Figure 101: SFEs modeled with Zernike-wise method, under homothetic assumption. Used WFE data: 55 first Noll Zernike modes of WFE (VB, 00° S/N).

- Coating SFE (L, H)

The two Coating's SFE, SFE_H and SFE_L, are thus proportional. We see a domed profile (in other words, mainly radial aberrations, as predicted when analyzing the results at 0° in the previous section). This domed profile is also eccentric by about 15 nm, in line with the OBJ measurements. The latter were already presented in Chapter 4 (Figure 35), but it is interesting to compare the two results. In (Figure 102, left), we again present the wavelength variation of the reflection band cut-off obtained by OBJ, which can be assimilated to a global SFE provided that the coating does indeed present homothetic SFE.

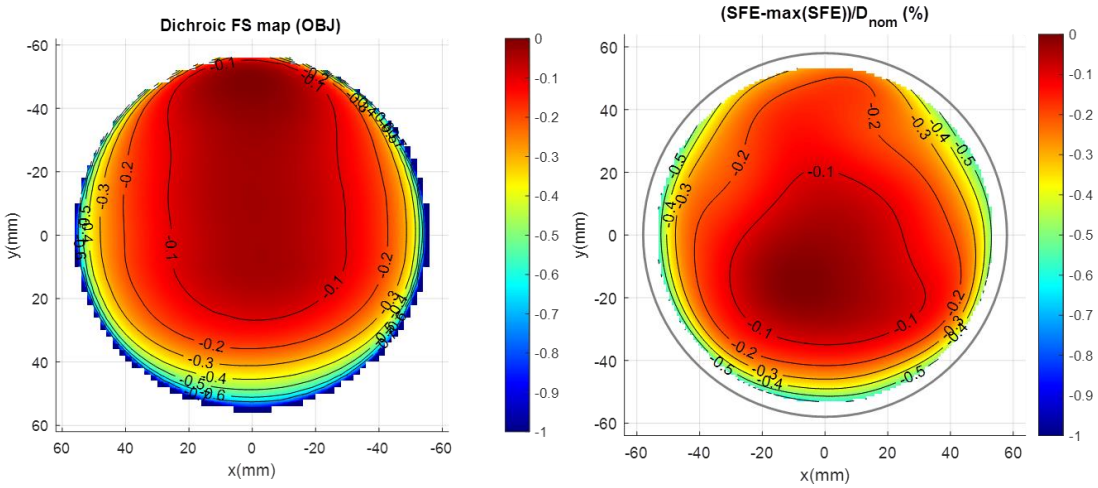

*Figure 102: (**Left**) Spectral reflectance shift homogeneity in percentage of λ for R=50%. (Right) modeled SFE_L+SFE_H, expressed relatively of coating thickness.*

On the right of Figure 102, we sum Figure 101's SFE_L and SFE_H, and we express them as a relative error with respect to the dichroic stack thickness (9.8 µm). We obtain then a similar map as OBJ's. By convention, OBJ defines the homogeneity as the relative variation with respect to the maximum. We therefore remove an offset on our map to match OBJ's convention. In addition, the two maps are not of the same diameter, which explains why the PTV of the OBJ map is higher than that modelled with the Zernike-wise method. Anyway, we can notice a close agreement between the level lines.

- Substrate SFE

The substrate SFE (Figure 101, right) shows a very large oblique trefoil (Z10) aberration, as suggested in the previous section. Since this trefoil does not appear on the substrate measurement data by Amos [54], it may be induced by the dichroic mirror holder. Finally, we note the "bump" in the center of the substrate SFE_S, with an amplitude of around 15 nm, which can also be seen on the Amos polishing map.

- Residuals on WFE

In Figure 103, we compare the measured WFE (top) with the modeled WFE from the homothetic model of the coating. We present WFEs at three example wavelengths: 600, 750 and 850 nm. The WFE are very similar, with a residual of around 5 nm RMS at these wavelengths. This residual was calculated for all wavelengths (Figure 103, bottom, yellow curve), and is between 4 and 6 nm RMS. This residual is therefore of the same order of magnitude as the current reproducibility of the OBSERVE bench.

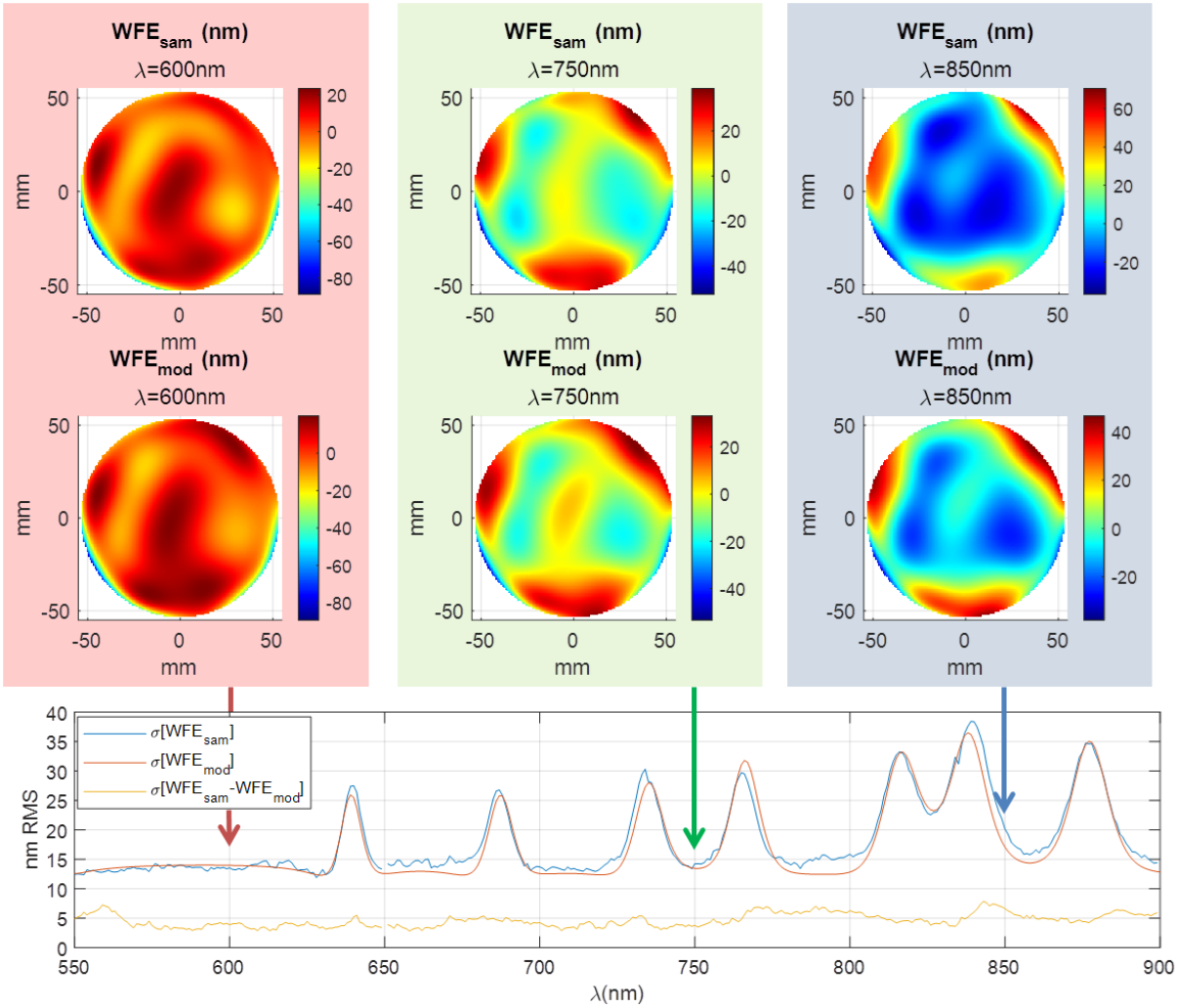

*Figure 103: Comparison between measured WFE (**top**) and modeled WFE (**middle**) at three wavelengths. (**Down**) Standard deviation of measured (blue), modeled (red) WFE, and difference (yellow) is plotted for each wavelength. Used data: WFE on VB, 00°, S/N), Tilts are removed.*

Case of different SFE_L and SFE_H, with a fixed substrate SFE

From now, we will assume that the two SFE in the coating are uncorrelated. As a first step, we will apply the Zernike-wise method, seeking SFE_L and SFE_H that are not proportional, and fixing the substrate SFE. We consider here SFE obtained during the homothetic fit, which seems realistic. The aim is to see whether adding a free parameter to the model leads to better results.

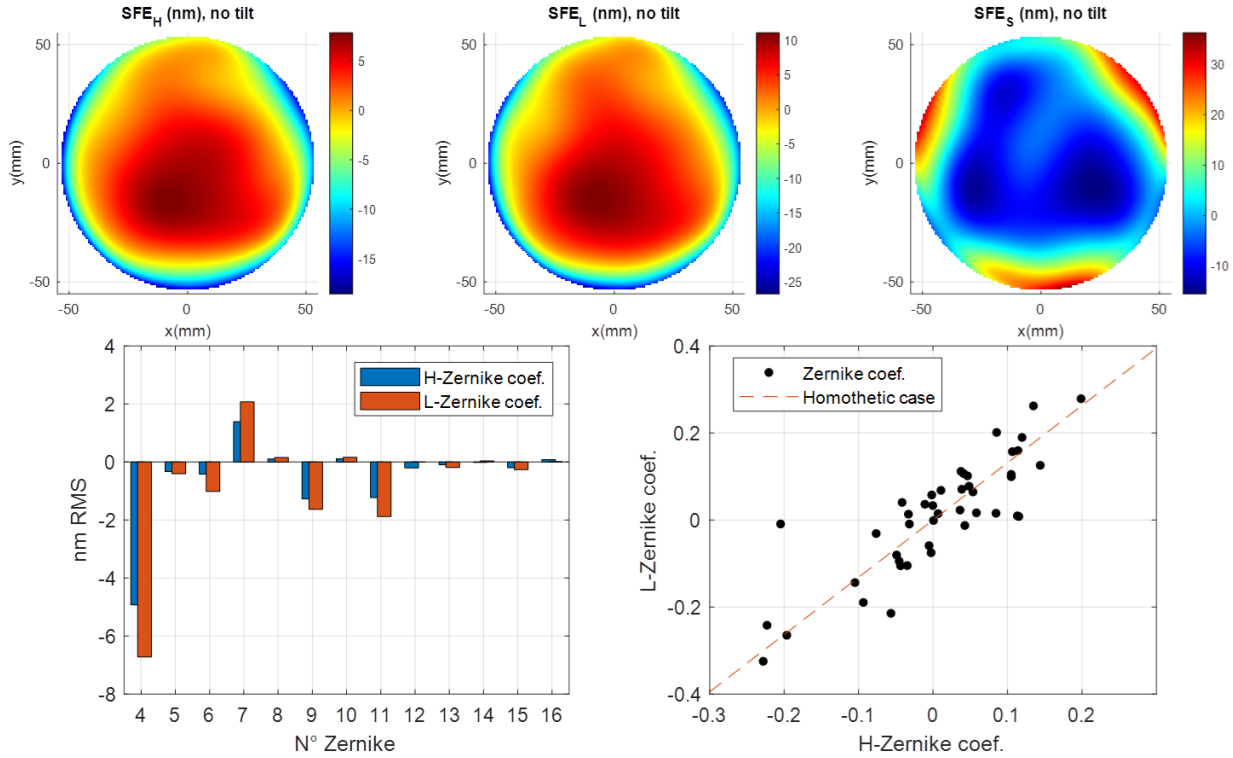

*Figure 104: (**Top**) SFEs modeled with Zernike-wise method, with fixed substrate SFE. (**Down left**), 16 first Zernike coefficients are plotted for coating SFEs. (**Down right**) SFE_L Zernike coefficients plotted in relation with SFE_H Zernike coefficients. Used WFE data: 55 first Noll Zernike coefficients of WFE (VB, 00° S/N).*

The SFE (L, H, and S) obtained are shown in Figure 104 (top). These are very similar, but not perfectly correlated as in the homothetic case, as shown by the Zernike decompositions at the bottom of Figure 104. On the left are the first modes, with a large focus term (Z4) for both materials. On the right, all the Z^{L} coefficients are plotted in relation with the Z^{H} coefficients, and we observe a slight dispersion compared with the homothetic case, which correspond to a straight line whose slope is to the ratio between the total thickness of the L layers and the H layers. In this situation, where the SFE of the substrate is imposed (from homothetic fit), the “homothetic” and “non-homothetic” results are therefore very similar with differences that are probably due to numerical precision of the solver.

Case of different SFE, with a free substrate SFE

Let us now proceed with the same application, but this time without fixing the substrate SFE. In Figure 105, we obtain very different results from those presented previously.

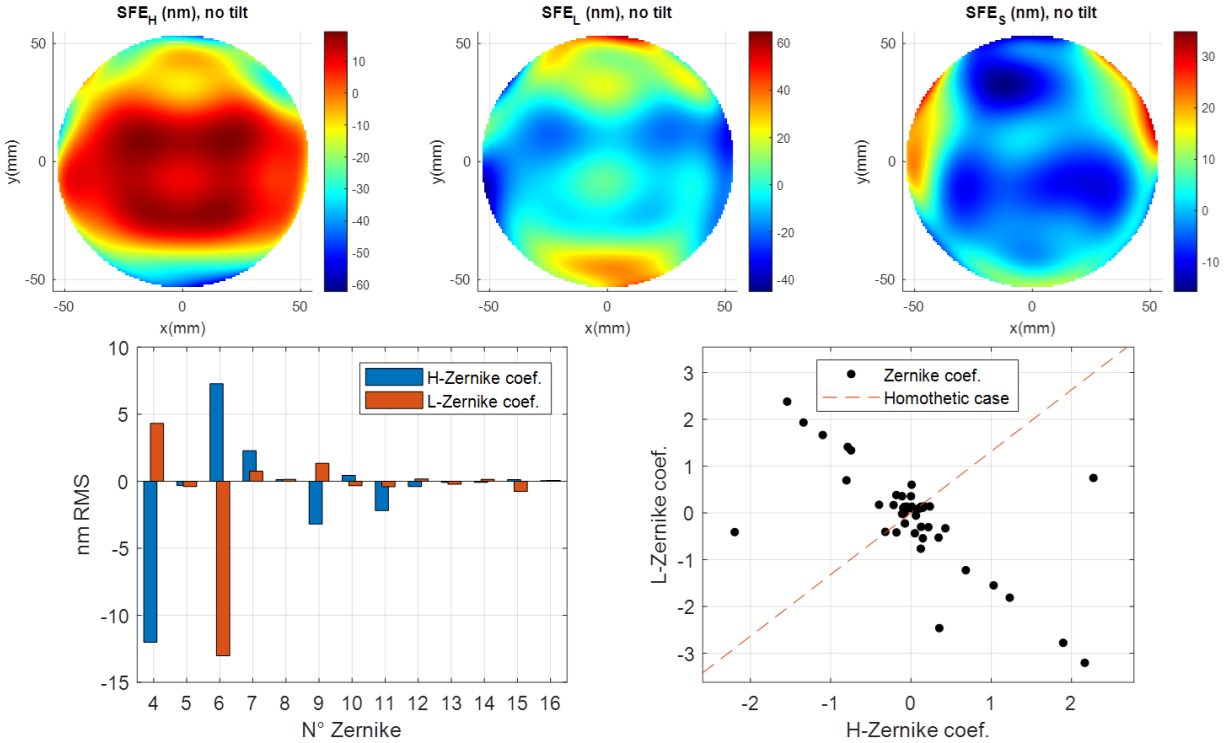

*Figure 105: (**Top**) SFEs modeled with Zernike-wise method, without fixed substrate SFE. (**Down left**), 16 first Zernike coefficients are plotted for coating SFEs. (**Down right**) SFE_L Zernike coefficients plotted in relation with SFE_H Zernike coefficients. Used WFE data: 55 first Noll Zernike coefficients of WFE (VB, 00° S/N).*

This time, SFE_L and SFE_H are very different, with a PTV value of around 80 nm for H and 100 nm for L (Figure 105, top), compared with 30 nm in the two previous cases. L and H Zernike coefficients also often appear to be opposed, as shown by the decomposition of the first modes (Figure 105, bottom left). The distribution of Z^L as a function of Z^H (right) in fact indicates an "anti-correlation" on several Zernike coefficients.

With such different SFE, we might expect the residual on the reconstructed WFE to be very bad. However, the WFE calculated by this model are equivalent to those obtained with the two previous models. Indeed, Figure 106 compares the residuals on the reconstructed WFE (excluding tilts) at all wavelengths obtained with the three models, represented as a cumulative distribution. It seems that the three models predict WFE almost identically, with a median residual of around 4.5 nm RMS, and a 95 % residual at 7 nm RMS. This unexpected result proves that several solutions (SFE_L, SFE_H, SFE_S) are possible, all of which minimizing the residual on the WFE. Filtering out some noisy aberrations and checking the models to oblique WFE will enable us to identify if one solution is preferable.

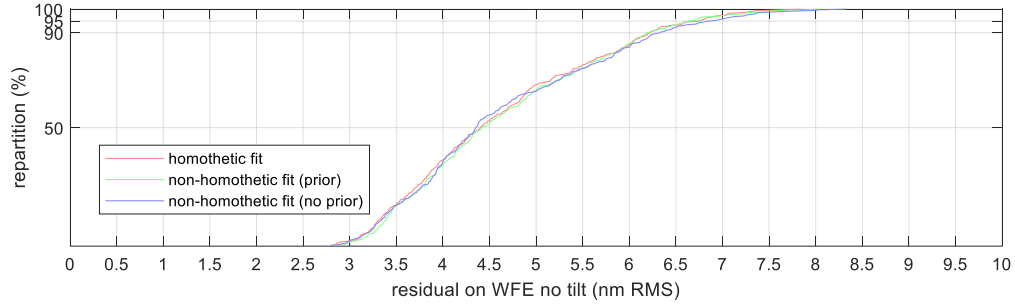

Figure 106: Residuals on WFE reconstruction (nm RMS) expressed as a cumulative distribution for the three models obtained with Zernike-wise method.

Furthermore, it seems that the total SFE of the coating (sum of SFE_L and SFE_L), is also comparable to the OBJ map. In Figure 107 we again compare the map measured by OBJ (Figure 35) with the equivalent map obtained with the model. Note that the left map on Figure 107 can be considered as a SFE map only in the case of a homothetic coating, which is not the case on the modeled map on the left.

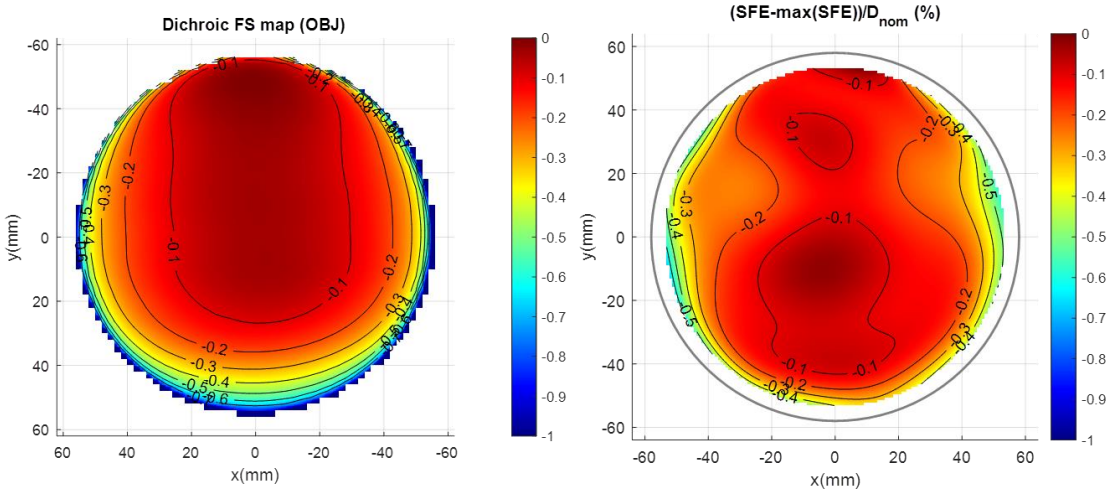

*Figure 107: (**Left**) Spectral reflectance shift homogeneity in percentage of λ for R=50%. (Right) modeled SFE_L+SFE_H, expressed relatively of coating thickness.*

The maps profiles are different, but their PTV is of the same order of magnitude. It therefore appears that SFE_L (80 nm PTV) and SFE_H (110 nm PTV) "compensate" for each other, leading to a total SFE with a low PTV value: close to 50 nm, or 0.5% of total coating thickness (Figure 107, right), and lead to WFE near to those we measured with the OBSERVE bench. Our opinion is that is unlikely that the deposition machine was set up in such a way as to obtain such opposite SFE for L and H materials. The most likely hypothesis is that the available data is not sufficiently qualitative to apply the Zernike-wise method with three unknowns (Z_k^L, Z_k^H and Z_k^S) up to k = 55 Zernike modes. We saw in Figure 99 that the measurements are indeed quite noisy, and it is possible that the algorithm for optimizing the Z_k^L, Z_k^H and Z_k^S Zernike modes has simply over-fitted the WFE Zernike modes. The result is therefore an optimal mathematical solution for minimizing the gap between modeled and measured WFE, but this is not necessarily the most realistic solution. It then probably constitutes a mathematical artifact similar to what was observed in Figure 95 (Chapter 6).

In the next section, we will take into account the noise in the measurement data to adapt the identification of a more realistic solution.

2.2. Models sensitivity to noise

Signal to noise ratio on WFE Zernike coefficients

On each Zernike mode of the measured WFE, a certain quantity of noise seems to be present, making more or less difficult the detection of WFE chromaticity due to the coating. To quantify the impact of this noise relative to the amplitude of each measured WFE Zernike aberration $Z_k^{Wsam}(\lambda)$, we introduce a SNR parameter for each of them.

We thus define the SNR as the ratio between the quadratic average of the Zernike coefficient over the entire visible band (containing **N = 350** wavelength samples) and the quadratic average of the (estimated) noise. For the k^{th} Zernike aberration, the SNR is then:

$$(\mathrm{SNR}_k)^2 = \frac{\frac{1}{N}\sum_{i=1}^{N} Z_k^{Wsam}(\lambda_i)^2}{\frac{1}{N}\sum_{i=1}^{N} \mathrm{noise_k}(\lambda_i)^2}$$

To estimate the $\boldsymbol{noise_k(\lambda)}$, we select the 570-620 nm wavelength range (**n = 50 samples**), for which the WFE due to the dichroic coating is theoretically nearly constant. This translates into constant Zernike coefficients $Z_k^{Wsam}(\lambda)$ over this band. The noise quadratic average thus corresponds to the RMS deviation of each Zernike coefficient over this band:

$$(\mathrm{SNR}_k)^2 = \frac{\frac{1}{N}\sum_{i=1}^{N} Z_k^{Wsam}(\lambda_i)^2}{\frac{1}{n}\sum_{i=1}^{N} [Z_k^{Wsam}(\lambda_i) - \mu_k]^2}$$

Here, μ_k is the median value of $Z_k^{Wsam}(\lambda)$ over the 570-620 nm range.

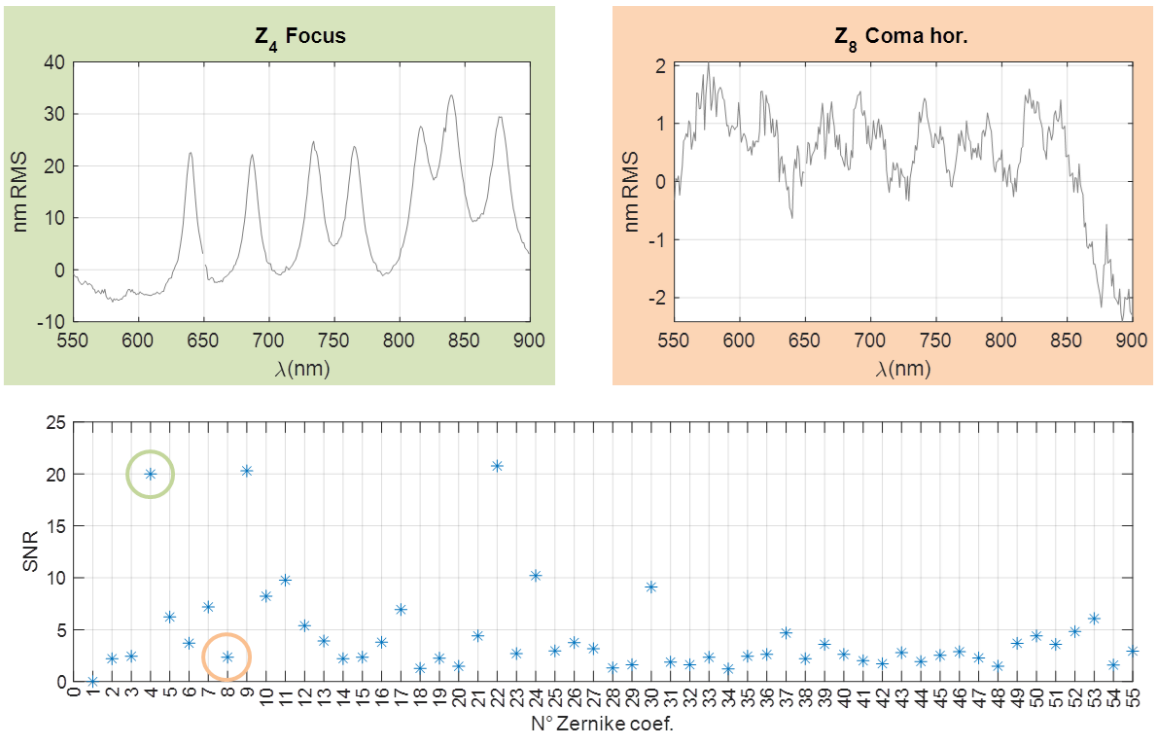

Figure 108: (Top) Example of measured WFE projected on two Zernike coefficients. (Down) the SNR for each Zernike of this WFE is calculated (VB, 0° in incidence, S/N).

In Figure 108 (down), we have calculated the SNR of the 55 Zernike modes of the WFE at 0° S/N. Most Zernike modes have an SNR between 1.5 and 5, especially those of high order (Z > 30). We can notice that 11 Zernike coefficients have an SNR above 5. Among the best SNRs, we find the Z4 (focus), which is indeed very little degraded by noise (see top left of Figure 108). Conversely, although low-order, the Z8 horizontal coma (right) is much more degraded. It will therefore be difficult to apply the Zernike-wise method to this aberration.

This noise level can also be calculated from WFE measurements on the dummy mirror – which is theoretically achromatic – (see chapter 5). In any case, the noise level seems fairly equivalent for all Zernike coefficients. The RMS value of the noise is often between 0.3 and 0.6 nm RMS (with the exception of tilts: around 4 nm RMS).

Noised aberration filtering

We therefore propose to set a lower limit below which it is not relevant to apply the Zernike-wise method. At the top of Figure 109, we again show the different SNRs calculated for the 55 Zernike modes of the WFE 0° S/N, with three limits on the SNR indicated (0, 3 and 5). We then calculate the residual on the homothetic reconstruction of the WFE at all wavelengths, retaining only the contributions of Zernike aberrations whose SNR is above a threshold, e.g. SNR > 5. We then plot the cumulative distribution of the residual on the WFE for each of the 3 cases (Figure 109, bottom). The red curve, for example, shows that if all Zernike modes are taken into account (even tilts) to calculate the WFE, the median residual is 8 nm RMS. The grey curve corresponds to the case where only tilts are ignored, (see Figure 106) with a median value of 4.5 nm RMS. This shows that filtering all WFE Zernike modes with an SNR below 3 leads to a median residual of 3.75 nm RMS, and 2.75 nm RMS with an SNR limit of 5. However, with an SNR limit of 5, only 11 Zernike modes are taken into account, which limits the interpretation of WFE maps.

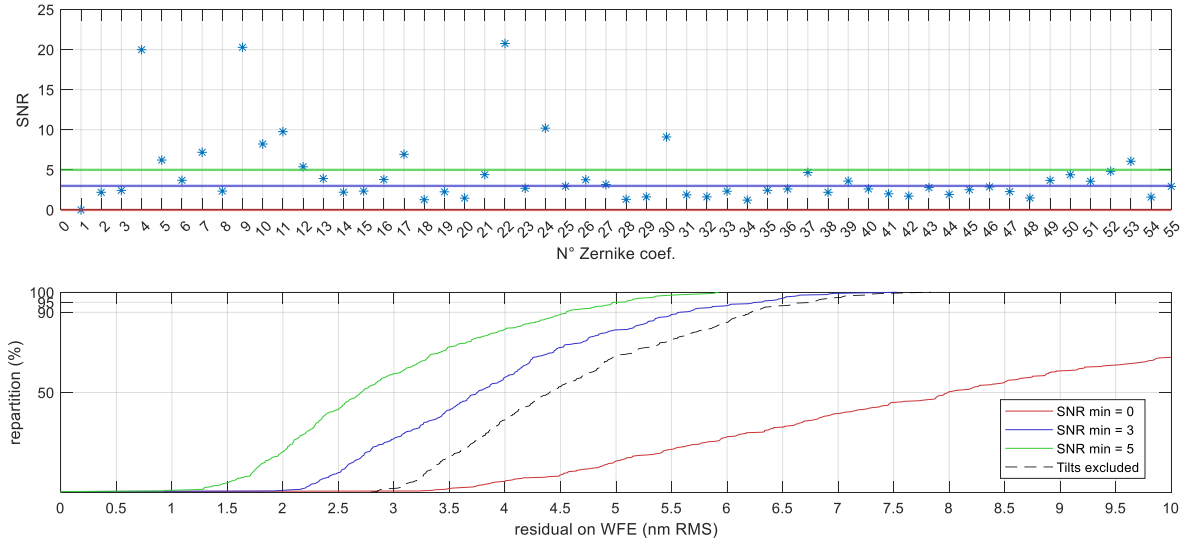

*Figure 109 (**top**) SNR for each Zernike of WFE measured on VB, 0° in incidence, S/N. (**Down**) Residuals on WFE (homothetic) reconstruction (nm RMS) expressed as a cumulative distribution for several levels of SNR used as threshold.*

In Figure 110 we now compare the Zernike distributions of WFE and SFE in the two previous simulations: with a fixed substrate on the left, and with a free substrate on the right. The color of each point indicates the SNR value of the corresponding WFE Zernike mode $Z_k^{Wsam}(\lambda)$ (Figure 109, top).

It is clear from the graph on the right that the "anti-correlated" Z^{L} and Z^{H} Zernike coefficient we observed in Figure 105 are precisely those with SNR values below 3 (in red).

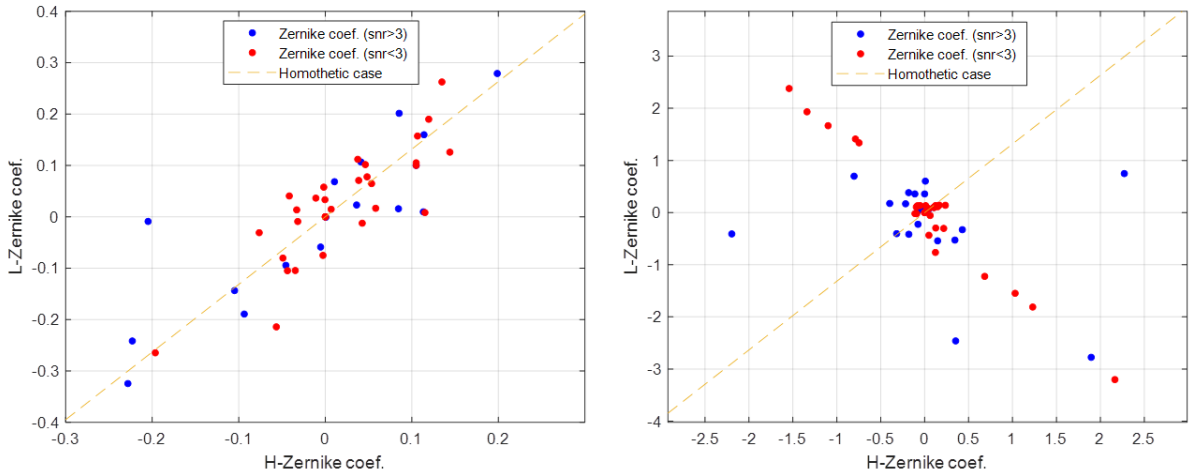

*Figure 110: SFE_L Zernike coefficients plotted in relation with SFE_H Zernike coefficients. (**Left**) results from Figure 104: fit with a fixed substrate. (**Right**) Results from Figure 105: fit with free substrate.*

A bad SNR on SFE Zernike modes therefore leads to bad identification of $\mathrm{SFE_L}$ and $\mathrm{SFE_H}$ Zernike modes when we apply an optimization algorithm aimed at identifying 3 variables simultaneously ($Z_k^{\mathrm{L}}, Z_k^{\mathrm{H}}$ and Z_k^{S}).
With only two variables sought (Z_k^{L} and Z_k^{H}), this "anti-correlation" does not arise and the Zernike modes remain correlated (Figure 110, left), but we tend to the homothetic solution.

Finally, in Figure 111 we computed the WFE residual for the three model solutions ("homothetic", "nonhomothetic with fixed substrate", "nonhomothetic with free substrate"), and with different filtering levels: tilts, SNR < 3, and SNR < 5. As seen in Figure 109, increasing the SNR limit reduces the residue on the WFE. However, it seems that none of the three models is really more accurate than the others. With an SNR limit of 5, all three models achieve a median residue on the WFE of 2.75 nm. Nevertheless, the "non-homothetic with free substrate" model (blue dotted curve) seems slightly less efficient than the two others when SNR > 5: its WFE residual at 95% is 6 nm RMS, and 5 nm RMS for the two others.

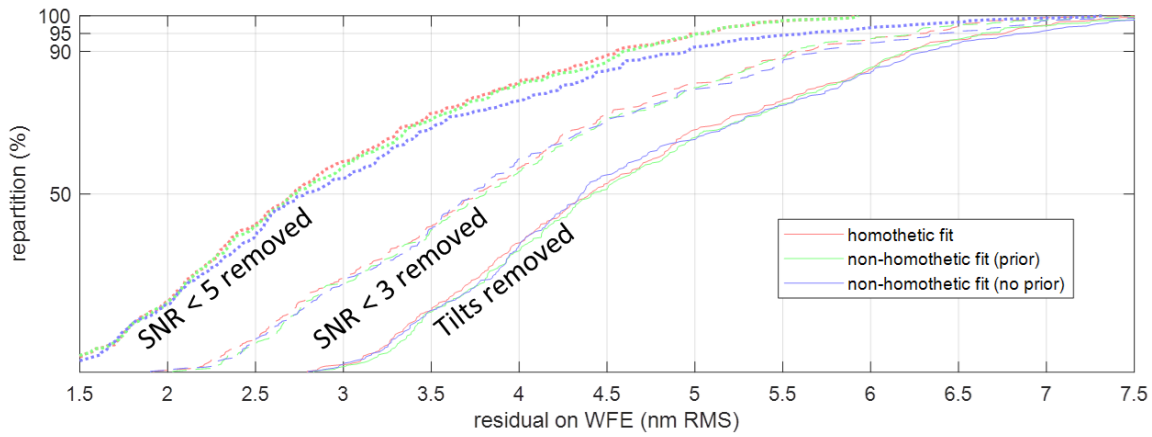

Figure 111: Residuals on WFE reconstruction (nm RMS) expressed as a cumulative distribution for the three models. The line style corresponds to different SNR used as threshold.

Aberration filtering allows the reduction of the residual on the WFE reconstruction by more than 1.5 nm RMS, with median residuals which reach 2.75 nm RMS for the three coating models tested. On the other hand, the results presented here do not really allow us to identify one model that is more efficient than the others. Averaging several measurements could reduce the noise level, improve the SNR, and surely help in identifying the best model.

Model degradation with simulated noise

We have seen in Figure 110 that an anti-correlation appears when the SNR of the WFE Zernike modes becomes too low, and this SNR is directly related to the measurement noise. To gain a better understanding of this phenomenon, we run a simulation identical to the one in Chapter 6, part 5.4.

1) We create a "reference" dichroic stack with different SFE_L, SFE_H and SFE_S. These two reference SFEs are generated from 55 random Zernike coefficients. We then calculate the WFE of this stack (without noise), which is the reference WFE.

2) We then generate noise randomly on each of the 55 Zernike modes, and at all wavelengths between 550 and 900 nm. The RMS value of this noise on each Zernike is adjusted to give, for example, 5 nm RMS over the whole "sample" WFE. Theoretically, the RMS value of the total noise on the WFE is $\sqrt{55} \approx 7.4$ times the RMS value of the noise for a single Zernike. The generation of this noise is identical to what was done in parts 4.2 and 5.4 of Chapter 6.

3) The Zernike-wise "nonhomothetic" method is then applied to this noisy WFE, and we obtain 55 Z_k^{L}, Z_k^{H} and Z_k^{S} defining a modeled stack.

We carried out the simulation for 5 WFE noise RMS: 0, 2.5, 5, 7.5 and 10 nm RMS. We thus obtain 5 modeled coatings. On Figure 113 we display the 55 $\left(Z_k^{\mathrm{H}};\ Z_k^{\mathrm{L}}\right)$ for each modeled stack.

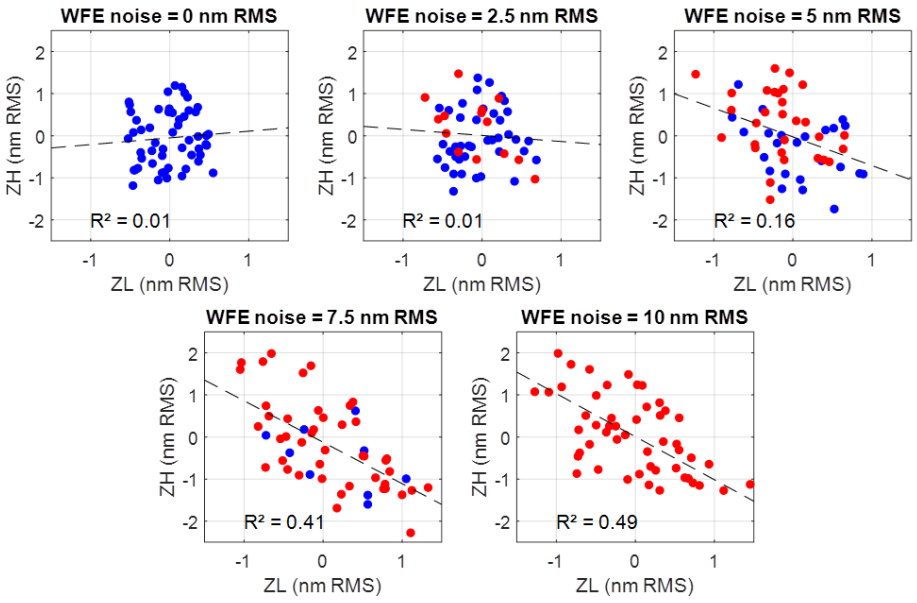

Figure 112: Simulation of SFEs $(Z_k^H;\ Z_k^L)$ reconstruction with Zernike-wise method, using simulated sample WFE with added random noise. ***Blue*** *dots are such* $SNR\left(Z_k^{Wsam}\right) > 3$. ***Red*** *dots:* $SNR\left(Z_k^{Wsam}\right) < 3$.

As the noise level increases, the points appear to form an anti-correlated distribution, similar to what we observed in the previous section. Also, we colored the points $\left(Z_k^{\mathrm{H}};\ Z_k^{\mathrm{L}}\right)$ according to the SNR of

the corresponding $Z_k^{Wsam}(\lambda)$. A red dot corresponds to an SNR < 3. Naturally, the higher the overall WFE noise, the lower the SNRs of the Zernike modes are. For each distribution, we calculate the coefficient of determination $\boldsymbol{R^2}$ using linear regression. This is almost zero in the "noise-free" case, where $\left(Z_k^{\mathrm{H}};\ Z_k^{\mathrm{L}}\right)$ correspond to the reference value. In the noisiest case, where almost all SNRs are below 3, we obtain an R^2 near 0.5.

This simulation thus shows that noise in the WFE measurement does indeed lead to anti-correlation in the SFEs modeled. However, in Figure 110 we observed a more pronounced anti-correlation, with overall lower SNRs. Thus, a random noise in the measurement is not enough to explain the anti-correlation in the results.

2.3. Models sensitivity to biases

We have seen that the nonhomothetic fit with Zernike-wise presents particular results, with SFE_L and SFE_H being **anti-correlated**. In the previous section, we identified that the noise present on the measured WFE's Zernike modes (and therefore their SNR) does not fully explain the fit results. Here we present several simulations which show that the anti-correlation in the nonhomothetic fit results has unexpected origins.

Achromatic bias

According to the Dummy mirror study (Chapter 5, part 2) we saw that the main measurement bias induced by the bench is achromatic. However, the only effect of achromatic noise is to add a random vertical offset to the $Z_k^{Wsam}(\lambda)$. By construction, the only impact on the model will be an error in identifying the Z_k^{S} and therefore the substrate's SFE. Indeed, the latter has an achromatic contribution to WFE (see Chapter 6, part 3.3). Thus, Z_k^{H} and Z_k^{L} theoretically do not depend on achromatic bias.

The previous results suggest that an error source **neither constant (achromatic) nor random (noise)** is causing the homothetic Zernike-wise method to misidentify chromatic variations in the WFE. A **chromatic bias** could therefore be the cause. Consequently, we carried out new analyses of the data obtained from the Dummy Mirror in order to confirm this assumption.

Chromatic bias identification

In addition to the achromatic bias, we observed features that oscillate with wavelength. On Figure 113 is showed the case of the 3 Zernike modes Z6, Z10, Z12, which we use again as an example, where these structures are visible (Figure 113, top). On Z12, for example, oscillations appear whose "period" is around 100 nm in wavelength, and whose amplitude is ± 0.5 nm RMS.

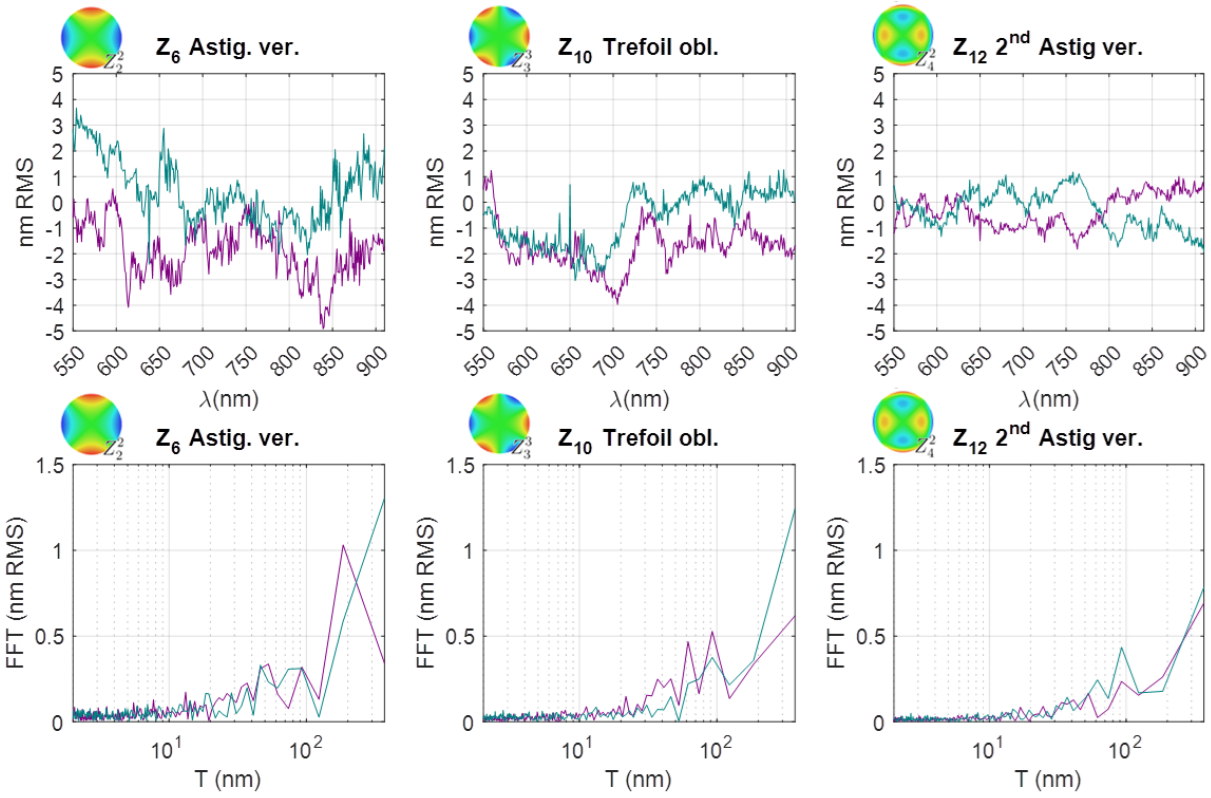

*Figure 113: (**Top**) Zernike projections (Z6, Z10, and Z12) of difference of dummy mirror WFE measurements between OBSERVE and Zygo, at 0° S/N (purple) and P/N (cyan). (**Down**) Fast Fourier Transform of these chromatic Zernike coefficients.*

At the bottom of Figure 113, we have applied a Fast Fourier Transform (FFT) to quantify these oscillating structures. For Z12, we find indeed a peak of 0.5 nm RMS in amplitude at T = 100 nm (P/N). For Z6 and Z10, we observe other oscillations, with amplitudes between 0.3 and 1.2 nm RMS, and periods between 50 and 300 nm in wavelength. These oscillations therefore constitute a chromatic bias induced by the OBSERVE bench or by the environment. The cause(s) of this bias need to be investigated as it will have a strong impact on the WFE final result and need to be removed.
As measurements are made at all wavelengths, and each measurement lasts one minute, these oscillations in the measurements correspond to time scale of several hours. The analysis of the bench's temporal stability in Chapter 5, part 1.2 showed that cleanroom temperature oscillations, with a period of around two hours is already correlated with oscillations in X and Y tilts. The cleanroom environment is therefore a probable cause of the chromatic bias identified here. More investigations must be done but are beyond the scope of this thesis.

Model degradation with simulated chromatic bias

To identify the impact of this bias on the results, we carried out a second simulation. We redefine a "reference" WFE in the same way as in part 2.2, and add a bias on each of the 55 $Z_k^{Wsam}(\lambda)$, defined by a sinusoidal function of amplitude ±1 nm RMS and period T_{bias}. Figure 114 shows the results for 6 values of T_{bias} between 0 nm (i.e. no bias) and 300 nm in wavelength, corresponding to what we observed in Figure 113, Chapter 5.

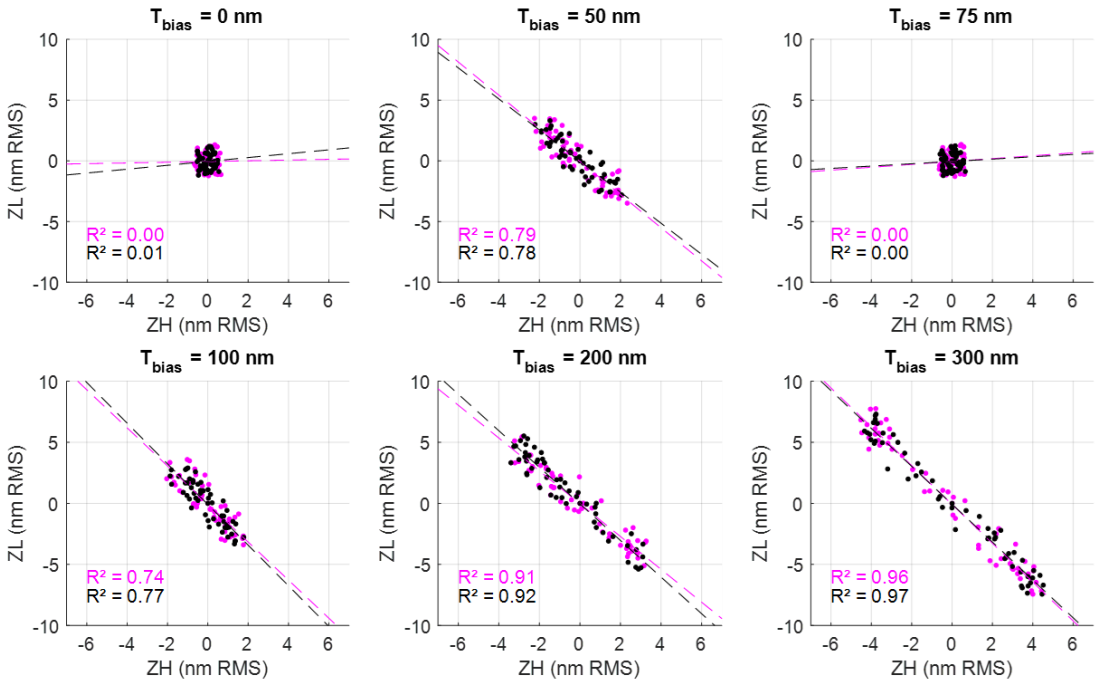

*Figure 114: Simulation of SFEs $(Z_k^H; Z_k^L)$ reconstruction with Zernike-wise method, using simulated sample WFE with added chromatic bias on each $Z_k^{Wsam}(\lambda)$. This bias is: $\boldsymbol{B(\lambda) = A.sin(2\pi\lambda/T_{bias} + \delta_k)}$. A = 1 nm, δ_k is random. Two independent simulations **(run 1, run 2)** were carried out.*

We ran the same simulation twice, changing the reference SFE and WFE. Each dot color corresponds to one of the two simulations. The different distributions and R^2 seem to indicate that the results are not dependent on the reference SFE. This time, anti-correlation seems to be very present depending on the value of T_{bias}. For high values such as 100 to 300 nm, we observe a very clear anti –correlation ($R^2 > 0.75$) similar to what was observed in the nonhomothetic model results (Figure 110).

This simulation thus seems to indicate that chromatic bias is the main cause of anti-correlation in the modeled SFE. This raises the question of why the Zernike-wise method is so sensitive to this bias, much more so than to random noise in the measurements.

Impact of the chromatic bias

In section 1.3 of this chapter, where we presented measurement results, we noted that the WFE of the dichroic mirror admits chromatic variations. At first order, we can identify a periodicity of these **variations, of around 50 nm wavelength** arisen from the GD of the coating. The periodicity of the chromatic bias identified in Chapter 5 appears to be of the same order of magnitude. Thus, the periodic oscillations of the chromatic bias **are likely to resonate** with the oscillations of the GD, Indeed, any variations of WFE according to this characteristic wavelength period will be interpreted as a contribution from the coating SFE. Consequently, the model is highly sensitive to chromatic bias, with a period close to 50 nm, corresponding to the "coating WFE period" (see Figure 114). Periods of T_{bias} = 100, 200, 300 nm correspond to lower-frequency harmonics, which also have an impact on the model results. After this thesis, further analyses will be performed to confirm or not this "resonance" effect.

The Zernike-wise method and the simulation tool developed in Chapter 6 is used to model the dichroic stack SFEs, but is also very useful for highlighting the criticality of some experimental errors, such as chromaticity bias. For the time being, we do not have worked out a strategy for

eliminating the chromatic bias. Indeed, the period, amplitude and phase shift of the chromatic bias oscillations seems to change for each aberration and each measurement.

After this thesis, we will work on a repetition of measurements to average out the biases (chromatic and achromatic), as well as the measurement noise. We will also work on frequency filtering of this bias to better understand and characterize it. For the remainder of this manuscript, we continue the analysis with oblique incidence measurements without taking chromatic bias into account anymore. However, we still consider the SNRs of Zernike aberrations, which also affect model accuracy.

3. CHECKING THE HOMOTHETIC MODEL WITH OBLIQUE INCIDENCE DATA

The aim here is to compute WFE at 19°, in P and S polarization, over the entire visible band, **from a model adjusted with 0° S/N data**. We will only test the homothetic model here. Although the nonhomothetic model enables us to calculate a WFE that matches the measured WFE as well as the homothetic model, we estimate that the anti-correlated SFEs obtained with this model are not realistic.

3.1. Model application to WFE at 19° in AOI

Application without correction

Figure 115 shows the results of applying the homothetic model obtained in the previous section at 19°, in P and S polarization. Similarly to section 2.2, we test three filtering cases for each model: “tilts only”, “Zernike coefficients such that SNR < 3”, then “SNR < 5”. The representation of the results is identical to that shown in Figure 111.

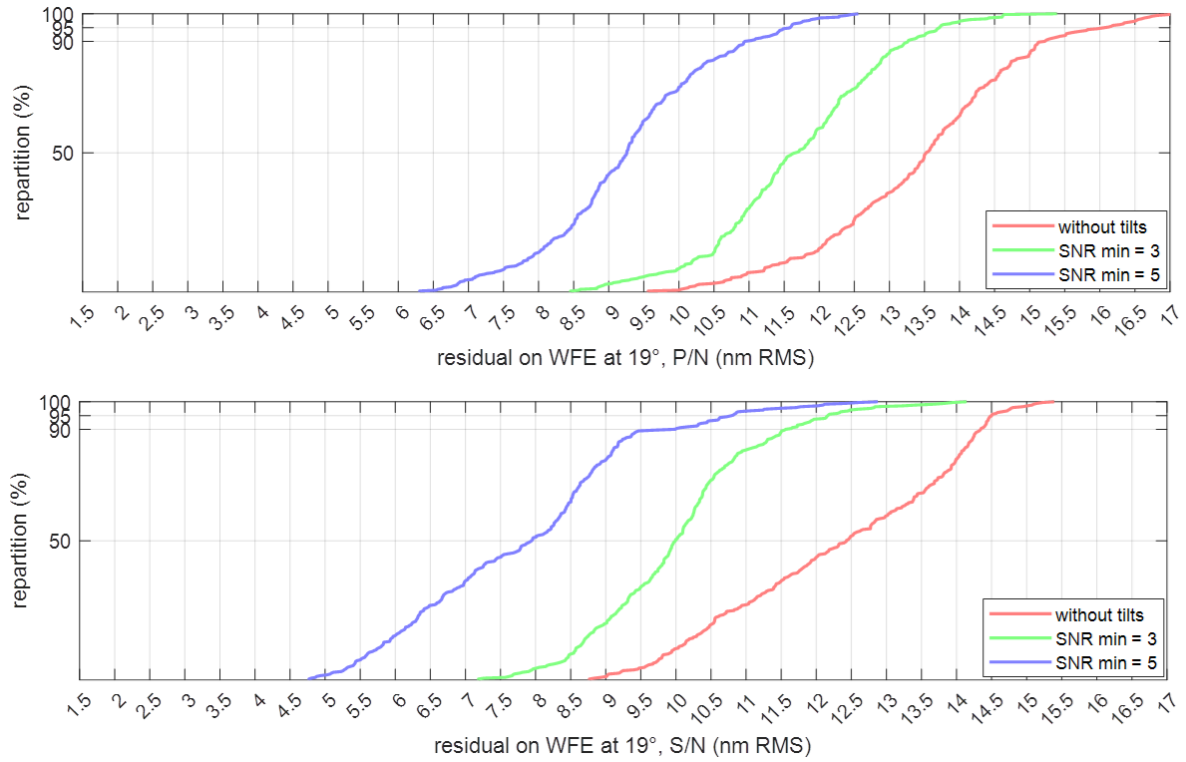

Figure 115: Residuals on WFE reconstruction at 19° (top: P/N, down: S/N) expressed as a cumulative distribution for the three cases. The line color corresponds to different SNR used as threshold.

For P polarization (Figure 115, top), the median residual on the WFE reconstruction at 19° is **13.5 nm RMS** (excluding tilts), and 9.25 nm RMS in the case where we filter out Zernike modes with SNRs below 5. In S polarization (Figure 115, down), the residuals are of the same order of magnitude.

The reproducibility residual induced by the change in the optical configuration of the bench can affect the results at 19° and be included in the residual between computed WFE and measured WFE. Indeed, tests carried out on the Dummy Mirror have shown that a random achromatic residual of around 6 nm RMS (Chapter 5, part 2.2) appears each time measurements are reproduced. This explains why we have residuals beyond 10 nm RMS in Figure 115.

Achromatic residual arising from reproducibility

Here we will identify the residual on the WFE that is only due to reproducing measurements with new bench settings. To quantify it (on the 19° S/N measurements, for example), we proceed as follows:

1) We compute the WFE maps at 19° on the visible band from the homothetic model obtained from the 0° measurements in part 2.1. This $\mathrm{WFE}_{19\mathrm{SN}}^{mod}(\lambda)$ is considered as a measurement that would have been obtained at 19° S/N.
2) We then subtract the actual WFE maps measured at 19° P/N: $\left(\mathrm{WFE}_{19\mathrm{SN}}^{sam}(\lambda)\right)$, giving $\Delta\mathrm{WFE}_{19\mathrm{SN}}(\lambda)$. This difference is therefore linked to the reproducibility of the bench, as if we had simply carried out the 19°S/N measurement twice.
3) Finally, we calculate the median of $\Delta\mathrm{WFE}_{19\mathrm{SN}}(\lambda)$ on the visible band, which corresponds to the achromatic residual between the two measurements linked to reproducibility, similar to what was observed in part 2.2 of Chapter 5 with the dummy mirror.

At the top of Figure 116, we have plotted the chromatic dispersion of the first 16 Zernike coefficients of $\Delta\mathrm{WFE}_{19\mathrm{SN}}(\lambda)$ (purple) and $\Delta\mathrm{WFE}_{19\mathrm{PN}}(\lambda)$ (cyan) that were calculated in **step 2**. The Whisker plot representation of the results is similar to Figure 71 in Chapter 5. We can see that the median of each Zernike is non-zero, confirming the existence of an achromatic bias on WFE. The median value of each Zernike coefficient can therefore be used to compute the achromatic WFE residual map in S/N and P/N (**step 3**).

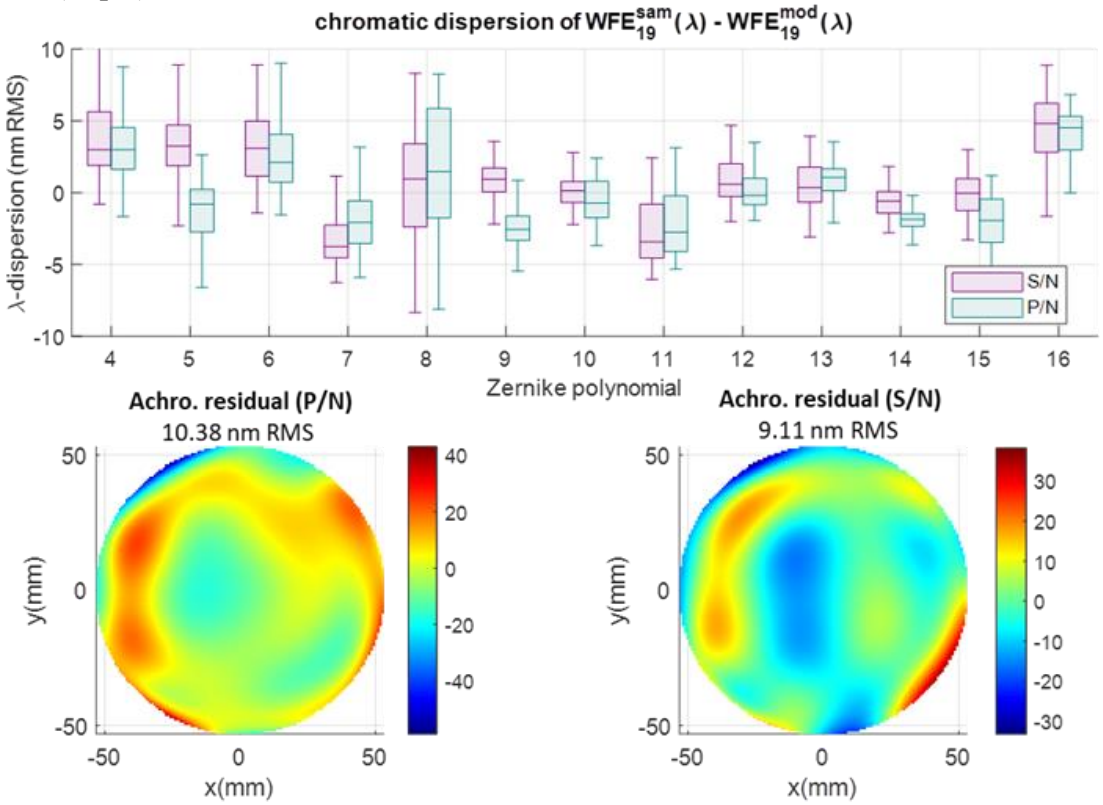

*Figure 116: (**Up**): Chromatic dispersion of the 16 first Zernike coefficients of the difference between measured and modeled WFE at 19°, P/N and S/N. (**Down, Left**) median residual map (without tilts) between measured WFEs at 19° P/N and modeled WFEs 19° P/N computed from homothetic model adjusted with 0° data. (**Down, Right**) Equivalent map computed with 19° S/N WFEs*

The lower part of Figure 116 shows the median maps obtained for 19° P/N (left) and 19° S/N (right). The two maps have an RMS value of **10.38 nm** for P/N and **9.11 nm** for S/N (without tilts). This means that approximately 10 nm RMS are added only by the bench settings.

It is important to understand that this median deviation is not equivalent to the median values in Figure 115. Here, we are interested in the deviation on the WFE maps, and then we **calculate the median map, which has an RMS of around 10 nm RMS**. In Figure 115, we calculate the RMS of the difference between the maps at each wavelength (which is necessarily positive), and then consider the median value of these RMS deviations (13.5 nm RMS), which is very different. It is therefore consistent to have a higher value in Figure 115.

Application with correction

We reproduce the analysis presented at the beginning of section 3.1 in Figure 115. This time, we correct the measured S/N and P/N data by first subtracting the achromatic residual identified in Figure 116. This does not mean that the WFE modeled at 19° is lacking of achromatic residual, but we decide here to ignore the achromatic difference between the two data sets.

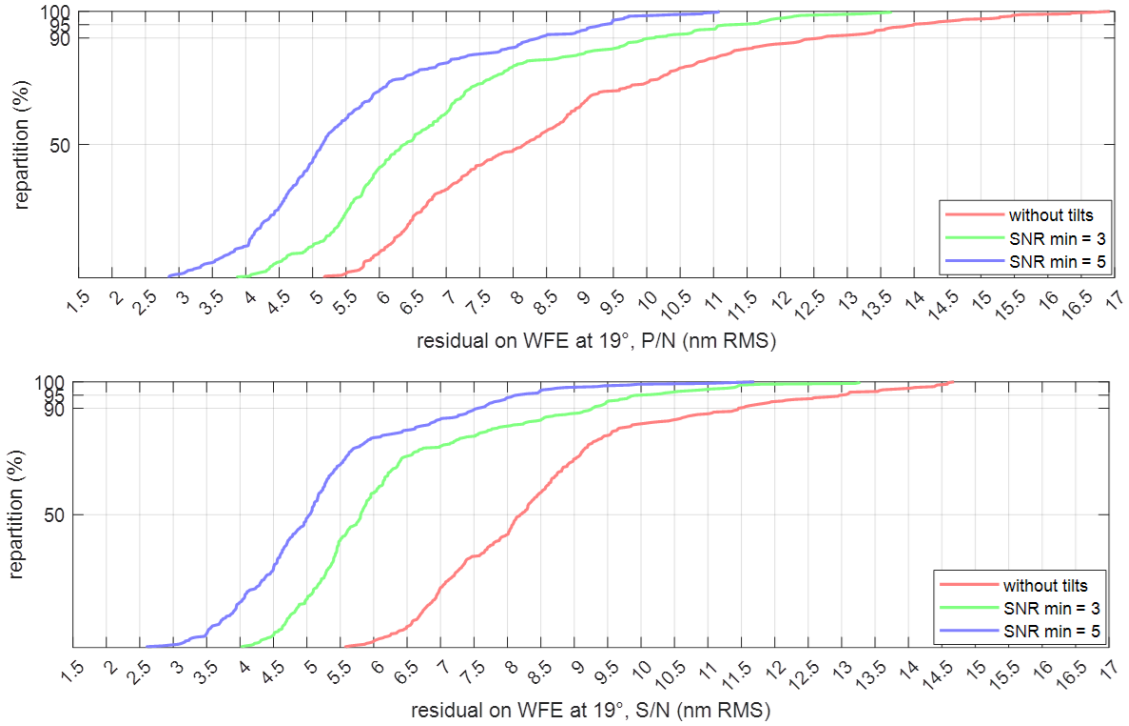

Figure 117: Residuals on WFE reconstruction at 19° (top: P/N, down: S/N) expressed as a cumulative distribution for the three cases. The line color corresponds to different SNR used as threshold. The achromatic residual (Figure 116) has been removed to all WFE measurement data at 19°.

Figure 117 shows that the differences between the modelled WFE at 19° and the **corrected** measured WFE at 19° are much smaller than in Figure 115. If we take the "19° P/N without tilt" case, we had a median residual of 13.5 nm RMS. **With the correction, this median residual is 8.3 nm RMS**. This result is logical, as we have removed a contribution of 10.4 nm RMS (Figure 116). The quadratic sum of 8.3 and 10.4 nm RMS corresponds indeed to 13.5 nm RMS. Considering the cases where we remove the Zernike modes from the WFE with SNR < 5; we obtain median residuals of **5 nm RMS**, in S/N and P/N.

The results presented here showed that it is necessary to take into account the reproducibility of measurements with the OBSERVE bench when applying the model. If the achromatic bias is truly achromatic and random, it will be necessary to repeat the measurements at 0° and 19° several times to get closer to the **actual** WFE of the dichroic mirror. On the other hand, if the chromatic bias is systematic, we may need to use our simulation tool in order to remove it.

3.2. Dichroic mirror modeling from oblique WFE data

Differences between SFE obtained from 0° and 19° WFE data.

In this final part of the chapter, we continue the analysis of WFE data at oblique incidence by applying the (homothetic) Zernike-wise method to WFE measurements at 19° P/N.

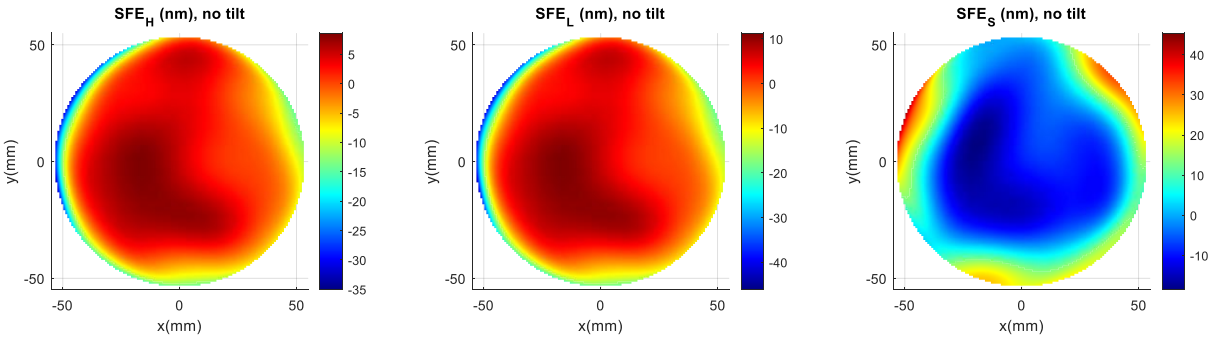

Figure 118: SFEs modeled with Zernike-wise method, under homothetic assumption. The used measured WFE data are 55 first Noll Zernike modes of WFE (VB, 19° P/N).

Figure 118 shows the three SFE obtained. The SFE of the substrate is similar to that presented in part 2.1 (see Figure 101), with a significant oblique trefoil aberration. The coating SFE, SFE_L and SFE_H, on the other hand, are quite different from those obtained at 0°. The SFEs we calculate by applying the Zernike-wise method at 0° and 19° incidence are theoretically identical if the following conditions are met:

- If the actual stack does indeed have homothetic SFEs, and if the thin-film stack we are considering is true.
- If the thin-film physics at oblique incidence is correctly taken into account in the equations of the Zernike method. This has been confirmed several times during this thesis by comparing our results with those of the Optilayer software.
- If bench reproducibility is zero. We know that the latter is of the order of 6 nm RMS and mainly adds an achromatic residue to the measured WFE. As the substrate also induces an achromatic WFE, this residual will mainly have an impact on the calculated SFE of the substrate.

Side effects

We have identified a final cause that could explain the differences between coating SFEs calculated from 0° and 19° data: **edge effects at 19°.** Indeed, it seems that the WFE obtained at 19° have an abnormally high variability compared with the model predictions. Figure 119 (top) shows the modelled and measured WFE at 19° P/N. We can clearly see that the measured WFEs admit very significant variations on their left edge, which was not the case at 0° (see Figure 103). Because of these unexpected edge variations, the RMS value of the maps (Figure 119, down, blue curve) is very high and very chromatic.

As these variations are mainly high spatial frequency aberrations, the Zernike-wise method reproduces the WFE with 55 Zernike modes with difficulty. A 5 nm RMS shift between the two WFE (difference between the blue and red curves) appears between 600 and 750 nm wavelength.

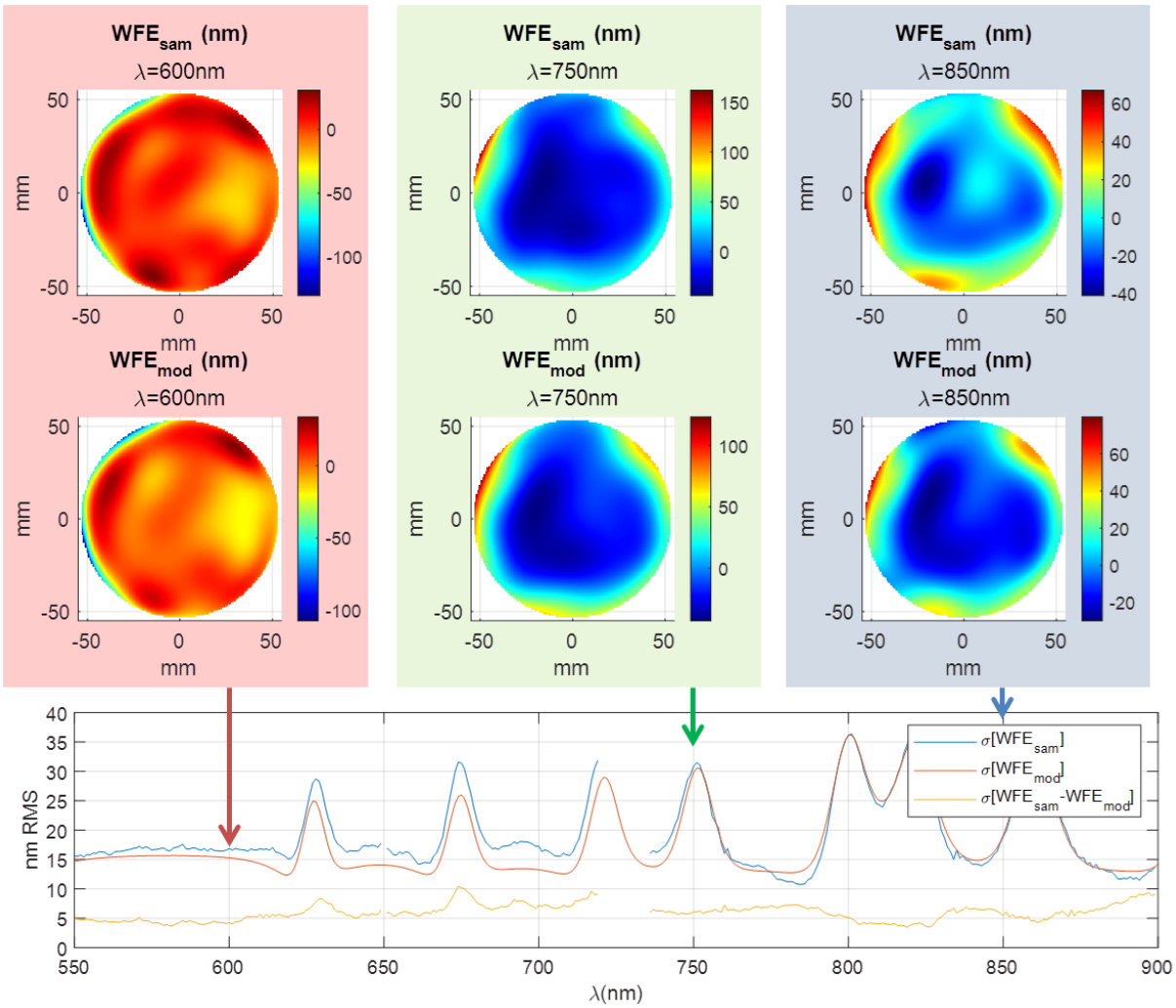

*Figure 119: Comparison between measured WFE (**top**) and modeled WFE (**middle**) at three wavelengths. (**Down**) Standard deviation of measured (blue), modeled (red) WFE, and difference (yellow) is plotted for each wavelength. Used data: WFE on VB, 19°, P/N), Tilts are removed.*

So far, we cannot explain the origin of these edge effects. It is possible that a slight decentering of the WFE maps of the dichroic mirror in relation to the reference plane mirror at 19° could be an explanation. At the moment this assumption is still to be looked into and then implement any necessary corrections using the analysis software.

For the moment, we tried to exclude the edge effects by selecting a smaller pupil diameter. On Figure 120 are the equivalent results to those shown in Figure 117, at 19° S/N. This time, we considered only the WFE on a diameter of 95 mm instead of 108 mm. The median residuals on the WFE are around **1 nm RMS lower** than those obtained on a full 108 mm pupil. Furthermore, we observe that the 95% quantile is 5.75 nm RMS (case where SNR < 5 are removed), compared with 8.5 nm RMS for a 108 mm diameter. Indeed, Figure 117 showed a break-up around the 75% quantile for all tested cases, which is absent here.

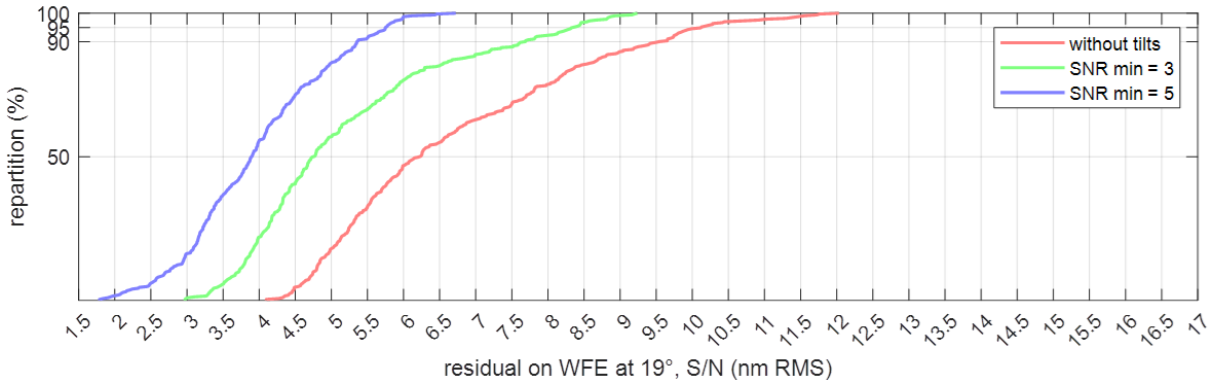

Figure 120: Residuals on WFE reconstruction at 19° expressed as a cumulative distribution for the three filtering cases. The achromatic residual has been removed to all WFE measurement data.

4. CONCLUSION

In this final chapter, we have used the OBSERVE bench with its current precision, which was achieved thanks to the tests carried out in Chapter 5. We have presented here all the WFE measurements we performed on the dichroic mirror during the thesis. The obtained measurements confirm that *Euclid* dichroic mirror does indeed induce a highly chromatic WFE, which can now be characterized using the OBSERVE bench. We then applied the Zernike-wise method, introduced in Chapter 6 to several data sets, notably 0° S/N. Unfortunately, the noise present in the measurements made it impossible to obtain relevant results with the analytical method (see Chapter 6, part 4.2), which was too sensitive. With the Zernike-wise method, we were able to identify the three SFE characterizing the entire dichroic mirror, in several cases: homothetic or non-homothetic. The noise in the measurement limits nevertheless the number of Zernike modes we can retrieve accurately.

All obtained models showed an equivalent performance for reconstructing the WFE with a median deviation of 4.5 nm RMS with respect to the measurements. However, this implies that several mathematical solutions of SFE lead to a same WFE, which means that the fit is degenerated and the actual coating SFE are more difficult to identify than expected. We need to increase the bench accuracy (for example with more averaged measurements) to fit the models properly. We estimate that the homothetic model is currently the best fit at our disposal, and we use it to predict the WFE at 19° (P and S). The reproducibility of the bench, of around 6 nm RMS, had to be taken into account, and we identified that the WFE measured at 19° admits greater chromatic variations than expected. These large variations seem to be due to edge effects, the origin of which is currently under investigations.

In addition, it turns out that the chromatic bias strongly affects the application of the Zernike-wise method. Indeed, this bias includes random chromatic variations whose oscillation period can be of the same order of magnitude as the WFE oscillations that are sought with the bench. This results in resonance effects to which the fit application is highly sensitive. Nevertheless, this shows that the Zernike-wise method and the simulation software presented in Chapter 6 are also very effective tools for analyzing OBSERVE results, and identifying sources of measurement errors that must be considered afterwards.

We have therefore been able to carry out an extensive characterization of the dichroic mirror using OBSERVE measurement data. The results we have obtained raise many questions, and the characterization of this mirror is far to be completed. Next, we plan to repeat the measurements several times to average the noise and reduce experimental biases. Reflectance measurements could be used in addition to further constrain the models.

Conclusion and perspectives

During this thesis, we implemented an innovative metrology bench OBSERVE, devoted to characterize the chromatic properties of the *Euclid* dichroic mirror. Using this bench, we were able to measure the WFE of the *Euclid* dichroic mirror Flight Spare and confirm that the WFE does induce highly chromatic variations, as had been first suspected and then theorized.

The experimental protocol to take data with the OBSERVE bench has been presented and error measurements have been estimated. We show that the bench is highly sensitive to the environment. We have defined several leads for improving the bench's repeatability (3 nm RMS) and above all reproducibility (6 nm RMS), which also include various types of experimental bias and error. Our final objective is a bench with reproducibility better than 2 nm RMS and this will be work out to optimize the experimental protocol and the knowledge of the LMA environment
Despite the present performances, we were able to observe high wavefront distortions, up to 40 nm rms, at specific wavelengths in good agreement with the expectations from the coating design. Besides, very steep variations of the WFE according to the wavelength have been also measured, typically 30 nm rms in less than 10nm, that fully justifies a fine characterization of the dichroic mirror.

We have also presented several methods for fitting models describing the dichroic coating based on physics of thin layers, in order to compute its behavior according to the wavelength, the angle of incidence and the polarization state. The main part of the modeling work presented in this thesis was carried out by simulation, with a series of sensitivity tests. These simulations have shown that it is possible to identify accurately the surface figure errors (SFE) for each material of the stack, either analytically or through multivariate optimization.
The first WFE data from OBSERVE has enabled us to feed the models and retrieve the actual SFE. At the moment, the bench has not yet a reproducibility of 2 nm RMS, which limits the calculation efficiency. It turns out that the models are sensitive to noise, but above all to some experimental biases that were identified during this phase of validation.

One of the goals of the modeling work was to establish a "nonhomothetic" model of the figure errors, i.e. one SFE per material, which is more generalist than the "homothetic" model, i.e. the same SFE. However, the limited precision of the data impacts the final result by producing some anti-correlation between the SFE of each material. To overcome this issue, we need to improve the data accuracy and perhaps correct some chromatic biases introduced by the bench itself. Indeed, the analysis of these data has highlighted the criticality of certain experimental biases, which have an impact not only on the calculation of the models but also on our understanding of the chromatic effects of the dichroic mirror. For the moment, the best model achieved so far, is a homothetic coating model, which reproduces the WFE with an accuracy of around 4.5 nm RMS, without considering any aberration filtering. The agreement is quite good with preliminary studies performed by the coating manufacturer and future improvements in data quantity and quality will enable us to refine the model.

The next step after the work presented in this thesis will be to do the complete characterization of the dichroic mirror, which involves carrying out the entire measurement campaign planned by the *Euclid* Consortium including for instance more oblique measurements. The reflected intensity and PSF of the dichroic mirror will be new areas of work, and will further increase our knowledge of the dichroic component. Once we have a sufficiently accurate "flight-spare" model of the dichroic mirror, it will be delivered to the *Euclid Consortium*, with the final aim of modeling the PSF induced by the flight component.

In conclusion, multi-spectral characterization of the WFE of dichroic mirrors has become an increasingly critical concern within the scientific community, driven by the precision needed for the future measurements in the area of the launch of ambitious current and future astronomical projects. While phase effects dependent on wavelength have been present, they have traditionally remained below the threshold of image quality requirements. However, the advent of ambitious scientific missions like *Euclid*, where the Point Spread Function (PSF) is of paramount importance, has shown the significance of the dichroic mirror coatings in this domain. It is now evident that such characterizations, facilitated by instruments like OBSERVE, will open the door of demands for upcoming projects with even more ambitious objectives. This underscores the evolving nature of optical instrumentation and the heightened precision required to meet the demands of cutting-edge astronomical exploration.